ABSTRACT

Title of dissertation: COMBUSTION INSTABILITY AND ACTIVE CONTROL: ALTERNATIVE FUELS, AUGMENTORS, AND MODELING HEAT RELEASE

Sammy Ace Park, Doctor of Philosophy, 2016

Dissertation directed by: Associate Professor Kenneth H. Yu
Department of Aerospace Engineering

Experimental and analytical studies were conducted to explore thermo-acoustic coupling during the onset of combustion instability in various air-breathing combustor configurations. These include a laboratory-scale 200-kW dump combustor and a 100-kW augmentor featuring a v-gutter flame holder. They were used to simulate main combustion chambers and afterburners in aero engines, respectively. The three primary themes of this work includes: 1) modeling heat release fluctuations for stability analysis, 2) conducting active combustion control with alternative fuels, and 3) demonstrating practical active control for augmentor instability suppression.

The phenomenon of combustion instabilities remains an unsolved problem in propulsion engines, mainly because of the difficulty in predicting the fluctuating component of heat release without extensive testing. A hybrid model was developed to describe both the temporal and spatial variations in dynamic heat release, using a separation of variables approach that requires only a limited amount of experimental data. The use of sinusoidal basis functions further reduced the amount of data

required. When the mean heat release behavior is known, the only experimental data needed for detailed stability analysis is one instantaneous picture of heat release at the peak pressure phase. This model was successfully tested in the dump combustor experiments, reproducing the correct sign of the overall Rayleigh index as well as the remarkably accurate spatial distribution pattern of fluctuating heat release.

Active combustion control was explored for fuel-flexible combustor operation using twelve different jet fuels including bio-synthetic and Fischer-Tropsch types. Analysis done using an actuated spray combustion model revealed that the combustion response times of these fuels were similar. Combined with experimental spray characterizations, this suggested that controller performance should remain effective with various alternative fuels. Active control experiments validated this analysis while demonstrating 50-70% reduction in the peak spectral amplitude. A new model augmentor was built and tested for combustion dynamics using schlieren and chemiluminescence techniques. Novel active control techniques including pulsed air injection were implemented and the results were compared with the pulsed fuel injection approach. The pulsed injection of secondary air worked just as effectively for suppressing the augmentor instability, setting up the possibility of more efficient actuation strategy.

COMBUSTION INSTABILITY AND ACTIVE CONTROL: ALTERNATIVE FUELS, AUGMENTORS, AND MODELING HEAT RELEASE

by

Sammy Ace Park

Dissertation submitted to the Faculty of the Graduate School of the
University of Maryland, College Park in partial fulfillment
of the requirements for the degree of
Doctor of Philosophy
2016

Advisory Committee:
Associate Professor Kenneth H. Yu, Chair/Advisor
Associate Professor Christopher Cadou
Professor Jungho Kim
Associate Professor Raymond Sedwick
Associate Professor Peter Sunderland

© Copyright by
Sammy Ace Park
2016

Dedication

To my parents, my sister, and all those
whose unwavering support allowed me to follow my dreams.

Acknowledgments

I would like to begin by expressing the utmost gratitude to my advisor Dr. Kenneth H. Yu, whose expertise, guidance, and kindness helped me throughout my graduate studies and allowed me to fulfill a life long dream. His door was always open for discussion, no matter the topic of conversation, and I always left feeling enlightened and inspired. In the same spirit, I would also like to thank the members of my committee (listed in alphabetical order by last name) Dr. Christopher Cadou, Dr. Jungho Kim, Dr. Raymond Sedwick and Dr. Peter Sunderland. It has been a long road leading up to the conclusion of my doctoral research and all of these individuals have had a lasting and meaningful impact on both my experience here and my work.

To my colleagues and friends at the Advanced Propulsion Research Laboratory, I would like to say that I literally could not have done this without all of you. Dr. Camilo Aguilera, a constant companion and a steadfast friend with whom I have shared many trials, tribulations, and successes over the many years we have known each other. Dr. Amardip Ghosh and Dr. Qina Diao, mentors who helped me get started in research and friends who were always there with kind words and encouragement. Joe Chung and Jason Burr, whom as undergraduate students spent many a late night in the lab helping me run my experiments and whom as graduate students have become great friends and colleagues. Vijay Ramasubramanian and Dr. Neal Smith, whom have always been willing to offer a helping hand or words of wisdom, I am glad to call you friends. Needless to say, all of you have been

like family to me, without whom I may have never been able to get through this experience in one piece.

To my girlfriend, Jinyoung Kim, who has supported me through both the good times and bad, and has endured more than I ever thought possible: Thank you.

Of course, I owe my deepest thanks to my family - my mother, my father, and my sister who have always stood by me and guided me through my career, and have pulled me through against impossible odds at times. Words cannot justly express the gratitude I owe them.

I would also like to acknowledge financial support from the Naval Air Warfare Center (NAVAIR) - Aircraft Division as well as the Air Force Office of Scientific Research (AFOSR) for all the projects discussed herein.

Truly, it is impossible to remember all and I sincerely apologize to those I've inadvertently omitted. From the bottom of my heart, thank you all!

Table of Contents

List of Tables

List of Figures

List of Abbreviations

Alphabet

A	Model Amplitude
c_p	Specific Heat Capacity at Constant Pressure
d	Diameter
E	Energy
g	Local Rayleigh Index
G	Global Rayleigh Index
h	Convective Heat Transfer Coefficient
h_{lg}	Heat of Vaporization
h_{rp}	Enthalpy of Reaction
k	Thermal Conductivity
Nu	Nusselt Number
p	Pressure
$\overline{p}$	Mean Pressure
p'	Pressure Oscillation
Pr	Prandtl Number
q	Heat Release Rate
$\overline{q}$	Mean Heat Release Rate
q'	Heat Release Rate Oscillation
R	Specific Gas Constant
Re	Reynolds Number
t	Time
T	Temperature
u	Flow Velocity
x	Longitudinal Location
z	Vectorized Spatial Location

Greek Symbols

α	Flame Area
ϵ	Acoustic Energy Density
γ	Ratio of Specific Heats
ν	Kinematic Viscosity
ψ	Model Phase
ρ	Density
τ	Time Period
θ	Pressure Phase

Subscripts

b	Boiling
f	Fuel
g	(Surrounding) Gas
i	Initial
in	Instability
l	Liquid
ref	Reference

1 Introduction

1.1 Background and Motivation

Combustion instability has been an inherent problem in high performance propulsion systems since the advent of rockets and turbojets in the mid-20th century. Unstable combustion is typified by large amplitude pressure oscillations driven by in-phase fluctuation of heat release. The presence of this phenomenon can lead to a number of negative consequences such as increased thermal and mechanical loads, the generation of noise and pollutants, increased plume signature, and, in some cases, catastrophic failure. In order to better understand and control this unwanted behavior, considerable research has been done on this topic over many decades.

One of the earliest explanations of combustion instability goes back to Lord Rayleigh's *The Theory of Sound* written in 1877 [1]. In this work, he emphasizes that the phase relationship between the pressure and heat release oscillations was critical for determining whether vibration is driven or suppressed. During Rayleigh's time, this was merely a scientific curiosity. However, early development of rockets and then afterburners were plagued with many problems, some of which were eventually linked to unstable combustion [2].

Despite the deceptively simple nature of Rayleigh's criteria, combustion instability involves a complex mix of flow and chemical processes. Initial research into the mechanisms of instability in augmentors was conducted by Rogers and Marble (1956) [3]. Even this early on, it was observed that vortex shedding due to bluff bodies played a large role in generating periodic heat release. This was further supported and elborated on by research done on dump combustors in the 1980s such as work done by Smith and Zukoski (1985) [4] and Poinsot et al. (1987) [5]. However, this is one of many elementary processes that have been linked with unsteady heat release and an effort to understand the fundamental mechanisms responsible for combustion instability continues to this day.

Given the apparent complexity in the processes involved in instability, many of the early solutions were a posteriori. This usually involves passive methods such as late-stage design changes to shift unwanted frequencies or the inclusion fixed elements such as acoustic liners, baffles and resonators, a practice that is still commonplace today. Unfortunately, these methods suffer from several drawbacks. The first is that they are costly and they are usually only effective for suppressing higher frequencies because the size of such systems are inversely proportional to the target frequency. Furthermore, they can only be designed for a narrow range of frequencies/operating conditions because of the fixed nature of their design. It would be ideal to predict combustion instability early in the design process using fundamental physics. However, despite strong advancement in computational study, insufficient progress has been made in our fundamental understanding of instability for it to be practical as a design tool as this subject is still inherently semi-empirical [2].

A newer technique was proposed in the 1980s called active instability control that was initially based on the principles of antisound developed by Williams (1984). The basic concept behind this technique lies in the aforementioned Rayleigh criterion, a natural consequence of which is that it is possible to actively suppress instability by establishing control over either the pressure or heat release fluctuations and forcing them out of phase with the other. Of the two oscillations, control over heat release through fuel actuation proved to be the more attractive solution because of the available chemical energy. Even small oscillations in heat release could be comparable to the total acoustic energy in the system and a powerful modifier of pressure oscillations, this leading to what is known as active combustion control. This type of active control system would be ideally suited for dealing with a wider range of lower instability frequencies due to the flexibility afforded by actuating fuel injection.

However, despite the potential of active combustion control as a risk reduction and enabling technology, the increased complexity of such a system has limited its implementation in actual propulsion systems. This is further complicated by the surge in interest in replacing/supplementing conventional aviation fuel with alternative fuels. Since the control authority of this system relies in large part on the combustion response of the actuated fuel, there is naturally a concern about its applicability and effectiveness on these fuel-flexible combustors.

Consequently, there is still much left to be done despite all that is already known about the nature of thermo-acoustic instability. This requires not only a deeper fundamental understanding to improve our abilities in modeling instability,

but also an exploration of related technologies when applied to a changing operational environment. Toward this end, my work in this dissertation seeks to address some the shortcomings listed above through further experiments and theoretical analysis.

1.2 Technical Objectives

The technical objectives of this work are as follows:

- Study the relationship between experimentally observed combustion dynamics to fundamental physical processes in vortex driven combustion instability in airbreathing engine configurations.
    1. Assess the accuracy of reconstructions of local heat release oscillations in the dump combustor based on a simple hybrid model utilizing a sinusoidal basis function and separation of variables approach
    2. Determine the minimum amount of empirical data required to properly characterize combustor stability using this method.
    3. Investigate relationships between this description of heat release to fundamental principles.
- Assess the performance of active combustion control using secondary fuel injection for fuel flexible operation.
    1. Demonstrate instability suppression using alternative fuels in secondary injection.

2. Determine the influence of fuel type on the optimal controller parameters and performance.

3. Perform systematic study of fuel properties to explain observed behaviors.

- Characterize augmentor instability and assess the performance of different active control strategies.

  1. Describe combustion dynamics during low frequency reheat buzz type instability.

  2. Assess the performance of various novel active combustion control techniques in the suppression of augmentor instability.

1.3 Scope of Present Work

This work experimentally investigated three different topics relating to the instability in airbreathing propulsion systems. The first study involves modeling the heat release oscillation during vortex driven instability in a dump combustor. During this type of phenomenon, unsteady combustion is closely tied to the hydrodynamic behavior of the fluid flow. Owing to the complexity of this relationship and the difficulty of making direct measurements within a combustion chamber, theoretical treatment of this subject is intrinsically semi-empirical. A simplified model is proposed with the intention of minimizing the required empirical data needed to accurately model the instability for the purpose of characterizing combustor stability. This minimum is sought with the goal of obtaining further insight into the mecha-

nisms of combustion instability and to provide a more practical means of conducting stability analysis during combustor design.

The second study involves investigating the influence of fuel type on the performance of active combustion control. Recently, there has been a surge in interest in using alternative fuels such as biofuels and Fischer-Tropsch fuels in existing propulsion systems. However, the authority of this type of control system relies in large part on the combustion response of secondary fuel injection. Since it utilizes a portion of the main fuel, the potential variation in fuel properties during fuel flexible operation may affect the performance of such a system. Therefore, instability suppression using alternative fuels is first demonstrated and then their effect on the optimal controller parameters and performance are investigated.

The third study involves an augmentor using a v-gutter type flameholder. Although the mechanism of instability in such a configuration has been studied, there is still a lack of detailed visualizations used to describe this process. Furthermore, several novel techniques of active combustion control are evaluated for use on this type of system configuration, including main fuel modulation and secondary air injection. The advantage of these techniques are that they require less invasive modifications to the combustor structure and attempts to utilize air, which is available in abundance in typical propulsion systems.

In this dissertation, the literature is reviewed in Chapter 2 with regards to the research that has already be done to investigate the mechanisms of instability as well as existing research in the control and suppression of the process. In Chapter 3, the experimental equipment is described and some key visual diagnostics techniques

are described. Chapter 4 presents the heat release modeling results as well as the subsequent stability analysis. Chapter 5 describes the results of active combustion control using various fuel types and reveals how the fuel type influences the controller. Chapter 6 examines the flow processes involved in augmentor instability as well as the results of the various active control techniques. Finally, the findings of this work is summarized in Chapter 7.

2 | Literature Review

2.1 Stability Analysis

One of the earliest descriptions of thermoacoustic coupling comes from Lord Rayleigh's (1877) *The Theory of Sound* [1] in which he observed that

> *If heat be periodically communicated to, and abstracted from, a mass of air vibrating (for example) in a cylinder bound by a piston, the effect produced will depend on upon the phase of the vibration at which the transfer of heat takes place. If heat be given to the air at the moment of greatest condensation, or to be taken from it at the moment of greatest rarefaction, the vibration is encouraged. On the other hand, if heat be given at the moment of greatest rarefaction, or abstracted at the moment of greatest condensation, the vibration is discouraged.*

Combustion instability is then the condition in which vibration is encouraged. This is the foundation of the Rayleigh's criterion, which is still used as a characterization of combustor stability.

This was further elaborated on in the mid-20th century by Putnam and Dennis (1954) [6], who stated that an elementary mathematical representation of Rayleigh's

criterion that must be satisfied for unstable combustion is given by the inequality as shown in Eq. 2.1.

$$\int_{\tau_{in}} q(t)p'(t)\,dt > 0 \tag{2.1}$$

Here τ_{in} is the period of instability, q is the rate of heat release, and p' is pressure fluctuation. This is consistent with Lord Rayleigh's observation in that if q and p' are in-phase with one another, as is required for unstable combustion, then the integral of their product must be greater than zero.

Early research such as those conducted by Roger and Marble (1956) [3], and Flandro and Jacobs (1973) [7] showed that flame dynamics is a key mechanism of instability (see §2.2). As such, mathematical representations of Rayleigh's criterion must also account for the spatial dependence, which can been seen in later works where it is also explicitly related to the change in the acoustic energy of the combustion system. The derivation and the corresponding assumptions based on the work of Chu and Kovasznay (1957) [8], Chu (1965) [9], and Culick (1976) [10] [11] are briefly reviewed below.

If a flow of perfect gas is assumed to be inviscid and stationary with negligible thermal conduction to its surroundings, then the differential conservation equations of mass (Eq. 2.2), momentum (Eq. 2.3), and energy (Eq. 2.4) in the longitudinal direction are as defined below.

$$\frac{\partial \rho}{\partial t} + \frac{\partial(\rho u)}{\partial x} = 0 \tag{2.2}$$

$$\rho\frac{\partial u}{\partial t} + \rho u\frac{\partial u}{\partial x} + \frac{\partial p}{\partial x} = 0 \tag{2.3}$$

$$\rho\frac{\partial e}{\partial t} + \rho u\frac{\partial e}{\partial x} = -p\frac{\partial u}{\partial x} + q \tag{2.4}$$

In these equations, t and x are the time and location, respectively, while ρ is the density, u is the flow velocity, p is the pressure, and e is the specific internal energy. Furthermore, the equation of state is given by the ideal gas law as shown in Eq. 2.5

$$p = \rho RT \tag{2.5}$$

where R is the specific gas constant and T is the temperature.

During the onset of instability, only small flow perturbations are considered and so a linear description of these parameters can be used that consists of a mean and fluctuating component as shown in Eqs. 2.6, 2.7, 2.8, and 2.9.

$$\rho(x,t) = \overline{\rho}(x) + \rho'(x,t) \tag{2.6}$$

$$u(x,t) = \overline{u}(x) + u'(x,t) \tag{2.7}$$

$$p(x,t) = \overline{p}(x) + p'(x,t) \tag{2.8}$$

$$q(x,t) = \overline{q}(x) + q'(x,t) \tag{2.9}$$

In these equations, the overbar indicates the mean and the prime represents the fluctuation. The change in acoustic energy inside the combustion chamber as shown in Eq. 2.10 can be obtained by substituting these separated parameters into and

manipulating the conservation equations such that

$$\frac{\partial \epsilon}{\partial t} + \overline{u}\frac{\partial \epsilon}{\partial x} = \frac{\gamma - 1}{\gamma}\frac{p'q'}{\overline{p}} - \left(\rho' u' \overline{u} + \frac{p'^2}{\overline{p}}\right)\frac{\partial \overline{u}}{\partial x} - \frac{\partial (u'p')}{\partial x} - \frac{u'p'}{\gamma \overline{p}}\frac{\partial p'}{\partial x} \tag{2.10}$$

where γ is the ratio of specific heats and ϵ is the acoustic energy density as defined in Eq. 2.11.

$$\epsilon = \frac{\overline{\rho} u'^2}{2} + \frac{p'^2}{2\gamma \overline{p}} \tag{2.11}$$

The first term in Eq. 2.10 can be physically interpreted as the kinetic acoustic energy, while the second term represents the potential acoustic energy. The right hand side can then be though of as the acoustic sources. For combustion instability, the heat release is the dominant source of acoustic energy and as such, Eq. 2.10 can be reduced to Eq. 2.12.

$$\frac{D\epsilon}{Dt} \approx \frac{\gamma - 1}{\gamma}\frac{p'q'}{\overline{p}} \tag{2.12}$$

Integrating this expression generates a familiar form of Rayleigh's criterion as the change in acoustic energy shown in Eq. 2.13.

$$\Delta E \approx \frac{\gamma - 1}{\gamma} \int_V \int_{\tau_{in}} \frac{p'q'}{\overline{p}}\, dt\, dV \tag{2.13}$$

This can also be used as the basis for a local Rayleigh index, $G(z)$, as defined in Eq. 2.14, which will be used to quantify the level of coupling that occurs between

pressure and heat release oscillations at a given location.

$$g(z) = \frac{1}{\tau_{in}} \int_{\tau_{in}} \frac{p'(z,t)q'(z,t)}{q_{ref}p_{ref}}\, dt \tag{2.14}$$

Note that this is just the non-dimensionalized time integral component of Eq. 2.13 and just as with Rayleigh's criterion, unstable combustion is represented by $g > 0$, while $g < 0$ indicates stable combustion and $g = 0$ describes limit-cycle behavior.

2.2 Combustion Dynamics

As illustrated by Rayleigh's criterion, combustion instability can be simply described as the generation of noise due to resonant coupling between pressure and heat release oscillations. In actuality, this phenomenon is a complex mix of coupled flow and chemical processes [12], and given its impact on high-performance propulsion systems, it has spurred considerable experimental and theoretical research [13] [14] [15] [16] [17] [18]. Of the numerous fundamental mechanisms [19] [20] that have been studied with respect to unstable combustion, this review will be mainly limited to flame/vortex interaction [21].

One of the earlier studies into the relationship between vortices and instability in high performance air-breathing propulsion systems was done by Roger and Marble (1956) [3]. They described high frequency "screech"-type instability[1] in ramjets and afterburners as resulting from periodic heat release caused by the transport

[1] There are three broad categories of instability that can be present in propulsion systems: (1) high frequency instability or "screech", (2) intermediate frequency instability or "buzz", and (3) low frequency instability or "chug". The categorization of a particular frequency depends on its wavelength with respect to the characteristic length of the combustor. [22]

of unburnt reactants into hot zones by vortices shed off a bluff body flameholder. Since the shear layer that formed the vortex is highly turbulent, the convected combustible material becomes well mixed with hot gas and burns intensely after some time leading to oscillating heat release. Instability would result if its phasing satisfies Rayleigh's criterion and it is of sufficient magnitude to overcoming any damping effects.

Smith and Zukoski (1985) [4] also described a similar mechanism of instability that was linked to the formation of large coherent vortical structures, this time in single dump combustors. They postulated that large velocity fluctuations near the flameholder caused by strong acoustic oscillations may produce large vortices at the same frequency. This would subsequently create fluctuations in heat release that would peak when the vortex impinged the combustor wall, which was properly phased to satisfy Rayleigh's criterion. An elaboration on this particular mechanism as low frequency, longitudinal mode instability in dump combustors by Sterling and Zukoski (1987) [23] [24].

In a detailed experimental study, Poinsot et al. (1987) [5] also show that can interaction between neighboring vortices can also lead to combustion instability. Vortex shedding was shown to occur when the velocity fluctuations at the inlet plane reaches its maximum. These large coherent structures then grow as they are convected downstream and interact with neighboring vortices. This interaction produces intense small scale turbulent mixing, which causes the fluctuating heat release to peak while the pressure oscillation is positive thus satisfying Rayleigh's criterion.

Yu et al. (1991) [25] showed that vortex driven instabilities can be segregated into two types: (1) acoustic mode and (2) convective mode. The acoustic mode is the phenomenon as described above by Smith and Zukoski (1985) [4], Sterling and Zukoski (1987) [23], and Poinsot et al. (1987) [5]. In this mode, both the vortex shedding and the resulting heat release fluctuation couple strongly with the combustor acoustics. However, in the convective mode, vortices are shed due to Kelvin-Helmholtz instability in the shear layer. These then interact with obstacles and reflect pressure waves that in turn modulate the shedding process. The key difference between the two modes is that while convective mode oscillations eventually couple with the acoustics, they need not occur at the sound wave eigenfrequencies.

As for augmentor systems in particular, low frequency "reheat buzz" instability was experimentally investigated in great detail by Langhorne et al. (1988) [26] [27]. For these experiments, the flame was stabilized in a conical gutter. In this configuration, Langhorne observed two distinct modes of instability: (1) convecting mode and (2) concurrent mode. In the convecting mode, perturbations in the flame convect downstream at the reactant velocity, creating regions of both driving and damping. On the other hand, during the concurrent mode, the leading edge of the flame travels downstream such that it closely follows the pressure. Consequently, the convecting mode is referred to as weak buzz while the concurrent mode is called established buzz.

More recently, instability research has also been extended to lean premixed combustors designed to reduce pollutant emission as it has been shown that these types of combustors are susceptible to similar types of instability [28] [29] [30] [31]

[32]. Current experimental studies on the mechanisms of combustion instability have been done by Ghoniem et al. (2005) [33] and Murat Altay et al. (2009) [34] [35]. Computational studies leveraging modern technology and techniques have been done by Poinsot et. al (1996) [36] [37] and Fureby (2000) [38]. Modern comprehensive overviews of combustion instability and its many fundamental mechanisms have been written by Culick (1988, 2001) [19] [2], Candel (1992, 2002) [39] [20], and Renard et al. (2000) [40]. Furthermore, a textbook on unsteady combustor physics covering many of the basic principles has been written by Lieuwen (2012) [41].

2.3 Instability Suppression

The earliest techniques for dealing with combustion instability fall under the category of *passive control*. There are two main methods to achieve instability suppression using this technique. The first natural solution is to redesign the combustor in order to alter its natural frequencies. The other is to dampen the resulting pressure fluctuations. As the category suggests, these dampening techniques involve fixed devices such as acoustic liners, baffles, and resonators. This is written about extensively in *Combustion-Driven Oscillations in Industry* by Putnam (1971) [42] as well as by Garrison et al. (1972) [43].

Unfortunately, despite the simplicity these types of solutions, they suffer from several drawbacks. One is that they are very costly, both in terms of time and money but also in terms performance. Another is that passive damping systems scale inversely with the target frequency and as such are only of practical use for

high frequency instability. Additionally, the static nature of these devices means that only a limited range of frequencies can be addressed by these types of systems.

The idea of *active instability control* seems to have originated from the work on "antisound", which is thoroughly reviewed by Williams (1984) [44]. Williams describes the principles by which acoustic fields can be mimicked and canceled by secondary sources. The key properties of active control is that it utilizes dynamic actuation controlled via feedback to affect combustor response. In contrast to passive methods, such a system could handle lower and wider ranges of instability frequencies. The flexibility provided by this type of system allows it to be used as a risk reduction/enabling technology.

A natural application of this technique to combustion instability is to neutralize the pressure oscillations that either contribute to or result from instability. This potential use was acknowledged by Williams in his original work. Indeed, early attempts at active control were done with loudspeakers in order to directly affect the acoustics, as done by Poinsot et al. (1989) [45] and Gulati and Mani (1992) [46].

However, it has been known that the acoustic energy involved is small compared to the available chemical energy [2]. Furthermore, Rayleigh's criterion does not distinguish whether pressure or heat release oscillations, if properly controlled, would lead to the suppression of instability. This is the fundamental principle behind *active combustion control*. Authority over the dynamic heat release could be achieved by diverting a small amount of fuel for dynamically actuated secondary injection as demonstrated by Langhorne (1990) [47]. Similar experiments were done at a laboratory-scale by Hantschk et al. (1996) [48], Yu et al. (1996,1998) [49] [50],

and Neumeier and Zinn (1996) [51]. Secondary fuel injection on a full-scale system was first done at Siemens by Seume et al. (1997) [52].

Other active control techniques involve disrupting the coherent structure as shown by McManus and Bowman (1990) [53] and Ghoniem et al. (2005) [54]. Bloxsidge et al. (1988) demonstrated instability suppression using a novel technique that involved the active control of the acoustic boundaries [55]. Lee et al. (2011) also demonstrated instability suppression by modifying liquid spray properties [56]. Recent research has involved the improvement of active control techniques through more advanced controller algorithms [57] [58] [59] [60] and subharmonic injection [61] [62]. An extensive overview of combustion control methods and technology is provided by Docquier and Candel (2002) [63].

3 | Experimental Methodology

3.1 Dump Combustor Setup

The active control experiments were performed on a 200 kW nominal power dump combustor. The combustor itself has a total length of 495.3 mm (19.5 in) with the dump plane located 152.4 mm (6 in) downstream of the beginning of the combustor. This combustor inlet section has a rectangular cross-section 38.1 mm (1.5 in) tall and 44.5 mm (1.75 in) wide. Immediately downstream of the dump plane is the test section which has a length of 228.6 mm (9 in) that ends at the nozzle. The cross-sectional area has a 57.2 mm (2.25 in) height and a 44.5 mm (1.75 in) width, giving the dump plane a height of 19.1 mm (0.75 in). A schematic of the combustor is shown in Fig. 3.1.

Two 25.4 mm (1 in) thick blocks are used to attach the combustor to a circular inlet pipe with a 50.8 mm (2 in) diameter, and were designed to seamlessly blend the circular and rectangular cross-sections as well as to house a flow straightener. This pipe is 2413 mm (95 in) long starting from an air-flow regulating orifice. The main fuel injection occurs close to this orifice in order to provide sufficient time for premixing. Moreover, gaseous ethylene was chosen as the main fuel in order to

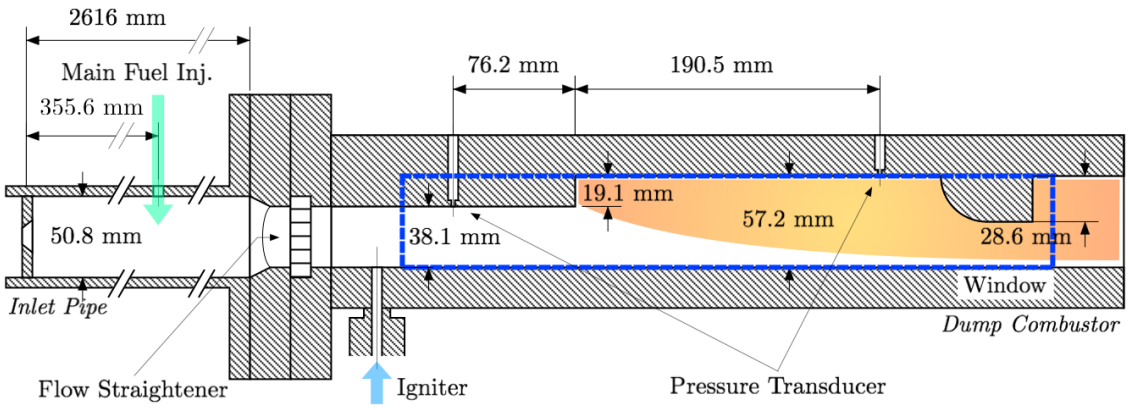

Figure 3.1: An illustrated schematic of the laboratory scale dump combustor.

simulate pre-vaporized fuel in the dump combustor. Although the flow was initially ignited using an pilot flame, combustion in the dump combustor was anchored at the dump plane and self-sustaining for the duration of the test.

A pair of flush-mounted pressure transducers (Kistler 211B5) were used to simultaneously measure the pressure oscillations in both the combustor inlet and test section. The pressure oscillations, along with the various fuel pressures, were recorded using a NI LabVIEW-based data acquisition system. Choked flow through metering orifices were used to obtain the targeted test conditions. A quartz glass window provided visual access into the test section which allowed for CH* chemiluminescence image capture of the flame. This process was synchronized with the pressure oscillation measurements using a National Instruments (NI) LabVIEW-based real-time control system. The reference point for all of the phase calculations was the negative-to-positive zero-crossing of the oscillating dump combustor pressure.

The active control system consisted of a dynamically actuated fuel injector that was controlled using the NI LabVIEW-based real-time control system and

synchronized with the pressure oscillation measurements. More specifically, the controller-based injection timing was designed to target the observed primary instability frequency. The injector was mounted in-line with a swirl-type atomizer at the dump plane such that the secondary fuel is injected into the shear layer at an angle of 45° with respect to the bulk flow direction. This configuration was based on a previous study on optimizing injection location as well as a characterization of the local Rayleigh index distribution discussed in the following sections. Furthermore, the fuel flow was distributed such that 92% was injected into the dump combustor as main fuel in terms of total thermal output.

3.2 Augmentor Setup

The experiments were performed on a 100 kW nominal power model augmentor setup. It is provided high enthalpy flow by a primary combustor installed immediately upstream. The two combustors are separated by an acoustic isolator that defines the augmentor's upstream boundary condition. A schematic of the augmentor is shown in Fig. 6.3. The primary combustor (not shown) is a stainless steel tube with a cross-sectional diameter of 76.2 mm (3 in) and a total length of 1219 mm (48 in). The very fuel-lean primary combustion is sustained with a pilot flame whereas the augmentor combustion is self-sustaining. The augmentor inlet has the same circular cross-section that transitions to a rectangle 57.2 mm (2.25 in) tall and 44.5 mm (1.75 in) wide. The circular inlet has a length of 717.6 mm (28.25 in) while the rectangular section is 616 mm (24.25 in) long with a transition that occurs over

a 25.4 mm (1 in) span. This puts the overall length of the augmentor at 1359 mm (53.5 in).

In this configuration, the excess air from the primary combustor was used in the augmentor to achieve after-burning. Gaseous ethylene was used as a surrogate fuel in both the primary combustor and the augmentor. The augmentor uses a v-gutter style flame-holder that has a height, h, of 19.1 mm (1.75 in) and is located 171.5 mm (6.75 in) downstream of the transition section. A rod that traverses the entire width of the augmentor is used as the fuel injector, which is located 139.7 mm (5.5 in) upstream of the flame-holder. A liquid fuel injector was also installed 25.4 mm (1 in) upstream of the of the augmentor fuel injector for experiments that required a supplement of conventional jet fuel.

A wall mounted pressure transducer (Kistler 211B5) was used near the transition to measure pressure oscillations in the augmentor combustion chamber. A thermocouple (type K) measured the flow temperature from the same longitudinal location, which averaged around 600 K for these experiments. These measurements, along with the various fuel and oxidizer pressures, were recorded using a LabVIEW-based data acquisition system. Choked flow through metering orifices were used to obtain the targeted test conditions. A pair of quartz glass windows provided visual access into the test section, and both chemiluminescence and schlieren image capture were synchronized with the pressure oscillation measurements using a LabVIEW-based real-time control system. The reference point for all of the phase calculations is the negative-to-positive zero-crossing of the oscillating pressure. The various control strategies tested on the augmentor are detailed in §6.1.

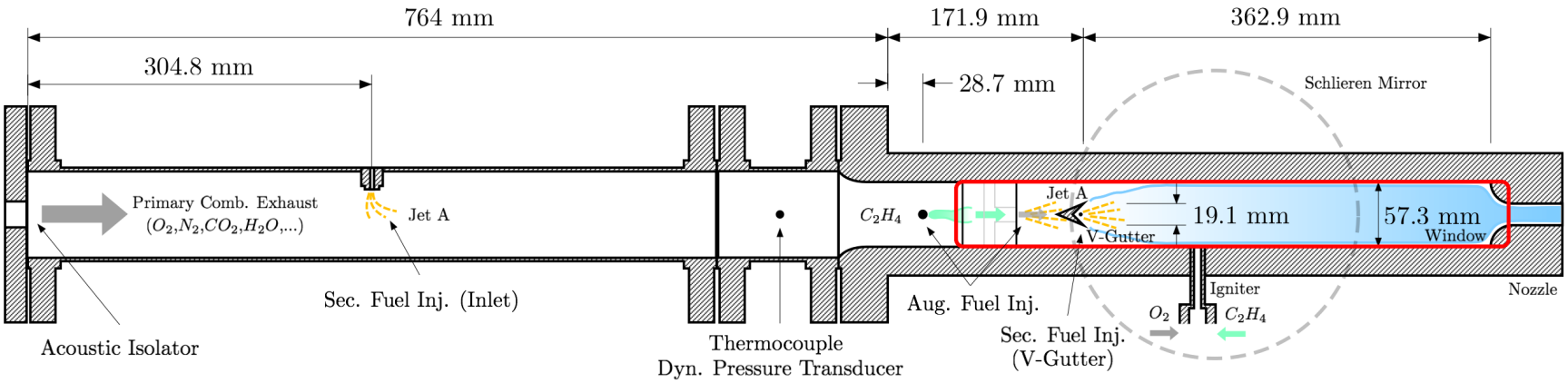

Figure 3.2: An illustrated schematic of the laboratory scale augmentor.

3.3 Brief Overview of Chemiluminescence

The basic principle behind chemiluminescence is that light is emitted at a very specific wavelength by the relaxation of excited radicals created by intermediate reactions of a combustion process. These radicals are concentrated in the flame ergo the luminescence intensity is indicative of combustion, which varies linearly with the rate of heat release [64]. For organic flames (i.e. those involving hydrocarbon fuels), excited CH-radicals (CH*) are created that emit light at approximately 4315 Å [65]. The mechanism by which CH* emit luminescence is beyond the scope of this overview but is covered in great detail in *The Spectroscopy of Flames* by Gaydon (1957) [65]. Hurle et al. (1968) [64] is an early example chemiluminescence being used as a visual diagnostic tool for instability research and it has since been used in many other experimental studies [66]. The same diagnostic technique is used to image the combustion process in this work. In order to visualize only the flame using CH*, an intensified charge-coupled device (ICCD) camera equipped with a 430 nm bandpass optical filter is used to image the flame through a quartz glass window. An intensified camera is used since the filter reduces the total amount of light entering the lens.

3.4 Brief Overview of Schlieren

Schlieren is one of the earliest visualization techniques used in the study of fluid flow structures. It uses the refraction of collimated light that is passed through

a test section to visualize density gradients in the flow. If a point light source is used to create the collimated beam of light it can be focused to a point after it has passed through the test section. Then a 'cutoff' can be used at the focal point to partially block light, which has the effect of uniformly reducing the intensity while increasing the contrast across the gradient. A simple illustration of this setup is shown in Fig. 3.4. This produces a *schlieren* image that represents the first derivative of the density in the direction of the cutoff. However, if a 'cutoff' is not used, then a similar image called a *shadowgraph* is generated that represents the second derivative of density. Both of these imaging techniques are described in detail by Settles (2001) [67]. For the augmentor experiments, schlieren images are captured during unstable combustion using a high-speed camera for the purpose of acquiring sequential images of the flow processes within a single cycle of instability.

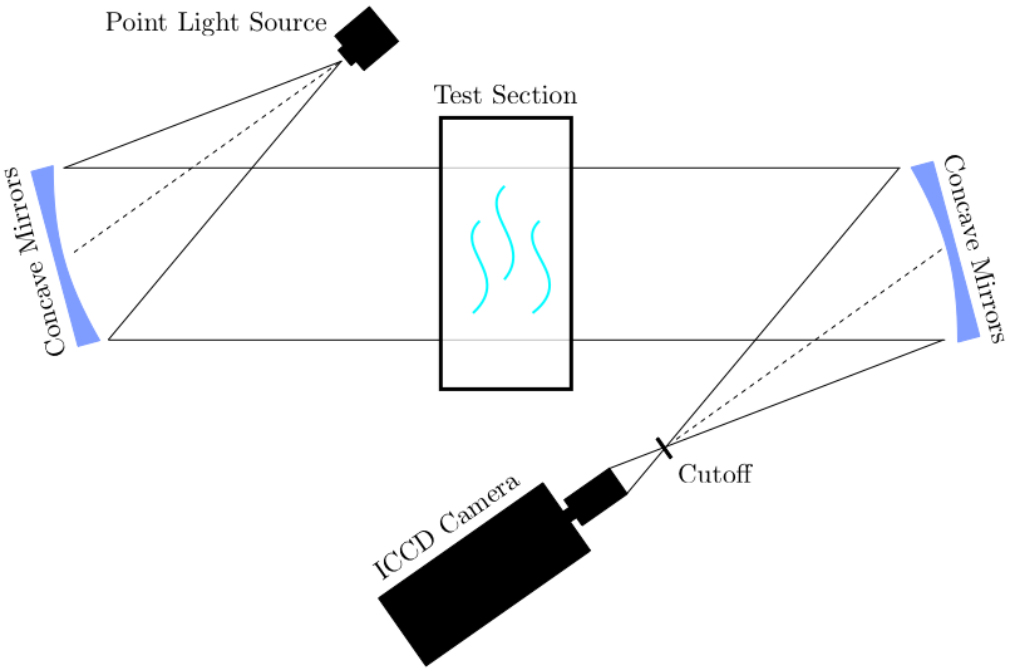

Figure 3.3: A simple illustration of a typical schlieren setup.

4 | Modeling Heat Release Oscillations for Combustor Stability Analysis

4.1 Experimental Results

In the experimental characterization of the flame, a flow velocity of 45±2 m/s and an equivalence ratio of 0.67±0.03 was targeted for naturally unstable operation of the combustor. At these conditions, pressure oscillations were predominantly observed at 150 Hz as indicated by Fig. 4.1. The dynamic flow structures are also shed at this frequency. It should be noted that the negative-to-positive zero crossing of the bandpass filtered dynamic pressure measurements taken near the nozzle were used as the reference phase (i.e. $\theta = 0$).

A select sample of phase locked images showing the instantaneous CH* chemiluminescence intensity are shown in Fig. 4.2. For this work, eight different pressure oscillation phases, θ (i.e. ωt), were selected for investigation. A set of 200 images were obtained and averaged for each θ. These phase-averaged images as well as the cycle-averaged image are shown in Fig. 4.3. The normalized local fluctuations of chemiluminescence intensity (Fig. 4.4) were obtained by subtracting the cycle-

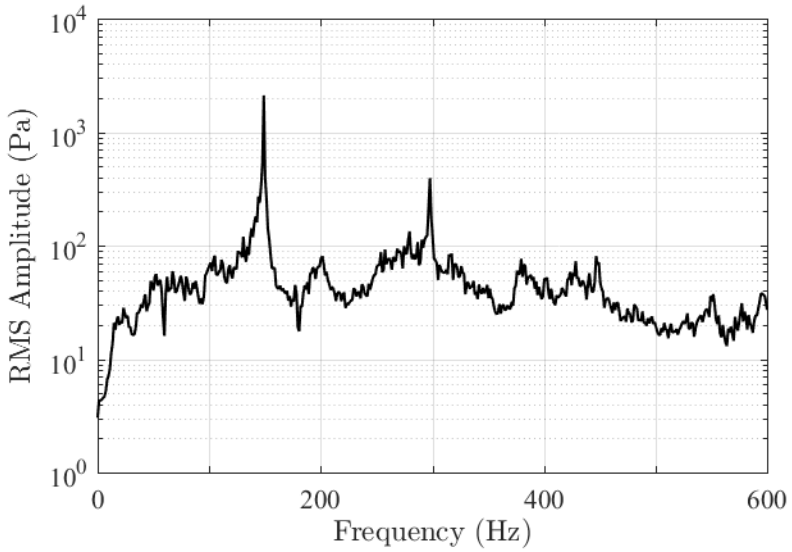

Figure 4.1: The frequency spectra for the pressure oscillations measured in the dump combustor (at the nozzle) during baseline operation.

average (Fig. 4.3b) from each of the phase-averages (Fig. 4.3a). These images (Fig. 4.4) constitute the normalized heat release oscillation maps.

4.2 Reduction of Parameters

If it is assumed that the temporal variations of q' can be described using a sinusoidal basis function, the number of required parameters to fully describe q' can be reduced to just the amplitude (A), heat release-phase (ψ) and time (t) as described in Eq. 4.1.

$$\frac{q'(z,\theta)}{q_{ref}} = A(z)sin(\theta + \psi(z)) = A(z)Im(e^{i\theta}e^{i\psi(z)}) \tag{4.1}$$

Both A and ψ are solely spatial functions and can be calibrated using experi-

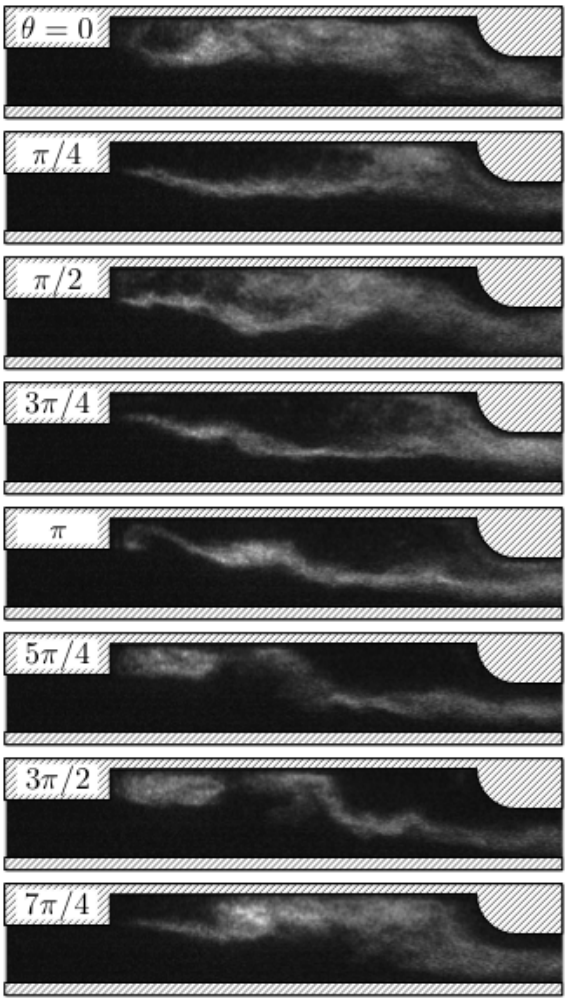

Figure 4.2: A sample set of near instantaneous phase-locked CH* chemiluminescence images for flame visualization.

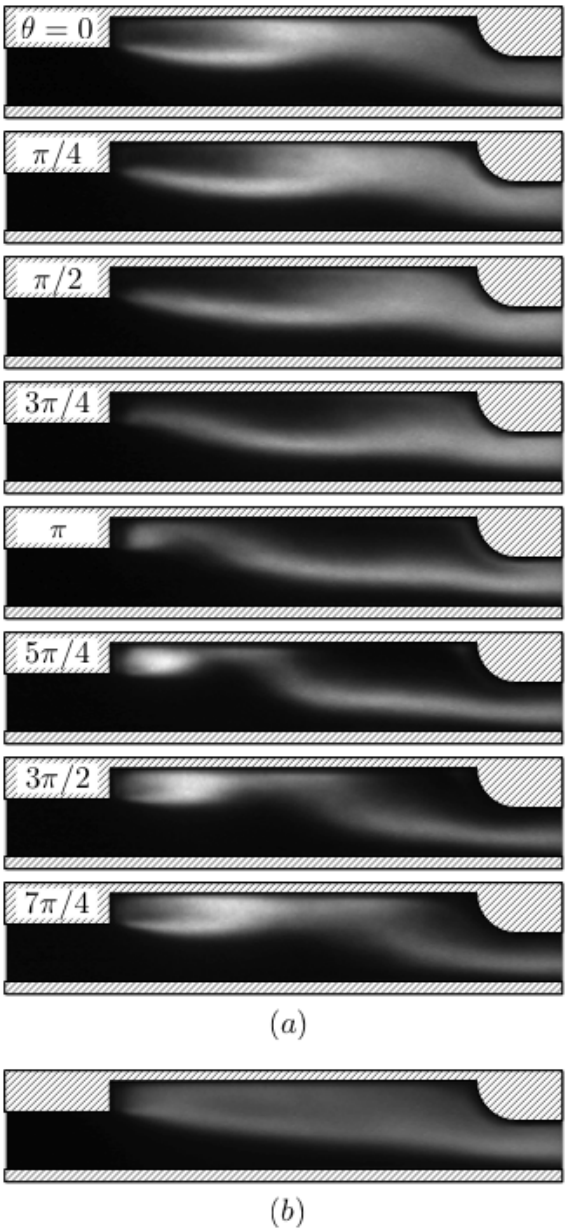

Figure 4.3: A set of CH* chemiluminescence images showing (a) phase-averaged and (b) cycle-averaged flame images.

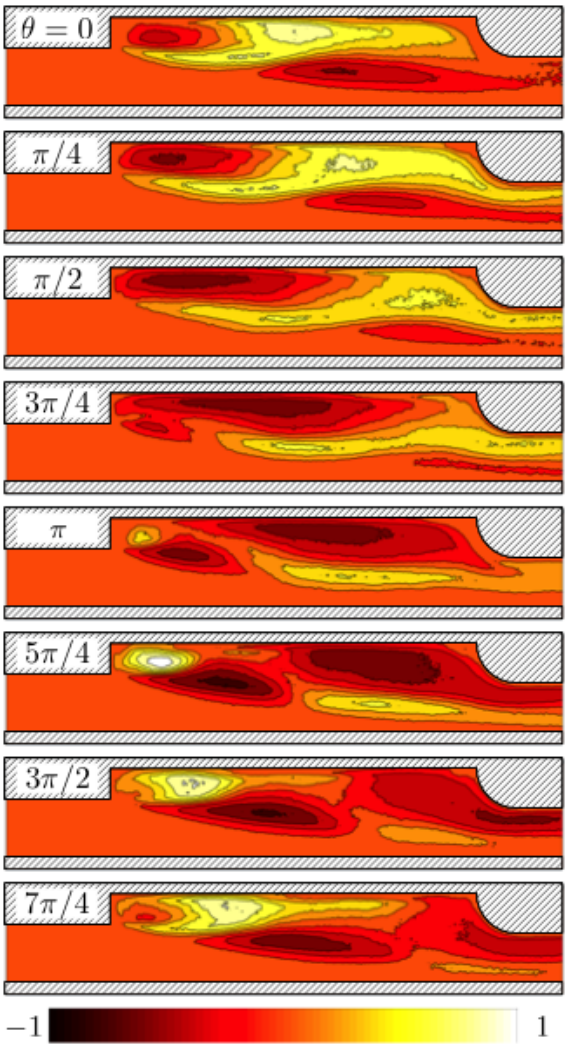

Figure 4.4: A map of spatially-resolved heat release at each phase directly calculated from experimental data.

mentally obtained results where A is given by Eq. 4.2.

$$A_{cal}(z) = \frac{\max_{\theta}(q'(z,\theta)) - \min_{\theta}(q'(z,\theta))}{q_{ref}} \tag{4.2}$$

Furthermore, ψ can be obtained by fitting the basis function to the temporal variation of heat release such that ψ minimizes the L2-norm of the model deviations as defined in Eq. 4.3. This represents the amount of local heat release deviation per *total* heat release in the unit area, and is used as a measure of how well q' is captured by the model. The total area is denoted by α.

$$\sigma(z) = \Big(\frac{1}{\alpha N}\sum_{i=1}^{N}\Big[A_{cal}(z)sin(\theta_i + \psi_{cal}(z)) - \frac{q'_{exp}(z,\theta_i)}{q_{ref}}\Big]^2\Big)^{\frac{1}{2}} \tag{4.3}$$

Visualizations of A_{cal} and ψ_{cal} are shown in Fig. 4.5 while σ_{cal} are shown in Fig. 4.6. Unsurprisingly, σ_{cal} is low over much of the combustion chamber which indicates a high model accuracy and substantiates the simplifying assumptions. This is clear when the model reconstructions, shown in Fig. 6.3, are compared against the experimentally obtained results (Fig. 4.4). Higher σ is concentrated in the region where the shear layer fluctuates. A closer examination of this region (Fig. 4.8) reveals that q' is non-sinusoidal and perhaps multi-modal in nature, which would not be captured by this uni-modal model.

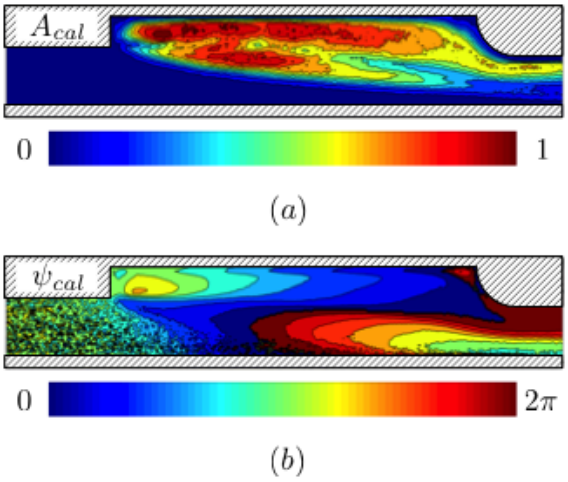

Figure 4.5: Maps showing the distribution of (a) local model amplitude, A_{cal}, and (b) local model phase, ψ_{cal}, calibrated using experimental data.

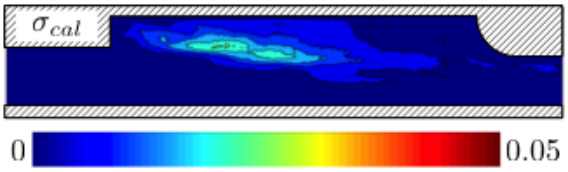

Figure 4.6: Maps showing the distribution of model error when using calibrated model parameters.

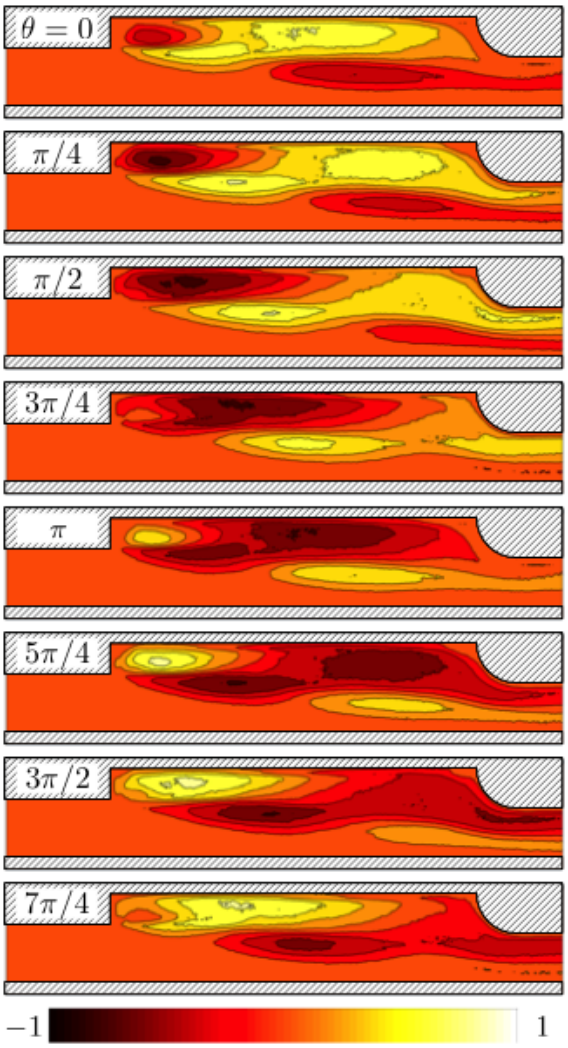

Figure 4.7: A map of spatially-resolved heat release at each phase reconstructed from the model using empirically calibrated parameters.

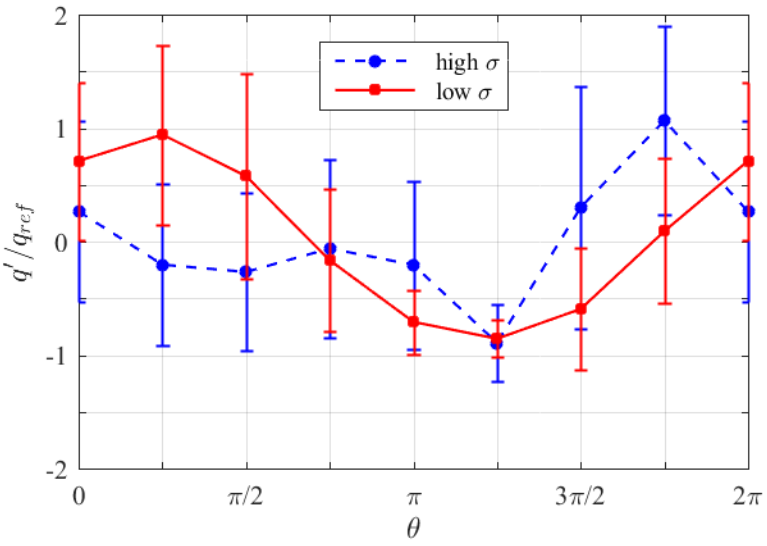

Figure 4.8: A comparison of the empirical heat release oscillations at locations with extreme values of σ.

4.3 Estimating Reduced Parameter Distributions

A simple manipulation of Eq. 4.1 shows that ψ is obtainable using only A and q' at $\theta = \pi/2$ (i.e. peak combustor pressure) as described in Eq. 4.4. Although there are many mathematical representations of this relation, this particular interpretation is most useful for stability analysis because the regions of elevated q' at the peak combustor pressure will couple most strongly during the onset of instability.

$$\psi_{est}(z) = Re\Big(arccos\Big[\frac{q'(z,\pi/2)}{A(z)}\Big]\Big) \tag{4.4}$$

This expression however requires foreknowledge of A in order to produce ψ. A physically intuitive estimate of A given the behavior of the flame is that $A_{est}(z) \propto \overline{q}(z)/q_{ref}$ (Fig. 4.9). A qualitative comparison between A_{est} (Fig. 4.5a) and A_{cal}

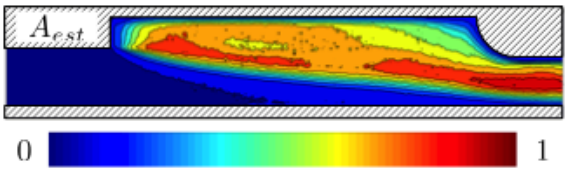

Figure 4.9: An estimated distribution of local model amplitude based on observations of the flame dynamics.

(Fig. 4.9) show that while there is some discrepancy at the nozzle, the two are largely similar. Furthermore, it should be noted that Eq. 4.4 can only determine if the q' is in- or out- of-phase with the pressure due to the properties of inverse cosine. This limitation introduces some additional errors to the model.

In order to see the influence of the phase limitation, let ψ_{cal} (Fig. 4.5) from the previous section be modified to artificially restrict the maximum to π, such that it becomes ψ_{lim} as shown in Fig. 4.10. This is possible because we are assuming this to be a cyclical phenomenon. Using the same A_{cal}, the model error for this phase limited case, σ_{lim}, is shown in Fig. 4.11. This distribution of σ_{lim} shows that additional errors are introduced in the recirculation zone and near the nozzle by restricting the range of ψ. That said, the model reconstruction shown in Fig. 4.12 strongly resembles the empirical results (Fig. 4.4).

With that in mind, the distribution of ψ_{est} is shown in Fig. 4.13. From σ_{est} shown in Fig. 4.14, the decrease in model accuracy is evident although it can be inferred that any additional discrepancies are largely due to estimating A_{est} with $\overline{q}$ and limiting ψ_{est} to a range between 0 and π. However, the modeled heat release oscillations shown in Fig. 6.3 were predictably able to capture the dynamic flow features observed inside the combustor.

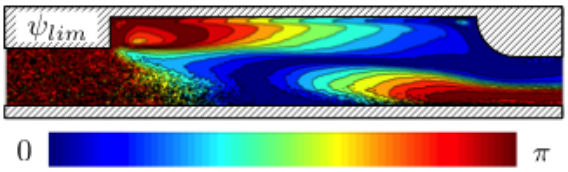

Figure 4.10: The calibrated local model phase distribution artificially restricted to a maximum value of π.

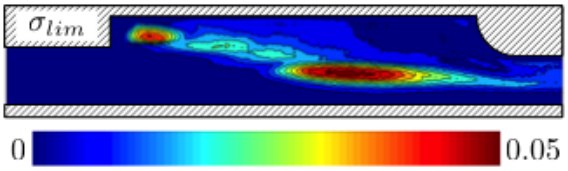

Figure 4.11: Maps showing the distribution of model error when using a restricted model parameters calibrated.

4.4 Characterizing Combustor Stability

The local Rayleigh index is a convenient way to express the distributed coupling of pressure and heat release oscillations throughout the combustor and is defined in this paper by Eq. 2.14. In these calculations, the combustor pressure oscillation as shown in Fig. 4.16 is used throughout the combustor as it is compact with respect to the instability wavelength. The reference pressure is given by the contribution of the combustor pressure to instability, which is approximately 2%.

The local Rayleigh index distributions calculated using the empirical data and the two models are shown in Fig. 4.17. A visual comparison of these results reveal not only a strong similarity between all of the local Rayleigh index distributions but also with q' at $\theta = \pi/2$. The mean local deviation of the model using estimated parameters was approximately 2.8% with respect to the experimentally obtained results. The global Rayleigh index given by Eq. 4.5 shows that a quantitative com-

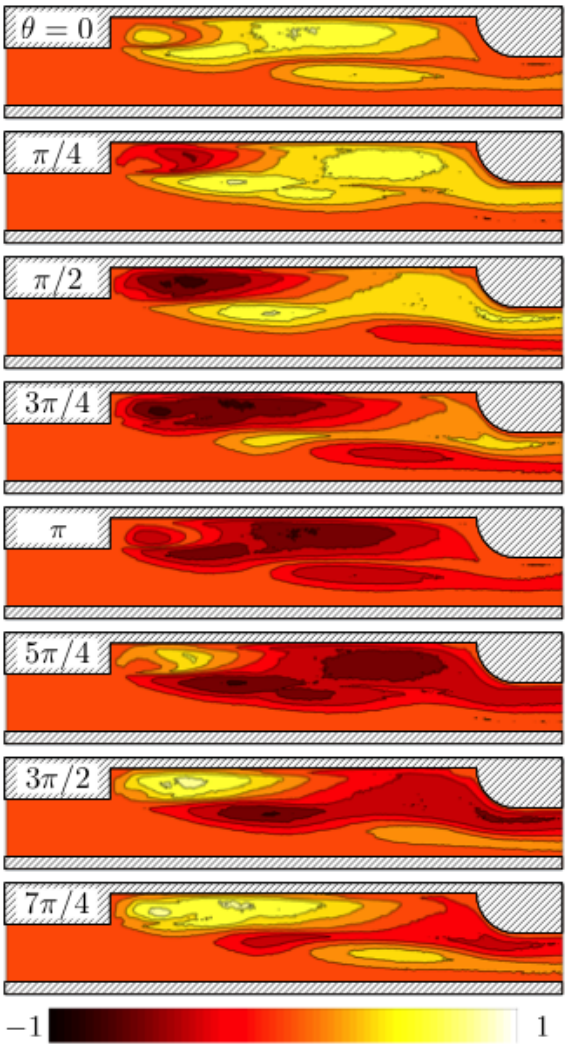

Figure 4.12: A map of spatially-resolved heat release at each phase reconstructed from the model using restricted parameters.

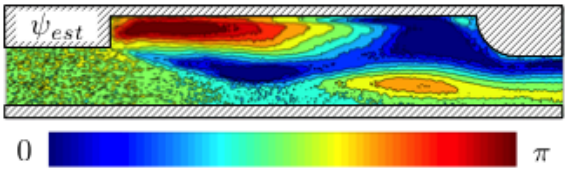

Figure 4.13: An estimated distribution of local model phase based on the proposed hybrid model.

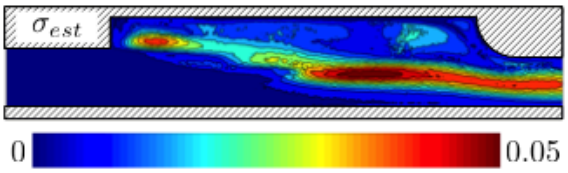

Figure 4.14: Maps showing the distribution of model error when using a estimated model parameters calibrated.

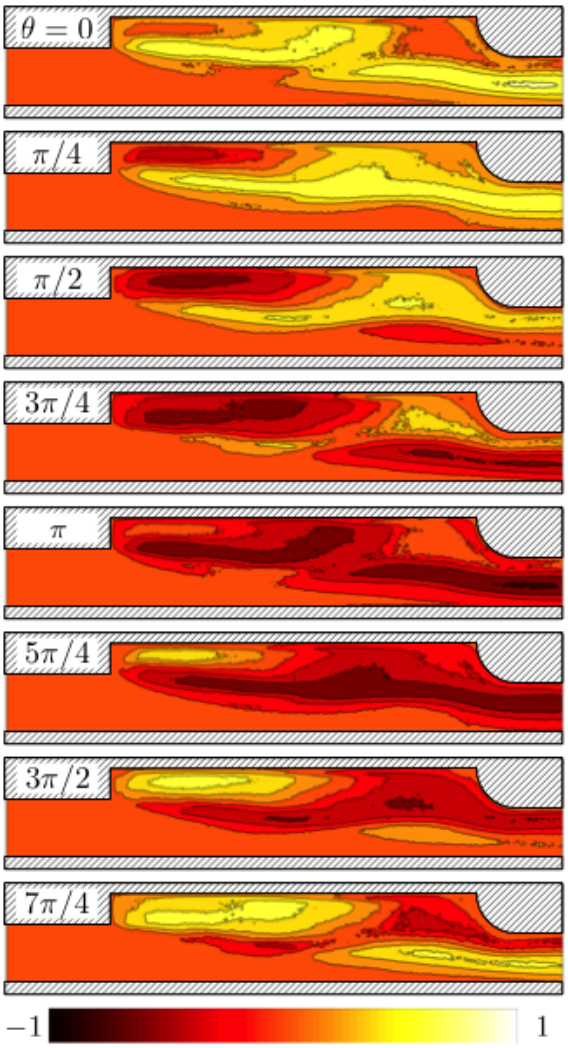

Figure 4.15: A map of spatially-resolved heat release at each phase reconstructed from the model using estimated parameters.

Table 4.1: Global Rayleigh index calculations using experimental and modeled results.

Data Type	G
Experimental Data	1.1 x 10^{-3}
Calibrated Model	1.0 x 10^{-3}
Restricted Model	1.3 x 10^{-3}
Estimated Model	1.4 x 10^{-3}

parison is also favorable for the proposed model used with the estimated parameters, and the calculated values shown in Table 4.1 are consistent with the experimental observations in that they both indicate marginally unstable combustion despite the aggregate global deviation of the model being roughly 28%.

$$G = \frac{1}{V\tau_{in}} \int_V \int_{\tau_{in}} \frac{p'(t)q'(z,t)}{p_{ref}q_{ref}}\, dt\, dV \tag{4.5}$$

These results indicate that modeling the heat release oscillations using estimated parameters produce accurate results when used in the stability analysis of a combustor at the onset of instability. More interestingly, it also shows that accurate heat release modeling can be accomplished using a very limited set of experimentally obtained results (which for our case is $\overline{q}$ and q' at $\theta = \pi/2$). With further development, the presence of strong vortex dynamics in all of these maps suggests that if the combusting vortices can be modeled at $\theta = \pi/2$ then it may be possible to also model q' without requiring any experimentally obtained data.

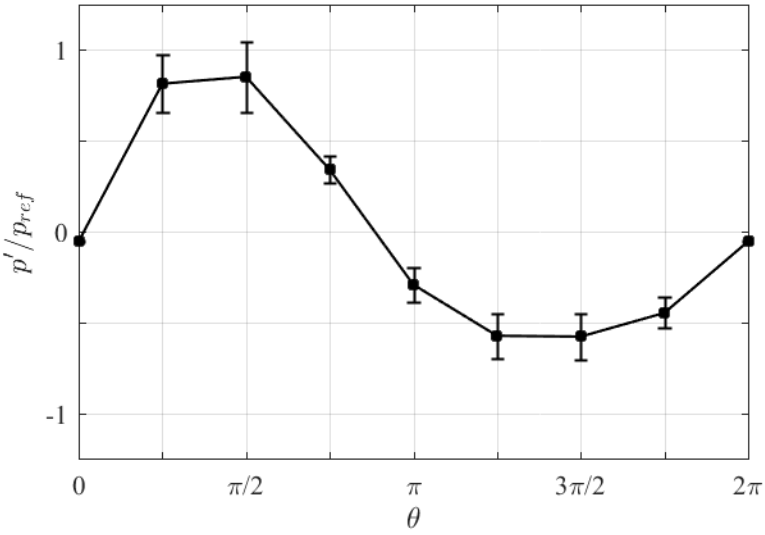

Figure 4.16: Average pressure oscillation measured during unstable operation of the dump combustor.

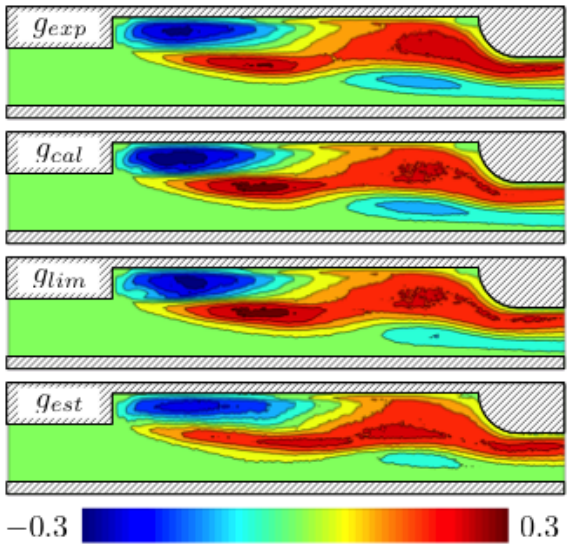

Figure 4.17: Maps showing the local Rayleigh index distributions for the experimental and modeled results.

5 | Active Combustion Control for Fuel-Flexible Combustors

5.1 Overview of Alternative Fuels

The process for converting biomass and coal into liquid fuel has been known for many decades. However, there has been a recent interest in utilizing these types of fuels in aviation. This is partly due to the improved methods for generating these fuels but also because of strong socio-economic and environmental reasons [68]. According to the National Energy Technology Laboratory of the Department of Energy, these types of alternative fuels would

> *...lessen dependence on foreign oil, reduce the number of different fuels required, and reduce environmental impacts because they [Fischer-Tropsch fuels] burn cleaner than other liquid fuels...* [69]

Furthermore, the Department of Defense is looking to use these fuels in aviation [69] [70] [71] and have successfully tested a 50:50 blend of alternative and conventional fuels in a flight of a B-52 jet [69].

Table 5.1: A list of all the tested fuel types.

Ref. No.	Fuel Type
1	JP-8
2	Jet A
3	1:1 blend of JP-8 and Bio-SPK HRJ (brand A)
4	1:1 blend of JP-8 and Bio-SPK HRJ (brand B)
5	Bio-SPK HRJ (brand A)
6	Bio-SPK HRJ (brand B)
7	1:1 blend of Jet A and FT-SPK (brand C)
8	1:1 blend of Jet A and FT-SPK (brand D)
9	1:1 blend of Jet A and FT-SPK (brand E)
10	FT-SPK (brand C)
11	FT-SPK (brand D)
12	FT-SPK (brand E)

In this work, two categories of alternative fuels are specifically tested. One is *Fischer-Tropsch* (FT) jet fuel which is created using the conversion of coal or biomass into liquid fuel using the catalytic Fischer-Tropsch process. The other is *synthetic biofuel* (Bio), which is based on oils extracted from plant sources. Detailed descriptions of these processes and fuels can be found in *Gas Turbine Combustion: Alternative Fuels and Emission* by Lefebvre and Ballal (2010) [72] as well as in reports by Edwards et. al. (2012) [70] and Bessee et. al. (2011) [71]. The fuels and mixtures used in the following experiments are listed in Table 5.1[1].

5.2 Influence of Fuel Properties

Two important factors that determine the control authority of the actuator are the time delays between the fuel injection and the subsequent heat release as well as

[1]SPK - Synthetic Paraffinic Kerosene; HRJ - Hydroprocessed Renewable Jet.

the magnitude of peak heat release. To begin, a simple analysis of droplet heating yields that the time required for heating a single fuel droplet through convection is given by Eq. 5.1, where we use the lumped capacity approach for computing time scales.

$$\tau_{heat} = \frac{\rho_f c_{p.f} d_0}{6h} log(\frac{T_g - T_{f,0}}{T_g - T_{f,boil}}) \tag{5.1}$$

Furthermore, the heat release from the droplet is given by Eq. 5.2, where the D^2-law is used to model transient heat release behavior.

$$q'(t^*) = \frac{\pi \rho_f h_{RP} d_0^3}{4\tau_{vap}} (1 - \frac{t^*}{\tau_{vap}})^{1/2} \tag{5.2}$$

For these equations, the heat of vaporization is calculated using Eq. 5.3, the convective heat transfer coefficient can be estimated using Eq. 5.4 [73], and $t^* = t - \tau_{heat}$.

$$\tau_{vap} = \frac{\rho_f h_{fg} d_0}{4h} (T_g - T_{f,boil}) \tag{5.3}$$

$$Nu = \frac{h d_0}{k_f} = 2 + \frac{0.555 Re^{1/2} Pr^{1/3}}{[1 + 1.232/RePr^{4/3}]^{1/2}} \tag{5.4}$$

Thus, the important fuel properties that influence the control authority of the secondary fuel injection system can be extracted from these equations. Edwards et. al. (2012) [70] and Bessee et. al. (2011) [71] published the measured values of these fuel properties, which are summarized in Table 5.2. Furthermore, chromatography of the fuel conducted by Edwards, et. al. (2012) [70] reveals each fuel is a mixture of long hydrocarbons, the composition of which differs with fuel type. Despite these

variations, the fuel properties of interest are similar across all tested fuel categories.

The overall heat release profile generated by the secondary fuel injection over time can be calculated by calculating Eqs. 5.1-5.4 using the values provided in Table 5.2 as well as the droplet size distribution of the spray. The latter is taken from Pang (2005) [74], whose fuel injection system inspired the one used for this experiment. Pang's data was used to generate a highly resolved map of the droplet size distribution as a function of time, which is shown in Fig. 5.1. The resulting heat release profiles for secondary fuel injection using the various fuel types are shown in Fig. 5.2. This result is a superposition of the combustion of the various droplet sizes in the spray. According to this simple model, both the Bio-SPK HRJ and the FT-SPK should perform nearly identically to conventional fuels.

More generally, these results show that the overall induction time of the secondary fuel spray requires less than $0.1\tau_{in}$ for all fuel categories. This suggests that the heating and combustion timescales of the secondary spray should be sufficiently small to allow for strong control authority over the combustion process without much variation between fuel types. It should also be noted that there is a second peak in the heat release that occurs at approximately $0.5\tau_{in}$.

5.3 Spray Quality and Actuator Performance

One conclusion that could be drawn of the previous analysis is that as long as the droplet size distributions are similar for all fuel types, they should perform similarly to the reference conventional fuel. This is also consistent with the droplet

Table 5.2: Properties of different fuel types as summarized from Edwards et al. (2012) and Bessee et al. (2011).

Fuel Prop.	JP-8 (Reference)	Bio-SPK HRJ	FT-SPK
$c_{p,f}$, @ 50°C, KJ/kg-K	1.97	2.4	2.4
p_{vap}, @ 40°C, KPa	5	7.5	7.5
h_{RP}, MJ/kg	43.1	44.3	44.1
k_f, pS/m	287	400	441
$T_{f,boil}$, °C	270	260	275
ν_f, @ 40°C, cSt	1.3	1.1	1.3
ρ_f, @ 15°C, kg/L	0.798	0.751	0.756

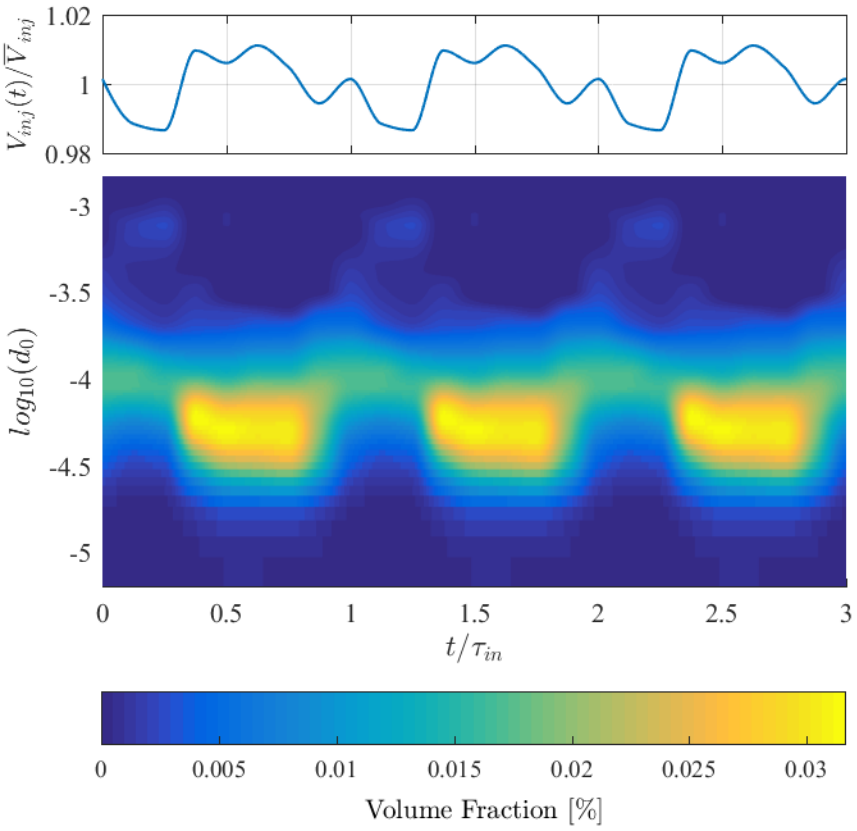

Figure 5.1: The variation in injected fuel volume and droplet size distribution as a function of time.

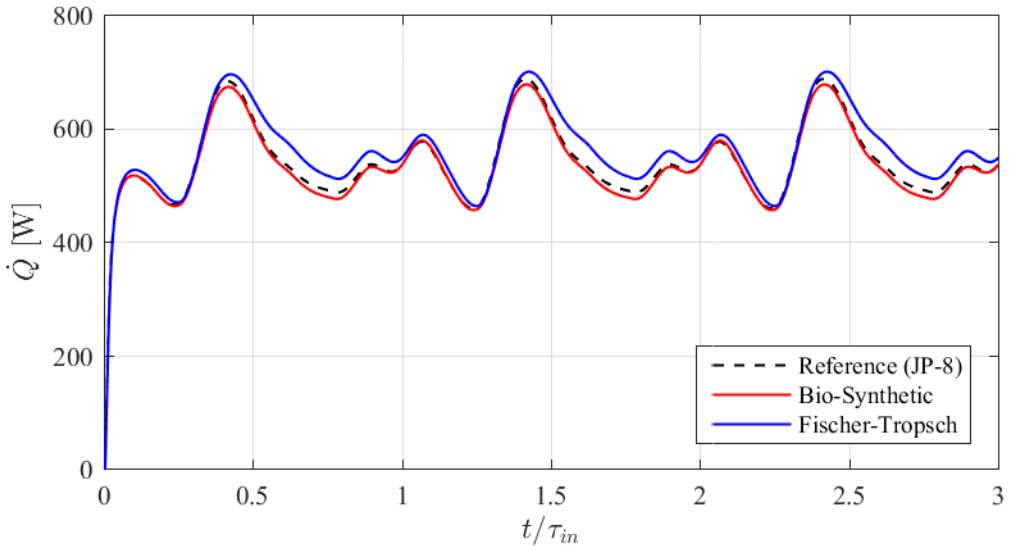

Figure 5.2: The heat release rate profile with respect to time for secondary fuel sprays of different fuel types.

heat and combustion theory (Eq. 5.1 - 5.4), which is strongly influenced by d_0. Therefore, off-line tests were done to visualize the actuated spray for each fuel type.

A sample set of the instantaneous phase-locked Mie-scattering spray images are shown in Fig. 5.3 - 5.14. These images were taken using a mock-up of the secondary fuel injection system used in the active control experiments. The actuator was operated at 150 Hz with a 50% duty cycle in order to simulate actual usage. A comparison of the spray patterns reveals that the time-evolution of the spray is qualitatively similar for all examined fuel types. This is especially true for the phase-averaged behavior.

The frequency responses of the actuator mass flow rates for all of the investigated fuel types are shown in Fig. 5.15. A summary of these results are also presented in Table 5.3. These measurable characteristics were invariant with fuel type, with an average flow rate of 0.2 gm/s and a maximum frequency response of

Table 5.3: Frequency and flow rate response of the various fuel types to actuated injection.

Ref. No.	Max. Freq. Response , Hz	Avg. Flow Rate, gm/s
1	550±50	0.21±0.02
2	550±50	0.21±0.02
3	550±50	0.20±0.02
4	550±50	0.19±0.02
5	550±50	0.21±0.02
6	550±50	0.21±0.02
7	550±50	0.20±0.02
8	550±50	0.20±0.02
9	550±50	0.21±0.02
10	550±50	0.21±0.02
11	550±50	0.21±0.02
12	550±50	0.20±0.02

550 Hz. Given the response time of the actuator, the more practical frequency limit is 300 Hz. This indicates that the performance of the injection system was also insensitive to the tested fuel types. All of these results suggest that there should be no meaningful impact of fuel type on the performance of active combustion control.

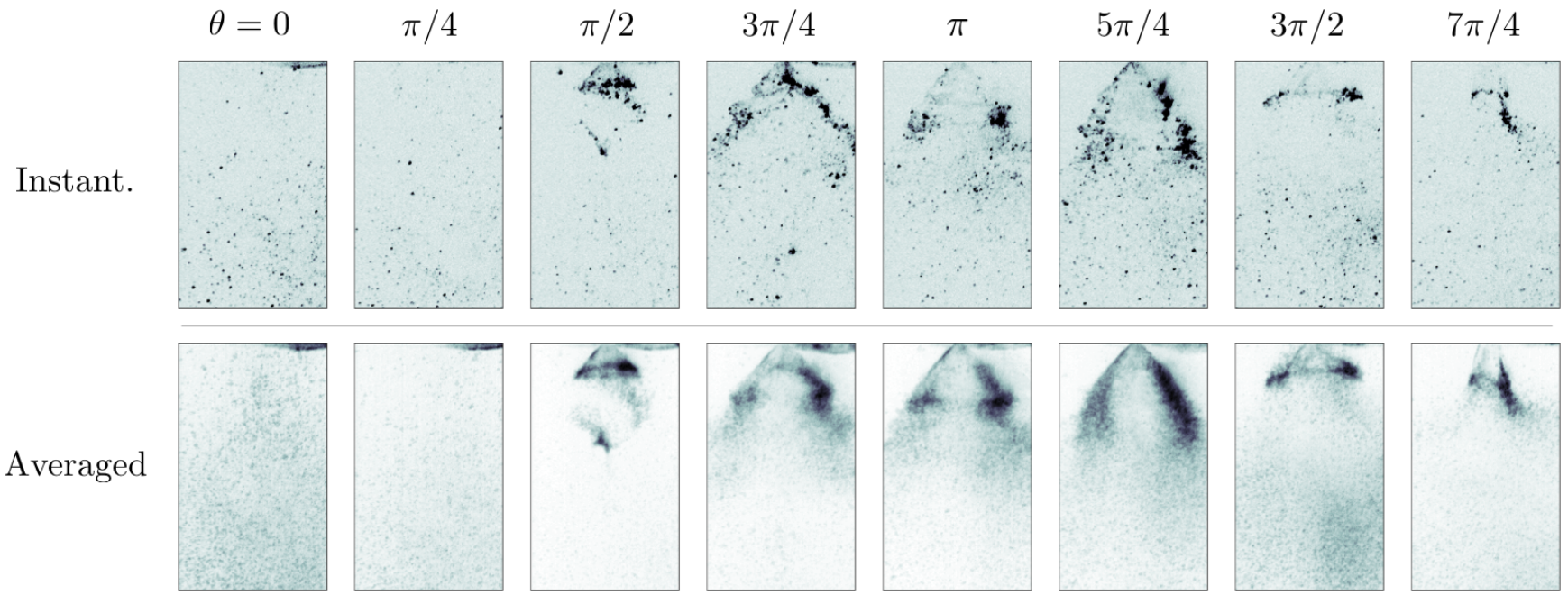

Figure 5.3: Both phase-locked instantaneous and phase-averaged Mie scattering images of the fuel spray using JP-8.

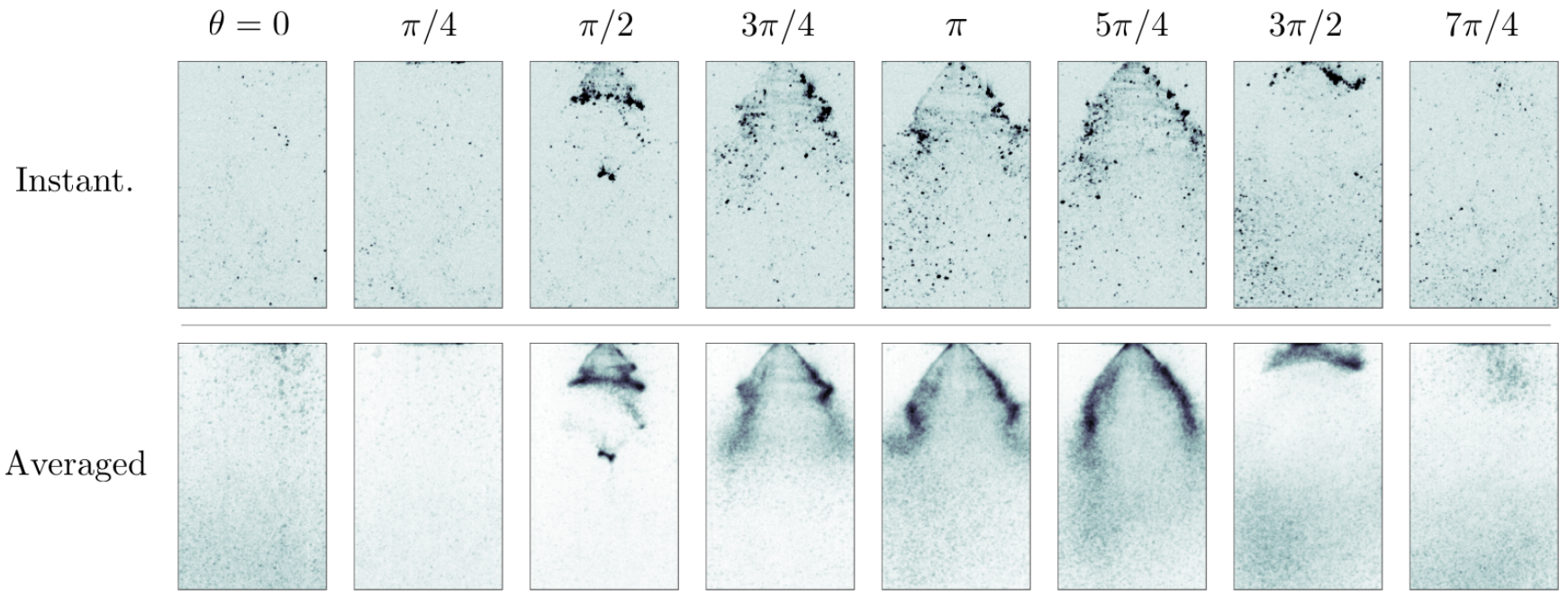

Figure 5.4: Both phase-locked instantaneous and phase-averaged Mie scattering images of the fuel spray using Jet A.

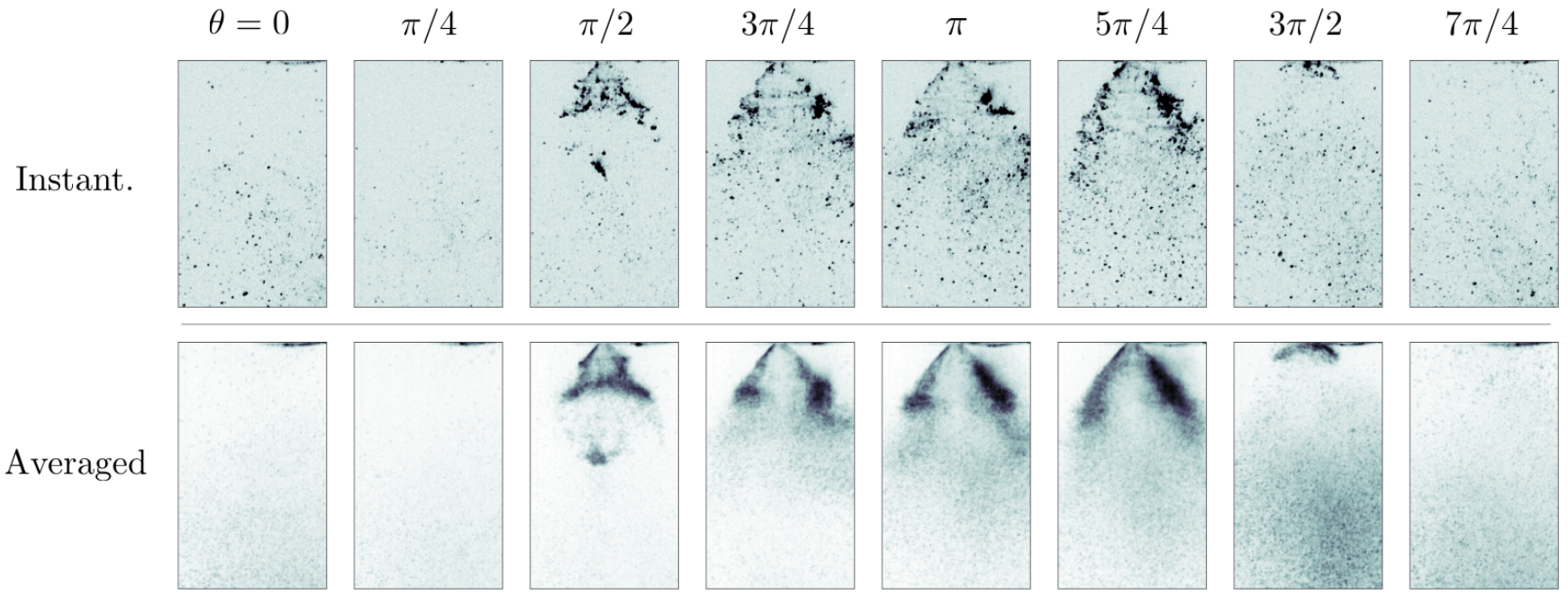

Figure 5.5: Both phase-locked instantaneous and phase-averaged Mie scattering images of the fuel spray using a 1:1 blend of JP-8 and Bio-SPK HRJ (Brand A).

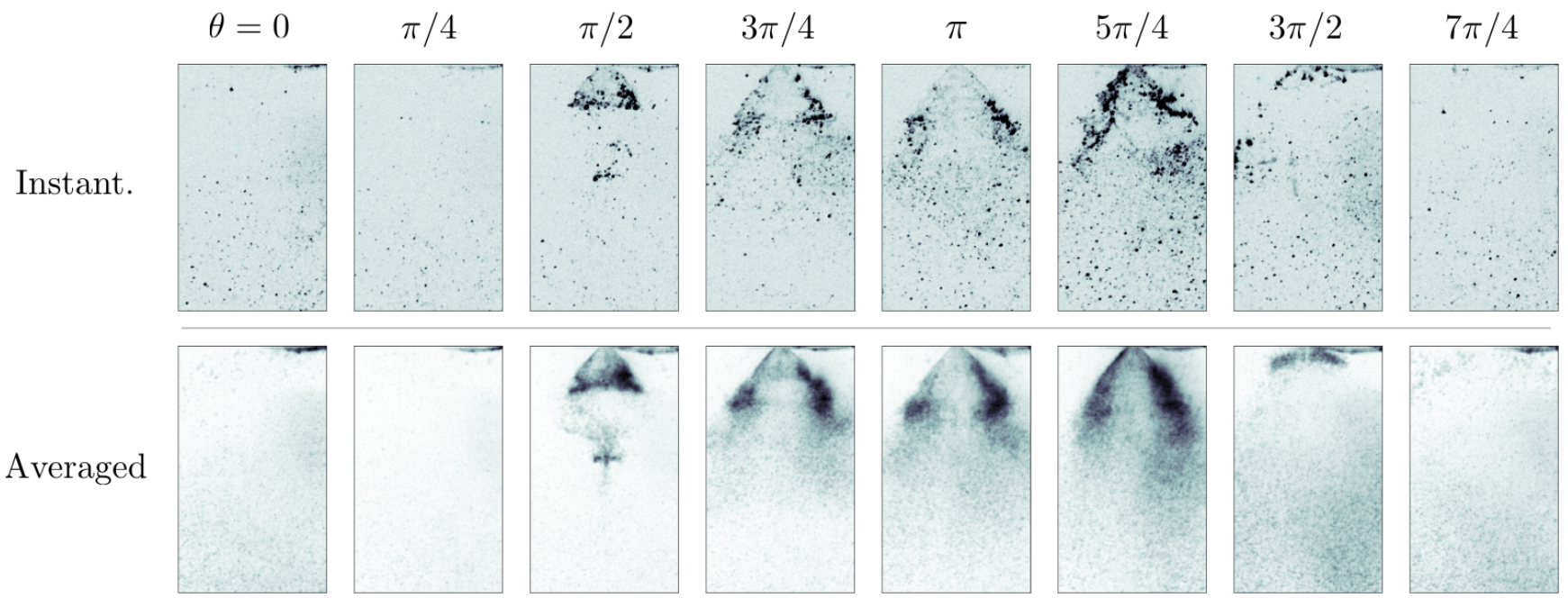

Figure 5.6: Both phase-locked instantaneous and phase-averaged Mie scattering images of the fuel spray using a 1:1 blend of JP-8 and Bio-SPK HRJ (Brand B).

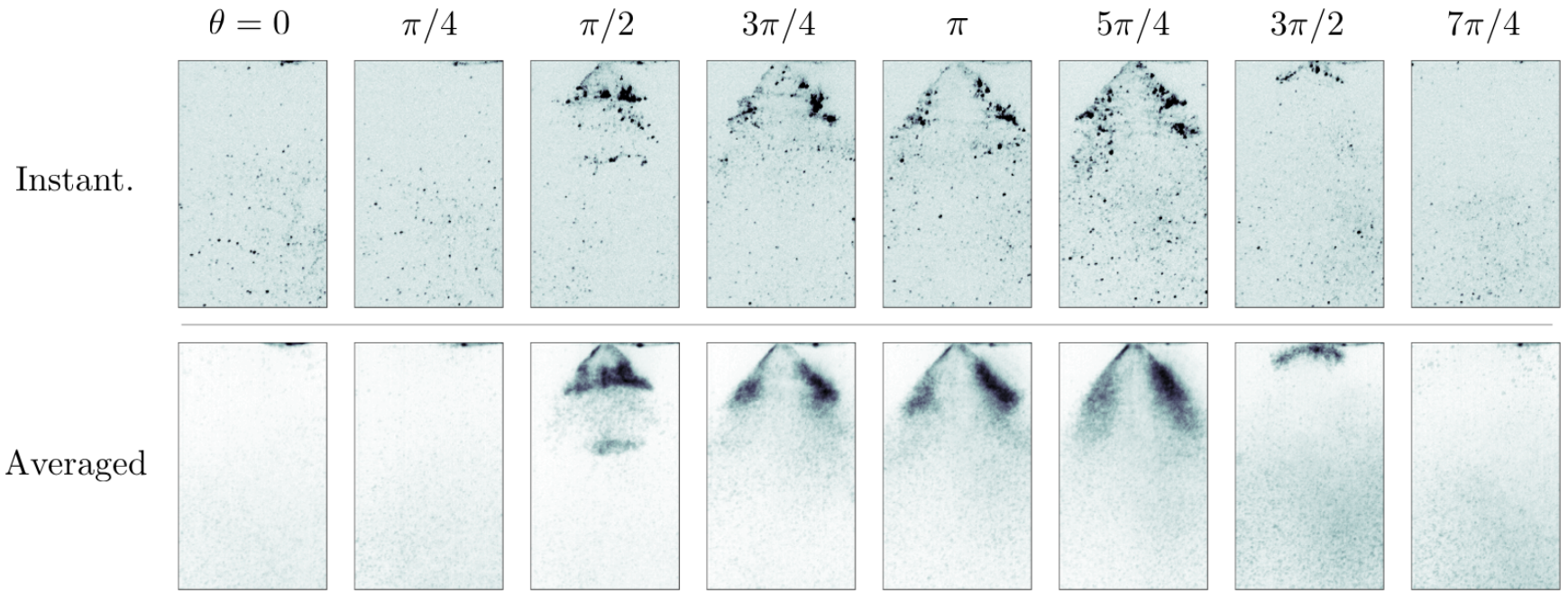

Figure 5.7: Both phase-locked instantaneous and phase-averaged Mie scattering images of the fuel spray using Bio-SPK HRJ (Brand A).

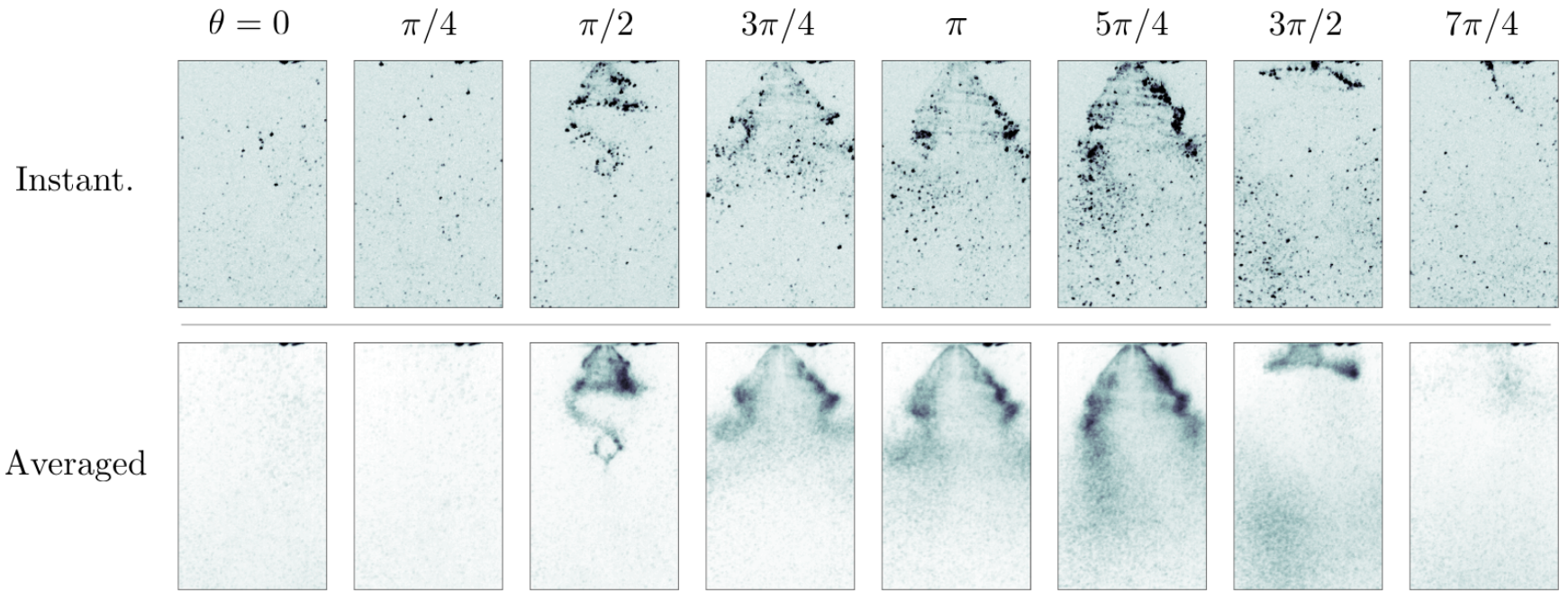

Figure 5.8: Both phase-locked instantaneous and phase-averaged Mie scattering images of the fuel spray using Bio-SPK HRJ (Brand B).

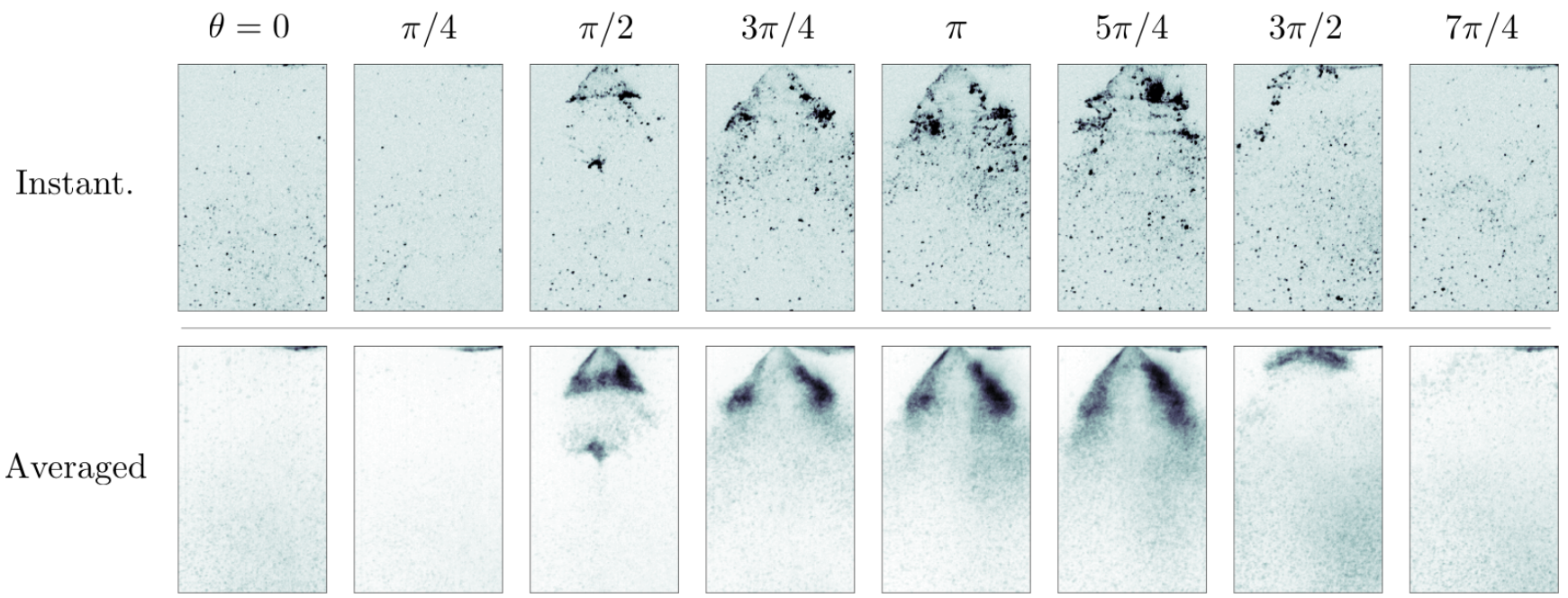

Figure 5.9: Both phase-locked instantaneous and phase-averaged Mie scattering images of the fuel spray using a 1:1 blend of Jet A and FT-SPK (Brand C).

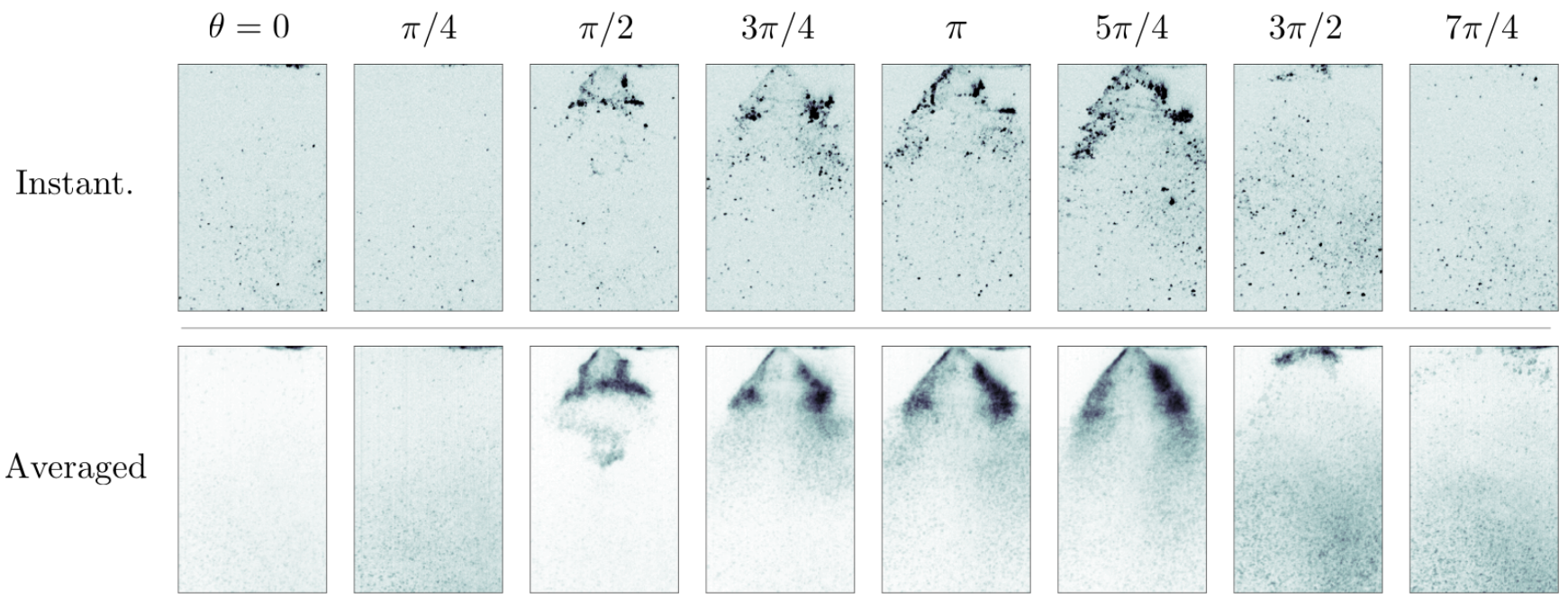

Figure 5.10: Both phase-locked instantaneous and phase-averaged Mie scattering images of the fuel spray using a 1:1 blend of Jet A and FT-SPK (Brand D).

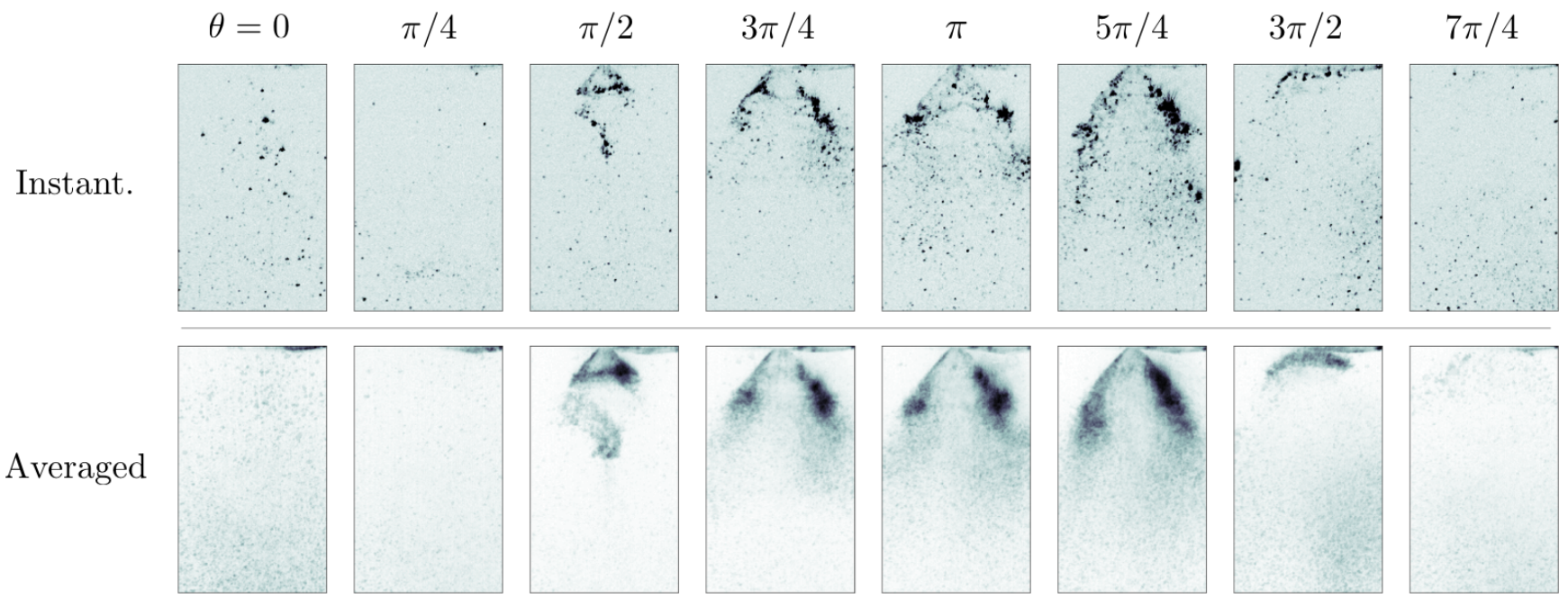

Figure 5.11: Both phase-locked instantaneous and phase-averaged Mie scattering images of the fuel spray using a 1:1 blend of Jet A and FT-SPK (Brand E).

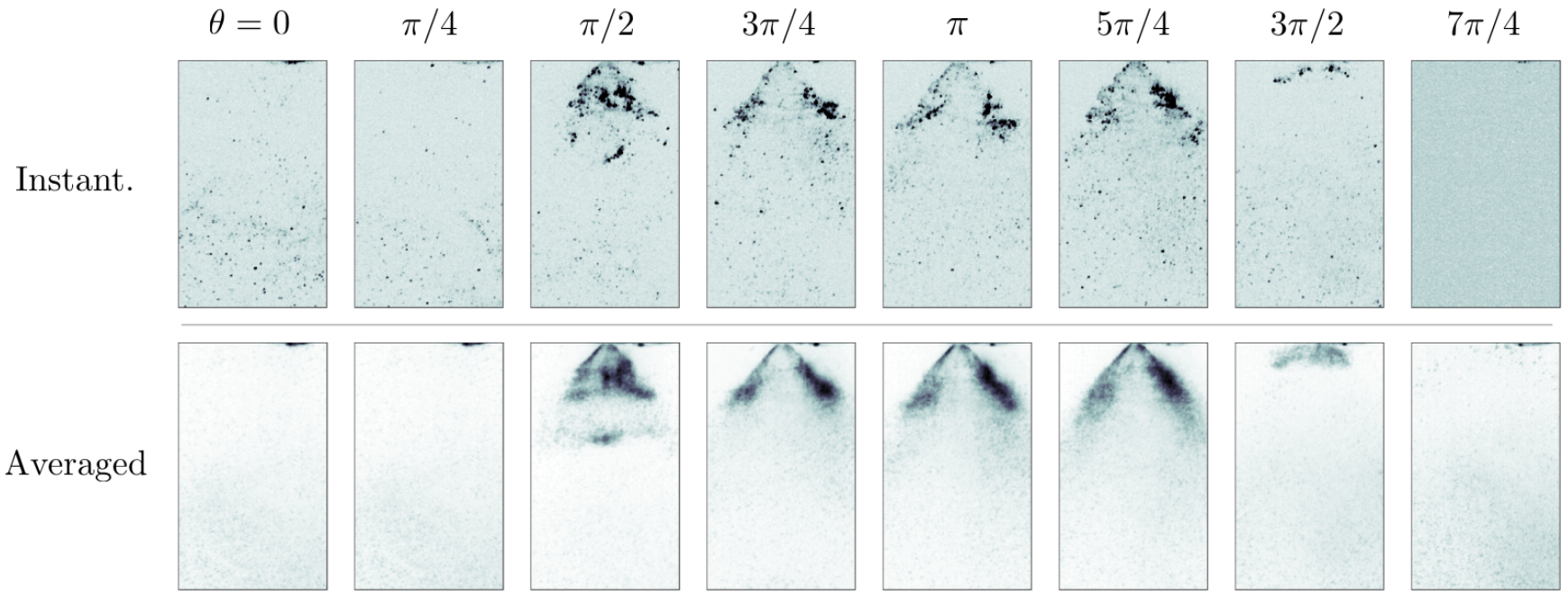

Figure 5.12: Both phase-locked instantaneous and phase-averaged Mie scattering images of the fuel spray using FT-SPK (Brand C).

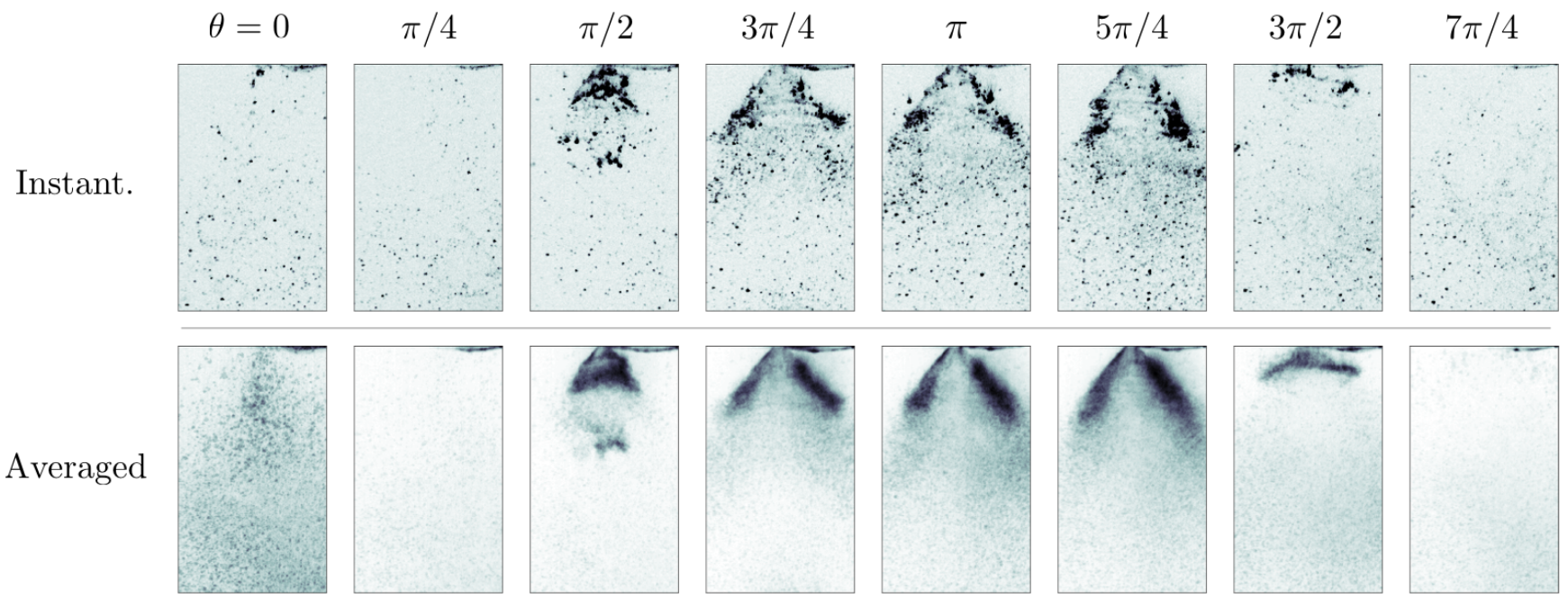

Figure 5.13: Both phase-locked instantaneous and phase-averaged Mie scattering images of the fuel spray using FT-SPK (Brand D).

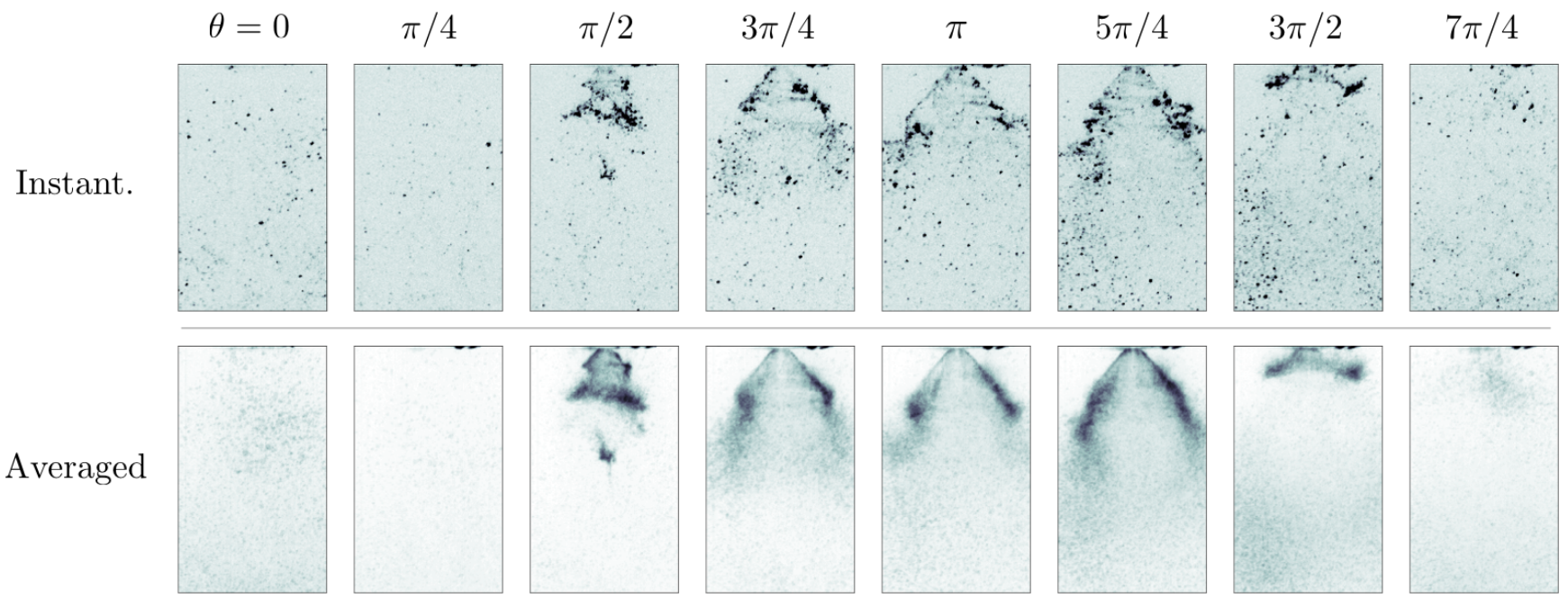

Figure 5.14: Both phase-locked instantaneous and phase-averaged Mie scattering images of the fuel spray using FT-SPK (Brand E).

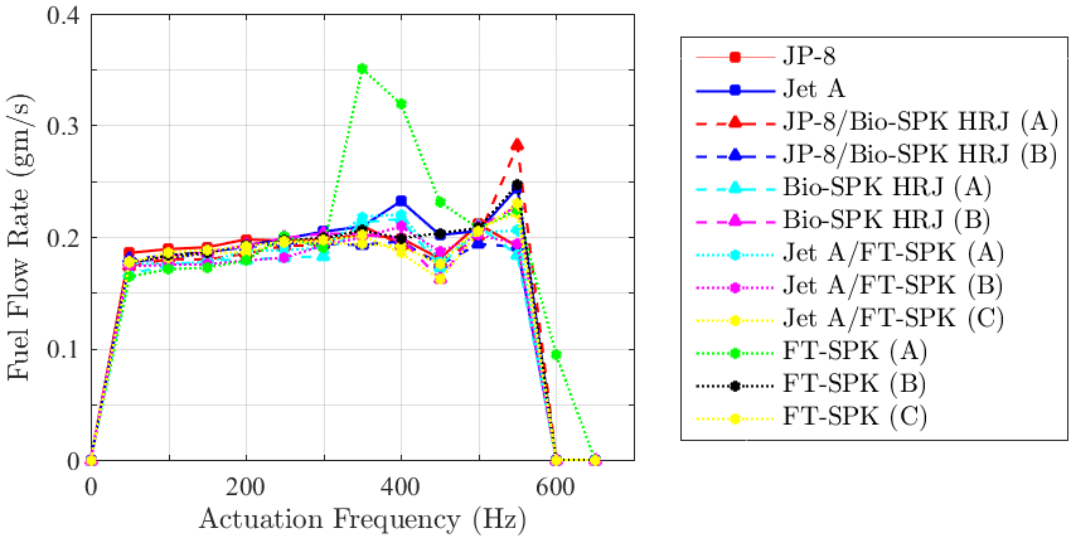

Figure 5.15: The frequency response of the fuel actuator with respect to flow rates for all tested fuel types.

5.4 Review of Baseline Instability Results

Naturally unstable operation was observed for the dump combustor at an inlet velocity of 45±2 m/s and a 0.67±0.03 equivalence ratio. The frequency spectra of the measured pressure oscillations, shown in Fig. 4.1, indicate that the primary instability frequency is 150 Hz. It should be noted that there is also some recorded fluctuations at 300 Hz, although the amplitude for this higher harmonic is relatively small in the baseline case. The other cases are discussed in following sections. Note that this baseline instability is the same as the one observed in §4.1.

Phase-averaged images of CH* chemiluminescence, shown in Fig. 4.3a, reveal that vortices are also shed from the dump plane at the observed instability frequency, as indicated by the roll-up of the flame. Furthermore, the frequency calculated using simple acoustic theory for the combined system of dump combustor

and inlet pipe is equivalent to the observed instability frequency. Consequently, the mechanism of this instability seems to be the result of coupling between the heat release oscillations associated with the convected flame and the combustor acoustics. The interaction between vortices and combustion that lead to thermo-acoustic instability has been throughly studied (§2.2). Chemiluminescence is often correlated with the heat release (§3.3) and a normalized distribution of its oscillation, where $q' = q - \overline{q}$, is shown in Fig. 4.4 These images show that the roll-up of flame caused by the vortices create periodic zones of heat release excess (red) and deficit (blue) that are convected with the flow.

The effect of this local heat release oscillation on the combustor stability can be visualized via the local Rayleigh index distribution shown in Fig. 4.17. For this work, a non-dimensional Rayleigh index is used as defined in Eq. 2.14. This distribution shows that the shear layer creates a region of positive Rayleigh index (red) while the recirculation zone is an area of negative Rayleigh index (red). In the context of the Rayleigh criterion discussed in §2.1, this indicates that the shear layer drives instability while the recirculation zone acts to suppress it. Note that this distribution is clearly influenced by the roll-up of the flame. Furthermore, this type of examination was used by Lee et. al. (2000) [75] to optimize secondary fuel injection for active combustion control, which has also previously been done for this particular experimental setup.

5.5 Active Combustion Control Results

For these tests, the fuel type used by the controller was varied to imitate the use of such a system on a fuel-flexible combustor. Ethylene was again used as the primary fuel to simulate pre-vaporized fuel. However, the flow rate was adjusted so that the combination of primary and secondary fuel flow rates resulted in the same overall equivalence ratio as in the baseline case. Furthermore, JP-8 and Jet A were used as reference fuels for performance comparisons. The frequency response and flow rates recorded during an offline calibration of alternative fuel injection is provided in Table 5.3.

A sample set of frequency spectra for pressure oscillations measured during the actively controlled experiments are shown in Fig. 5.16 - 5.23. The full dataset for all of the fuel types are provided in Appendix A. For each of the fuel types used in active control, the injection timing parameter was varied in order to investigate the effect of the fuel type on the controller setting. To show the combustor response to changes in injection timing, the peak amplitude for 150 Hz and 300 Hz oscillations are plotted against injection timing as demonstrated in Fig. 5.24. Figure 5.25 - 5.35 shows this relationship for all of the fuel types tested. These results show that the amplitude of the targeted frequency is significantly reduced. Under individually tuned optimal settings, up to 94% reduction of the 150 Hz amplitude is achieved with all of the investigated fuel types. However, this is accompanied by a substantial increase in the amplitude of the higher harmonic oscillations at 300 Hz. Despite this, an overall reduction of up to 64% is observed even when considering the behavior of

both frequencies. These results also show that response of the instability amplitudes to changes in injection timing parameter is qualitatively similar for all tested fuel types.

The optimal injection phase delay for each fuel type is shown in Fig. 5.36. These results indicate that the optimal controller setting consistently remains near 0 for each fuel type, which has the practical implication that the controller does not need to be re-calibrated for each fuel type. This is further reinforced by a summary of the suppression performance for each fuel type shown in Fig. 5.37. Overall instability suppression based on fuel specific tuning of the controller parameter is compared against a case where the parameter is fixed at the fuel independent optimal setting. In either configuration, approximately 50% reduction in the overall instability is observed along with some fuel-dependent variation. The results detailed in the previous sections strongly indicate that the active control system using secondary fuel injection is insensitive to fuel type, as predicted by previous analysis.

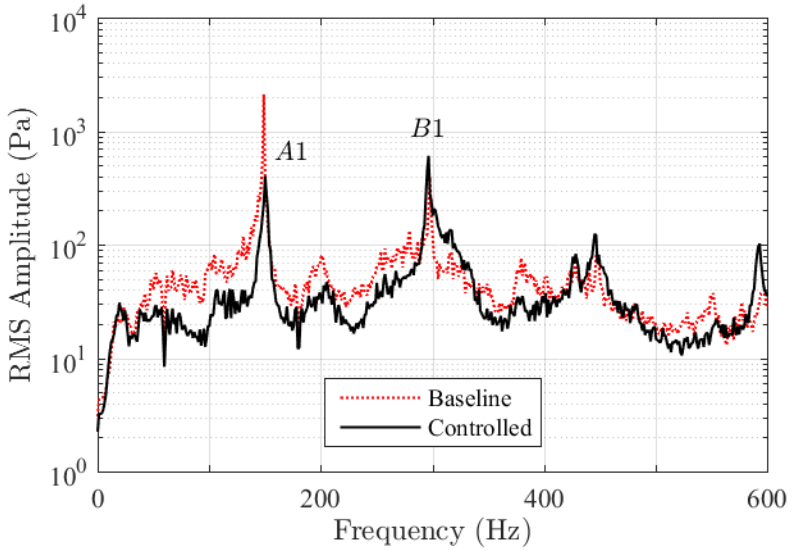

Figure 5.16: The frequency spectra for the pressure oscillations measured in the dump combustor while injecting JP8 at setting $\theta = 0$.

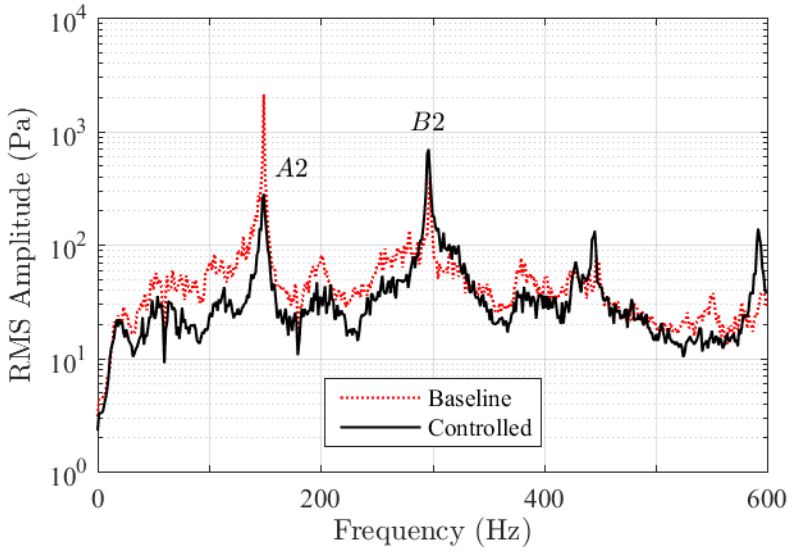

Figure 5.17: The frequency spectra for the pressure oscillations measured in the dump combustor while injecting JP8 at setting $\theta = \pi/4$.

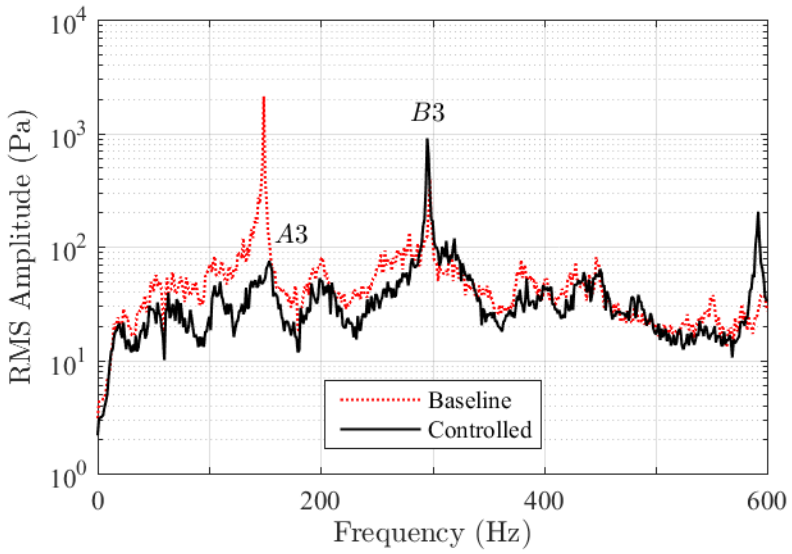

Figure 5.18: The frequency spectra for the pressure oscillations measured in the dump combustor while injecting JP8 at setting $\theta = \pi/2$.

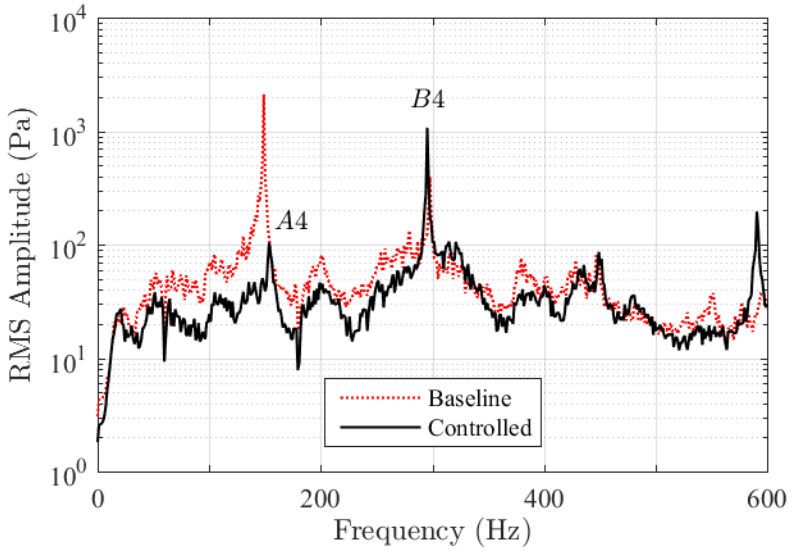

Figure 5.19: The frequency spectra for the pressure oscillations measured in the dump combustor while injecting JP8 at setting $\theta = 3\pi/4$.

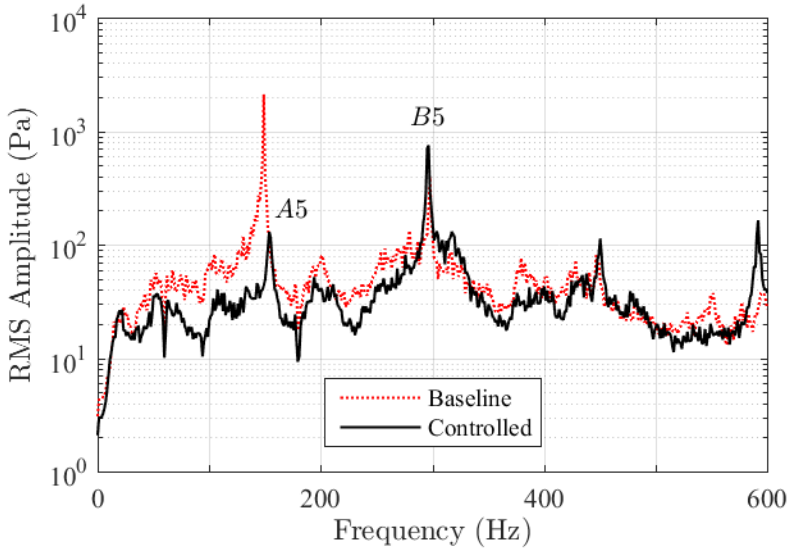

Figure 5.20: The frequency spectra for the pressure oscillations measured in the dump combustor while injecting JP8 at setting $\theta = \pi$.

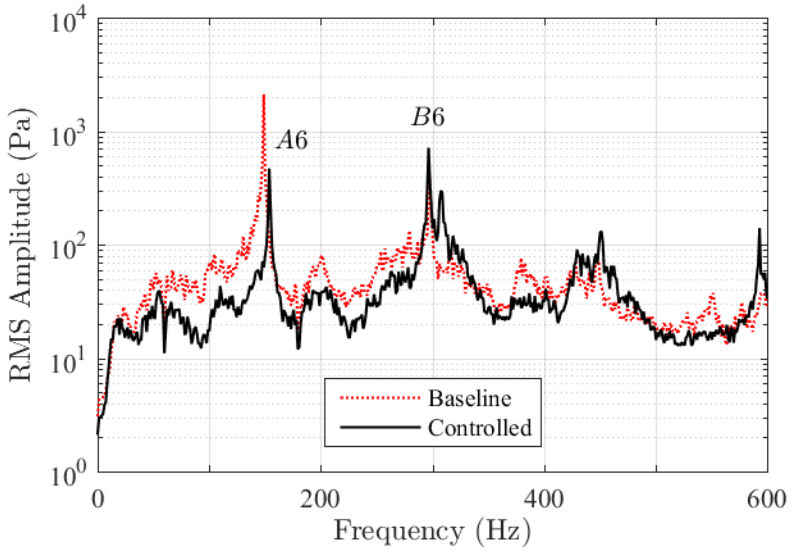

Figure 5.21: The frequency spectra for the pressure oscillations measured in the dump combustor while injecting JP8 at setting $\theta = 5\pi/4$.

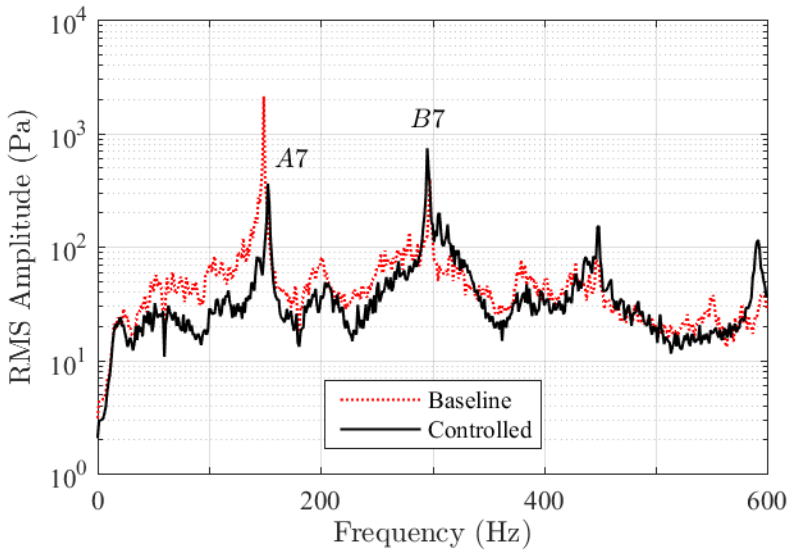

Figure 5.22: The frequency spectra for the pressure oscillations measured in the dump combustor while injecting JP8 at setting $\theta = 3\pi/2$.

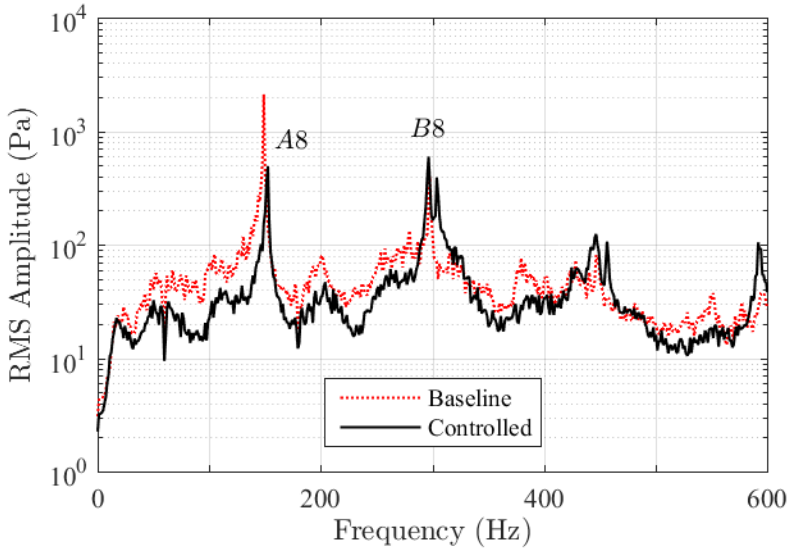

Figure 5.23: The frequency spectra for the pressure oscillations measured in the dump combustor while injecting JP8 at setting $\theta = 7\pi/4$.

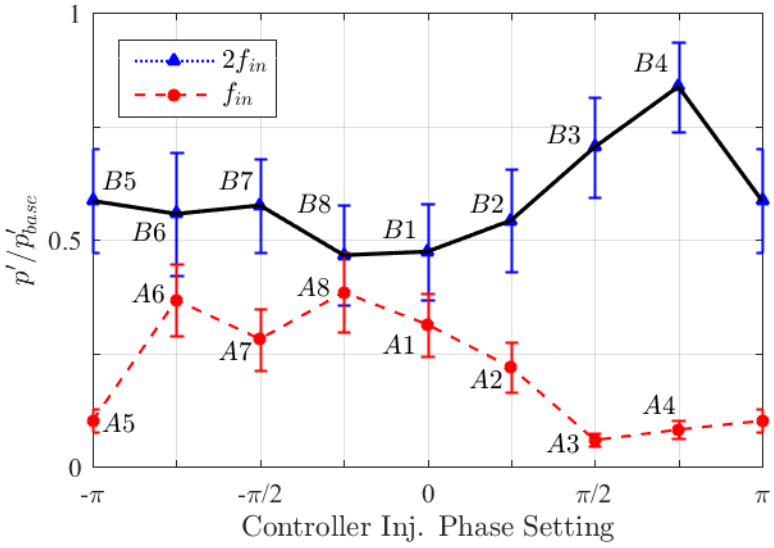

Figure 5.24: The active control performance/combustor pressure oscillation response to changes in controller injection phase setting when using JP-8.

5.6 Flame Response

The instantaneous phase-locked CH* chemiluminescence images are shown in Fig. 5.38 - 5.49. Note that the flame images are similar for all of the examined fuel types. It is clear from these images that the coherence of the vortices shed from the dump plane has been disturbed such that the flame is now more consistent over the time. Periodic variation in the flame has also been reduced with respect to the primary instability frequency, although this seems to have been replaced with oscillations at the higher harmonic as seen in the concurrent pressure oscillations. These observations are the case for all of the investigated fuel types. Since the actuator response was insensitive to fuel type, the effect of injection on the flow and combustion dynamics should be and is indeed similar for all of the tested fuel types.

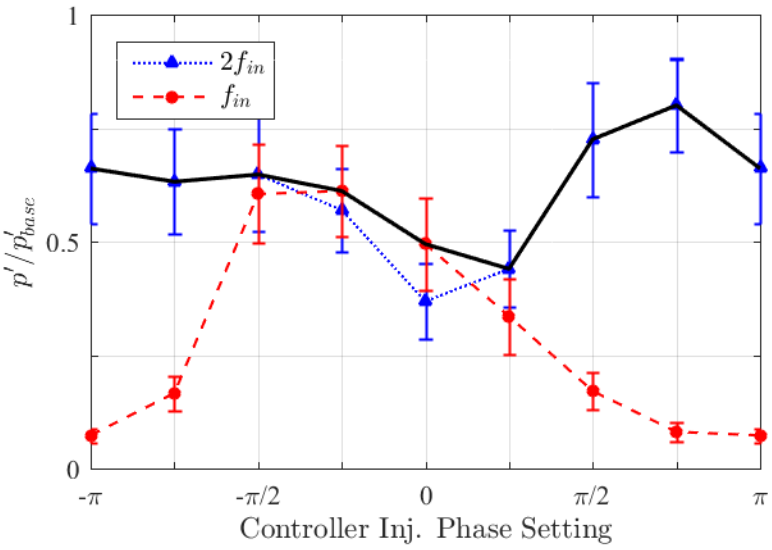

Figure 5.25: The active control performance/combustor pressure oscillation response to changes in controller injection phase setting when using Jet A.

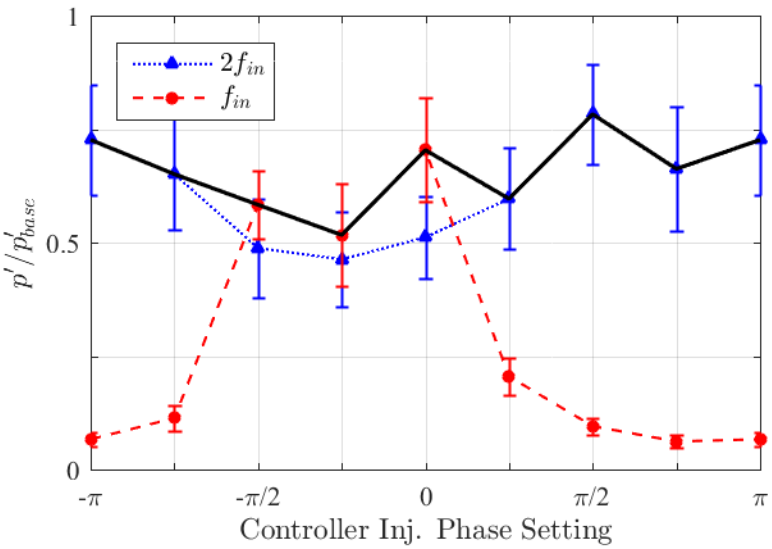

Figure 5.26: The active control performance/combustor pressure oscillation response to changes in controller injection phase setting when using a 1:1 blend of JP-8 and Bio-SPK HRJ (Brand A).

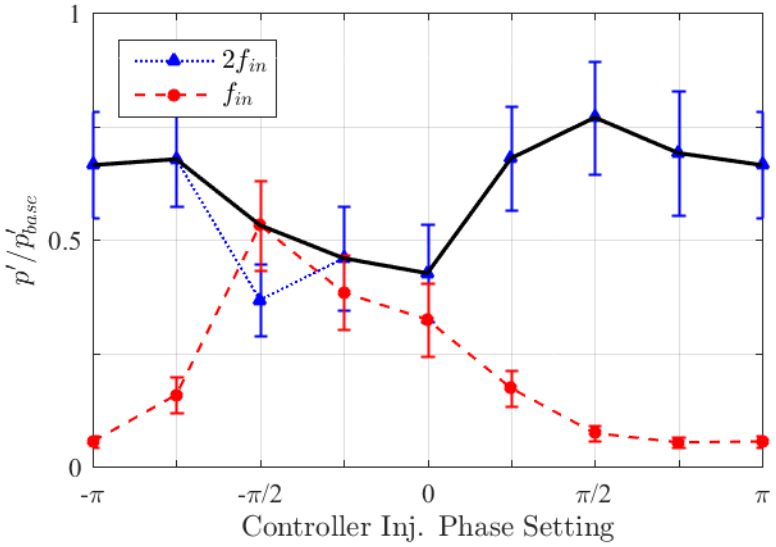

Figure 5.27: The active control performance/combustor pressure oscillation response to changes in controller injection phase setting when using 1:1 blend of JP-8 and Bio-SPK HRJ (Brand B).

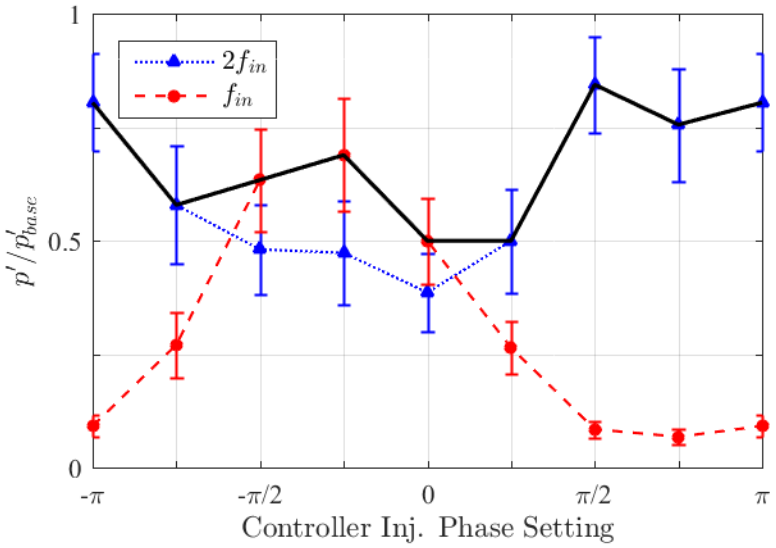

Figure 5.28: The active control performance/combustor pressure oscillation response to changes in controller injection phase setting when using Bio-SPK HRJ (Brand A).

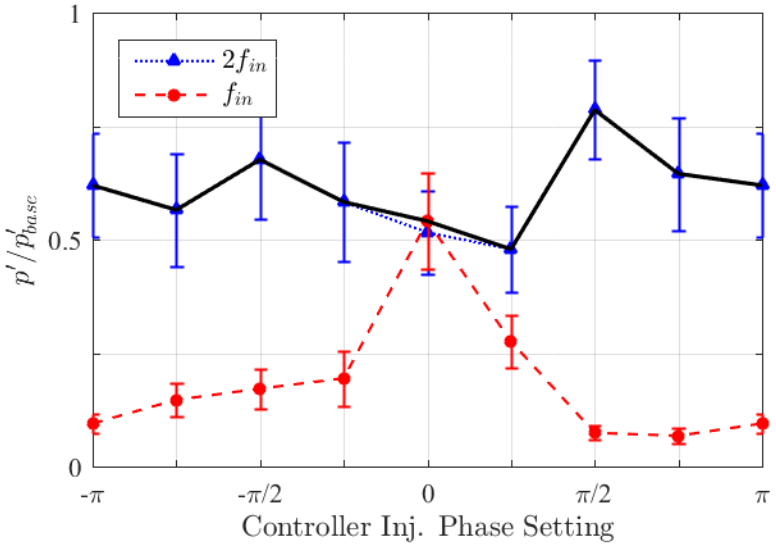

Figure 5.29: The active control performance/combustor pressure oscillation response to changes in controller injection phase setting when using Bio-SPK HRJ (Brand B).

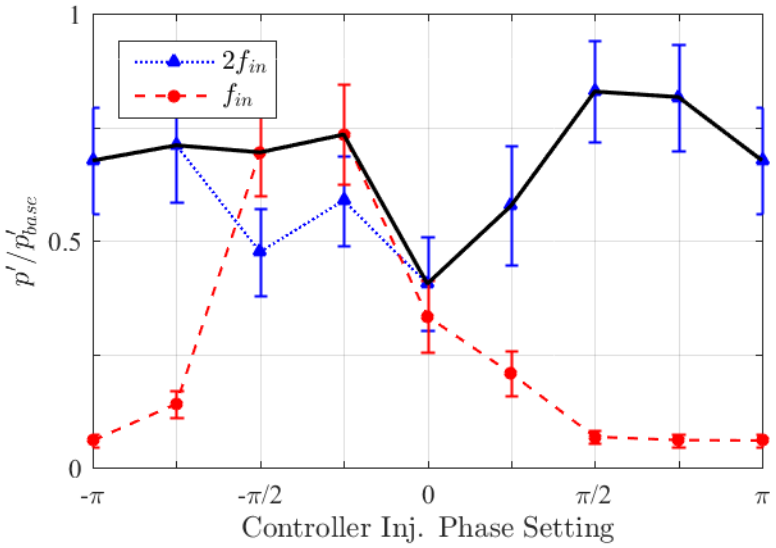

Figure 5.30: The active control performance/combustor pressure oscillation response to changes in controller injection phase setting when using a 1:1 blend of Jet A and FT-SPK (Brand C).

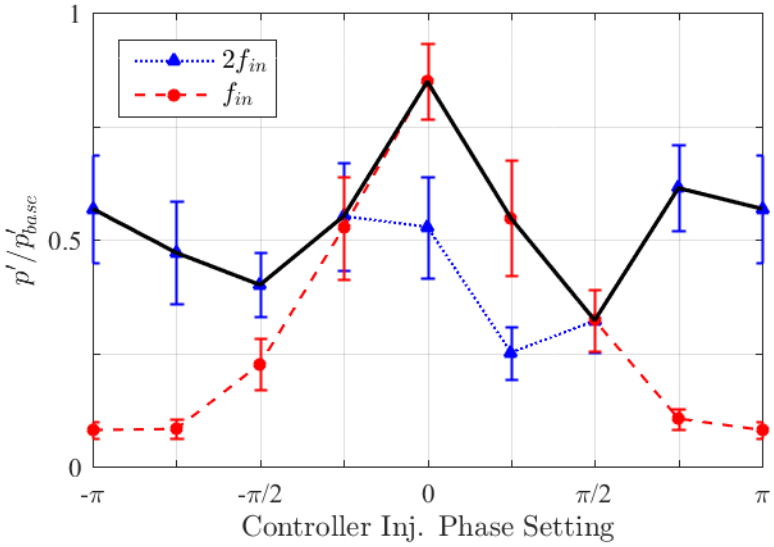

Figure 5.31: The active control performance/combustor pressure oscillation response to changes in controller injection phase setting when using a 1:1 blend of Jet A and FT-SPK (Brand D).

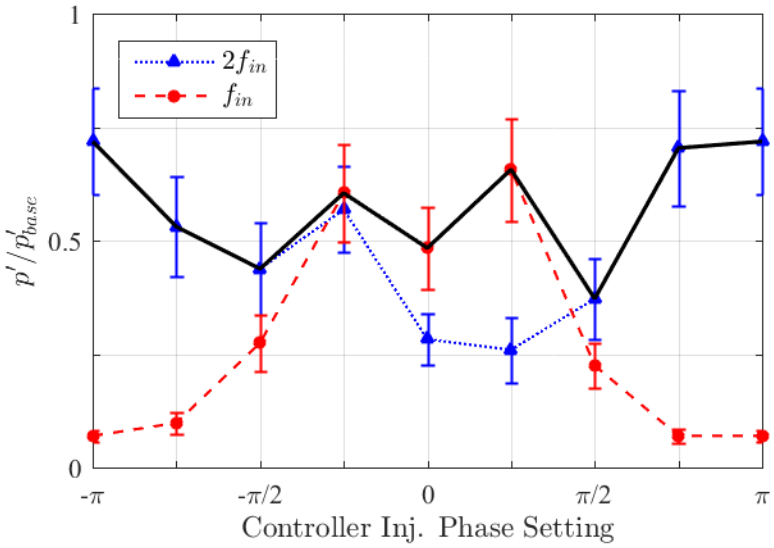

Figure 5.32: The active control performance/combustor pressure oscillation response to changes in controller injection phase setting when using a 1:1 blend of Jet A and FT-SPK (Brand E).

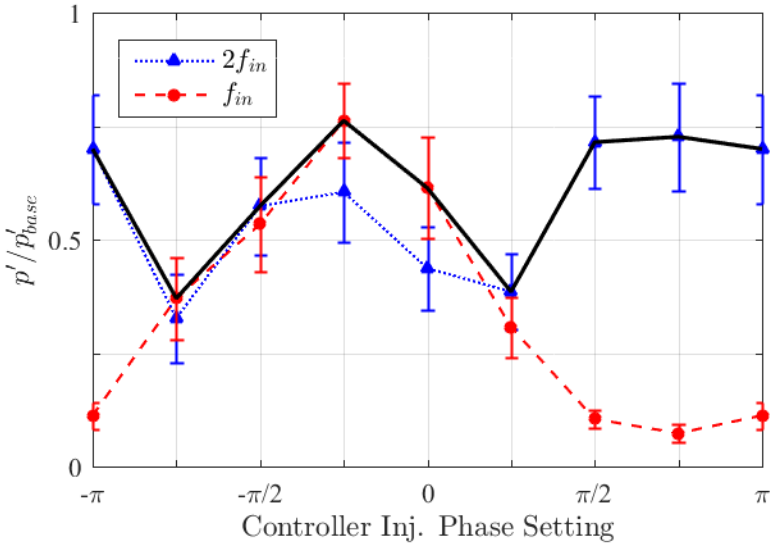

Figure 5.33: The active control performance/combustor pressure oscillation response to changes in controller injection phase setting when using FT-SPK (Brand C).

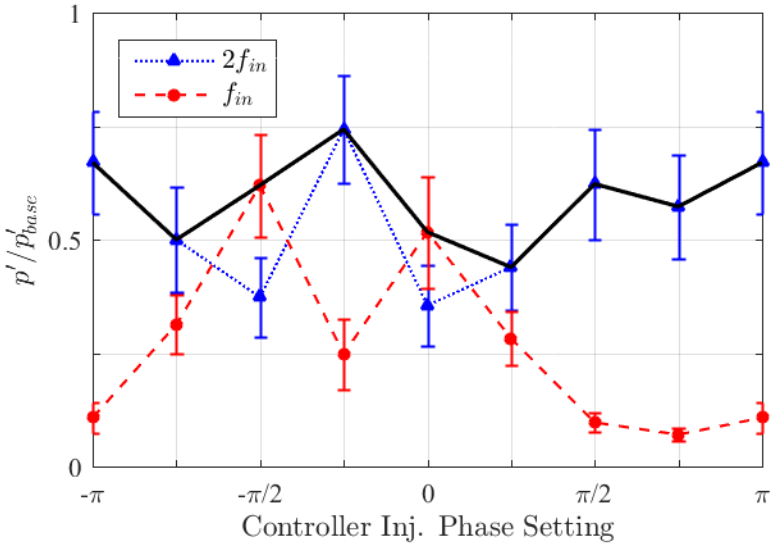

Figure 5.34: The active control performance/combustor pressure oscillation response to changes in controller injection phase setting when using FT-SPK (Brand D).

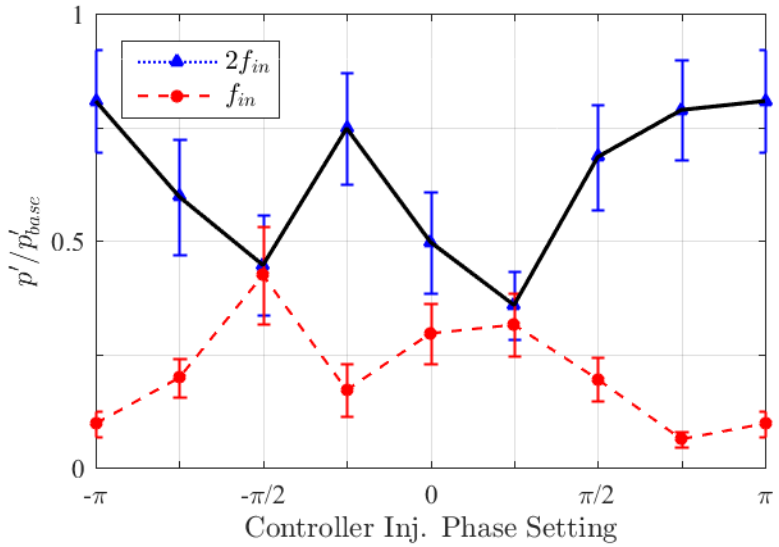

Figure 5.35: The active control performance/combustor pressure oscillation response to changes in controller injection phase setting when using FT-SPK (Brand E).

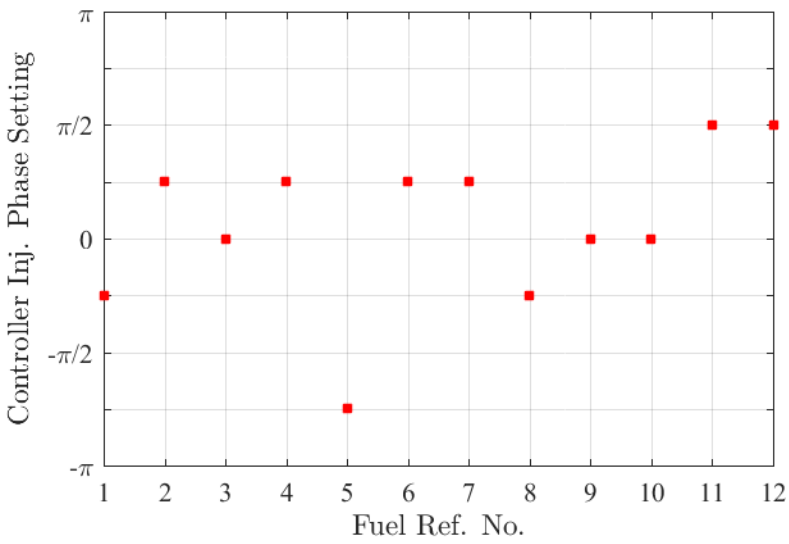

Figure 5.36: The optimal controller setting when using various fuel types for maximal overall instability suppression.

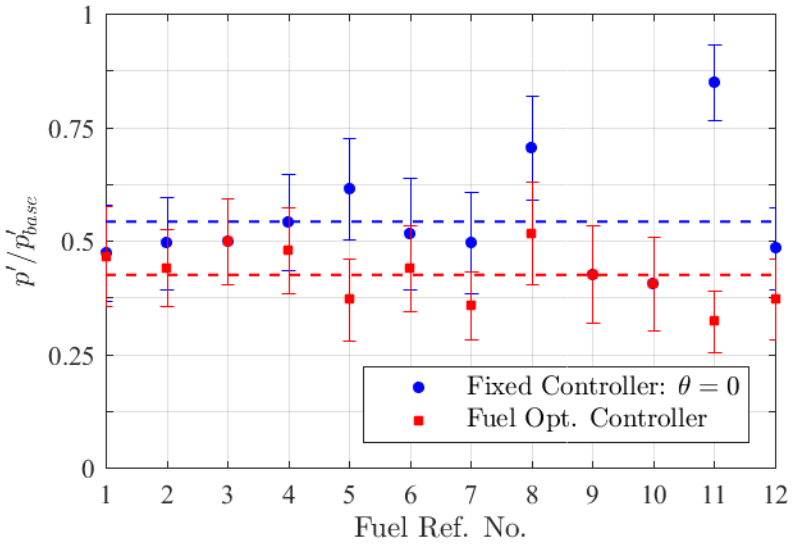

Figure 5.37: A performance comparison between a controller under fuel specific optimized parameter and a fixed parameter operations.

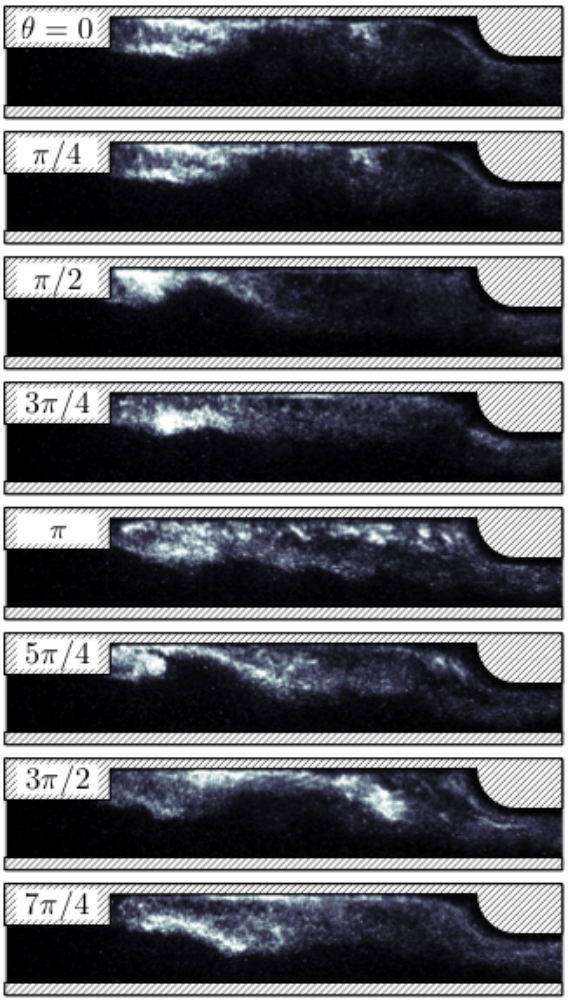

Figure 5.38: Phase-locked CH* chemiluminescence of the flame during actively control combustion using JP-8.

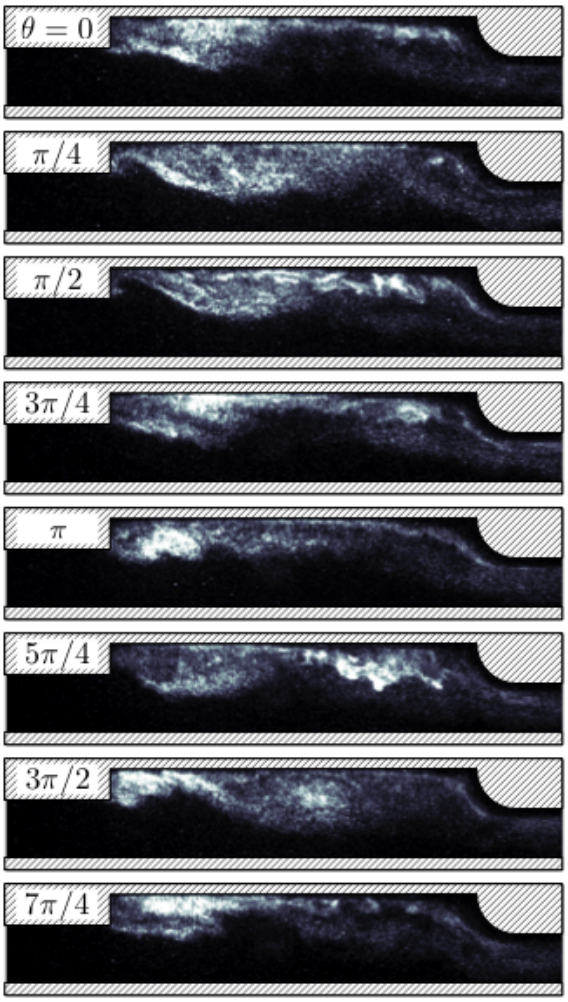

Figure 5.39: Phase-locked CH* chemiluminescence of the flame during actively control combustion using Jet A.

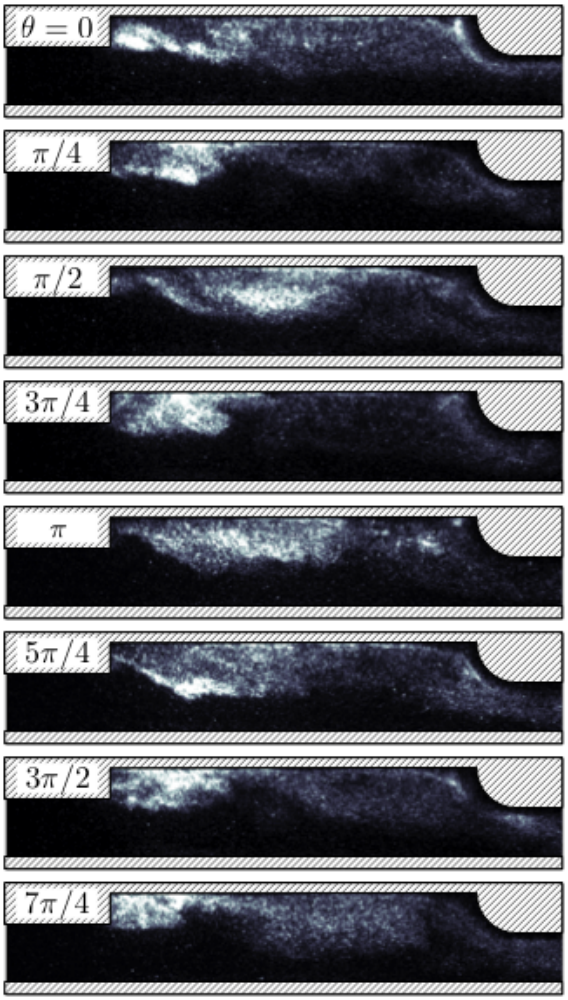

Figure 5.40: Phase-locked CH* chemiluminescence of the flame during actively control combustion using a 1:1 blend of JP-8 and Bio-SPK HRJ (Brand A).

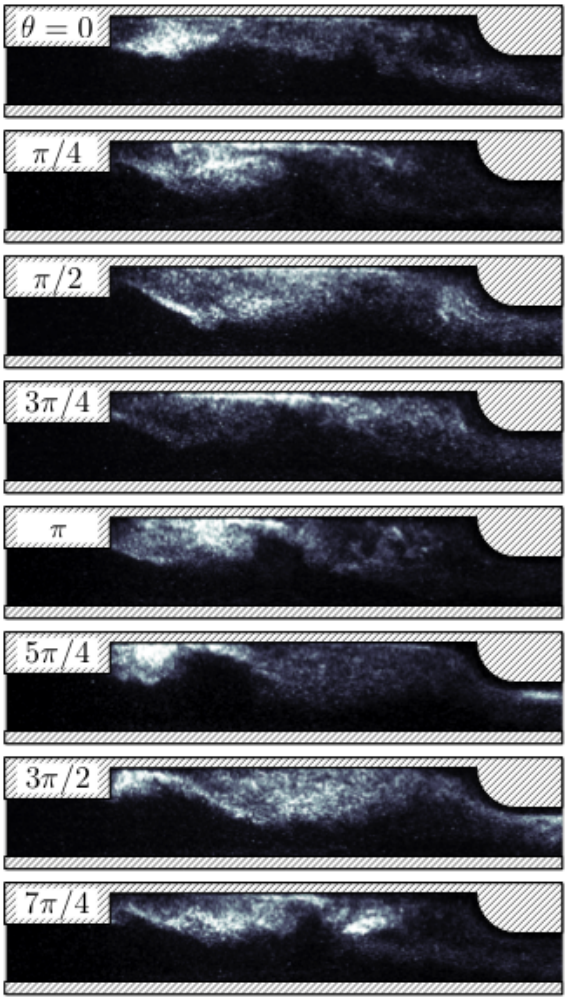

Figure 5.41: Phase-locked CH* chemiluminescence of the flame during actively control combustion using a 1:1 blend of JP-8 and Bio-SPK HRJ (Brand B).

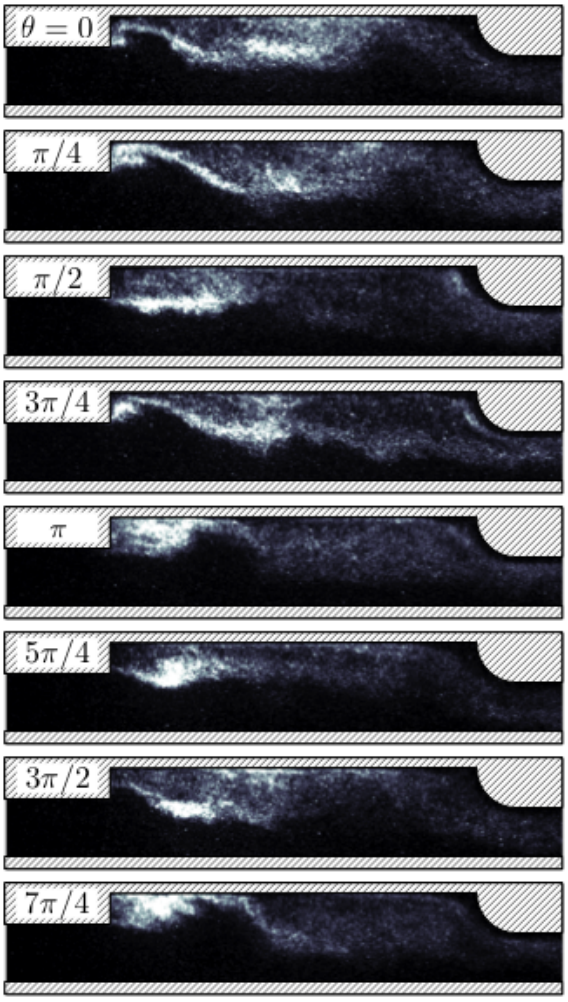

Figure 5.42: Phase-locked CH* chemiluminescence of the flame during actively control combustion using Bio-SPK HRJ (Brand A).

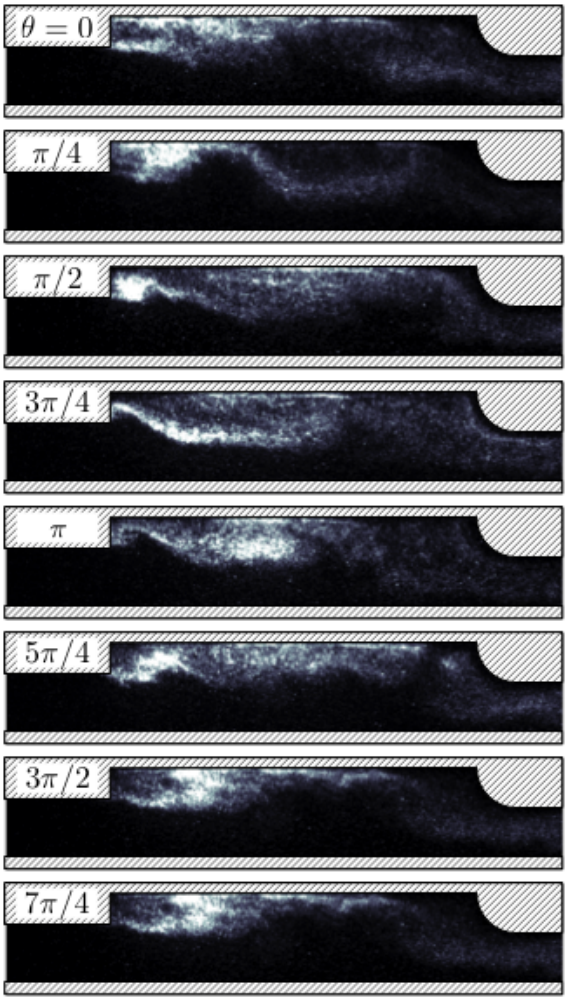

Figure 5.43: Phase-locked CH* chemiluminescence of the flame during actively control combustion using Bio-SPK HRJ (Brand A).

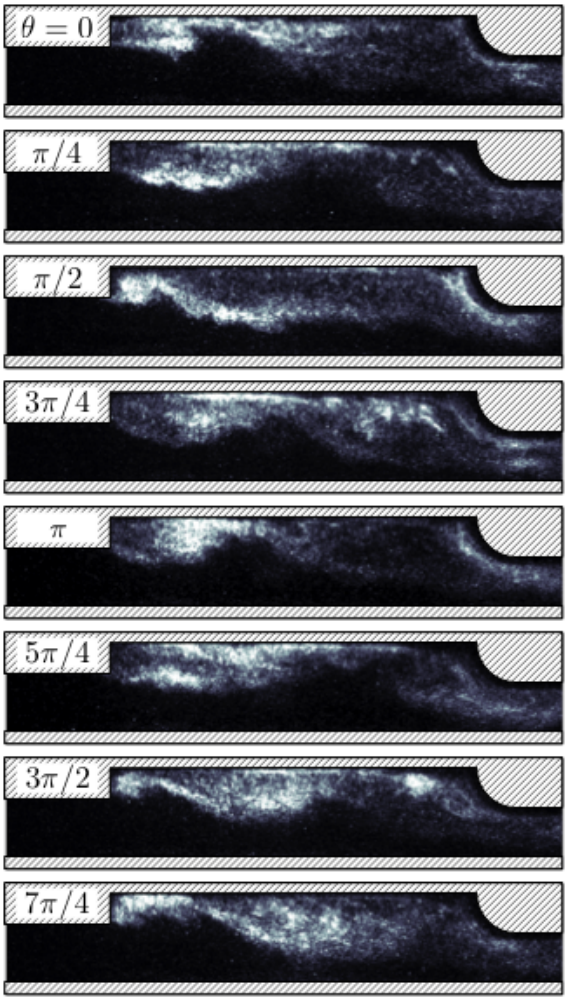

Figure 5.44: Phase-locked CH* chemiluminescence of the flame during actively control combustion using a 1:1 blend of Jet A and FT-SPK (Brand C).

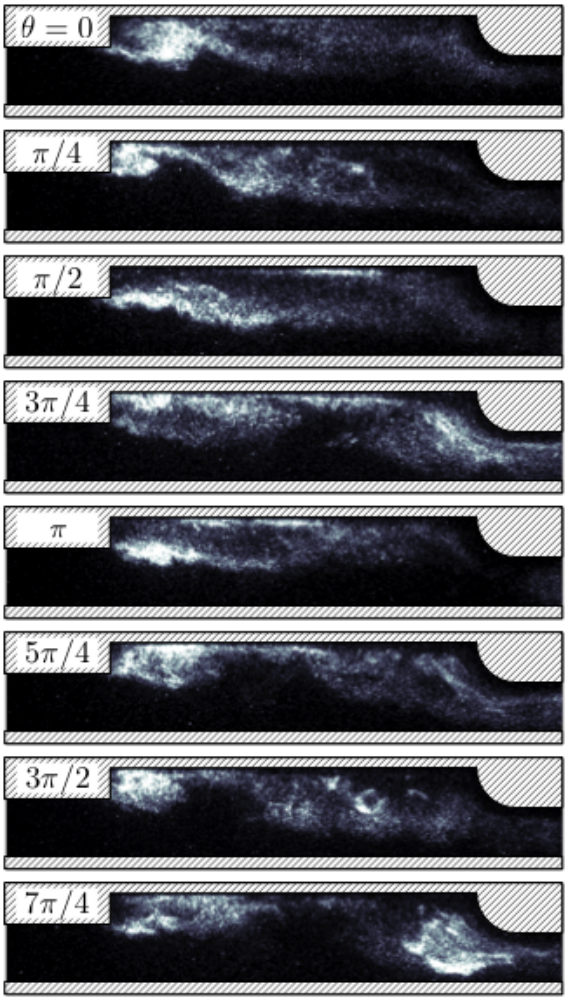

Figure 5.45: Phase-locked CH* chemiluminescence of the flame during actively control combustion using a 1:1 blend of Jet A and FT-SPK (Brand D).

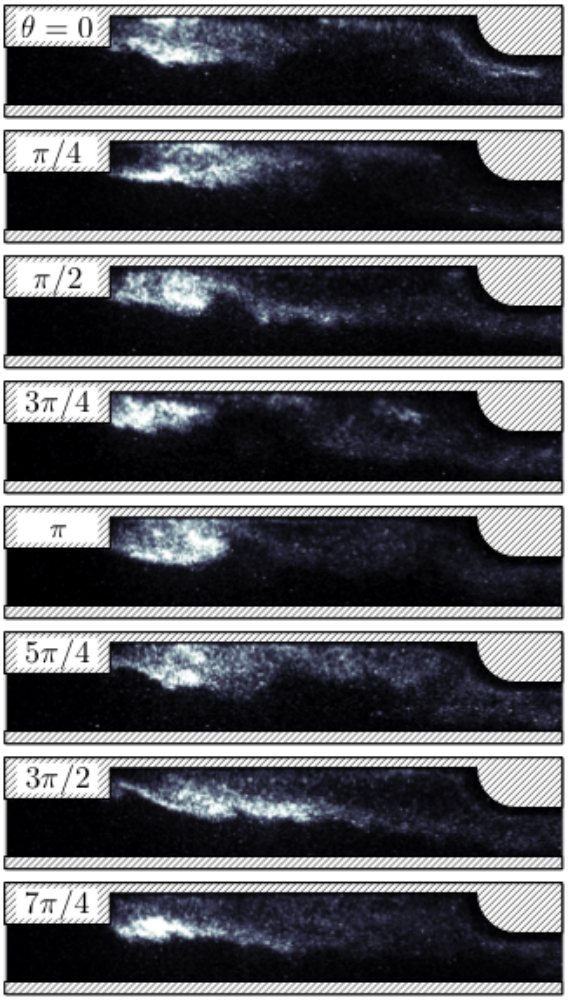

Figure 5.46: Phase-locked CH* chemiluminescence of the flame during actively control combustion using a 1:1 blend of Jet A and FT-SPK (Brand E).

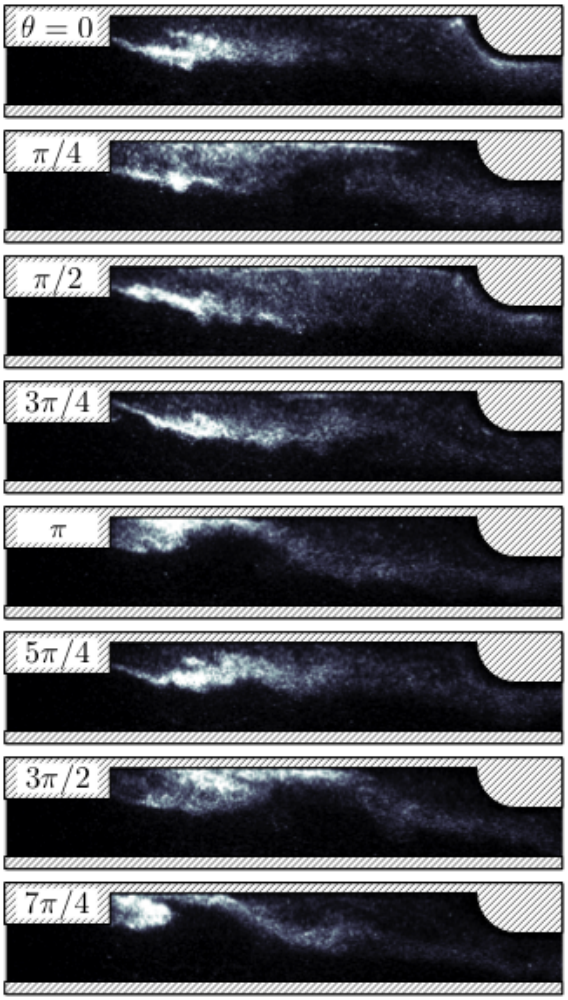

Figure 5.47: Phase-locked CH* chemiluminescence of the flame during actively control combustion using FT-SPK (Brand C).

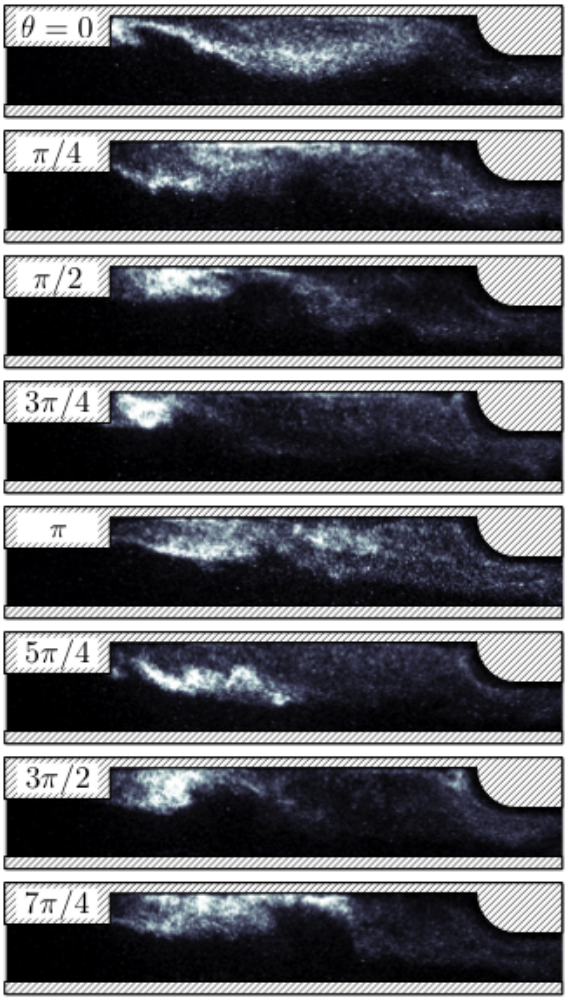

Figure 5.48: Phase-locked CH* chemiluminescence of the flame during actively control combustion using FT-SPK (Brand D).

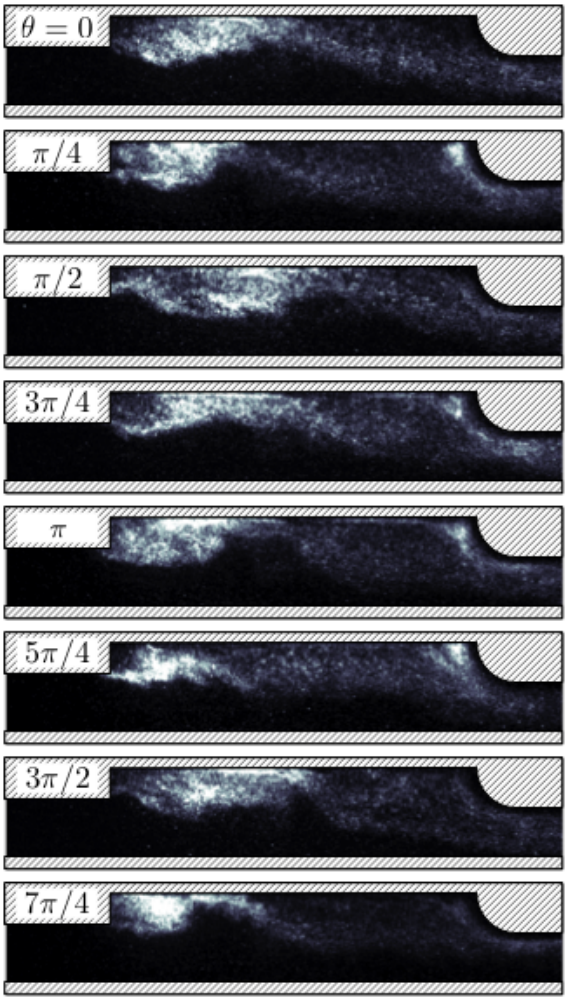

Figure 5.49: Phase-locked CH* chemiluminescence of the flame during actively control combustion using FT-SPK (Brand E).

6 | Practical Active Control for Suppression of Augmentor Instability

6.1 Active Control Strategies

Three different approaches for applying active combustion control to the augmentor were investigated. The first was a conventional secondary fuel injection approach where a small amount of fuel is diverted and injected in a different location with dynamic actuation. Among the active control approaches investigated in the present work, the disadvantages of this technique are that the additions and modifications that must be made to the combustor design. While less intrusive than current passive solutions, the installation of a secondary fuel injector requires additional hardware that also adds potential points of failure. Nevertheless, secondary fuel injection is a flexible solution that can be used in a wide range of instability scenarios. For this study, a custom-made actuator consisting of an off-the-shelf high-performance automotive fuel injector was used in series with an atomizer to inject Jet A. The secondary fuel injector was closely coupled with the atomizer in order to optimize the frequency response of the combined system, and could be installed

in either the test section immediately downstream of the flame-holder or upstream in the augmentor inlet.

The second ACC approach was through main fuel modulation where a small amount of the augmentor's fuel is dynamically actuated back into the fuel line prior to injection. This is more practical than secondary fuel injection since it only requires modifications to the fuel line as opposed to the combustor itself. However, the additional complexity and difficulty of diverting and actuating fuel still poses a problem for this approach. Therefore, the third approach was to use secondary air injection where a small amount of air is actuated directly into the main fuel line prior to injection. This retains the advantage of not having to modify the combustor directly and adds to that the benefit of actuating air (instead of fuel), which is present in abundant quantities and simpler to implement. In both cases, a direct drive valve (Textron) mounted to the main fuel line performed the actuation. Gaseous ethylene was used for both the simulated pre-vaporized augmentor fuel and the actuated fuel in these tests. Then the secondary air injection approach was adapted and applied to the augmentor where the fuel was partially liquid. In this case, the air was actuated directly over the atomizer rather than attached to the augmentor fuel line. A new baseline was established for the partially liquid fuel configuration. A summary of the associated test conditions for each strategy is shown in Table 6.1.

For all of the approaches, the injection was performed at the observed instability frequency and phase controlled via closed-loop controller. The dynamic pressure data was appropriately band-pass filtered through a hardware filter and

Table 6.1: Summary of active control test configurations.

ACC Strategy	Baseline ϕ_{aug}	Injection Location	Atomization
Secondary Fuel Injection	0.8±0.02	Inlet/V-Gutter	Swirl/Plain
	0.6±0.03	V-Gutter	Swirl/Plain
Primary Fuel Modulation	0.9±0.03	Aug. Fuel Line	–
Secondary Air Injection	0.9±0.03	Aug. Fuel Line	–/Swirl

provided to the controller for timing purposes. The phasing was calculated using the negative-to-positive zero crossing of the oscillating pressure signal as a reference.

6.2 Description of Augmentor Instability

Several unstable conditions were targeted for suppression using active combustion control. Details of the targeted conditions are shown in Table 6.2 and the frequency spectra of the oscillating pressure are shown in Fig. 6.1 - 6.4. The observed instability frequency was 135±5 Hz for all of the test cases. It is can be seen from these results that the peak instability amplitude decreases with decreasing augmentor equivalence ratio, with the largest peak occurring somewhat lower than stoichiometric. These results constitute a set of baselines for evaluating the performance of active control at the various test conditions.

The mechanism of this instability appears to be the result of coupling between heat release associated with large-scale 'flapping' of the flame and the acoustics of the augmentor section. The Helmholtz resonance frequency calculated using the inlet and test section of the augmentor as the resonator is equivalent to the observed instability frequency. The phase-locked chemiluminescence and sequential

Table 6.2: Test Conditions for naturally unstable augmentor operation.

Ref. No.	U_{aug}, m/s	ϕ_{pri}	ϕ_{aug}
1	30±2	0.25±0.02	0.6±0.03
2	30±2	0.25±0.02	0.7±0.03
3	30±2	0.25±0.02	0.8±0.02
4	30±2	0.25±0.02	0.9±0.03

high-speed schlieren data presented in Fig. 6.5 show that the flame motion also occurs at this frequency. This is shown with greater temporal resolution in the larger set of nonsequential phase-locked schlieren images shown in Fig. 6.6 along with the average pressure oscillation cycle. In both figures, the red triangles indicate the measured timing of the image capture with respect to the pressure oscillation.

These images reveal that the pressure oscillation cycle begins with a large flame area and, consequently, the temperature rises as heat is generated over most of the test section (i). This in combination with the nozzle causes the pressure to rise in the augmentor starting at the nozzle. The rise in downstream pressure acts to slow the bulk flow and forces the flame to spread outwards toward the outer walls(ii). These walls quench and contract the flame to the flame-holder(iii). At this point, the pressure oscillation reaches its apex and begins to fall, as the much more compact flame is no longer able to sustain pressure growth. This allows the fresh reactants to move more freely around the flame-holder, which enlarges the reaction zone in the gutter wake and pushes the combustion products out of the test section while simultaneously extending the flame (iv). Combustion is again occurring over most of the test section and the cycle repeats. The subsequent motion of the flame takes on the appearance of flapping.

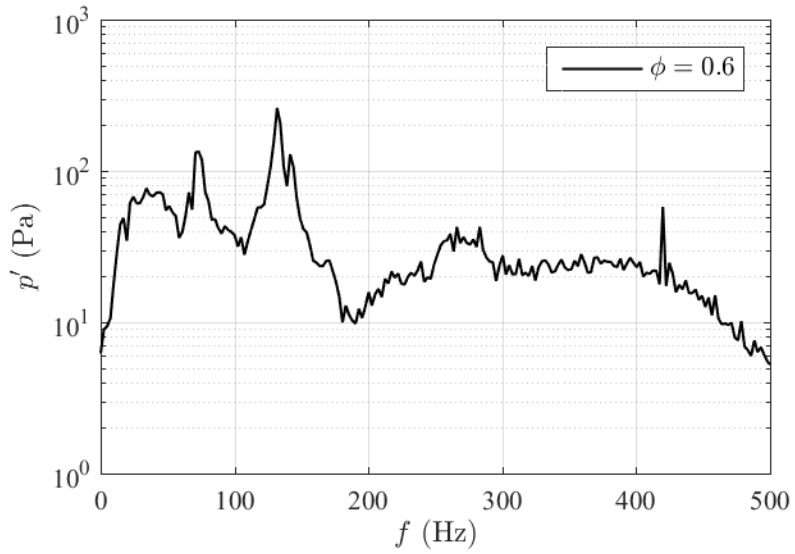

Figure 6.1: The frequency spectrum of the pressure oscillations during test case 1 (from Table 6.2).

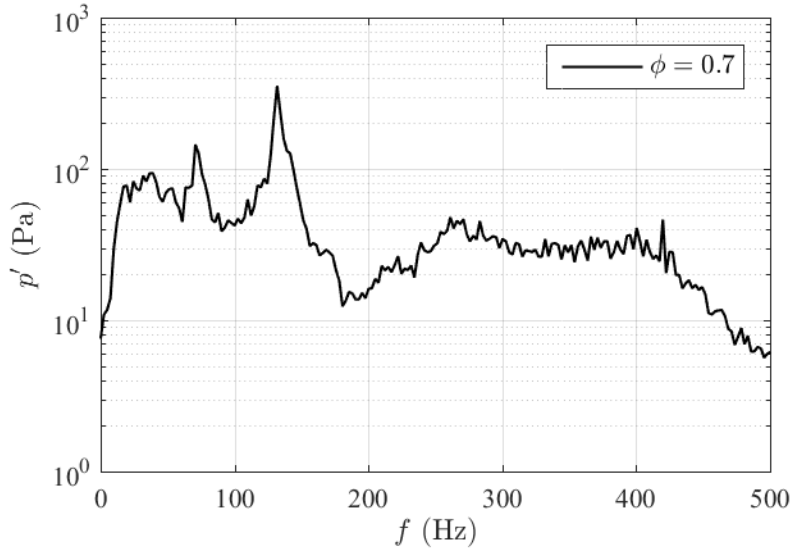

Figure 6.2: The frequency spectrum of the pressure oscillations during test case 2 (from Table 6.2).

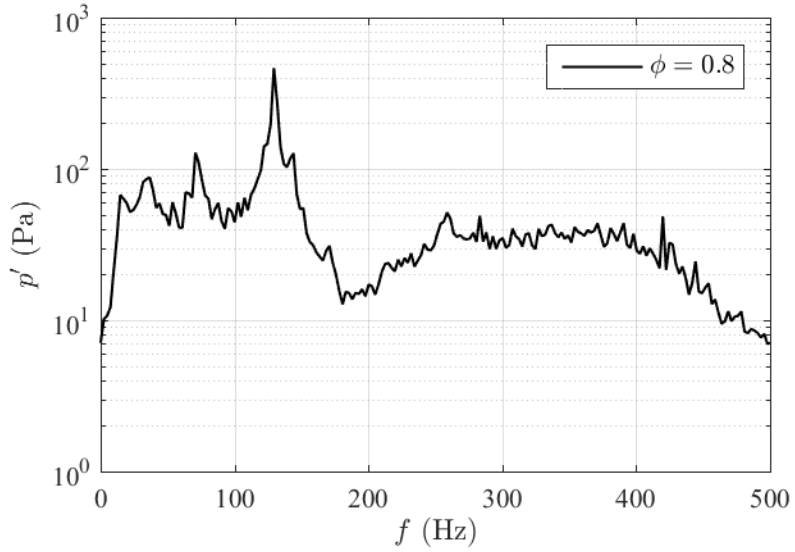

Figure 6.3: The frequency spectrum of the pressure oscillations during test case 3 (from Table 6.2).

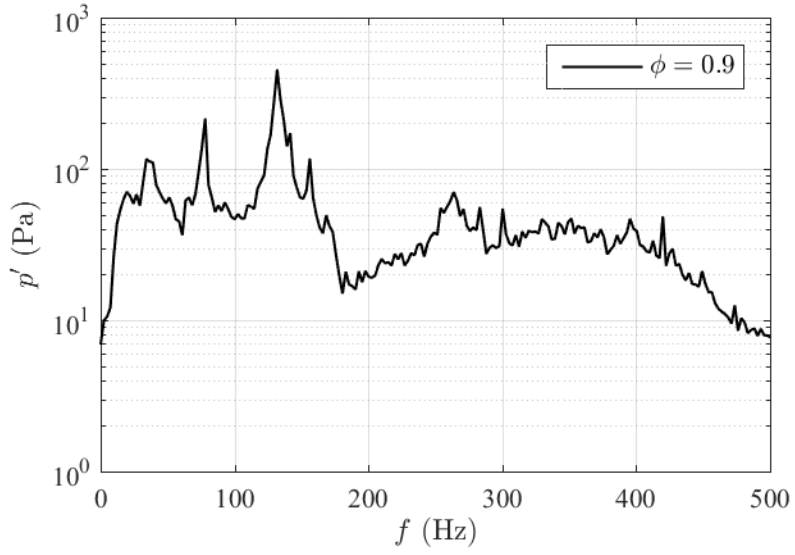

Figure 6.4: The frequency spectrum of the pressure oscillations during test case 4 (from Table 6.2).

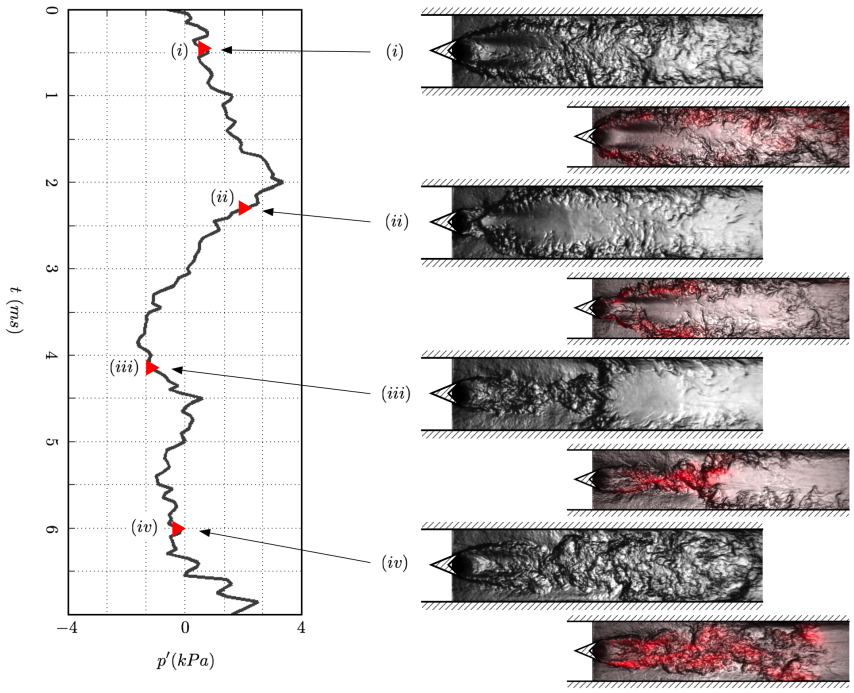

Figure 6.5: Sequential high-speed schlieren images for a single pressure oscillation cycle along with representative schlieren images superimposed with CH* chemiluminescence.

6.3 Secondary Fuel Injection Results

For this approach, the injection location and the atomizer type were varied to optimize ACC and augmentor performance. The need for optimizing the injector location was demonstrated by Lee, et. al. (2000) [75]. Therefore, the secondary fuel injector was installed in either the v-gutter wake or the inlet to investigate the effect of injection location. Furthermore, the injector could be mounted with either a swirl-type or plain-orifice-type atomizer, where the latter is expected to produce a spray with coarser droplets.

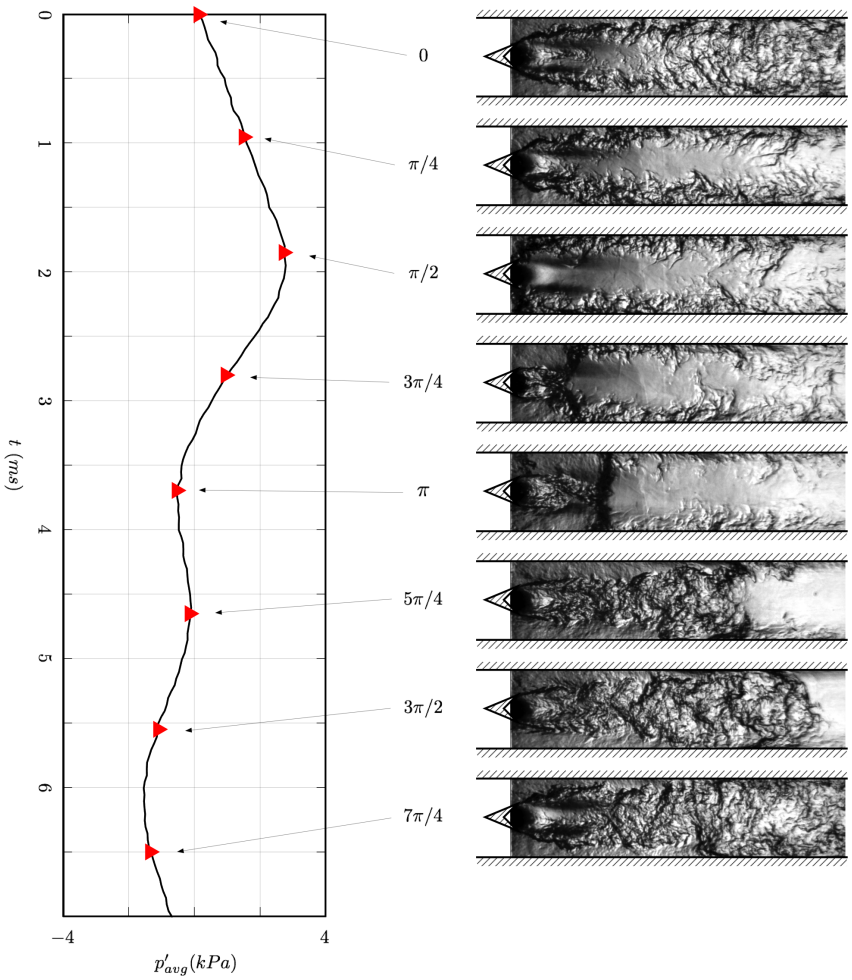

Figure 6.6: Nonsequential schlieren images over an average pressure oscillation cycle.

6.3.1 Effect of Injection Location

The results of the active control tests with varying secondary fuel injection locations are shown in Fig. 6.7. The results show that there was small suppression when injecting at the upstream location, which clearly demonstrates that ACC is not effective in this configuration. Increasing the flow residence time of the actuated sprays allows for greater fuel vaporization but also seems to attenuate fuel actuation. The combination of these effects along with the fine spray generated by the swirl atomizer could have resulted in the ACC system simply increasing the level of premixed fuel entering the test section to near baseline levels.

On the other hand, injection into the flame-holder wake produced a moderate amount of reduction in the peak instability amplitude. However, the suppression was insensitive to changes to the injection phasing. Furthermore, the reduction in peak instability amplitude is comparable to those attained by simply reducing the augmentor equivalence ratio by the secondary fuel amount as represented in the figure by steady injection at a lower equivalence ratio. This is possibly due to the use of a plain-orifice-type atomizer for secondary injection in this case. The results suggest that the volumetric heat release was reduced, most likely due to the poor atomization of the actuated spray. This could have altered the heat release pattern such that the premixed gaseous fuel was primarily responsible for the combustion inside the augmentor test section. So while instability was suppressed, any beneficial results are probably linked to the reduction in volumetric combustion efficiency.

Based on the results of these tests, any secondary injection location where the

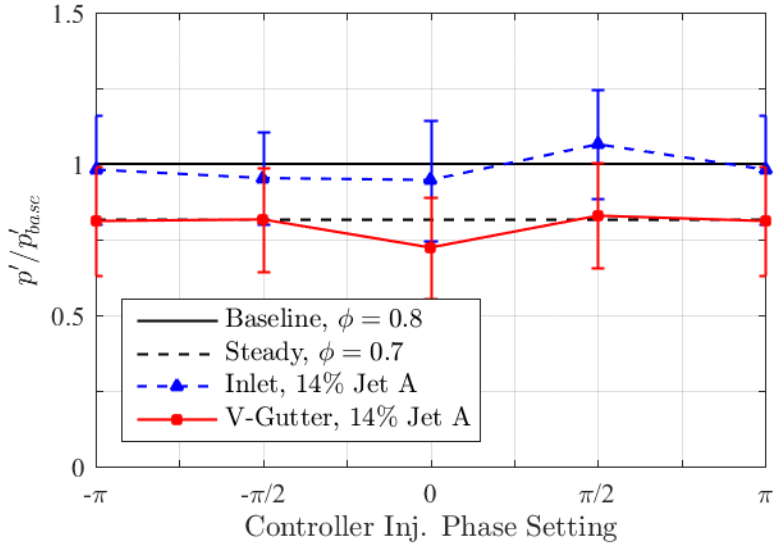

Figure 6.7: The active control performance/augmentor pressure oscillation response to changes in controller injection phase setting for different injector locations.

level of premixing is increased should be avoided, especially if the actuation of the fuel can also be attenuated. As such, secondary injection that occurs far upstream of the test section should be particularly avoided. Since the atomizers were varied between the two sets of tests, the influence of fuel atomization is reserved for the next section.

6.3.2 Effect of Fuel Atomization

The performance of the custom actuation system using a swirl-type atomizer was previously measured [74] and the sauter mean diameter (SMD) was found to be approximately 50 μm. Furthermore, the SMD of the spray produced using a plain-orifice-type atomizer can be calculated using Eq. 6.1, as described by Elkotb (1982) [76]. This equation estimates the SMD of the plain-orifice-type atomizer to

be approximately 270 μm, which is much coarser than swirl-type as expected.

$$SMD = 6156\nu_L^{0.395}(\sigma\rho_L)^{0.737}\rho_A^{0.06}\Delta P_L^{-0.54}\mu m \tag{6.1}$$

The active control test results comparing atomizer type are shown in Fig. 6.8. Based on the previous results, the atomizer comparison tests were conducted with secondary fuel injection into the flame-holder wake. In contrast to the coarse spray, the finer spray produced a clear dependence on injection phasing. At the optimal setting, the suppression amount was comparable to the coarse spray results, while other non-optimal settings produced amplified oscillations. This demonstrates that timing-based ACC can successfully suppress instability without large compromises in volumetric combustion efficiency if the droplets are kept sufficiently small. Up to 37% suppression of the peak instability amplitude was achieved using properly phased active control.

The ACC tests have shown that for this particular combustor, secondary fuel injection works best when the fuel spray is fine and done close to the flame. The main advantage of timing-based ACC is the improvement of combustion efficiency that accompanies instability suppression. Furthermore, the results indicate that the premixed fuel plays an important role in determining the level of instability, and approaches that increase the level of premixed fuel can adversely affect instability.

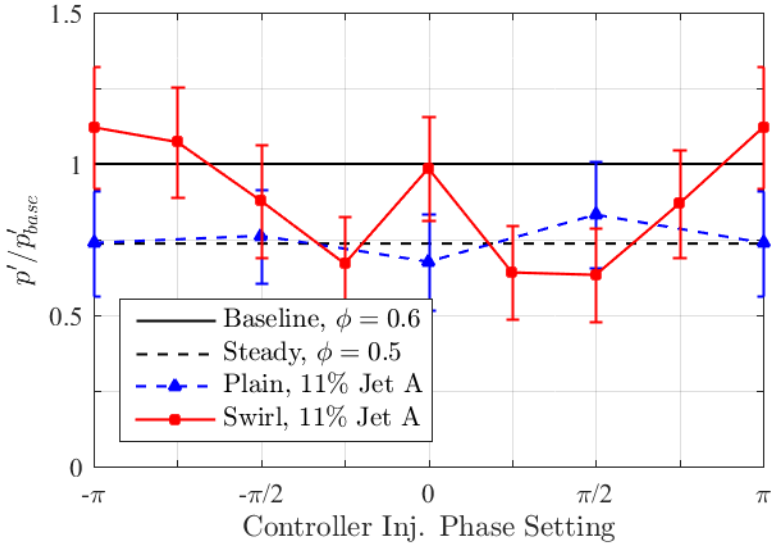

Figure 6.8: The active control performance/augmentor pressure oscillation response to changes in controller injection phase setting using different atomization techniques.

6.4 Main Fuel Modulation Results

For this approach, a small percentage of the gaseous ethylene augmentor fuel was actuated back into the fuel line via closed-loop control prior to injection into the augmentor. The benefits of this technique are that hardware modifications are limited and the premixed local equivalence ratio is directly targeted. The results of the active control tests investigating the performance of main fuel modulation with respect to the controller setting are shown in Fig. 6.9. These results clearly show that modulating the main fuel has a strong dependence on closed-loop controlled injection phasing. During non-optimal control there was a significant increase in the instability amplitude. However, a reduction of up to 45% in the peak instability amplitude was demonstrated under optimal controller settings, which suggests that this technique has meaningful control authority over the combustion process.

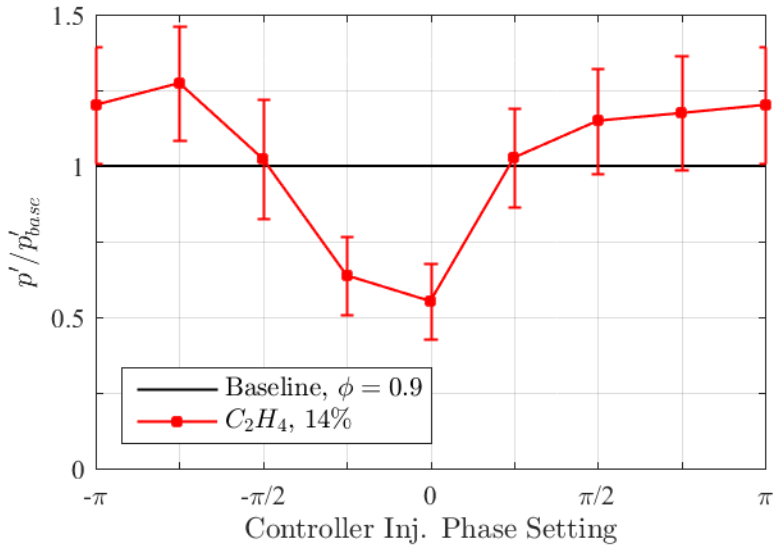

Figure 6.9: The active control performance/augmentor pressure oscillation response to changes in controller injection phase when using main fuel modulation.

This was not completely unexpected since earlier tests have shown that premixed augmentor fuel plays a large role in determining the level of instability. In effect, this approach directly affects the local equivalence ratio of the premixed fuel-air mixture supplied to the test section. These results are promising because of the benefits of the main fuel modulation as described in previous sections. However, it should be noted that these experiments were conducted using gaseous ethylene to simulate pre-vaporized fuel and it is not necessarily applicable in cases where the augmentor is injecting liquid directly into the combustion system.

6.5 Secondary Air Injection Results

The basic principle behind secondary air injection is the same as main fuel modulation described in the previous section. The main difference lies in the actuated fluid. The benefit of using air is that it is simpler to use and it is available in

abundant quantities in a typical aircraft engine. For the present work, secondary air injection is first tested with gaseous ethylene main fuel, and then adapted and investigated for use with liquid main fuel injection.

6.5.1 Gaseous Augmentor Fuel

The results of ACC evaluations using secondary air injection with varying controller settings are shown in Fig. 6.10. These results clearly show that secondary air injection also has a strong dependence on closed-looped controlled injection phasing. It was demonstrated that while under non-optimal settings there is a significant increase in the instability, while a reduction of up to 47% in the peak amplitude was demonstrated under optimal settings.

Given the results shown in the previous section, it is not entirely surprising that secondary air injection performed well since this approach directly affects main fuel injection and therefore, the local premixed equivalence ratio. The surprising aspect of these results is that it is nearly identical to the performance of main fuel modulation. It should be noted that the only difference between main fuel modulation and secondary air injection (both with gaseous ethylene) is the fluid that is actuated into the main fuel line. The optimal controller setting for both cases was $\theta = 0 \pm \pi/4$, which is incidentally also the optimal controller setting for secondary fuel injection. This insensitivity to the controlled fluid requires further investigation. However, an early hypothesis is that the fluid injection causes fuel line pressure changes, which modulates the fuel flow rates at the augmentor injectors.

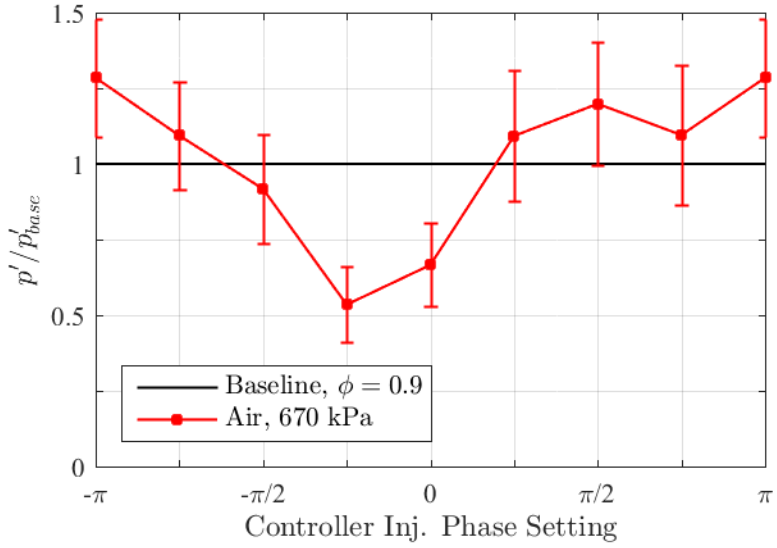

Figure 6.10: The active control performance/augmentor pressure oscillation response to changes in controller injection phase when using main fuel modulation with actuated air injection.

These results are especially promising because the approach retains the advantage of main fuel modulation while adding the further benefit of actuating air. However, these tests were again conducted using gaseous ethylene to simulate pre-vaporized fuel. In the following sections, this technique is adapted and investigated for use with liquid augmentor fuel.

6.5.2 Liquid Augmentor Fuel

Based on the success of the main fuel modulation approach and the subsequent success of secondary air injection (both using gaseous ethylene as the augmentor fuel), the secondary air injection method was adapted to work with liquid main fuel. For this case, a new baseline was established in which the augmentor fuel largely consisted of gaseous ethylene with a supplement of Jet A. The frequency spectra

of the oscillating pressure, along with an accompanying sample pressure oscillations time trace, are shown in Fig. 6.11. Under these new operating conditions the peak instability amplitude was increased by nearly 50% of the previous equivalent baseline. To achieve this, air was steadily injected across the face of the flush-mounted swirl-type atomizer in order to prevent the liquid fuel from collecting at the opposite wall and avoiding combustion. The air injection in this configuration was sufficient to meaningfully affect the spray trajectory. Without the air injection, the fuel penetration was such that the liquid fuel was not properly delivered to the flame and the resulting instability was comparable to previous baseline levels. Such suppression, while potentially effective, would come with a severe cost to volumetric combustion efficiency.

The results of the active control tests investigating the performance of secondary air injection with respect to the controller settings are shown in Fig. 6.12. These results reveal that secondary air injection has a weak dependence on closed-loop phase control when used with liquid fuel. That said, under optimal controller settings, up to 29% reduction in the peak instability amplitude was observed. The optimal controller setting seems to be offset by approximately π compared to the other control strategies, which may be due to how the instability suppression was achieved. The suppression seems to be a result of periodic shifting of the transverse equivalence ratio distribution due to the injector configuration. This process periodically deprived the augmentor of fuel by allowing it to collect along the opposite wall, thereby temporarily decreasing the effective equivalence ratio in the combustion region and subsequently decreasing the instability amplitude. In this way, suppression

was observed with air actuation, albeit with a penalty in the volumetric combustion efficiency.

Just as with the baseline, since only a relatively small percentage of the augmentor fuel was liquid, there was a relatively large gaseous premixed component that played a large role in determining the stability characteristics of the augmentor. Despite this, there was considerable suppression in the peak instability amplitude and some dependence on injection phasing, although it was accompanied by a reduction in combustion efficiency. Furthermore, it was demonstrated that air injection was able to affect the liquid fuel spray in a meaningful way. Therefore, despite the weak dependence on the controller parameter, it seems reasonable to assume that this behavior is a response to changes in the actuation phase delay given the observed combustion dynamics of the augmentor. This suggests that if the approach was further adapted to affect all of the augmentor fuel injection, which would then be entirely liquid fuel based, it may be possible to achieve greater control authority. This could also further reduce the hardware modifications required for this approach, which were quite extensive due to limitations of the experimental setup.

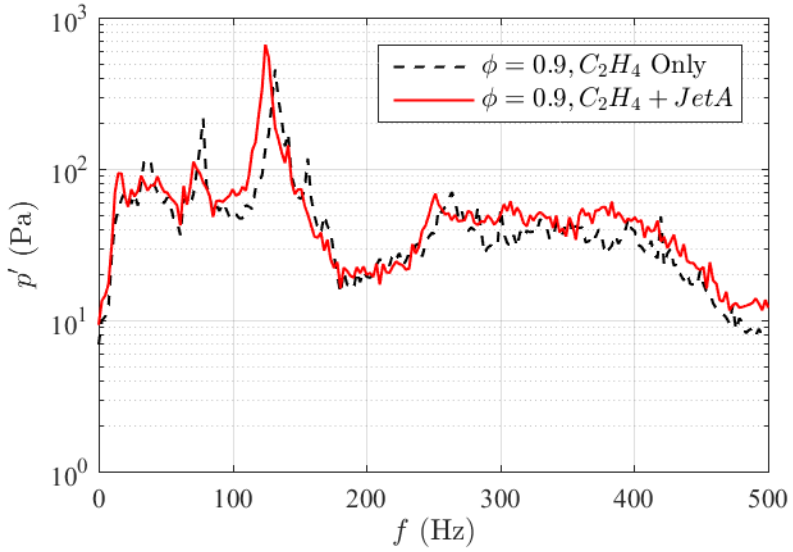

Figure 6.11: A comparison of pressure oscillation frequency spectra for liquid- and gas- fueled configurations of the augmentor.

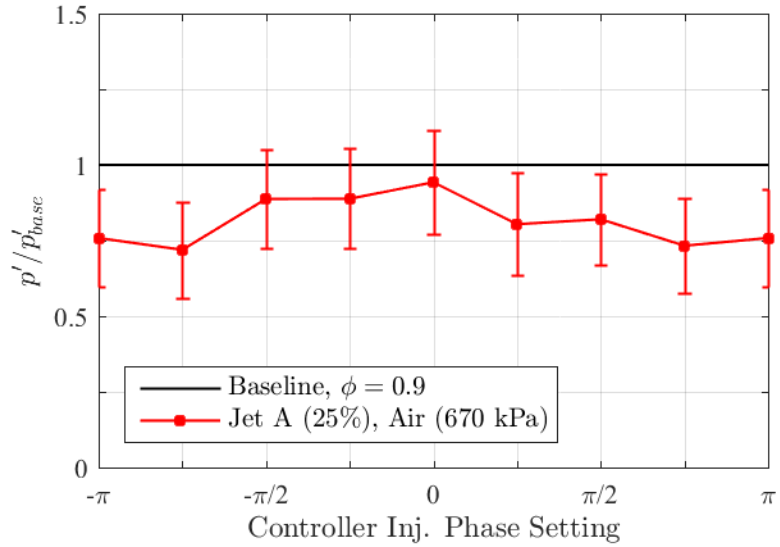

Figure 6.12: The active control performance/augmentor pressure oscillation response to changes in controller phase setting when using secondary air injection with a partially liquid fueled combustor.

7 | Summary and Conclusion

7.1 Modeling Heat Release

A model of heat release oscillations was proposed and evaluated to describe the onset of vortex driven heat release oscillations. This model relied on a separation of variables approach using a sinusoidal basis function. The model parameters, amplitude and phase, of the local variations in heat release were found to be purely spatial functions that could be calibrated using experimentally obtained results. These included phase locked CH* chemiluminescence images and high frequency dynamic pressure measurements from inside the combustion chamber. A spectral analysis of the measured combustor pressure oscillations indicated instability at 150 Hz, the same as the shedding frequency of the observed vortex structures.

Modeling of the heat release oscillations when using the calibrated parameters with the model approach proved to be accurate, resulting in insignificant deviations. Although the calibration of parameters using empirical data ensured that the modeled heat release oscillation would be relatively accurate, this result validates the simplifying assumptions that are integral to the model itself. Any minor discrepancies were restricted to the shear layer region where there were large vortex

movements, which could have triggered non-sinusoidal and possibly multi-modal heat release oscillations.

To improve the practicality of the model proposed in this paper, a trigonometric function mapping heat release oscillation at peak combustor pressure to the spatially varying phase difference between pressure and heat release oscillation was presented. It was shown that heat release measurements taken at the timing of the peak pressure phase was sufficient to model spatially and temporally resolved heat release oscillations. However, additional discrepancies in the model were observed near the nozzle location. Further analysis revealed that these were due to inaccuracies in the estimation of amplitude and the restriction on the phase distribution.

Stability analysis can be more practically accomplished using this approach to modeling variations in heat release, which can subsequently be used to map the local Rayleigh index. These maps are useful for identifying regions in the combustors that can be targeted to effectively suppress instability. The local Rayleigh index maps generated using both the modeled and experimental results were shown to be remarkably similar to each other and to the heat release oscillation map for the peak combustor pressure despite the additional discrepancies introduced by the estimation of model parameters. The mean local deviation of the rayleigh index model using estimated parameters was approximately 2.8% with respect to the experimentally obtained results. Importantly, this method significantly reduces the amount of experimentally obtained data required for a fully descriptive model of dynamic heat release. Furthermore, the global Rayleigh indices are consistent with the experimental observations in that they both indicate marginally unstable combustion

despite the aggregate global deviation of the model being roughly 28%. Lastly, the presence of strong vortex dynamics in these devices suggests that the heat release at the peak pressure phase can be modeled with combusting vortices. This opens up the possibility of modeling the heat release oscillation based purely on fundamental physical principles.

7.2 Alternative Fuel Study

Active combustion control using alternative fuels was used to successfully suppress thermo-acoustic instability in a laboratory-scale dump combustor. Twelve different fuel types were investigated including conventional fuels and mixtures. A naturally unstable condition occurring at an inlet velocity of 45 m/s and an equivalence ratio of 0.67 was targeted for active control experiments. In the baseline case, relatively large pressure oscillations were observed at 150 Hz. For control purposes, approximately 8% of the fuel was used in secondary fuel injection, in terms of total thermal output. Under optimal settings, the overall peak spectral amplitude of pressure oscillations was suppressed by up 64%. If one were to consider only the targeted primary instability frequency, up to 94% suppression was achieved.

The secondary fuel injection timing was varied for each fuel to observe the influence of controller fuel type on its setting. The results showed that the response of the combustor to changes in injection timing were similar for all investigated fuel types. Furthermore, the optimal injection timing and the level of instability suppression was similar across all examined fuel types. The latter stayed true even

at fixed injection timing, indicating that the controller was insensitive to the tested fuel types.

Instantaneous and phase-averaged mie-scattering images of the spray showed no significant differences in the spray pattern across the fuel types. The measured flow rate and maximum actuation frequency also exhibited a similar invariance. In addition, CH* chemiluminescence was used to visualize the flame in both baseline and controlled cases. Whereas the flame exhibited strong coherent behavior in the baseline (such as roll-up and convection due the vortices formed at the dump plane), the flame was much more distributed and steady in the controlled cases.

When combustion chemistry was investigated using a simplified droplet combustion model, the relevant fuel properties for determining the heat release response of the secondary fuel injection were found to be nearly equivalent, according to the published literature. These similarities may explain why the fuels performed similarly when used with secondary fuel injection. The model also revealed that for each fuel type, the peak heat release for the spray occurs soon after injection with respect to the instability period. This shows that secondary fuel injection using these fuel types should be able to provide control authority over the combustion process, which is consistent with the observed experimental results. Furthermore, the analysis suggests that the secondary fuel injection may be actively promoting the higher harmonic oscillations observed in the active control experiments.

The present work not only demonstrated that alternative fuels could be used in secondary fuel injection for suppressing combustion instabilities, but it also established that closed-loop active control can be used to enable fuel-flexible combustor

operation without sacrificing performance. Furthermore, this can be accomplished without modification to the controller for each fuel type.

7.3 Augmentor Study

Combustion instability mechanisms and ACC effectiveness were investigated in a model augmentor featuring a v-gutter flame-holder. Phase-resolved schlieren and CH* chemiluminescence images indicated large-scale flapping motion of the flame associated with the observed instability. The active combustion control performance was investigated as a function of injection location, method and injectant type using a small amount of dynamically injected reactant flow that was closed-loop controlled with respect to the pressure oscillation. Two different actuation strategies were investigated, which included main fuel modulation as well as secondary fuel and air injections.

The active control experiments revealed that a strategy using secondary fuel injection required optimizing the actuator location in such a way as to affect the transient fueling in the combustion region. While meaningful suppression of instability was demonstrated using this strategy, these results were eclipsed by the substantial reduction in instability amplitude achieved by simply forcing actuated fluid into the augmentor fuel line. The latter required less modification to the combustor hardware and a small amount of additional air injection at the instability frequency proved to be just as effective as actuated fuel injection in this case.

With respect to secondary fuel injection, it was further observed that an ap-

proach that increased the level of premixing adversely affected combustion instability in the augmentor. Furthermore, it was seen how relatively coarse droplets in the secondary fuel spray was not suitable for timing based ACC. However, it could still be useful in a combustion control approach relying on local equivalence ratio modification. Finally, timing based ACC was demonstrated on an augmentor and it was shown that finer atomization of the secondary fuel sprays was required for such a system to work. In this study, pulsed fuel sprays with a SMD of 40$\sim$60 μm produced phase-dependent results.

Based on the success of the main fuel modulation approach and the subsequent success of secondary air injection (both using gaseous ethylene as the main fuel), the secondary air injection method was adapted to work with liquid fuel. For this case, a new baseline was established in which the main fuel injection consisted of mostly gaseous ethylene but also air-assisted liquid jet fuel injected upstream of the flame-holder. Active control tests demonstrated that substantial suppression of instability was achieved using closed-loop controlled actuation of air injection. Unfortunately, injection phase dependence was weak and relatively more extensive hardware modifications were utilized. However, it should be possible to address these issues in future iterations of the approach.

A comparison of strategies indicates that, of those investigated, actuating a fluid into the pre-vaporized fuel line is the best approach for suppressing low-frequency combustion instability in an augmentor. In addition to its performance, this technique also reduces the required hardware modifications and offers similar flexibility to that of secondary fuel injection. Moreover, it does this while not re-

ducing combustion efficiency.

7.4 Key Contributions

The key contributions from this work are summarized below:

- Modeling Heat Release Oscillation for Stability Assessment

    1. A sinusoidal hybrid model of local heat release oscillation was sufficient to predict stability characteristics accurately. The heat release model contains only two parameters, which consist of the amplitude, A, and phase, ψ for each local position. The minimum set of data for model construction is the heat release pattern at one instant as well as the mean. It turns out that knowledge of heat release at p' maximum yields the most accurate results for stability prediction. The mathematical model developed for this work supports this finding.

    2. The significance of the finding is that it may be possible to model the heat release oscillation using the trajectory of large-scale vortical structures.

- Effect of Alternative Fuels on Control Parameters

    1. Active combustion control using secondary fuel injection was demonstrated with a variety of secondary fuel types. The controller parameter, especially the phase delay, was insensitive to the alternative fuel type.

    2. The practical implication of this result is that such a system can be used in a fuel flexible combustor without requiring alterations for each fuel

type.

- Active Control of Augmentor Instability

    1. Augmentor instability was characterized under various speed and equivalence ratios. The augmentor stability map was constructed for the first time and showed unexpected regimes of instability, quite different from the primary combustor case.

    2. Using secondary fuel or air to directly modulate the main fuel flow had a significant impact on the suppression of thermo-acoustic instability in an augmentor. This suggest that 1) in a pre-vaporized configuration, less invasive modifications are required on the combustor itself and 2) when liquid fuel is directly injected into the augmentor, suppression can be achieved without sacrificing combustion efficiency.

    3. Dynamic flame behaviors accompanying thermo-acoustic instability were visualized for both dump combustor and augmentor. For the augmentor, a flapping motion of the flame that coupled with pressure oscillations was identified and described.

7.5 Future Work

While the direction of progress shown in this work is promising and encouraging, research into combustion instability and active combustion control is by no means complete. This study has revealed several areas in need of further research.

In this dissertation, it has been shown that heat release in an unstable dump combustor can be modeled using a minimal empirical dataset. However, there are indications of a strong relationship between the reduced model parameters and the dynamic flow structures present in the combustion chamber. Additional work could be done to firmly establish this relationship and to see if it is possible to develop this into a physics based model for more practical stability analysis.

Exploratory experiments performed with higher enthalpy exhaust flow supplied to the augmentor resulted is marked different combustion behavior (not shown). Also, the stability map generated for the augmentor (also not shown) revealed interesting behavior for certain sets of operating conditions were regions of stable and unstable combustion with variations in augmentor equivalence ratio is separated by blow-off conditions. Additional experiments should be performed to investigate these unusual combustor behaviors.

Furthermore, secondary air injection was shown in this study to be quite effective at instability suppression while reducing the hardware modification requirement. However, this result is mostly applicable for use with prevaporized fuel. Additional work could be done to see if design improvements would allow for similar gains when applying this technique to liquid fueled combustors.

Appendix A | Supplemental Experimental Data for Chapter 5

Jet A:

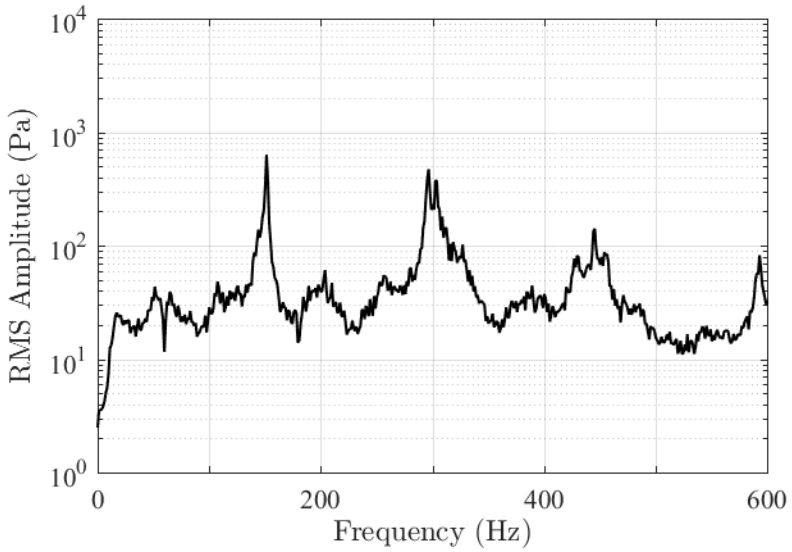

Figure A.1: The frequency spectrum for the pressure oscillations measured in the dump combustor while injecting Jet A at $\theta = 0$.

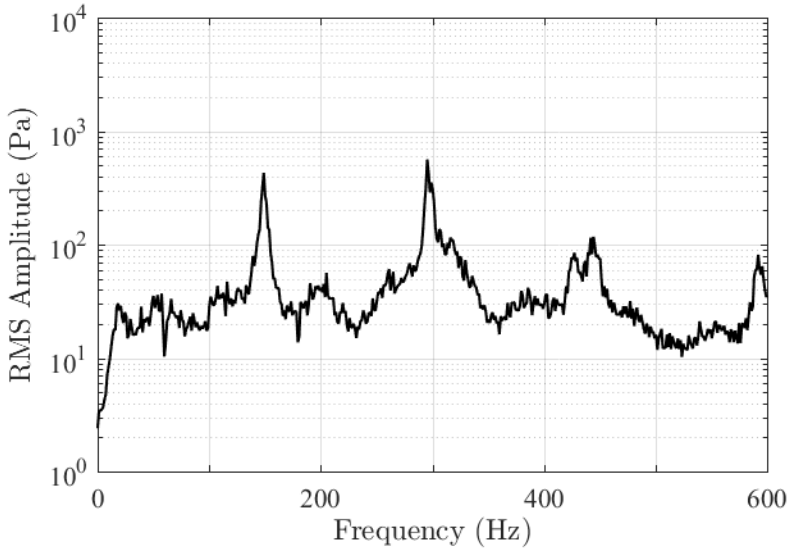

Figure A.2: The frequency spectrum for the pressure oscillations measured in the dump combustor while injecting Jet A at $\theta = \pi/4$.

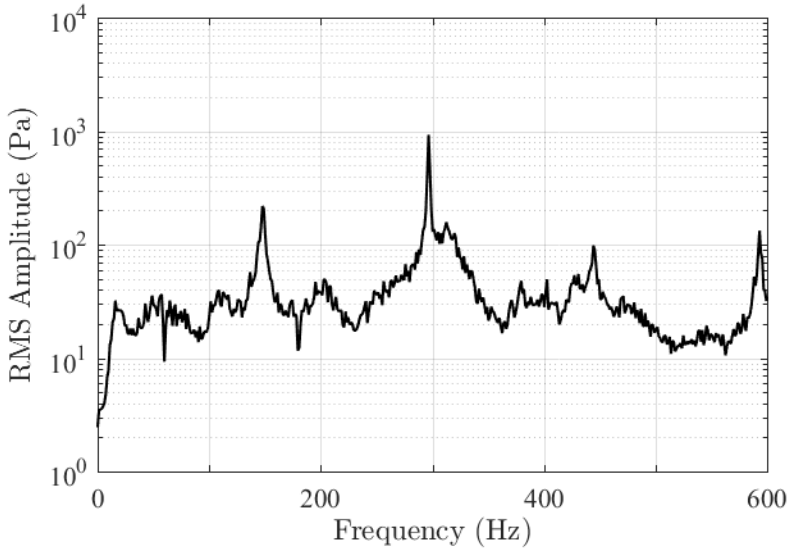

Figure A.3: The frequency spectrum for the pressure oscillations measured in the dump combustor while injecting Jet A at $\theta = \pi/2$.

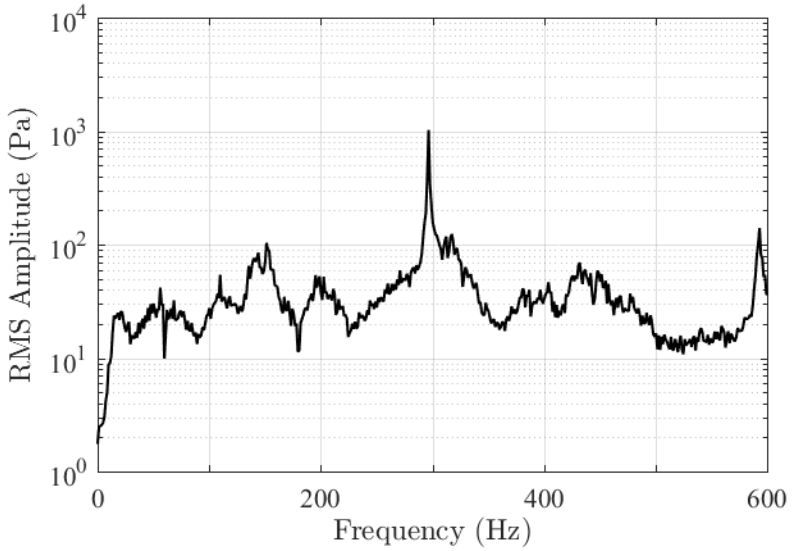

Figure A.4: The frequency spectrum for the pressure oscillations measured in the dump combustor while injecting Jet A at $\theta = 3\pi/4$.

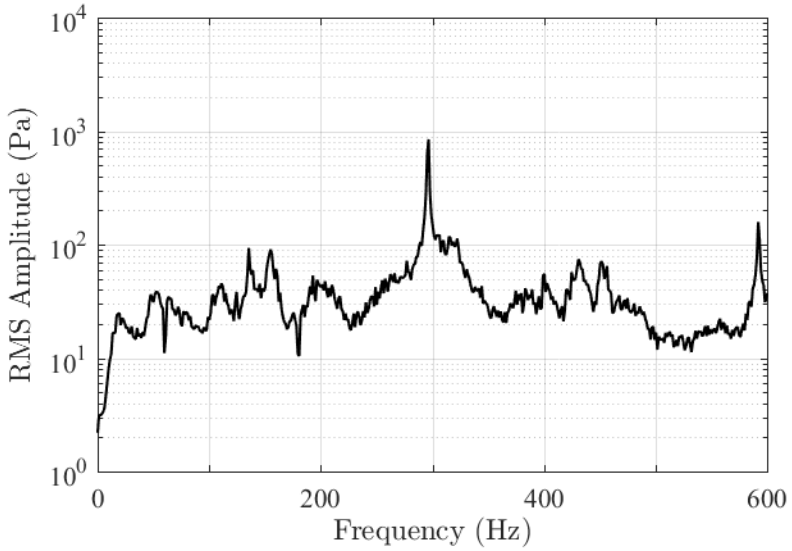

Figure A.5: The frequency spectrum for the pressure oscillations measured in the dump combustor while injecting Jet A at $\theta = \pi$.

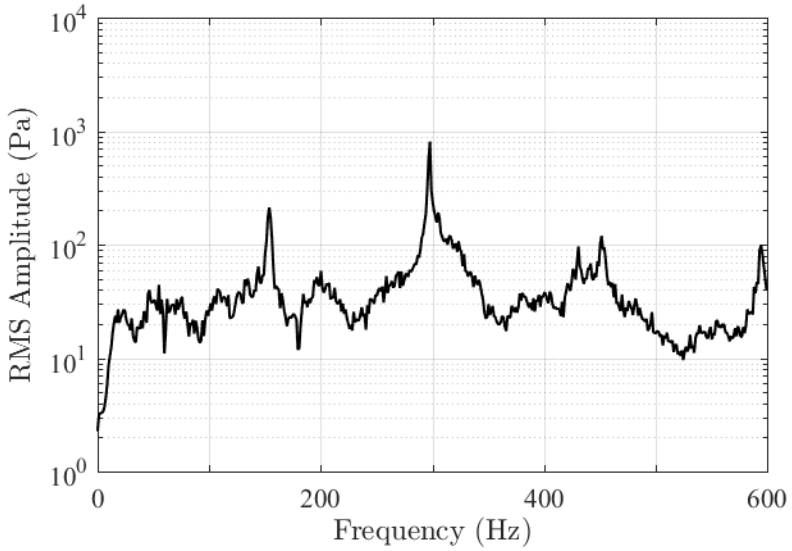

Figure A.6: The frequency spectrum for the pressure oscillations measured in the dump combustor while injecting Jet A at $\theta = 5\pi/4$.

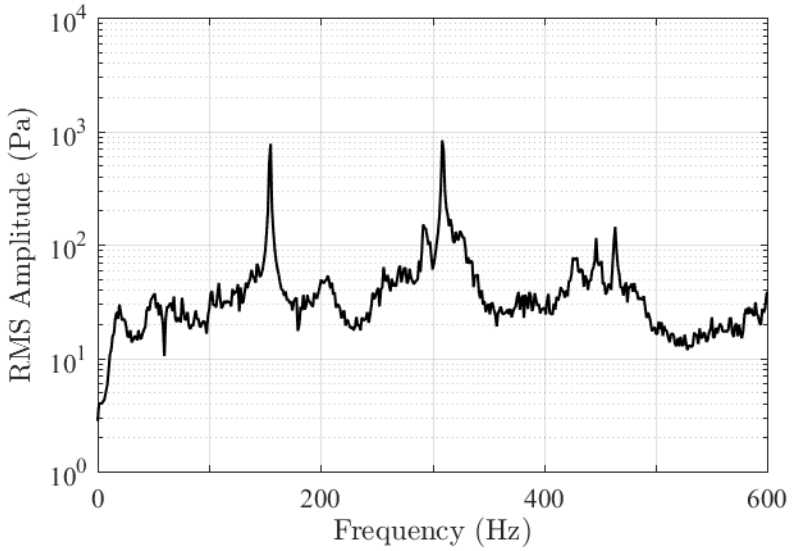

Figure A.7: The frequency spectrum for the pressure oscillations measured in the dump combustor while injecting Jet A at $\theta = 3\pi/2$.

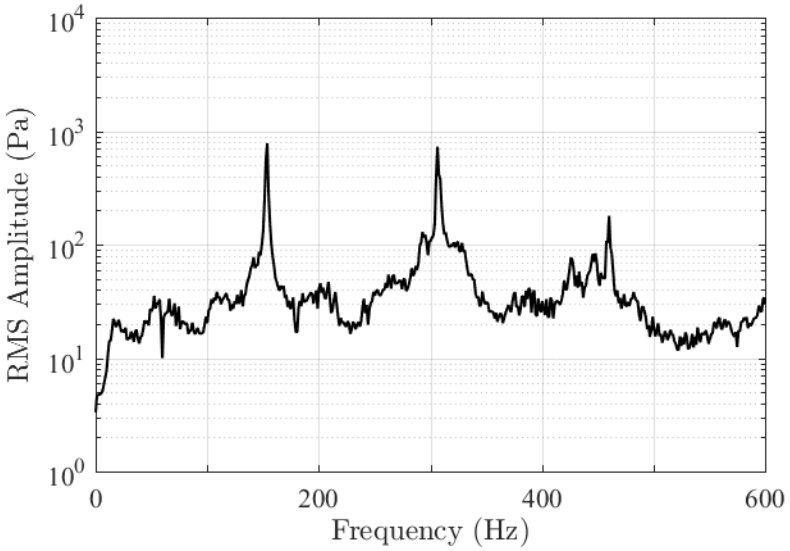

Figure A.8: The frequency spectrum for the pressure oscillations measured in the dump combustor while injecting Jet A at $\theta = 7\pi/4$.

1:1 blend of JP-8 and Bio-SPK HRJ (Brand A):

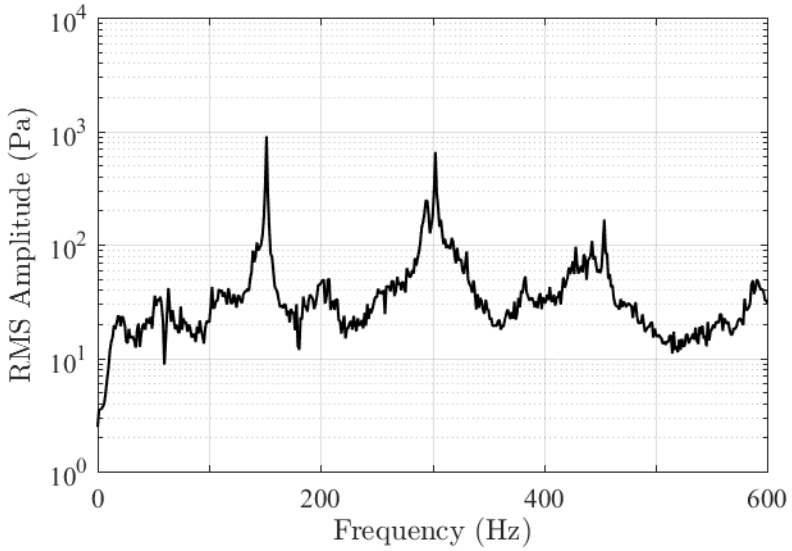

Figure A.9: The frequency spectrum for the pressure oscillations measured in the dump combustor while injecting 1:1 blend of JP-8 and Bio-SPK HRJ (Brand A) at $\theta = 0$.

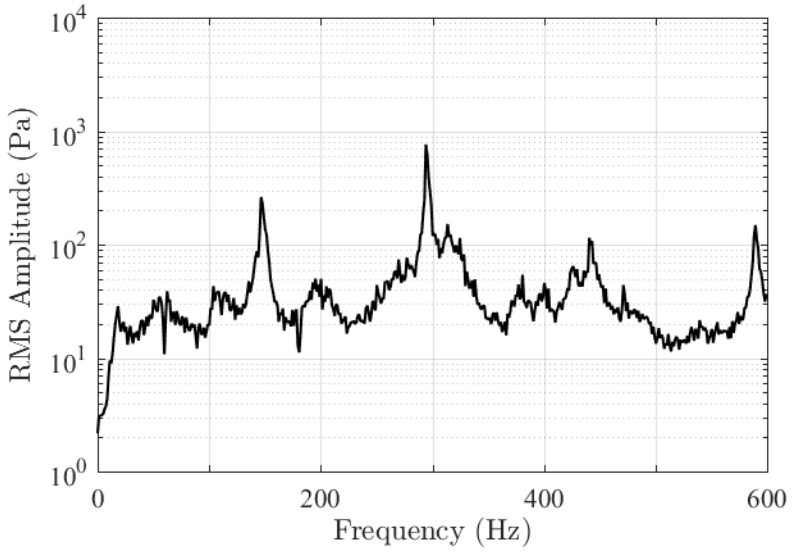

Figure A.10: The frequency spectrum for the pressure oscillations measured in the dump combustor while injecting 1:1 blend of JP-8 and Bio-SPK HRJ (Brand A) at $\theta = \pi/4$.

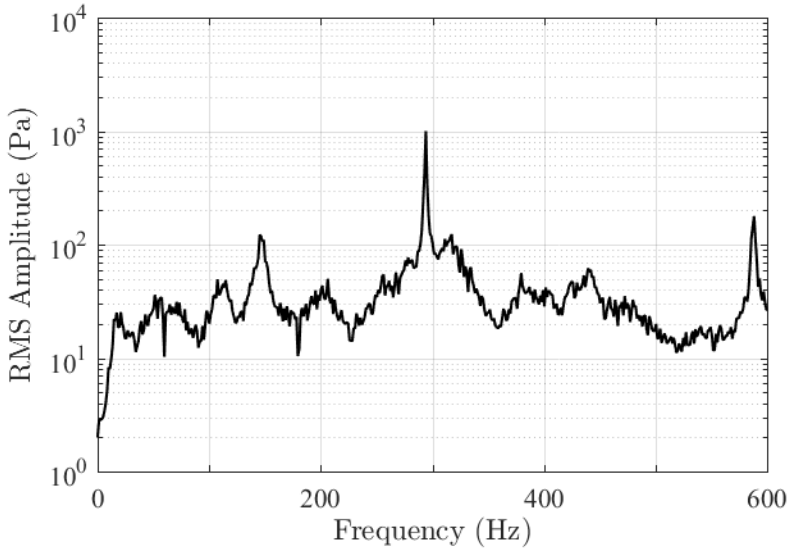

Figure A.11: The frequency spectrum for the pressure oscillations measured in the dump combustor while injecting 1:1 blend of JP-8 and Bio-SPK HRJ (Brand A) at $\theta = \pi/2$.

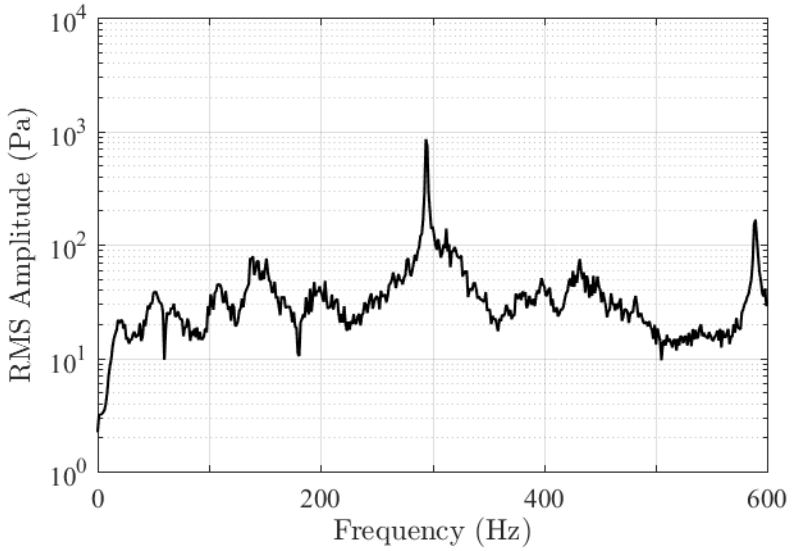

Figure A.12: The frequency spectrum for the pressure oscillations measured in the dump combustor while injecting 1:1 blend of JP-8 and Bio-SPK HRJ (Brand A) at $\theta = 3\pi/4$.

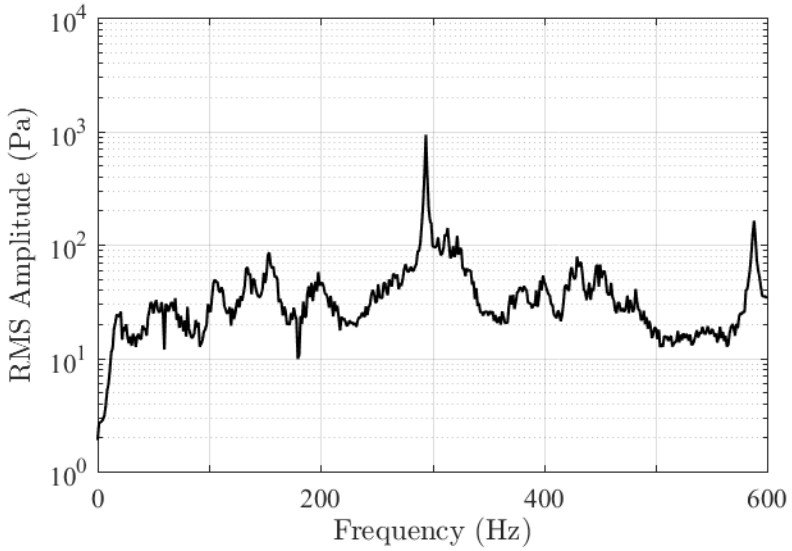

Figure A.13: The frequency spectrum for the pressure oscillations measured in the dump combustor while injecting 1:1 blend of JP-8 and Bio-SPK HRJ (Brand A) at $\theta = \pi$.

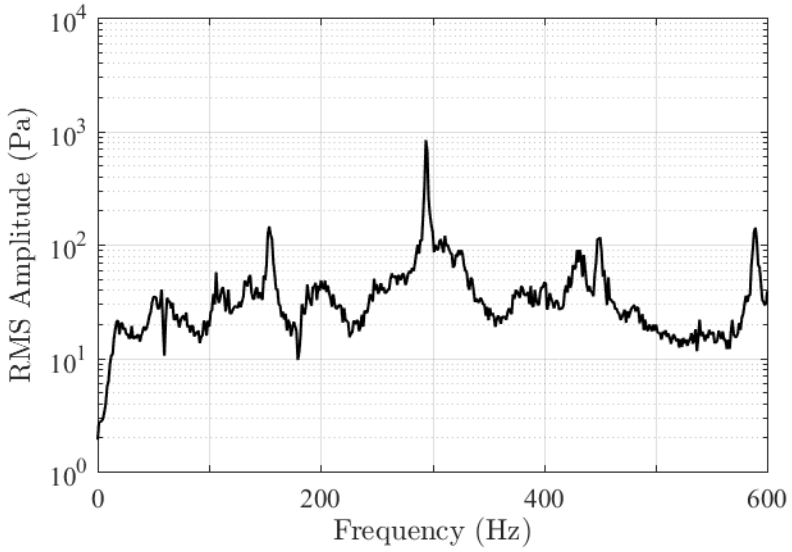

Figure A.14: The frequency spectrum for the pressure oscillations measured in the dump combustor while injecting 1:1 blend of JP-8 and Bio-SPK HRJ (Brand A) at $\theta = 5\pi/4$.

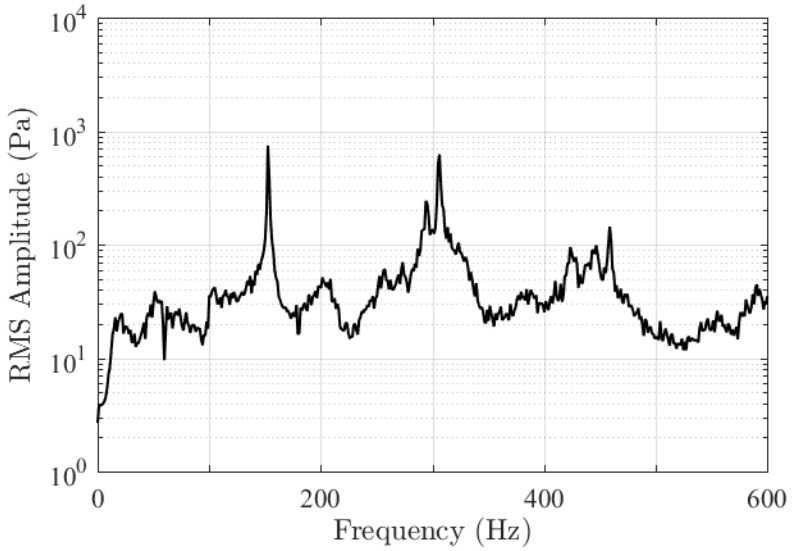

Figure A.15: The frequency spectrum for the pressure oscillations measured in the dump combustor while injecting 1:1 blend of JP-8 and Bio-SPK HRJ (Brand A) at $\theta = 3\pi/2$.

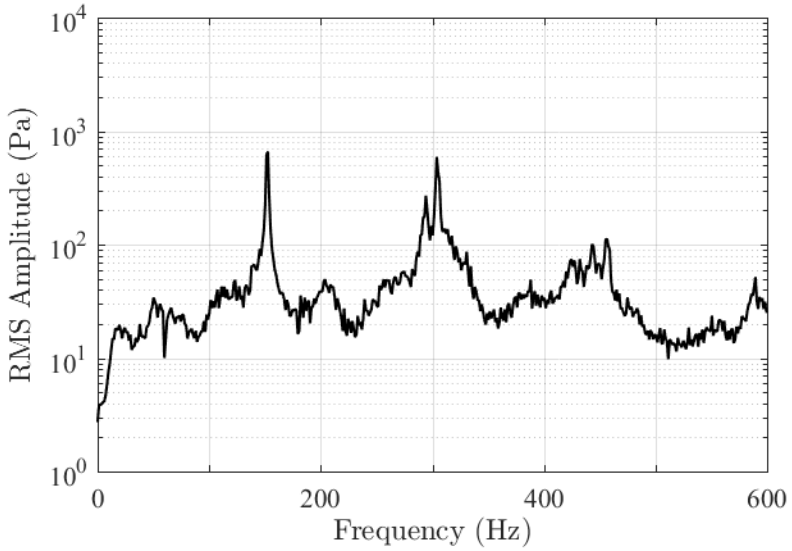

Figure A.16: The frequency spectrum for the pressure oscillations measured in the dump combustor while injecting 1:1 blend of JP-8 and Bio-SPK HRJ (Brand A) at $\theta = 7\pi/4$.

1:1 blend of JP-8 and Bio-SPK HRJ (Brand B):

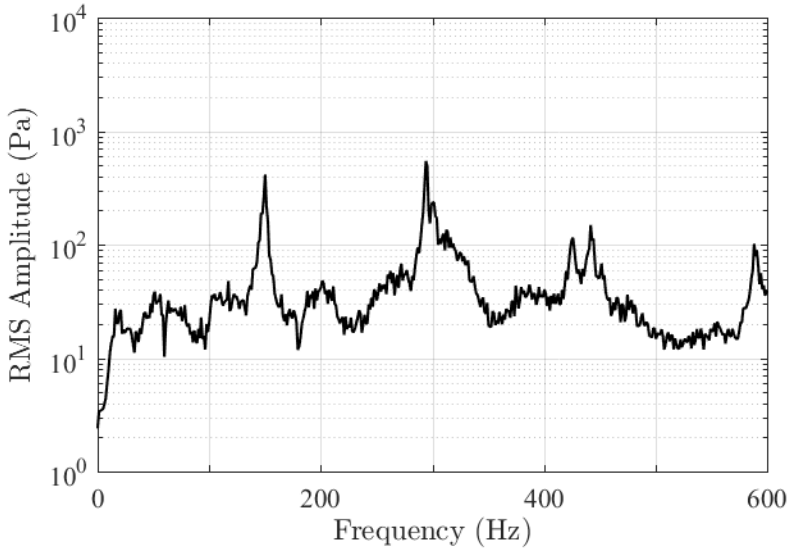

Figure A.17: The frequency spectrum for the pressure oscillations measured in the dump combustor while injecting 1:1 blend of JP-8 and Bio-SPK HRJ (Brand B) at $\theta = 0$.

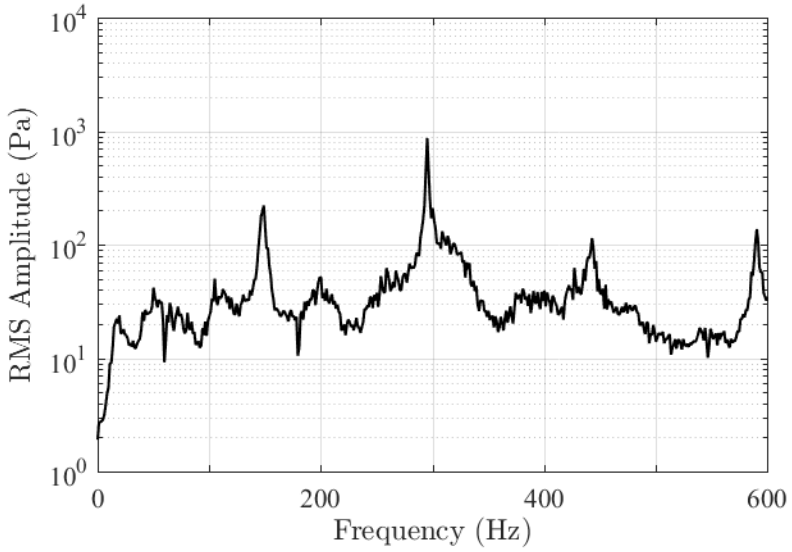

Figure A.18: The frequency spectrum for the pressure oscillations measured in the dump combustor while injecting 1:1 blend of JP-8 and Bio-SPK HRJ (Brand B) at $\theta = \pi/4$.

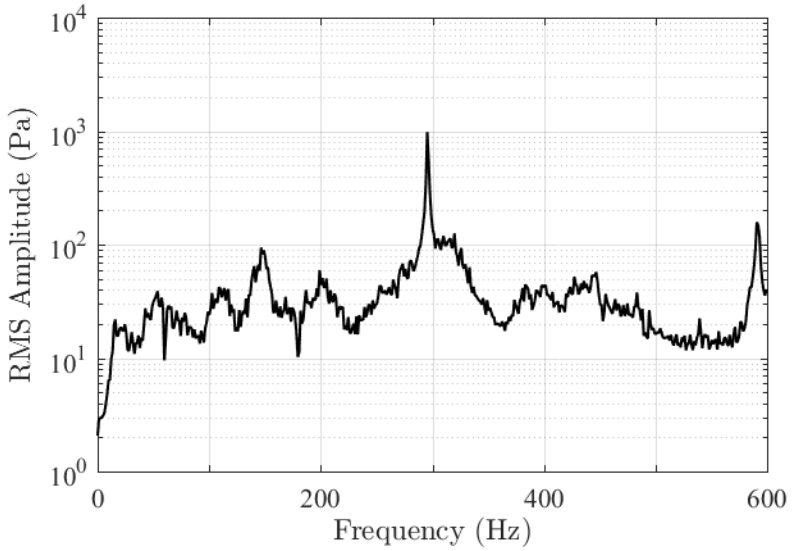

Figure A.19: The frequency spectrum for the pressure oscillations measured in the dump combustor while injecting 1:1 blend of JP-8 and Bio-SPK HRJ (Brand B) at $\theta = \pi/2$.

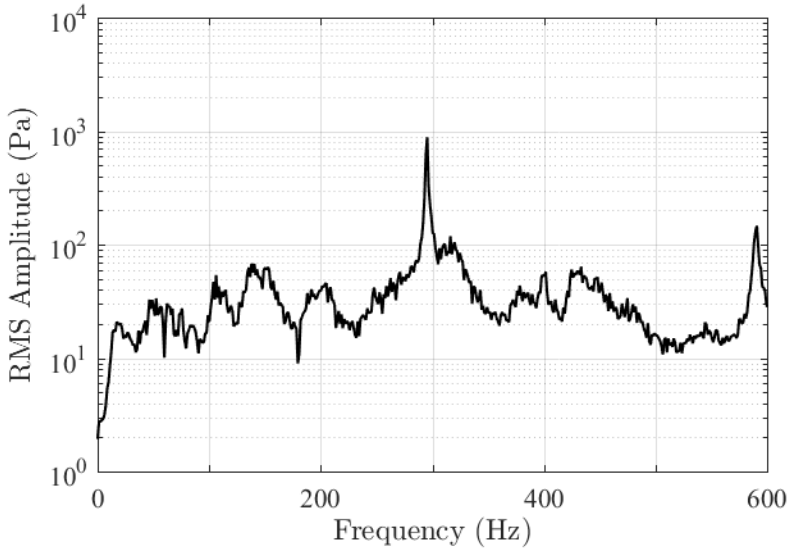

Figure A.20: The frequency spectrum for the pressure oscillations measured in the dump combustor while injecting 1:1 blend of JP-8 and Bio-SPK HRJ (Brand B) at $\theta = 3\pi/4$.

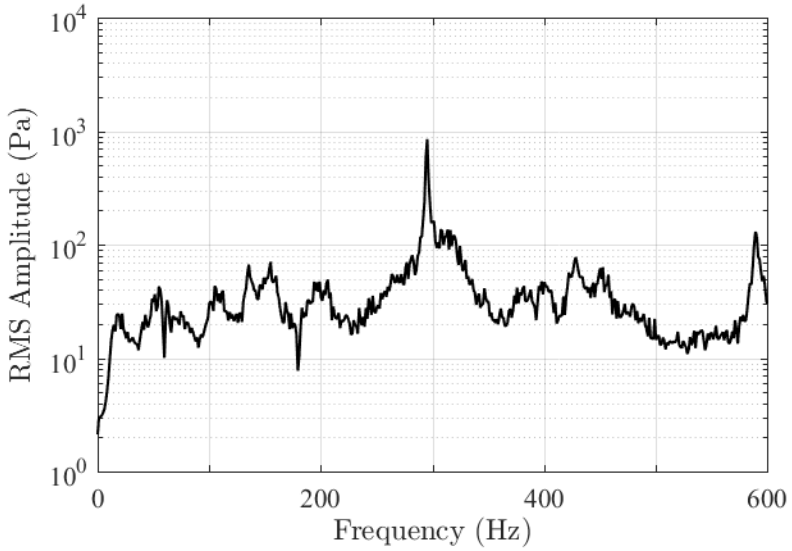

Figure A.21: The frequency spectrum for the pressure oscillations measured in the dump combustor while injecting 1:1 blend of JP-8 and Bio-SPK HRJ (Brand B) at $\theta = \pi$.

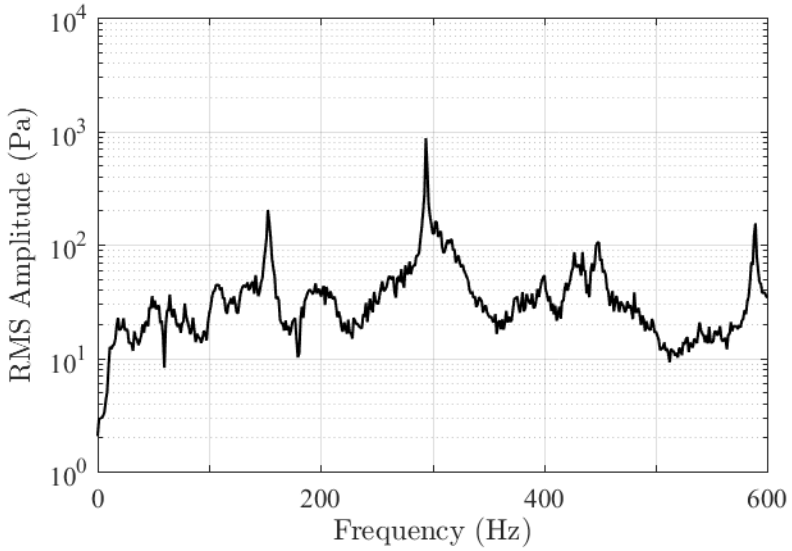

Figure A.22: The frequency spectrum for the pressure oscillations measured in the dump combustor while injecting 1:1 blend of JP-8 and Bio-SPK HRJ (Brand B) at $\theta = 5\pi/4$.

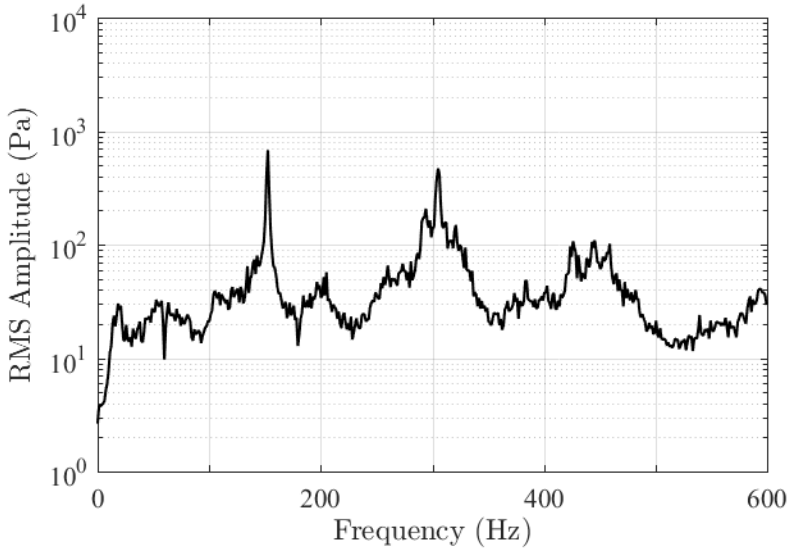

Figure A.23: The frequency spectrum for the pressure oscillations measured in the dump combustor while injecting 1:1 blend of JP-8 and Bio-SPK HRJ (Brand B) at $\theta = 3\pi/2$.

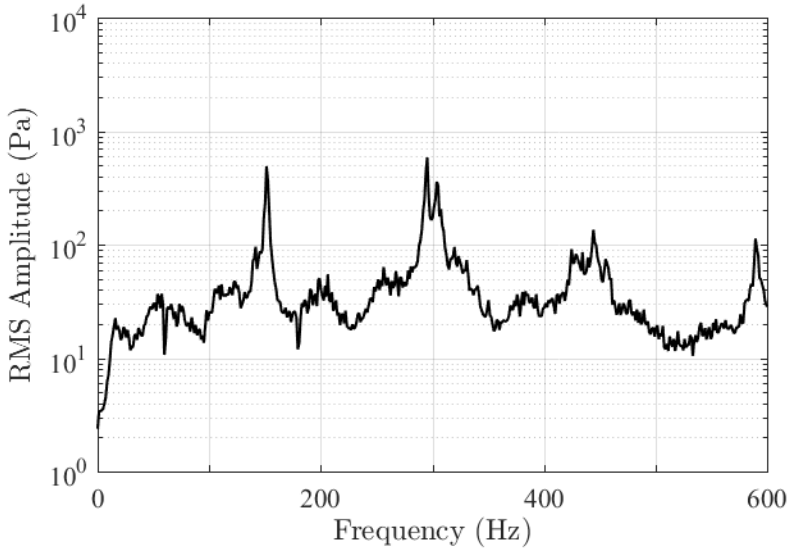

Figure A.24: The frequency spectrum for the pressure oscillations measured in the dump combustor while injecting 1:1 blend of JP-8 and Bio-SPK HRJ (Brand B) at $\theta = 7\pi/4$.

Bio-SPK HRJ (Brand A):

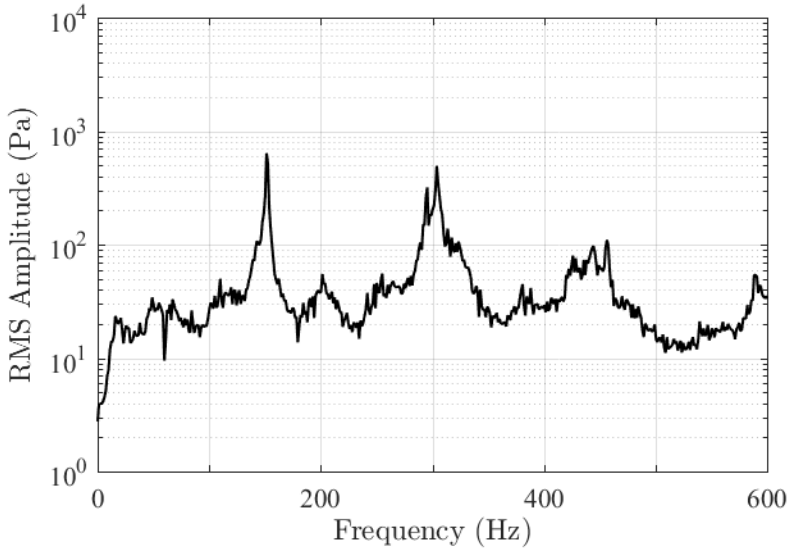

Figure A.25: The frequency spectrum for the pressure oscillations measured in the dump combustor while injecting Bio-SPK HRJ (Brand A) at $\theta = 0$.

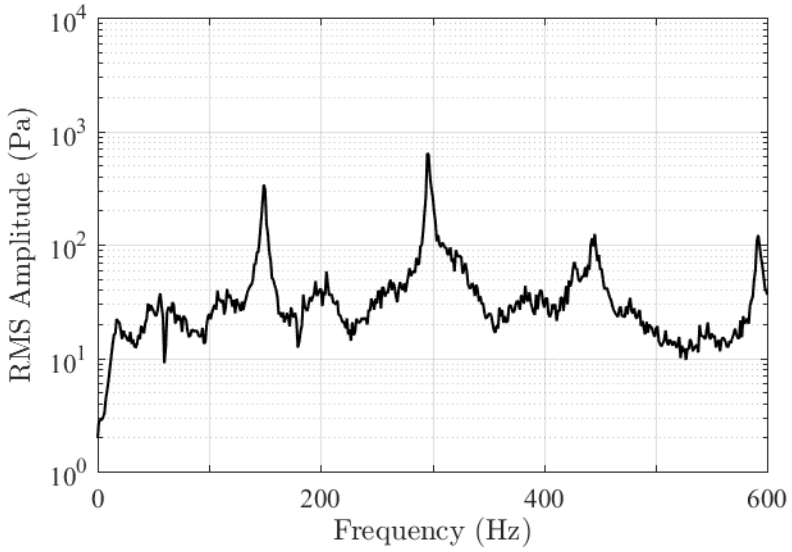

Figure A.26: The frequency spectrum for the pressure oscillations measured in the dump combustor while injecting Bio-SPK HRJ (Brand A) at $\theta = \pi/4$.

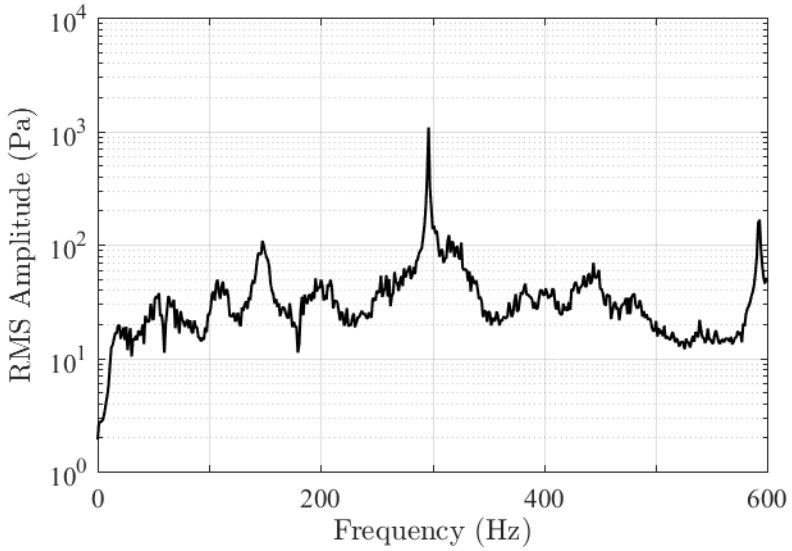

Figure A.27: The frequency spectrum for the pressure oscillations measured in the dump combustor while injecting Bio-SPK HRJ (Brand A) at $\theta = \pi/2$.

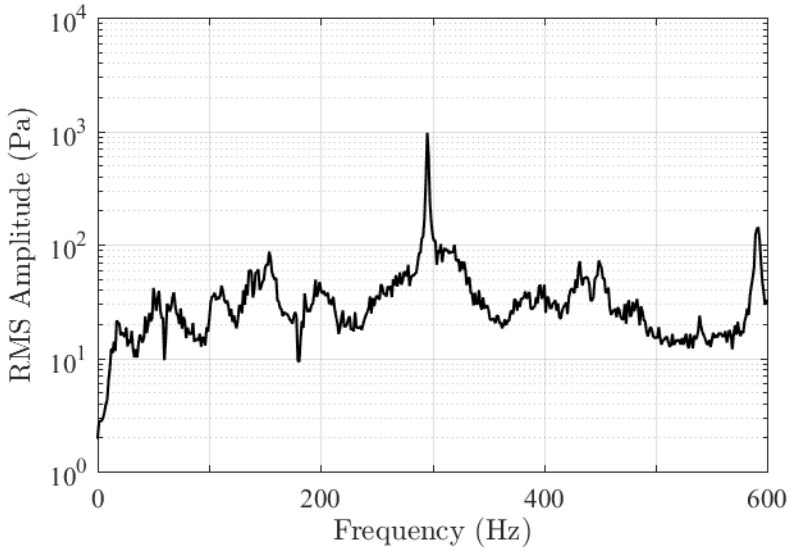

Figure A.28: The frequency spectrum for the pressure oscillations measured in the dump combustor while injecting Bio-SPK HRJ (Brand A) at $\theta = 3\pi/4$.

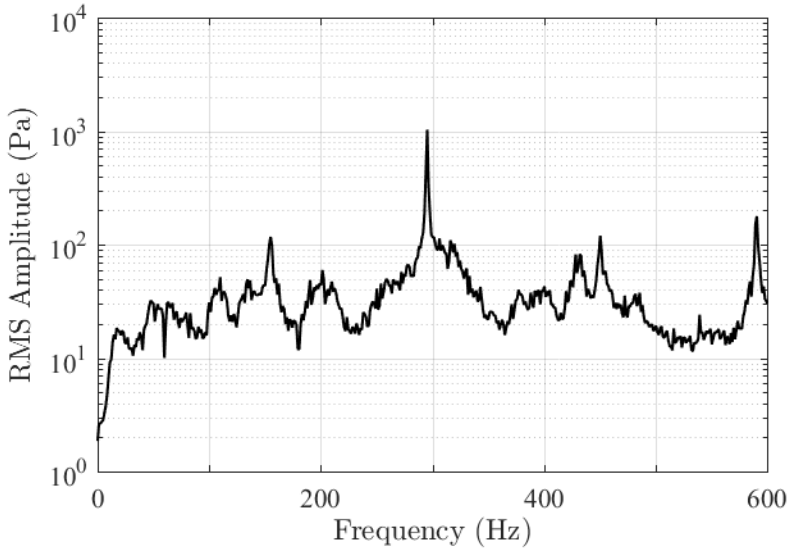

Figure A.29: The frequency spectrum for the pressure oscillations measured in the dump combustor while injecting Bio-SPK HRJ (Brand A) at $\theta = \pi$.

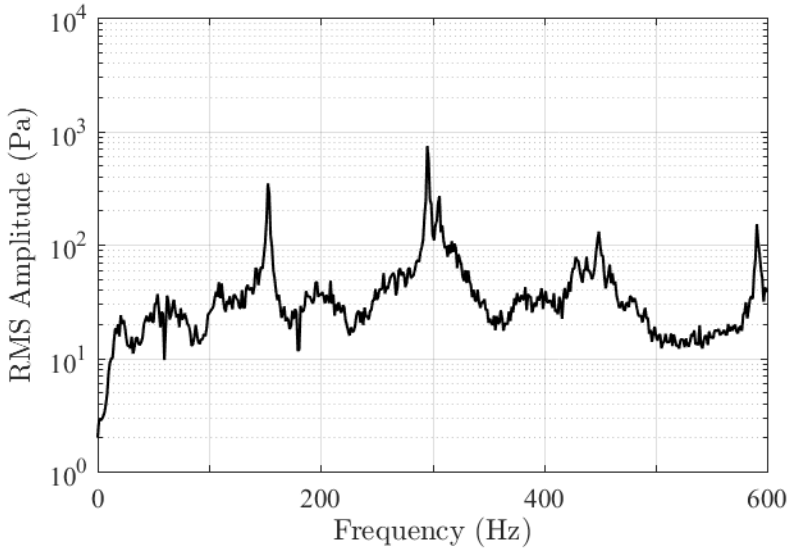

Figure A.30: The frequency spectrum for the pressure oscillations measured in the dump combustor while injecting Bio-SPK HRJ (Brand A) at $\theta = 5\pi/4$.

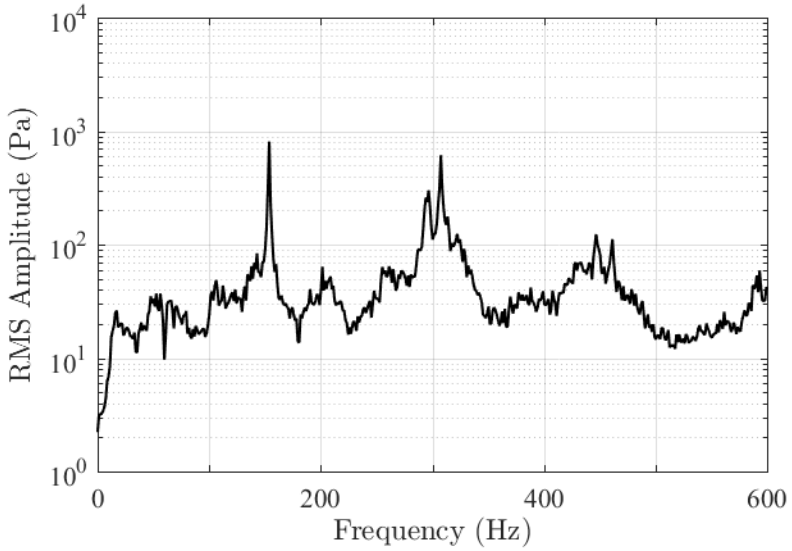

Figure A.31: The frequency spectrum for the pressure oscillations measured in the dump combustor while injecting Bio-SPK HRJ (Brand A) at $\theta = 3\pi/2$.

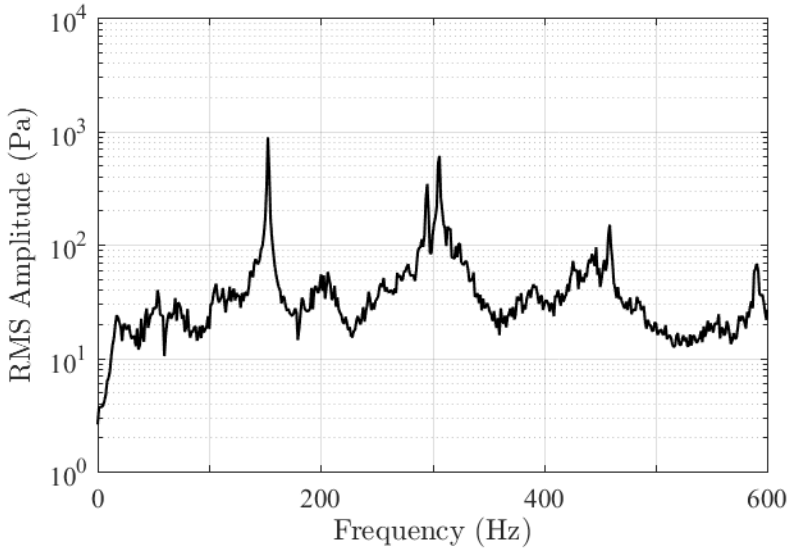

Figure A.32: The frequency spectrum for the pressure oscillations measured in the dump combustor while injecting Bio-SPK HRJ (Brand A) at $\theta = 7\pi/4$.

Bio-SPK HRJ (Brand B):

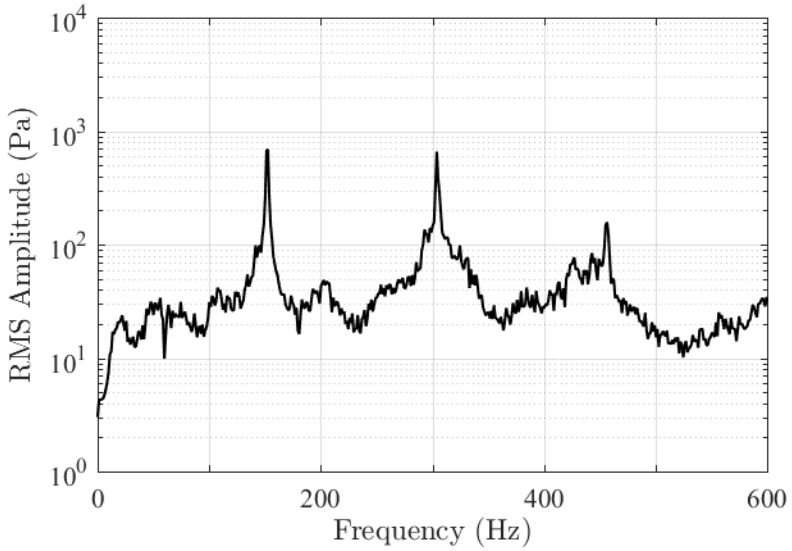

Figure A.33: The frequency spectrum for the pressure oscillations measured in the dump combustor while injecting Bio-SPK HRJ (Brand B) at $\theta = 0$.

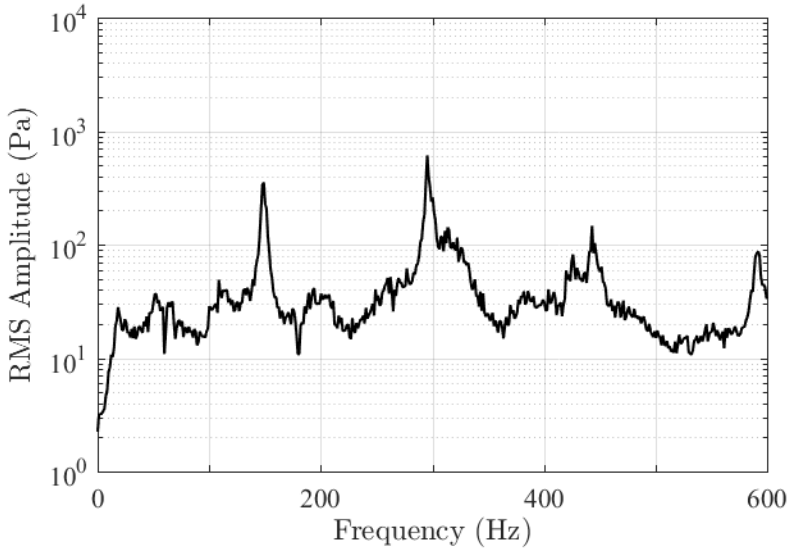

Figure A.34: The frequency spectrum for the pressure oscillations measured in the dump combustor while injecting Bio-SPK HRJ (Brand B) at $\theta = \pi/4$.

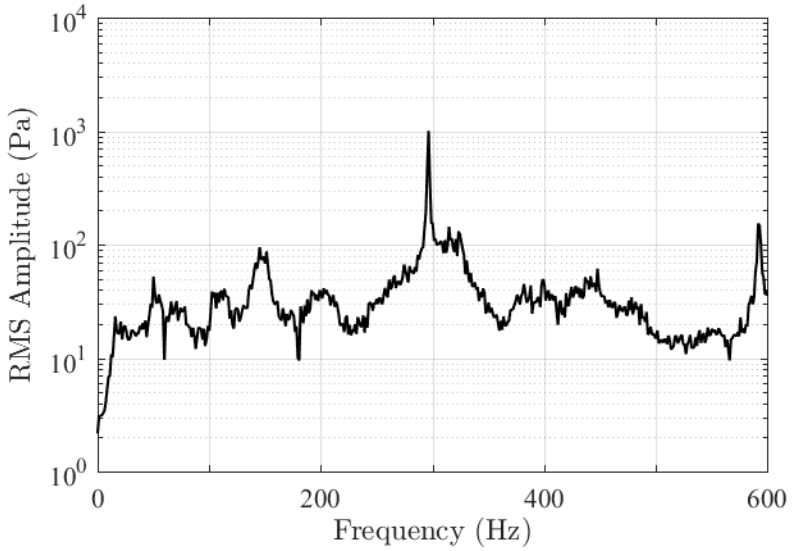

Figure A.35: The frequency spectrum for the pressure oscillations measured in the dump combustor while injecting Bio-SPK HRJ (Brand B) at $\theta = \pi/2$.

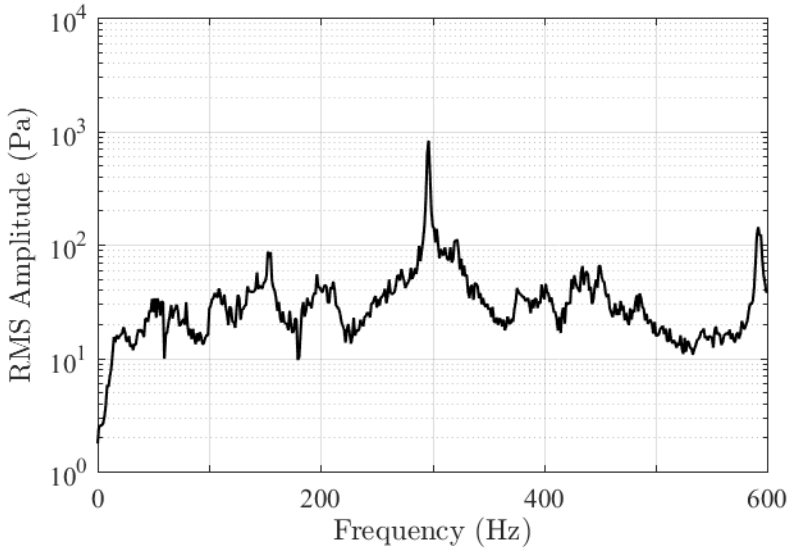

Figure A.36: The frequency spectrum for the pressure oscillations measured in the dump combustor while injecting Bio-SPK HRJ (Brand B) at $\theta = 3\pi/4$.

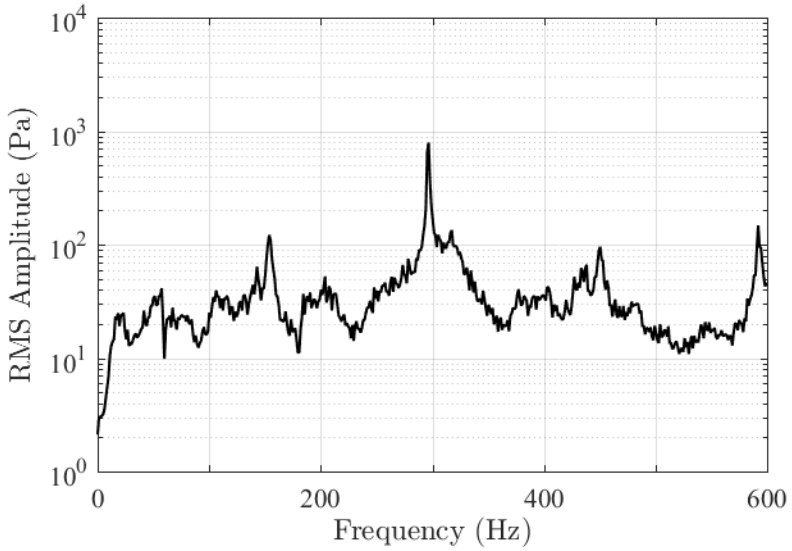

Figure A.37: The frequency spectrum for the pressure oscillations measured in the dump combustor while injecting Bio-SPK HRJ (Brand B) at $\theta = \pi$.

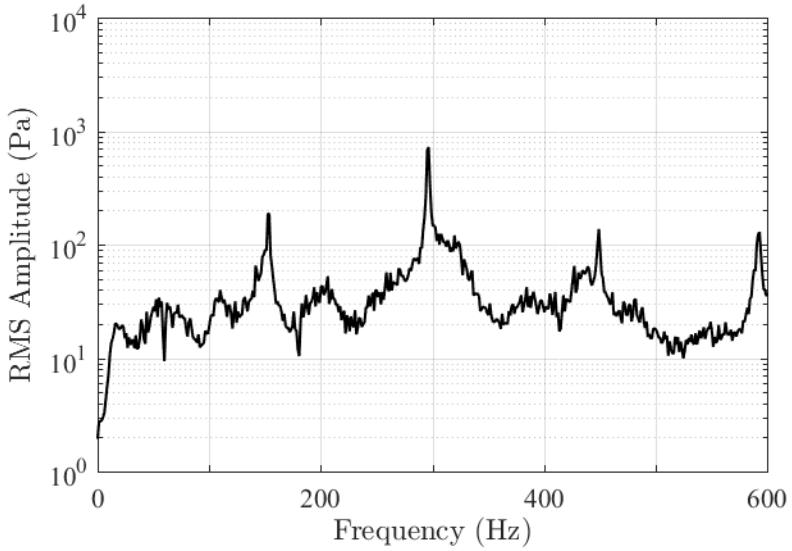

Figure A.38: The frequency spectrum for the pressure oscillations measured in the dump combustor while injecting Bio-SPK HRJ (Brand B) at $\theta = 5\pi/4$.

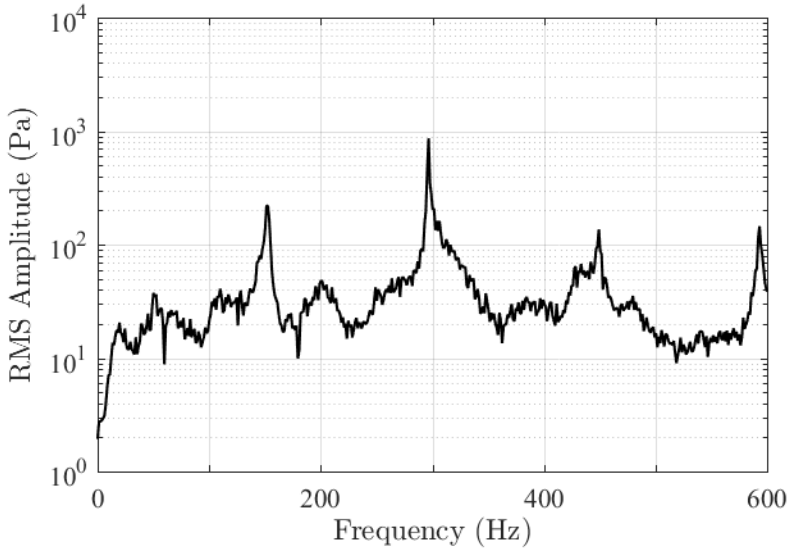

Figure A.39: The frequency spectrum for the pressure oscillations measured in the dump combustor while injecting Bio-SPK HRJ (Brand B) at $\theta = 3\pi/2$.

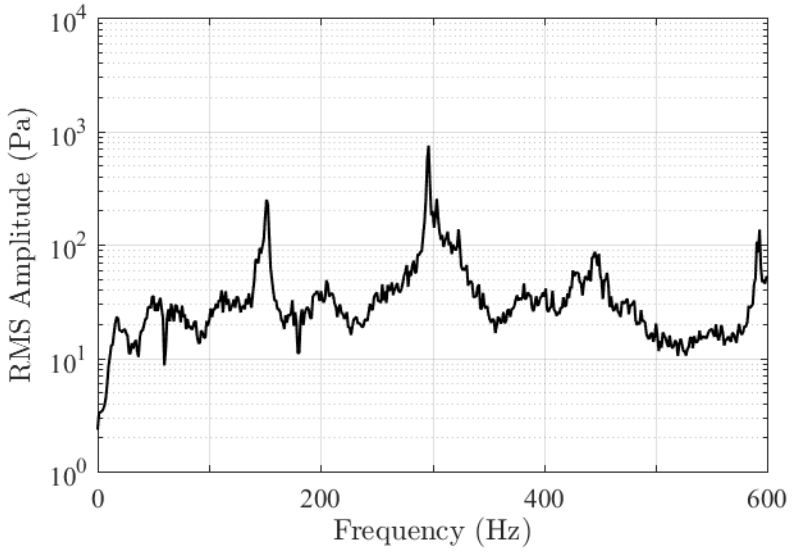

Figure A.40: The frequency spectrum for the pressure oscillations measured in the dump combustor while injecting Bio-SPK HRJ (Brand B) at $\theta = 7\pi/4$.

1:1 blend of Jet A and FT-SPK (Brand C):

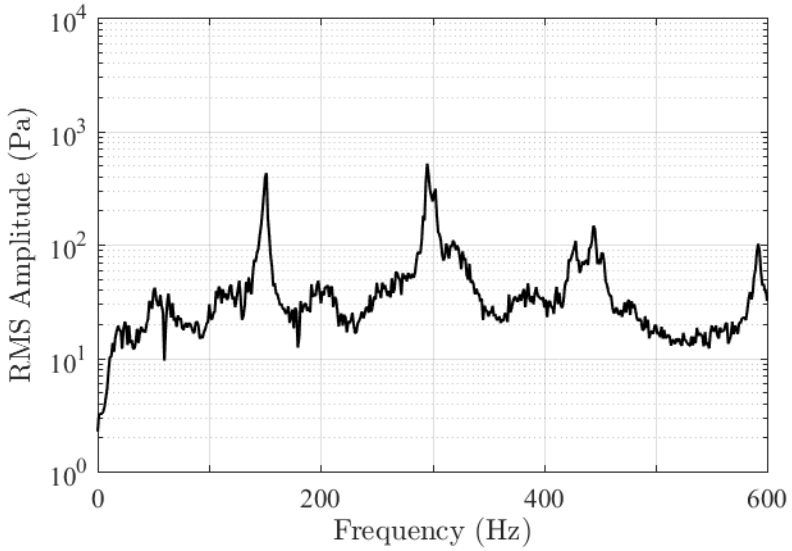

Figure A.41: The frequency spectrum for the pressure oscillations measured in the dump combustor while injecting 1:1 blend of Jet A and FT-SPK (Brand C) at $\theta = 0$.

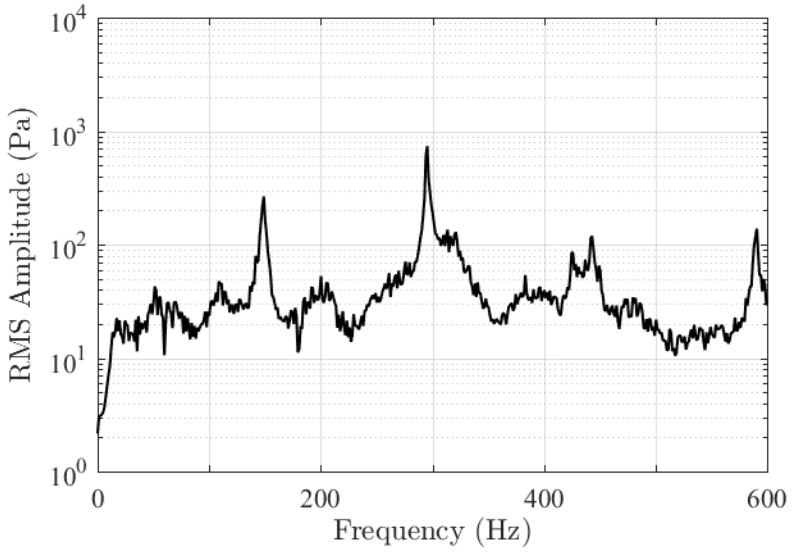

Figure A.42: The frequency spectrum for the pressure oscillations measured in the dump combustor while injecting 1:1 blend of Jet A and FT-SPK (Brand C) at $\theta = \pi/4$.

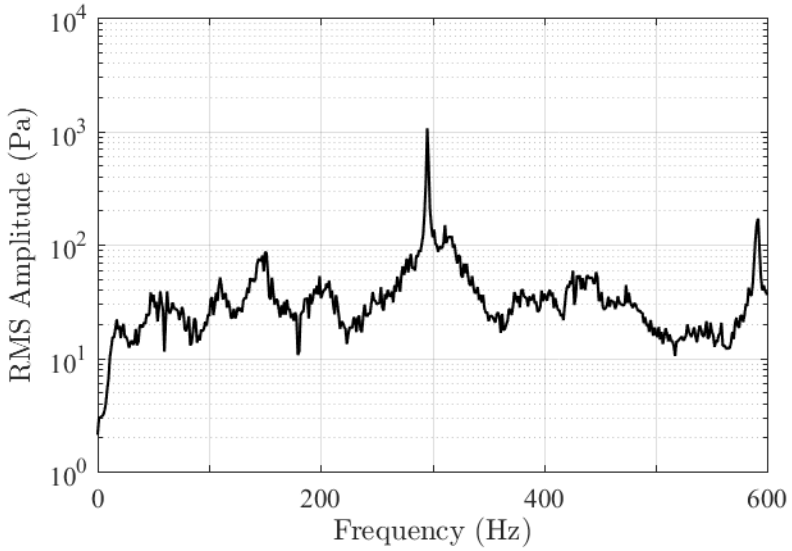

Figure A.43: The frequency spectrum for the pressure oscillations measured in the dump combustor while injecting 1:1 blend of Jet A and FT-SPK (Brand C) at $\theta = \pi/2$.

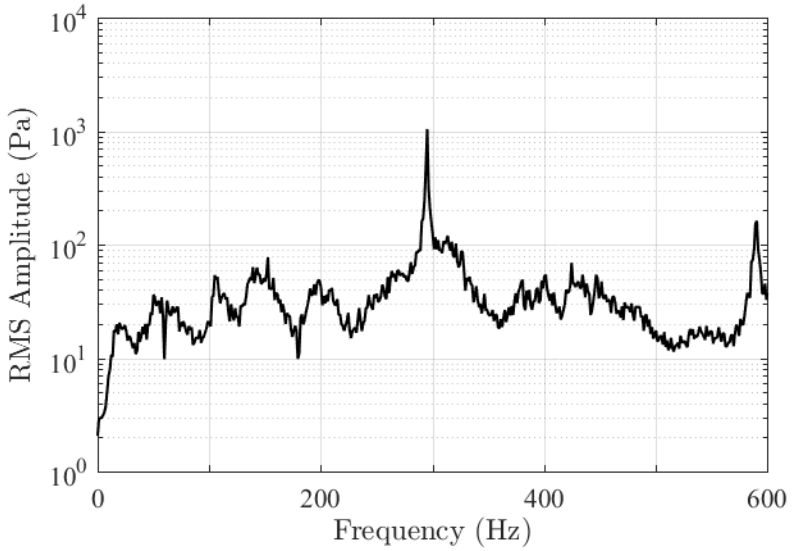

Figure A.44: The frequency spectrum for the pressure oscillations measured in the dump combustor while injecting 1:1 blend of Jet A and FT-SPK (Brand C) at $\theta = 3\pi/4$.

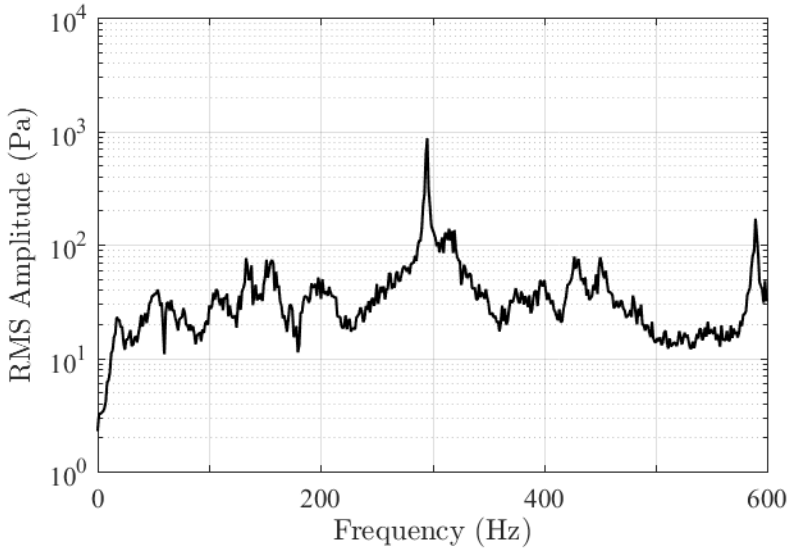

Figure A.45: The frequency spectrum for the pressure oscillations measured in the dump combustor while injecting 1:1 blend of Jet A and FT-SPK (Brand C) at $\theta = \pi$.

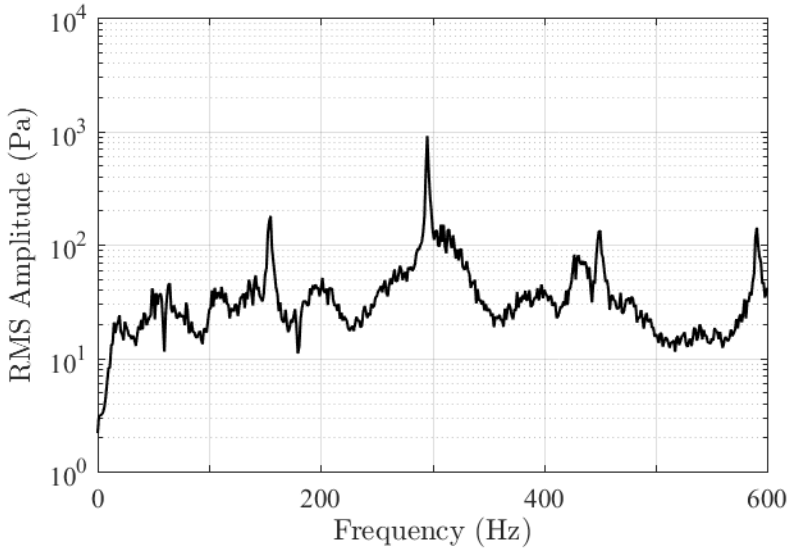

Figure A.46: The frequency spectrum for the pressure oscillations measured in the dump combustor while injecting 1:1 blend of Jet A and FT-SPK (Brand C) at $\theta = 5\pi/4$.

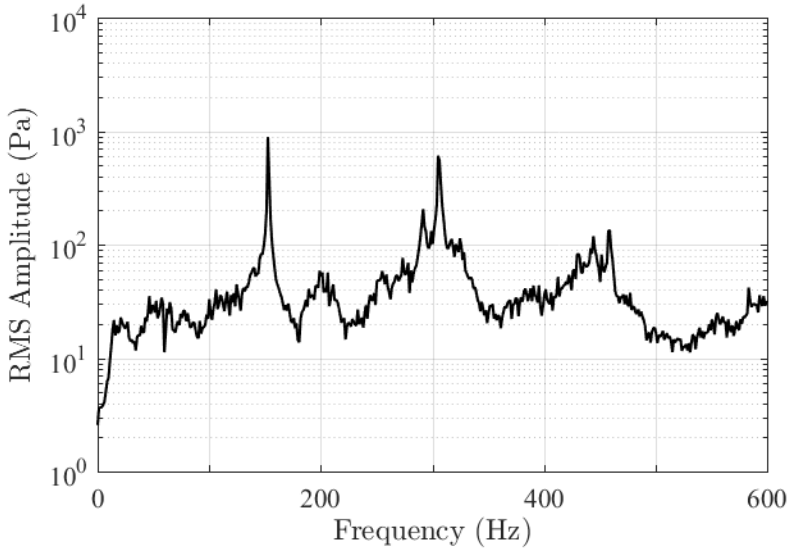

Figure A.47: The frequency spectrum for the pressure oscillations measured in the dump combustor while injecting 1:1 blend of Jet A and FT-SPK (Brand C) at $\theta = 3\pi/2$.

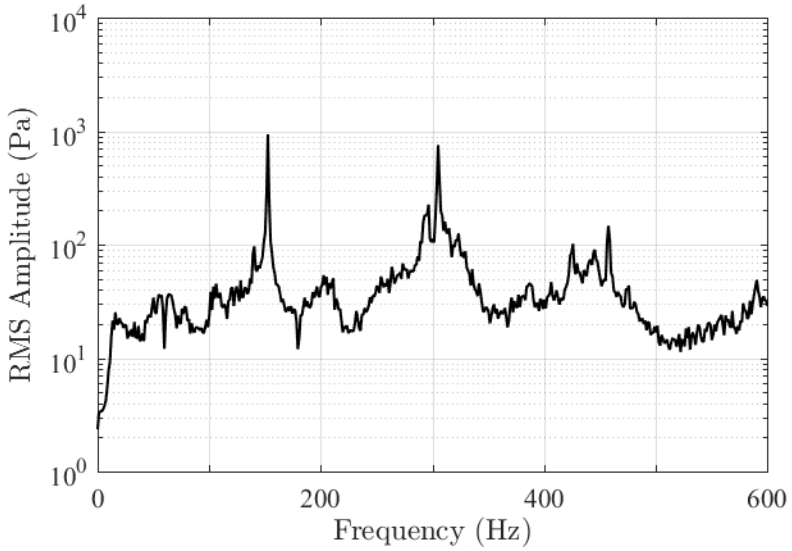

Figure A.48: The frequency spectrum for the pressure oscillations measured in the dump combustor while injecting 1:1 blend of Jet A and FT-SPK (Brand C) at $\theta = 7\pi/4$.

1:1 blend of Jet A and FT-SPK (Brand D):

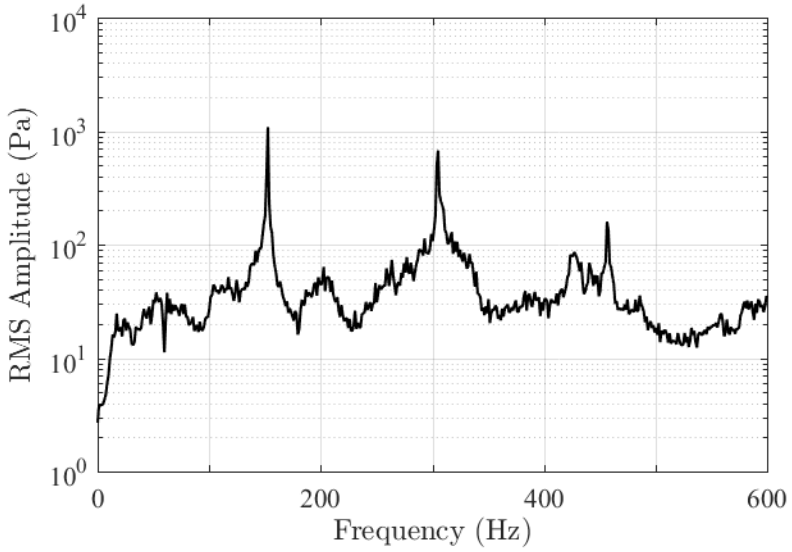

Figure A.49: The frequency spectrum for the pressure oscillations measured in the dump combustor while injecting 1:1 blend of Jet A and FT-SPK (Brand D) at $\theta = 0$.

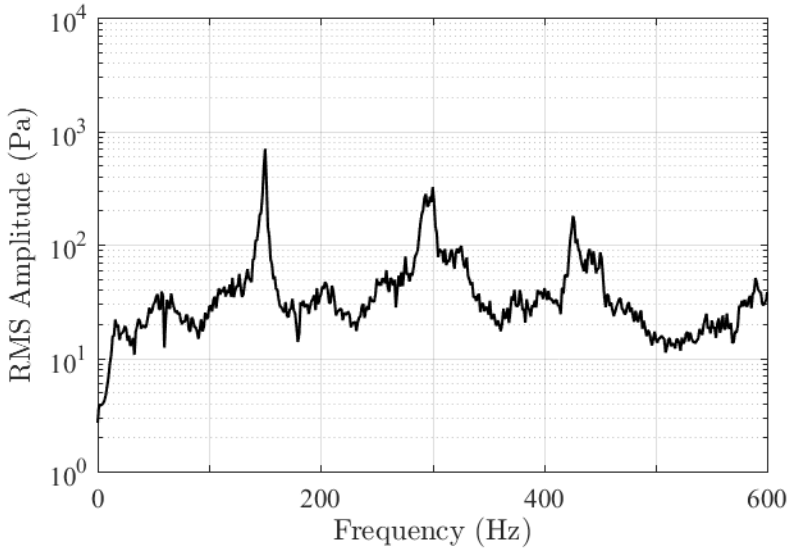

Figure A.50: The frequency spectrum for the pressure oscillations measured in the dump combustor while injecting 1:1 blend of Jet A and FT-SPK (Brand D) at $\theta = \pi/4$.

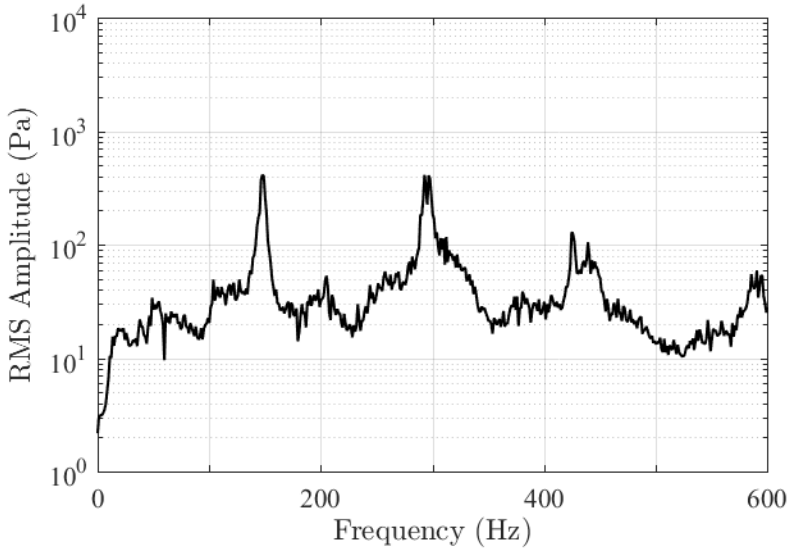

Figure A.51: The frequency spectrum for the pressure oscillations measured in the dump combustor while injecting 1:1 blend of Jet A and FT-SPK (Brand D) at $\theta = \pi/2$.

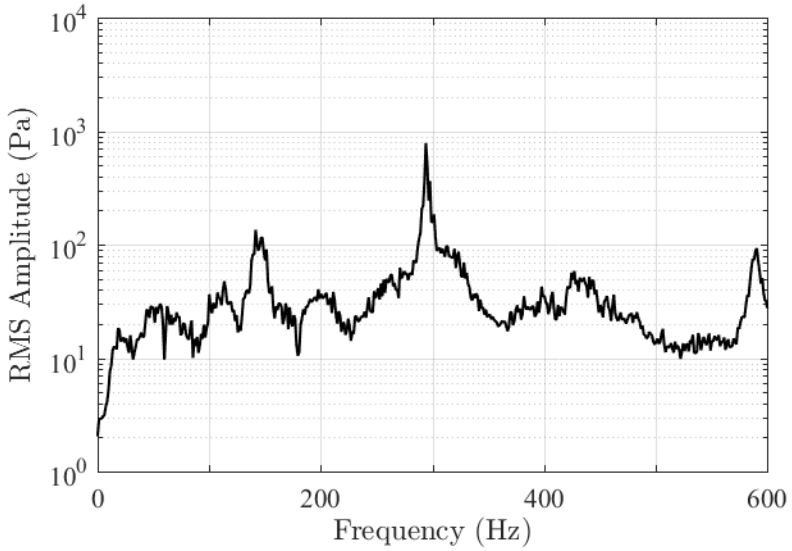

Figure A.52: The frequency spectrum for the pressure oscillations measured in the dump combustor while injecting 1:1 blend of Jet A and FT-SPK (Brand D) at $\theta = 3\pi/4$.

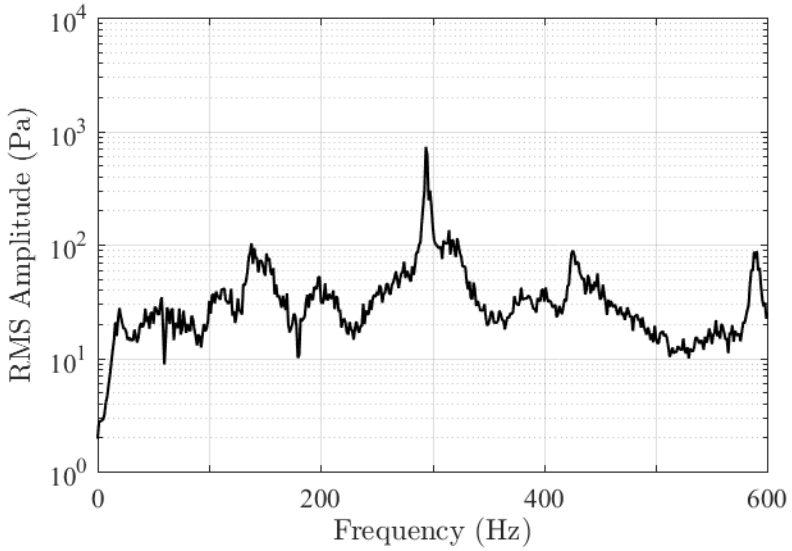

Figure A.53: The frequency spectrum for the pressure oscillations measured in the dump combustor while injecting 1:1 blend of Jet A and FT-SPK (Brand D) at $\theta = \pi$.

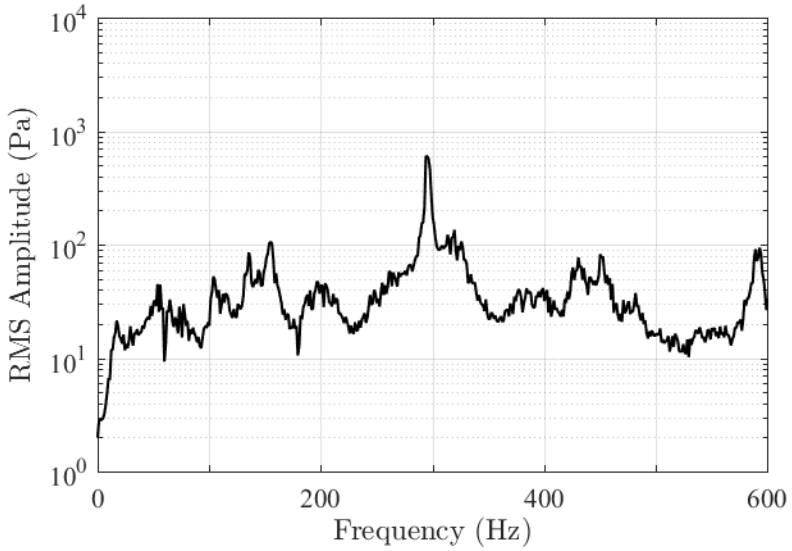

Figure A.54: The frequency spectrum for the pressure oscillations measured in the dump combustor while injecting 1:1 blend of Jet A and FT-SPK (Brand D) at $\theta = 5\pi/4$.

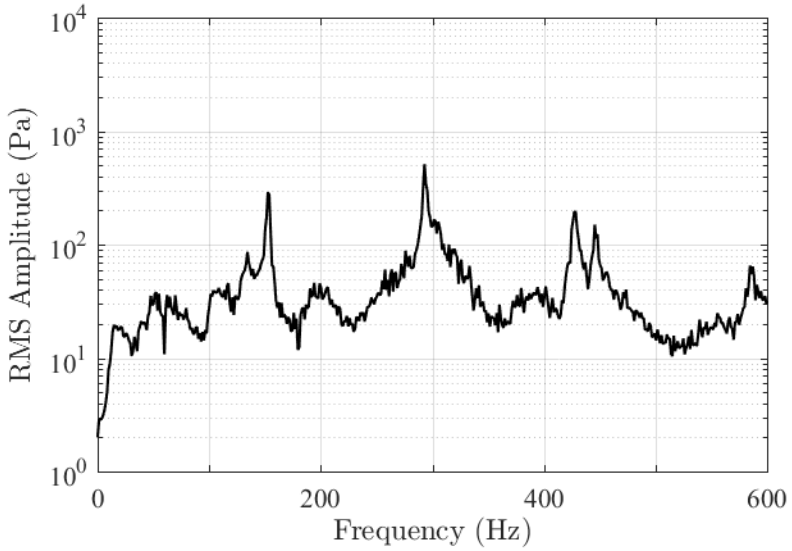

Figure A.55: The frequency spectrum for the pressure oscillations measured in the dump combustor while injecting 1:1 blend of Jet A and FT-SPK (Brand D) at $\theta = 3\pi/2$.

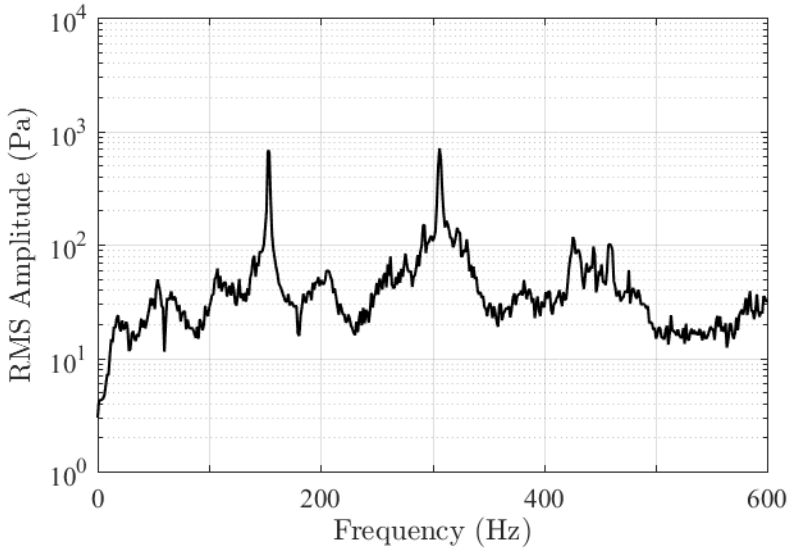

Figure A.56: The frequency spectrum for the pressure oscillations measured in the dump combustor while injecting 1:1 blend of Jet A and FT-SPK (Brand D) at $\theta = 7\pi/4$.

1:1 blend of Jet A and FT-SPK (Brand E):

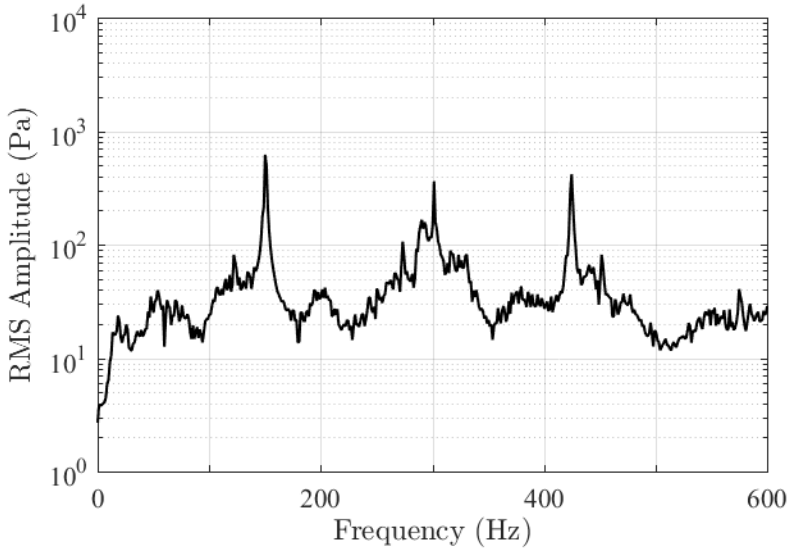

Figure A.57: The frequency spectrum for the pressure oscillations measured in the dump combustor while injecting 1:1 blend of Jet A and FT-SPK (Brand E) at $\theta = 0$.

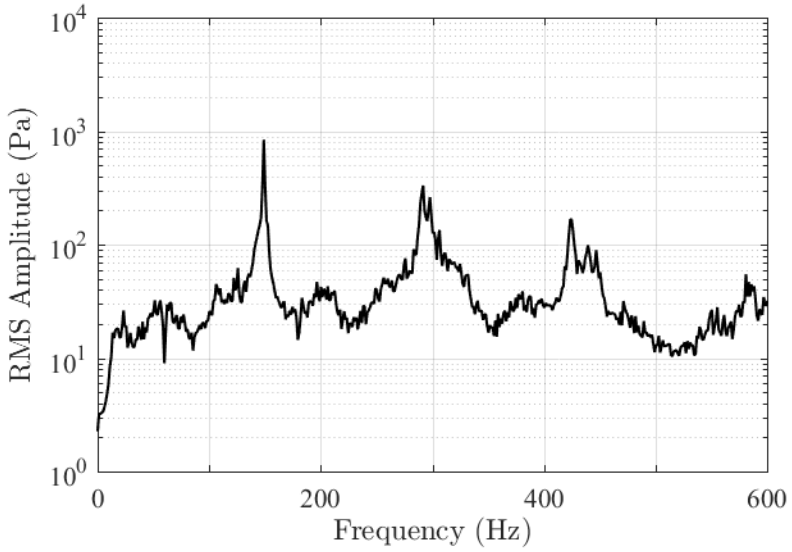

Figure A.58: The frequency spectrum for the pressure oscillations measured in the dump combustor while injecting 1:1 blend of Jet A and FT-SPK (Brand E) at $\theta = \pi/4$.

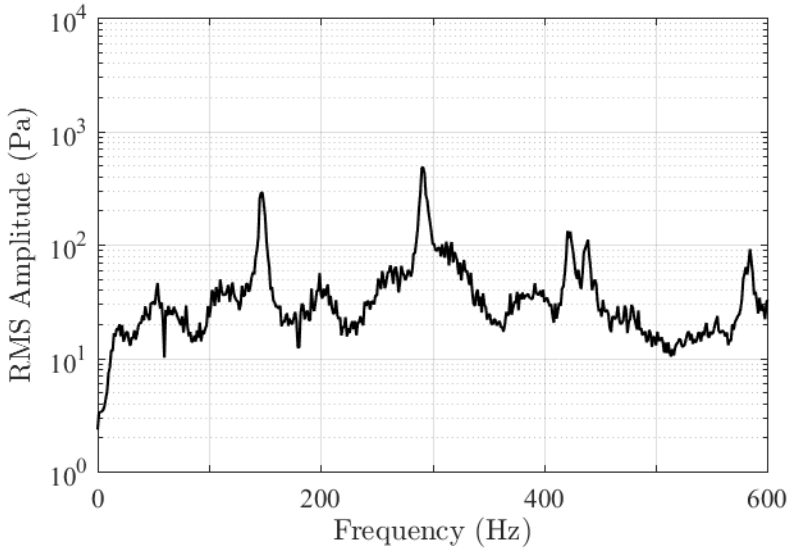

Figure A.59: The frequency spectrum for the pressure oscillations measured in the dump combustor while injecting 1:1 blend of Jet A and FT-SPK (Brand E) at $\theta = \pi/2$.

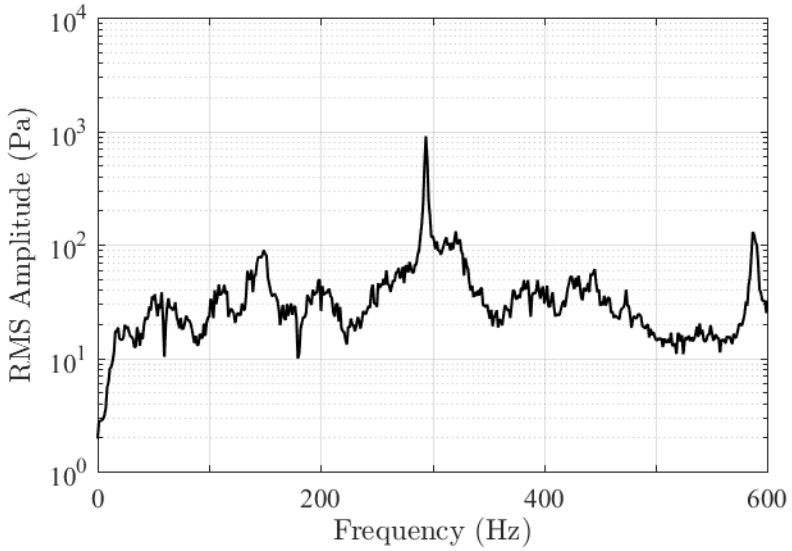

Figure A.60: The frequency spectrum for the pressure oscillations measured in the dump combustor while injecting 1:1 blend of Jet A and FT-SPK (Brand E) at $\theta = 3\pi/4$.

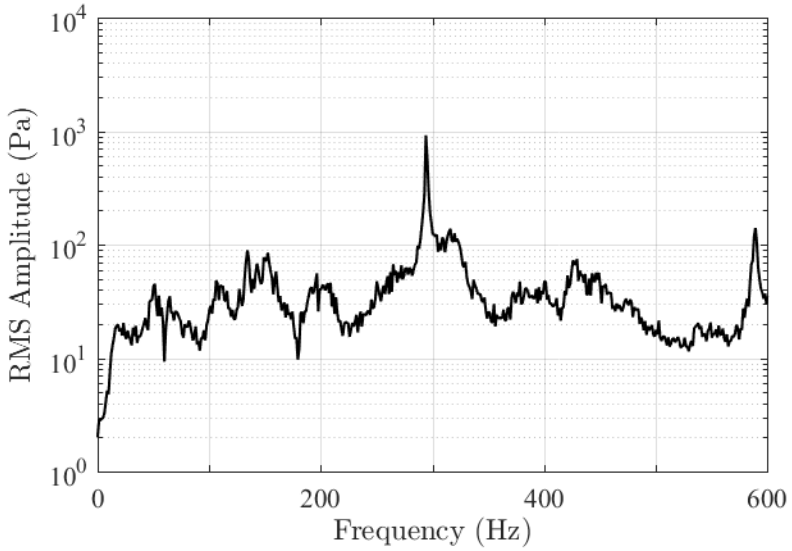

Figure A.61: The frequency spectrum for the pressure oscillations measured in the dump combustor while injecting 1:1 blend of Jet A and FT-SPK (Brand E) at $\theta = \pi$.

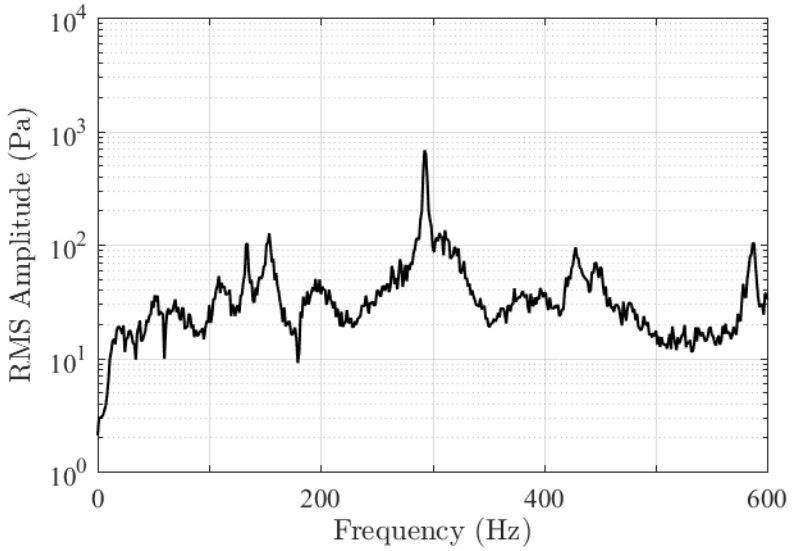

Figure A.62: The frequency spectrum for the pressure oscillations measured in the dump combustor while injecting 1:1 blend of Jet A and FT-SPK (Brand E) at $\theta = 5\pi/4$.

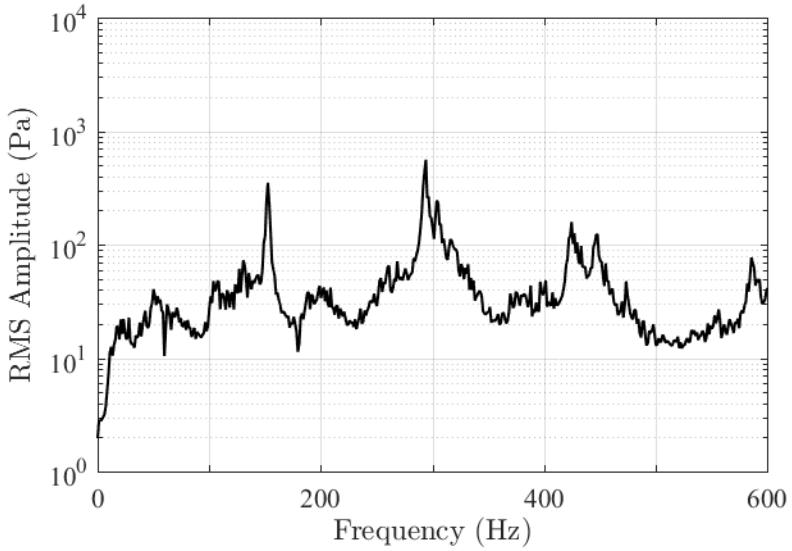

Figure A.63: The frequency spectrum for the pressure oscillations measured in the dump combustor while injecting 1:1 blend of Jet A and FT-SPK (Brand E) at $\theta = 3\pi/2$.

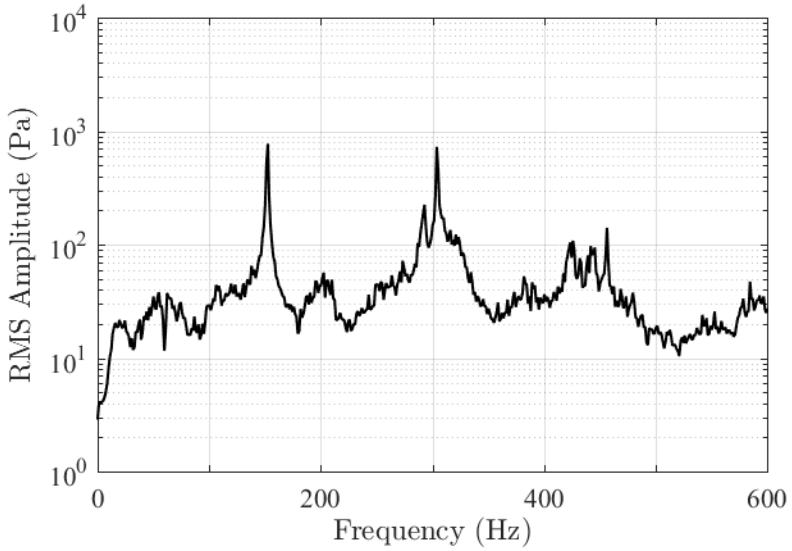

Figure A.64: The frequency spectrum for the pressure oscillations measured in the dump combustor while injecting 1:1 blend of Jet A and FT-SPK (Brand E) at $\theta = 7\pi/4$.

FT-SPK (Brand C):

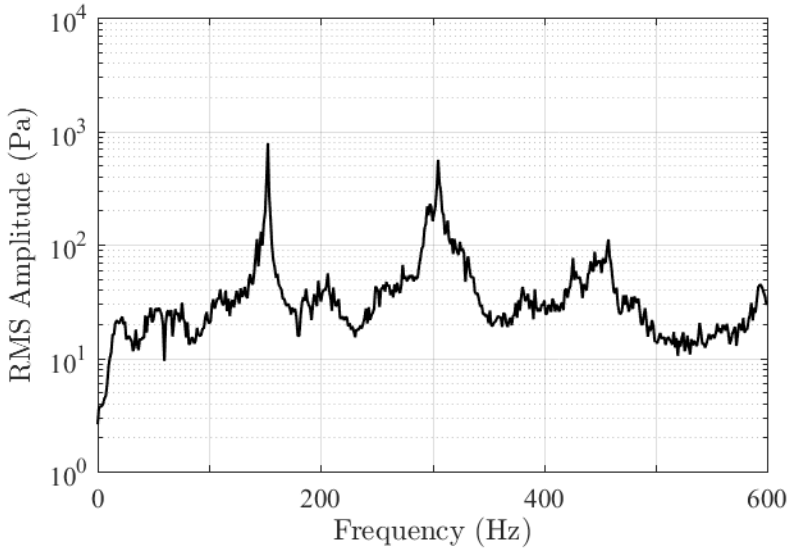

Figure A.65: The frequency spectrum for the pressure oscillations measured in the dump combustor while injecting FT-SPK (Brand C) at $\theta = 0$.

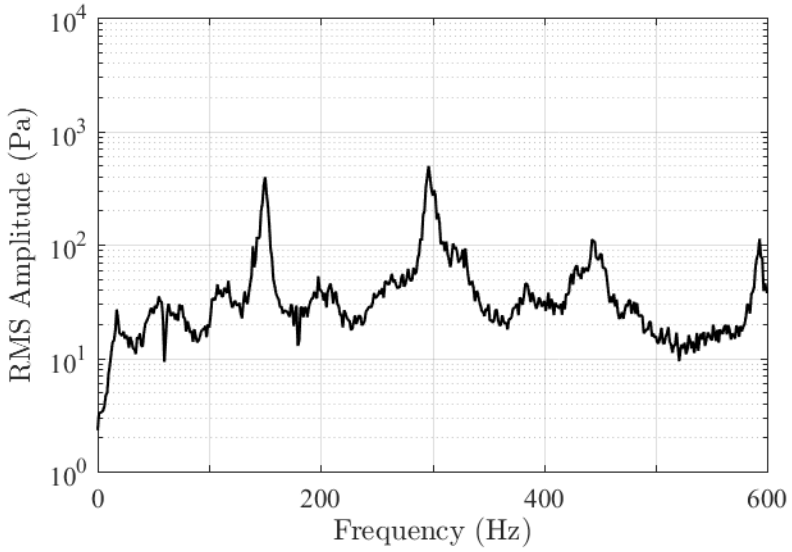

Figure A.66: The frequency spectrum for the pressure oscillations measured in the dump combustor while injecting FT-SPK (Brand C) at $\theta = \pi/4$.

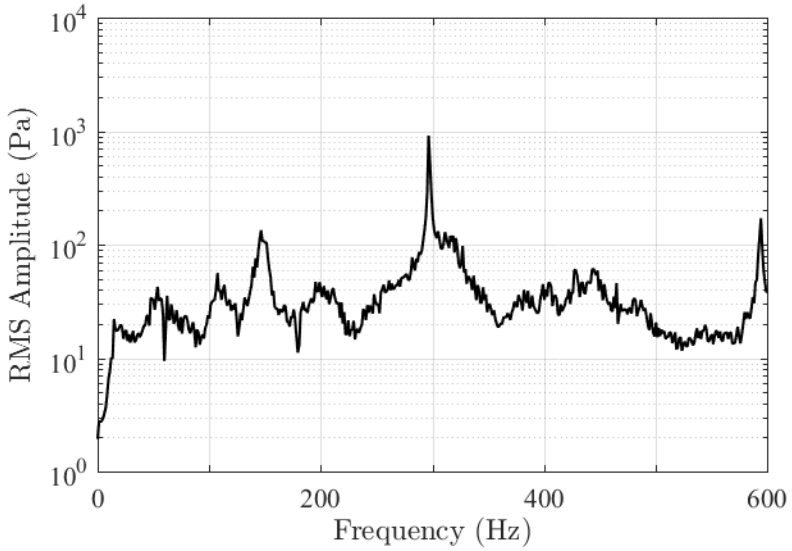

Figure A.67: The frequency spectrum for the pressure oscillations measured in the dump combustor while injecting FT-SPK (Brand C) at $\theta = \pi/2$.

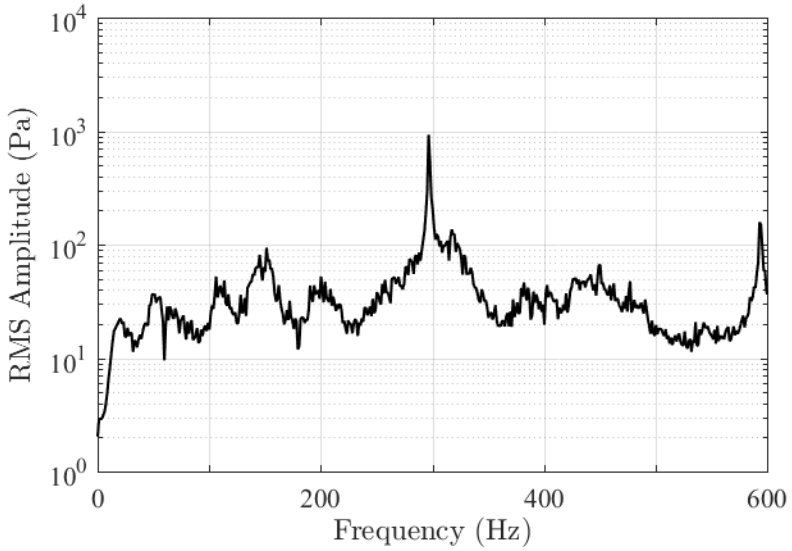

Figure A.68: The frequency spectrum for the pressure oscillations measured in the dump combustor while injecting FT-SPK (Brand C) at $\theta = 3\pi/4$.

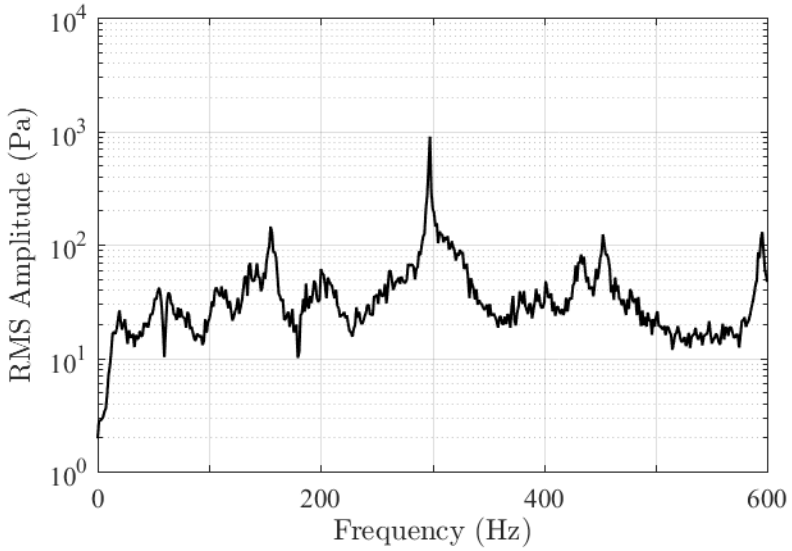

Figure A.69: The frequency spectrum for the pressure oscillations measured in the dump combustor while injecting FT-SPK (Brand C) at $\theta = \pi$.

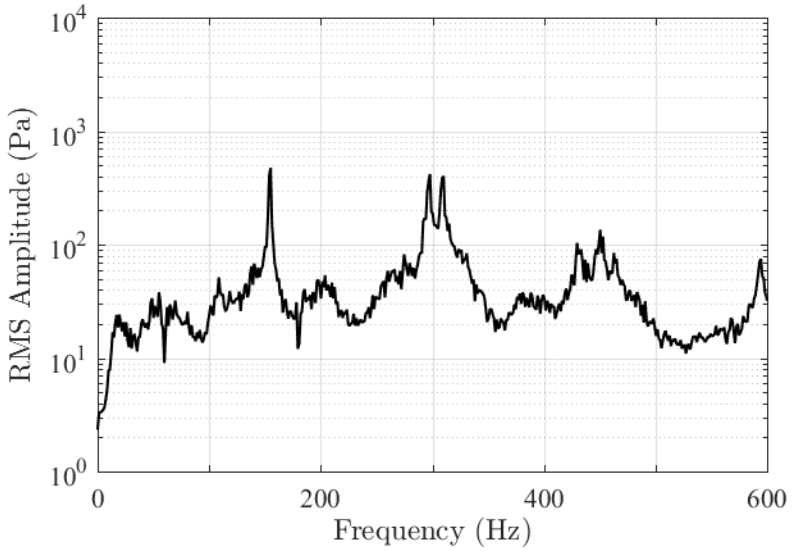

Figure A.70: The frequency spectrum for the pressure oscillations measured in the dump combustor while injecting FT-SPK (Brand C) at $\theta = 5\pi/4$.

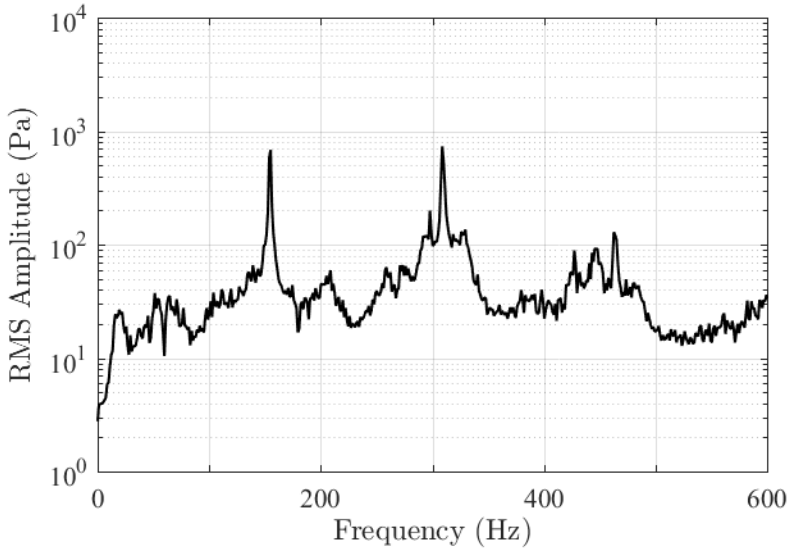

Figure A.71: The frequency spectrum for the pressure oscillations measured in the dump combustor while injecting FT-SPK (Brand C) at $\theta = 3\pi/2$.

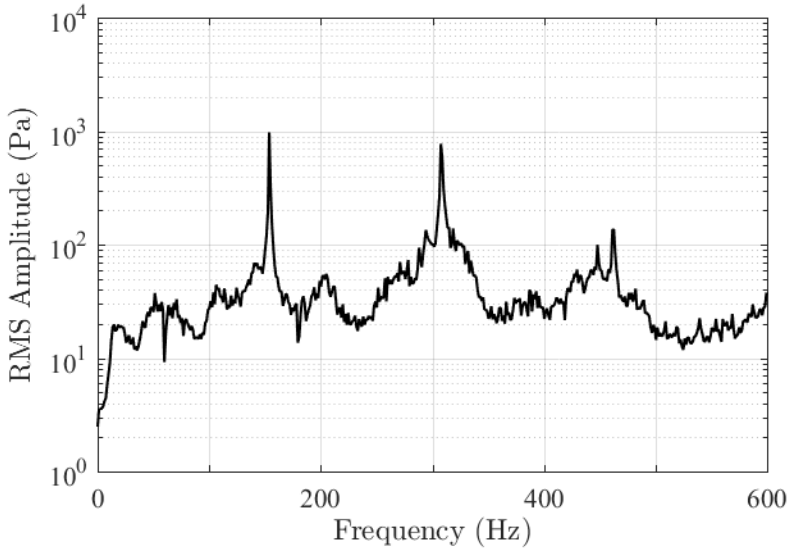

Figure A.72: The frequency spectrum for the pressure oscillations measured in the dump combustor while injecting FT-SPK (Brand C) at $\theta = 7\pi/4$.

FT-SPK (Brand D):

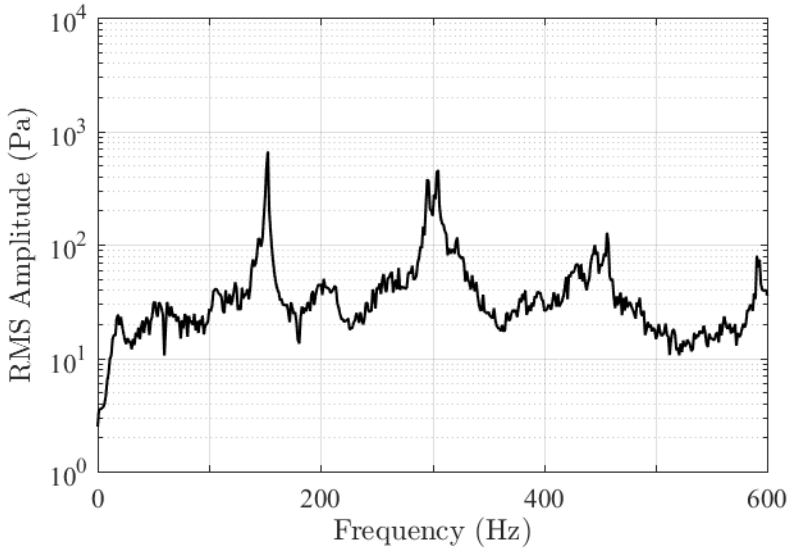

Figure A.73: The frequency spectrum for the pressure oscillations measured in the dump combustor while injecting FT-SPK (Brand D) at $\theta = 0$.

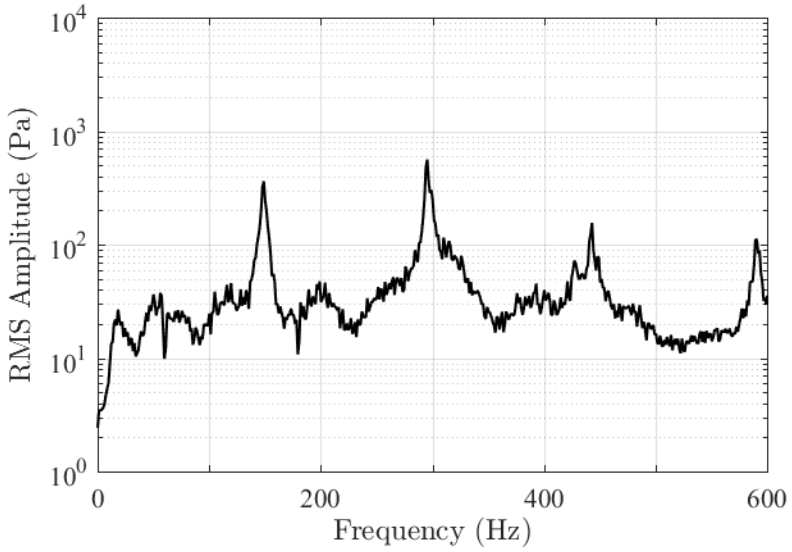

Figure A.74: The frequency spectrum for the pressure oscillations measured in the dump combustor while injecting FT-SPK (Brand D) at $\theta = \pi/4$.

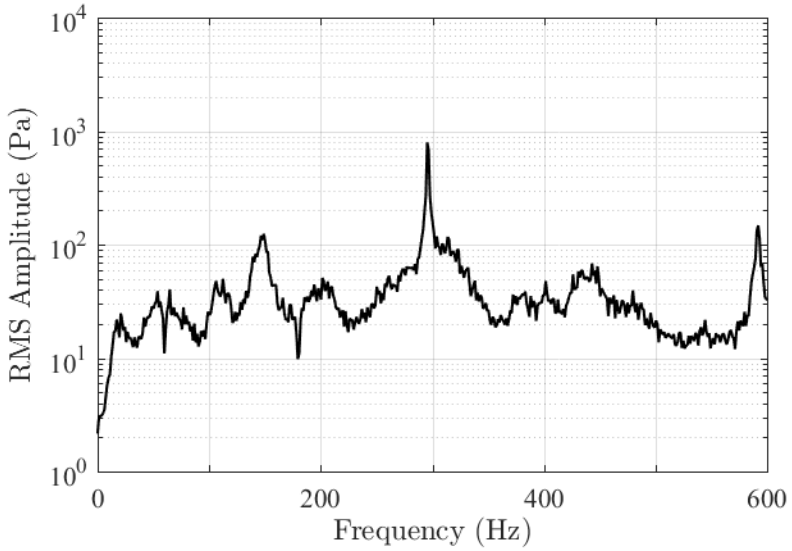

Figure A.75: The frequency spectrum for the pressure oscillations measured in the dump combustor while injecting FT-SPK (Brand D) at $\theta = \pi/2$.

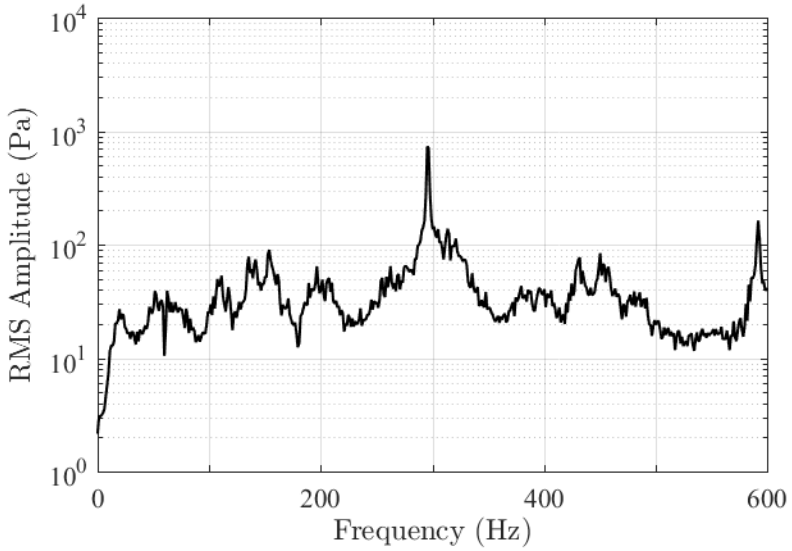

Figure A.76: The frequency spectrum for the pressure oscillations measured in the dump combustor while injecting FT-SPK (Brand D) at $\theta = 3\pi/4$.

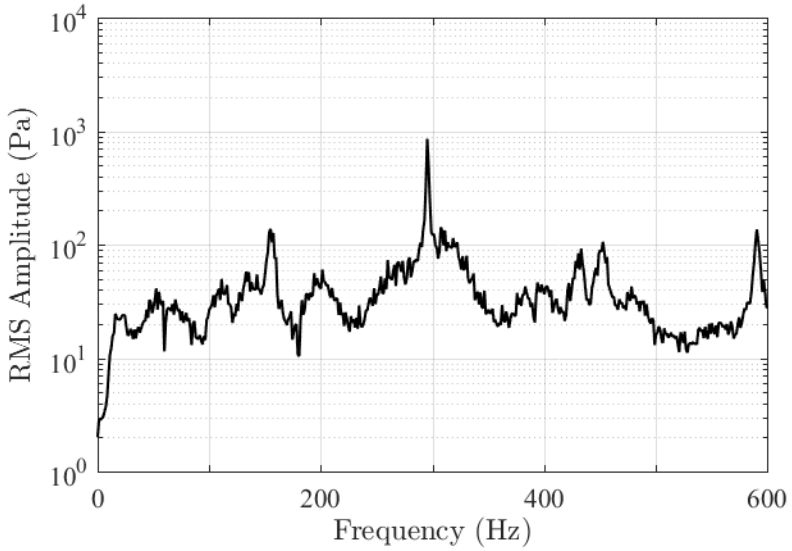

Figure A.77: The frequency spectrum for the pressure oscillations measured in the dump combustor while injecting FT-SPK (Brand D) at $\theta = \pi$.

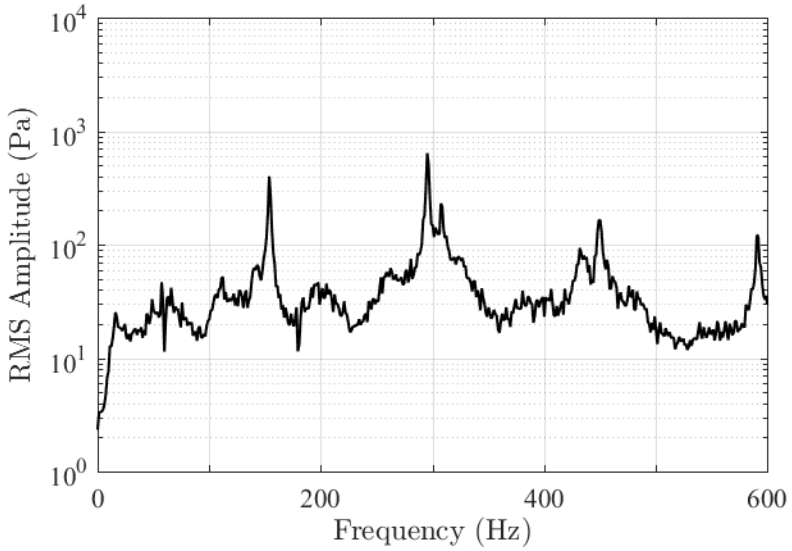

Figure A.78: The frequency spectrum for the pressure oscillations measured in the dump combustor while injecting FT-SPK (Brand D) at $\theta = 5\pi/4$.

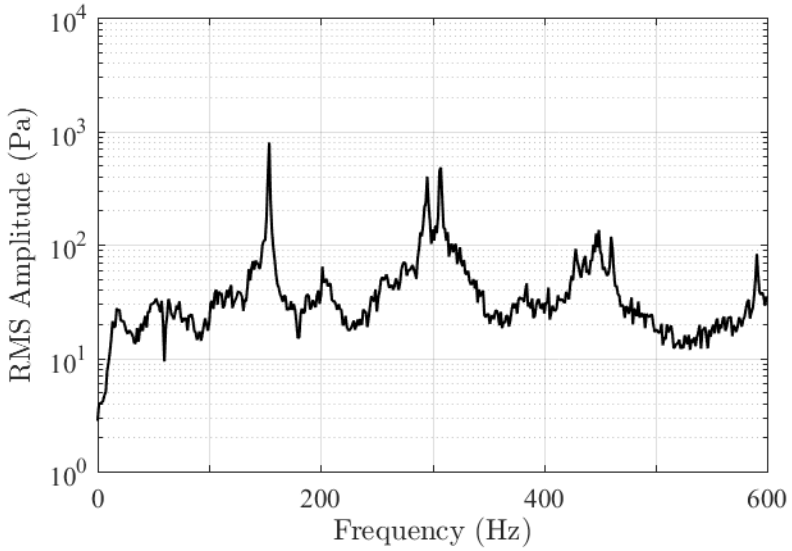

Figure A.79: The frequency spectrum for the pressure oscillations measured in the dump combustor while injecting FT-SPK (Brand D) at $\theta = 3\pi/2$.

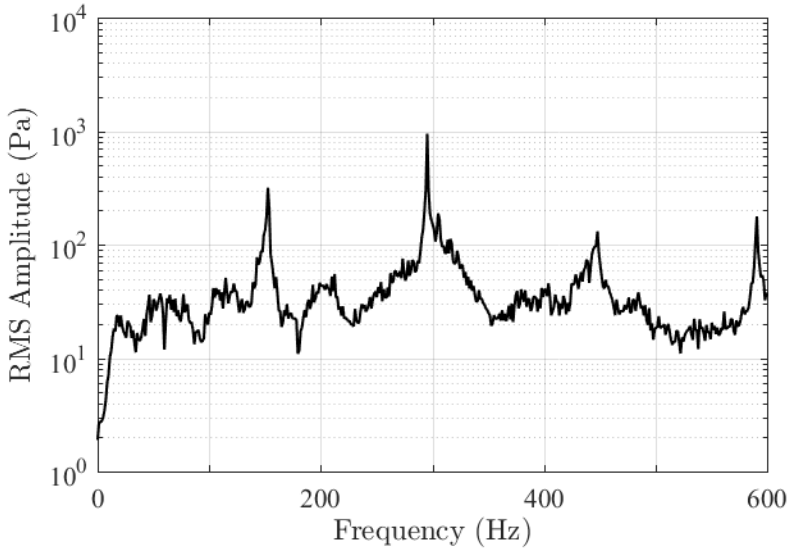

Figure A.80: The frequency spectrum for the pressure oscillations measured in the dump combustor while injecting FT-SPK (Brand D) at $\theta = 7\pi/4$.

FT-SPK (Brand E):

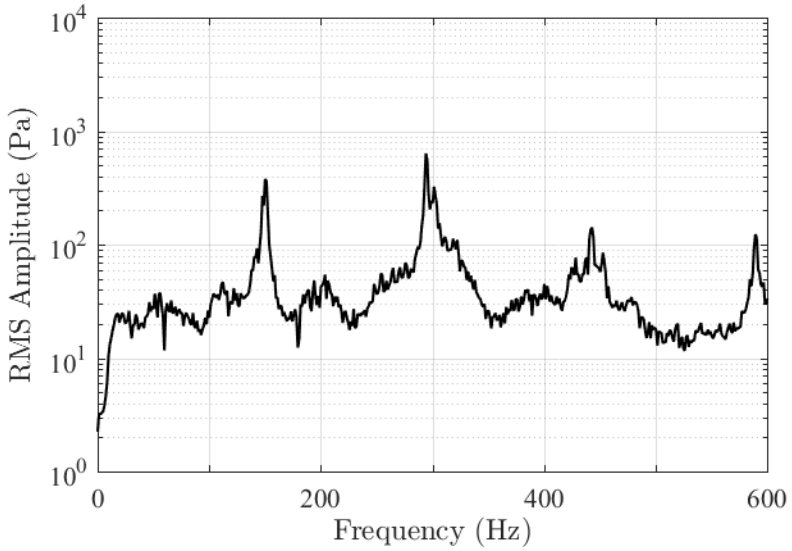

Figure A.81: The frequency spectrum for the pressure oscillations measured in the dump combustor while injecting FT-SPK (Brand E) at $\theta = 0$.

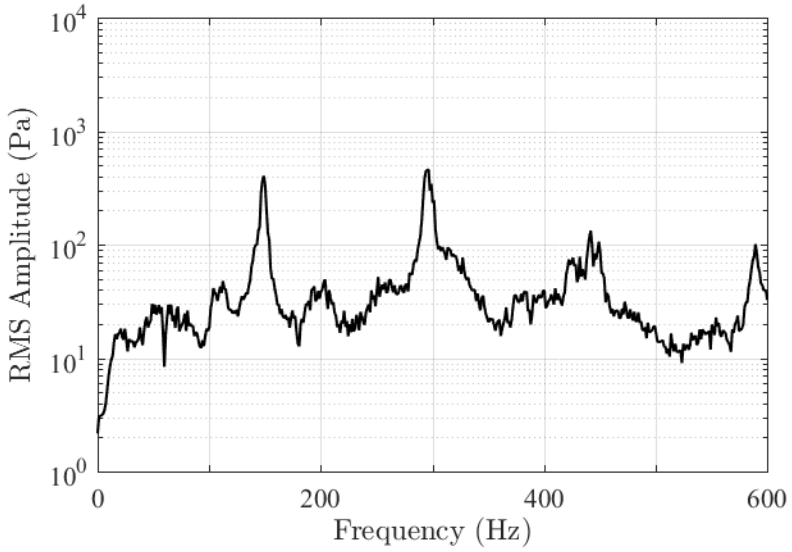

Figure A.82: The frequency spectrum for the pressure oscillations measured in the dump combustor while injecting FT-SPK (Brand E) at $\theta = \pi/4$.

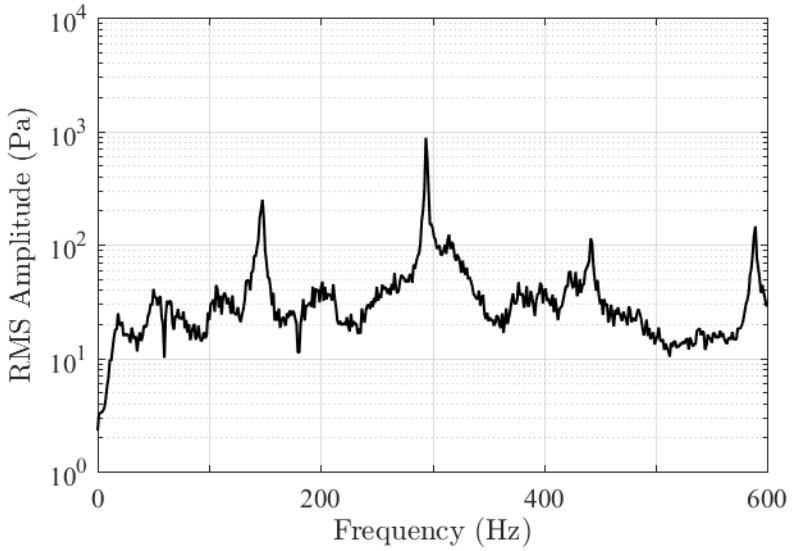

Figure A.83: The frequency spectrum for the pressure oscillations measured in the dump combustor while injecting FT-SPK (Brand E) at $\theta = \pi/2$.

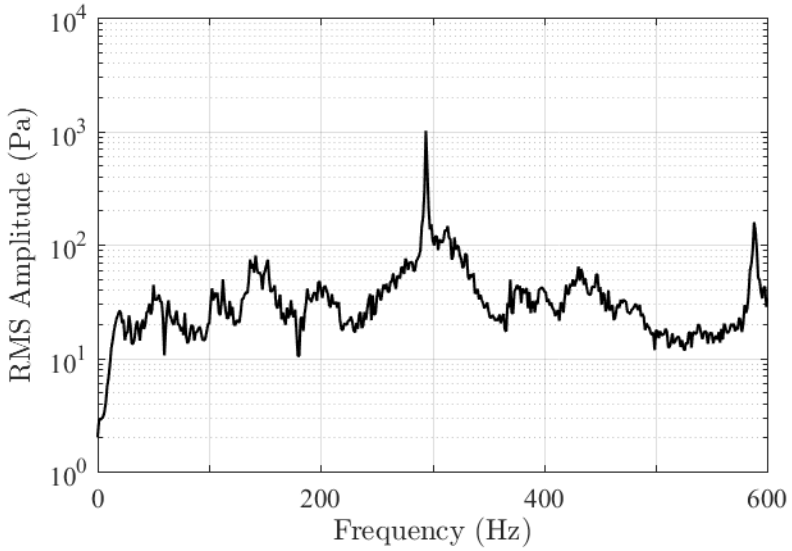

Figure A.84: The frequency spectrum for the pressure oscillations measured in the dump combustor while injecting FT-SPK (Brand E) at $\theta = 3\pi/4$.

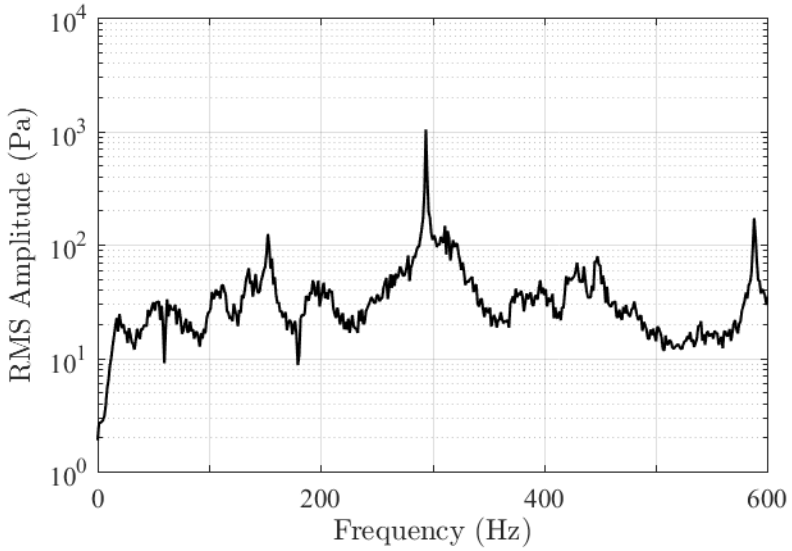

Figure A.85: The frequency spectrum for the pressure oscillations measured in the dump combustor while injecting FT-SPK (Brand E) at $\theta = \pi$.

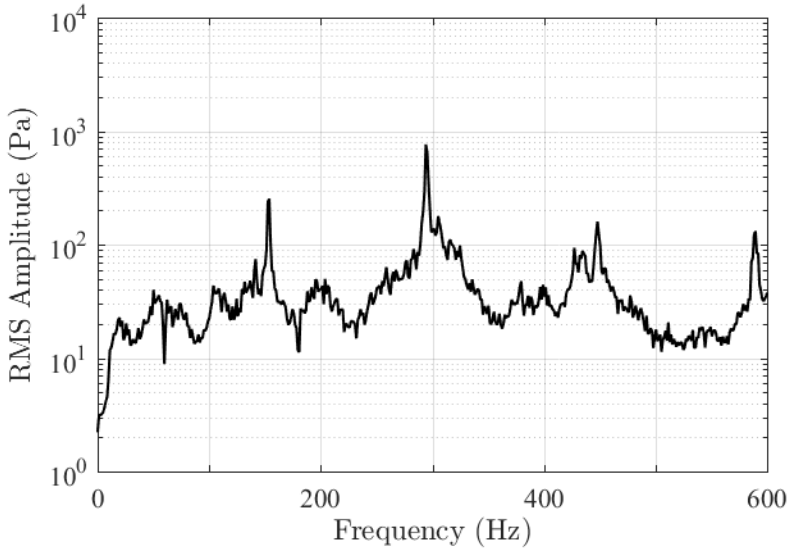

Figure A.86: The frequency spectrum for the pressure oscillations measured in the dump combustor while injecting FT-SPK (Brand E) at $\theta = 5\pi/4$.

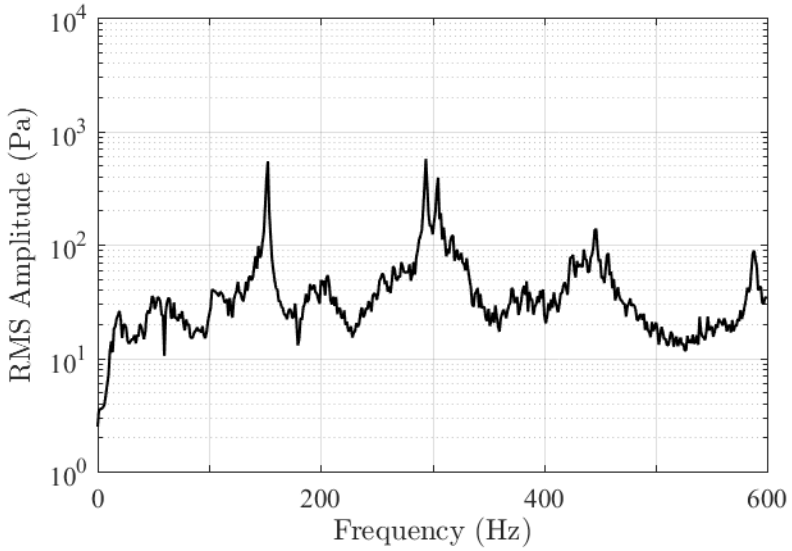

Figure A.87: The frequency spectrum for the pressure oscillations measured in the dump combustor while injecting FT-SPK (Brand E) at $\theta = 3\pi/2$.

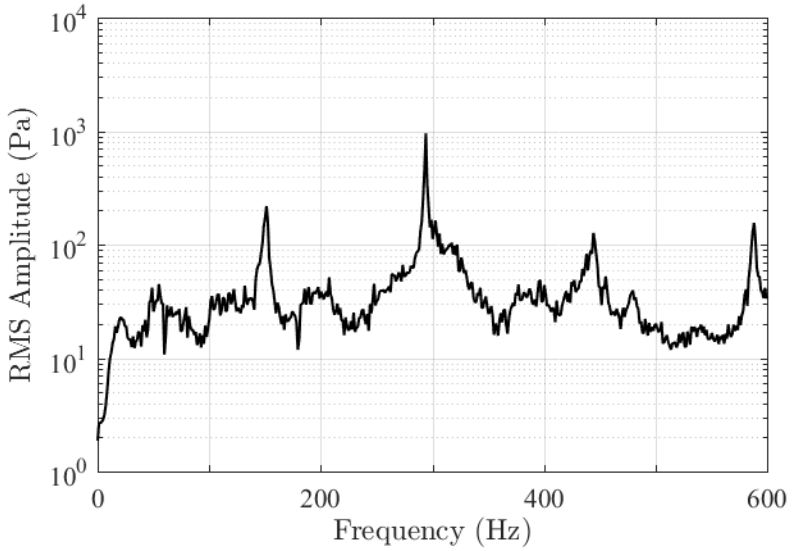

Figure A.88: The frequency spectrum for the pressure oscillations measured in the dump combustor while injecting FT-SPK (Brand E) at $\theta = 7\pi/4$.

Appendix B | Supplemental Experimental Data for Chapter 6

Secondary Fuel Injection:
Inlet Injection for $\phi_{aug} = 0.8$*:*

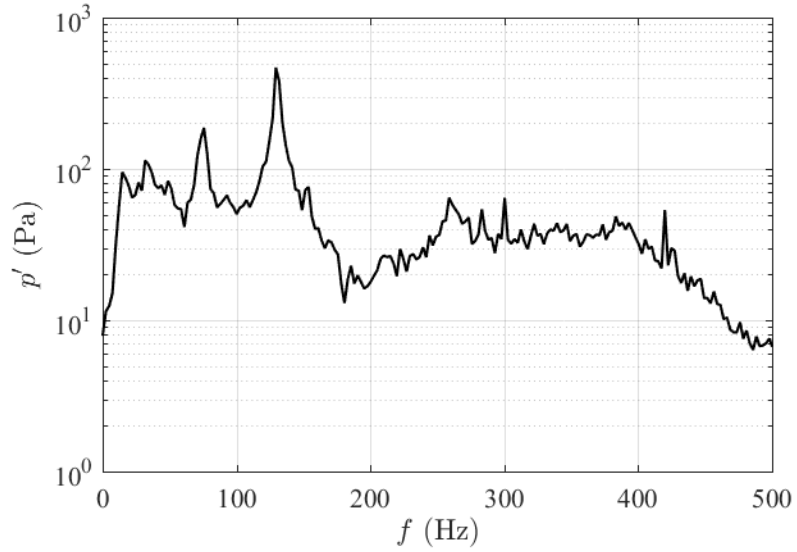

Figure B.1: The frequency spectrum for the pressure oscillations measured in the augmentor while performing secondary fuel injection at $\theta = 0$.

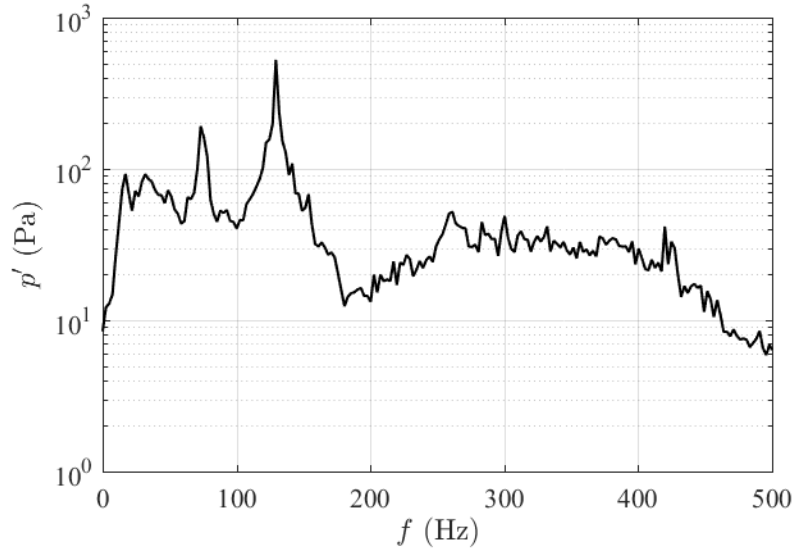

Figure B.2: The frequency spectrum for the pressure oscillations measured in the augmentor while performing secondary fuel injection at $\theta = \pi/2$.

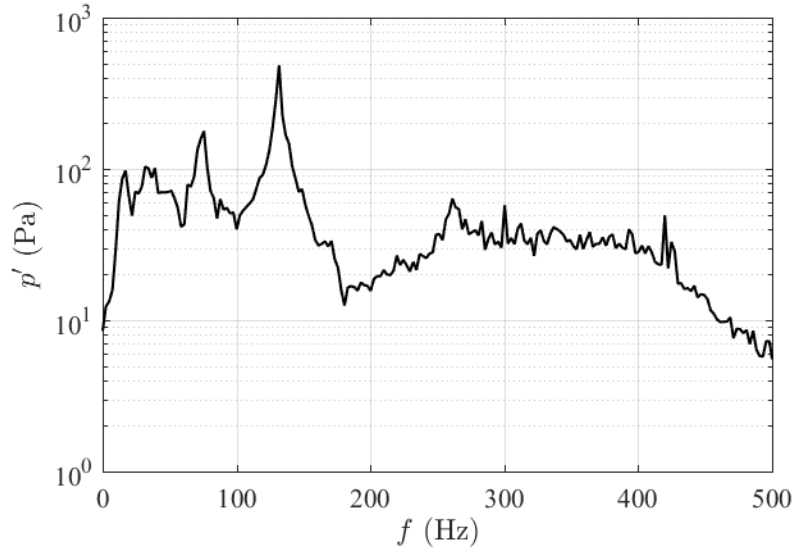

Figure B.3: The frequency spectrum for the pressure oscillations measured in the augmentor while performing secondary fuel injection at $\theta = \pi$.

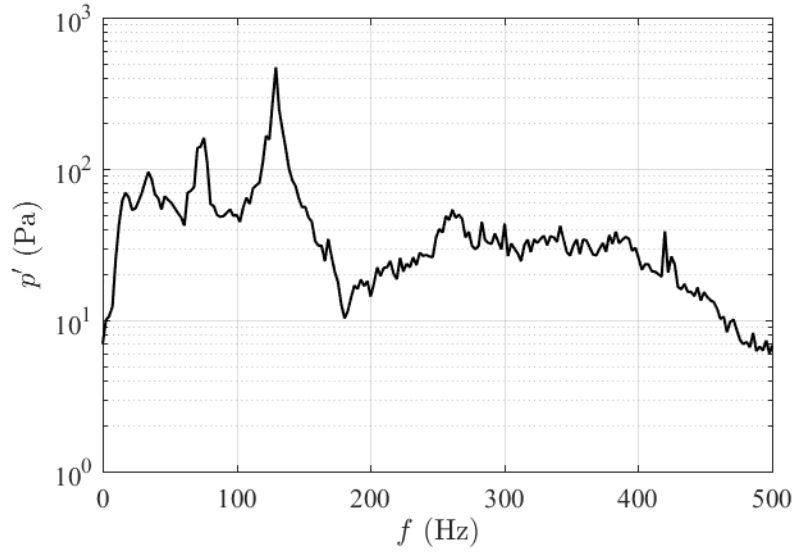

Figure B.4: The frequency spectrum for the pressure oscillations measured in the augmentor while performing secondary fuel injection at $\theta = 3\pi/2$.

V-Gutter Injection for $\phi_{aug} = 0.8$:

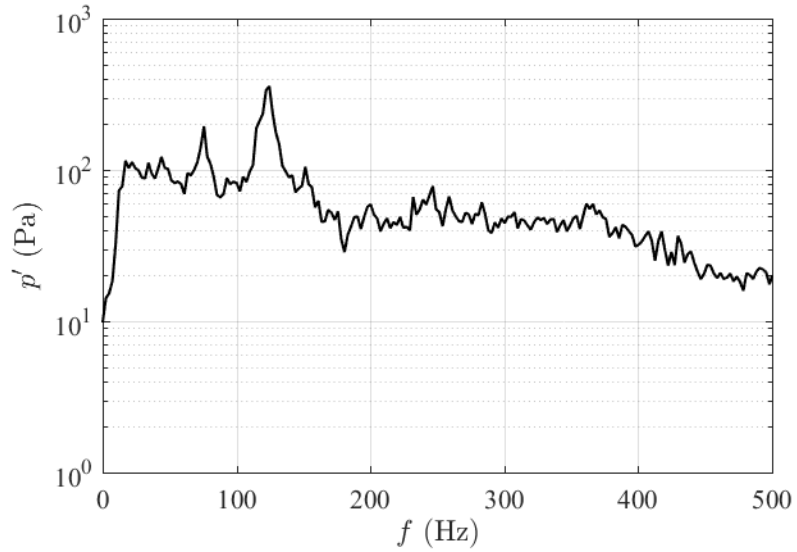

Figure B.5: The frequency spectrum for the pressure oscillations measured in the augmentor while performing secondary fuel injection at $\theta = \pi/4$.

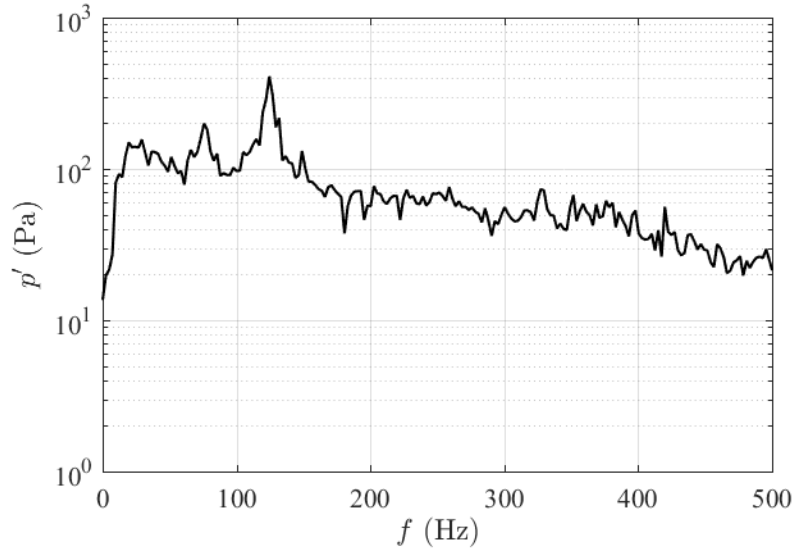

Figure B.6: The frequency spectrum for the pressure oscillations measured in the augmentor while performing secondary fuel injection at $\theta = \pi/4$.

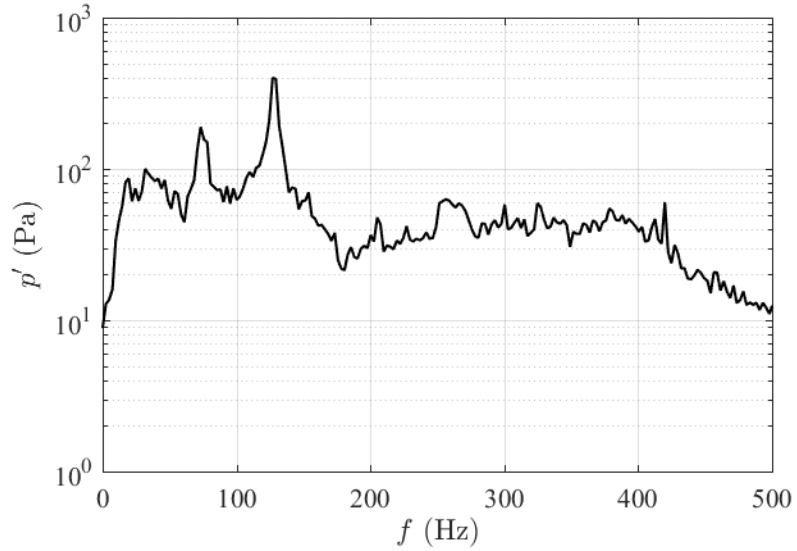

Figure B.7: The frequency spectrum for the pressure oscillations measured in the augmentor while performing secondary fuel injection at $\theta = \pi/4$.

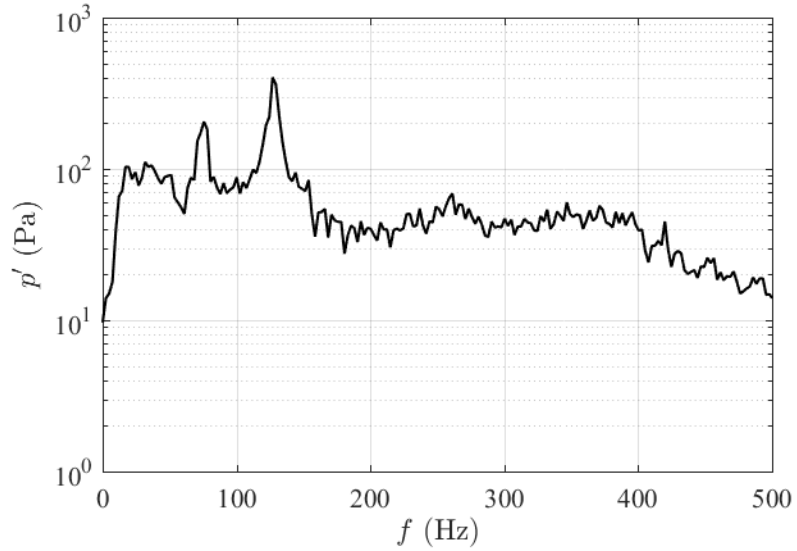

Figure B.8: The frequency spectrum for the pressure oscillations measured in the augmentor while performing secondary fuel injection at $\theta = \pi/4$.

Pressure Atomized Fuel injection at $\phi_{aug} = 0.6$:

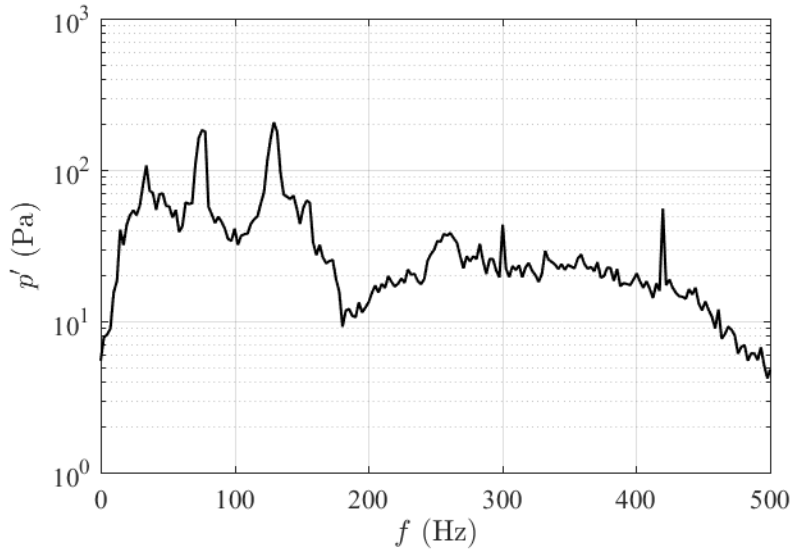

Figure B.9: The frequency spectrum for the pressure oscillations measured in the augmentor while performing secondary fuel injection at $\theta = 0$.

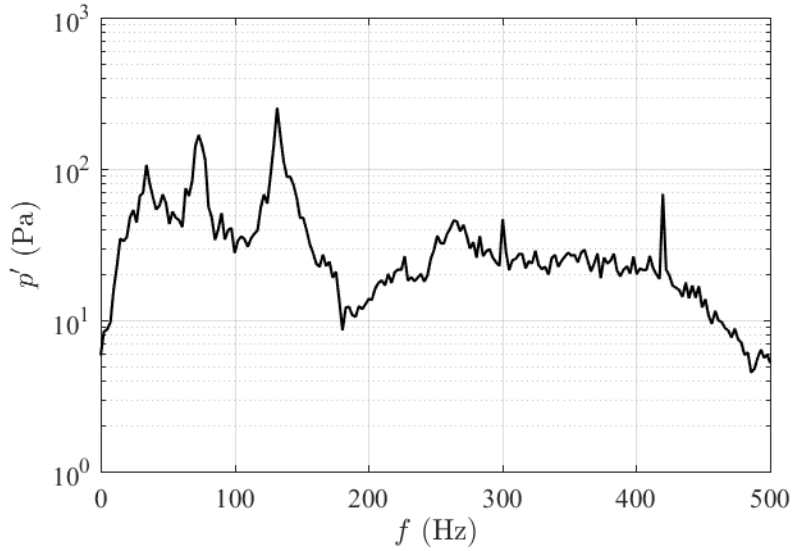

Figure B.10: The frequency spectrum for the pressure oscillations measured in the augmentor while performing secondary fuel injection at $\theta = \pi/2$.

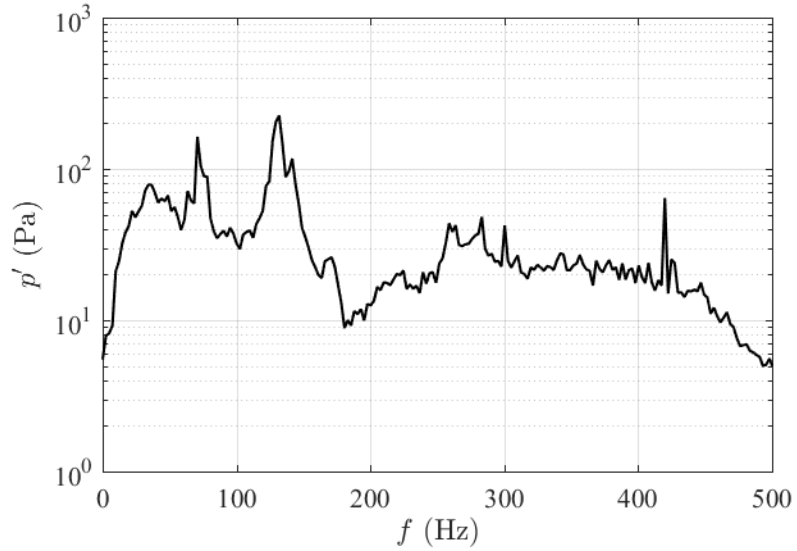

Figure B.11: The frequency spectrum for the pressure oscillations measured in the augmentor while performing secondary fuel injection at $\theta = \pi$.

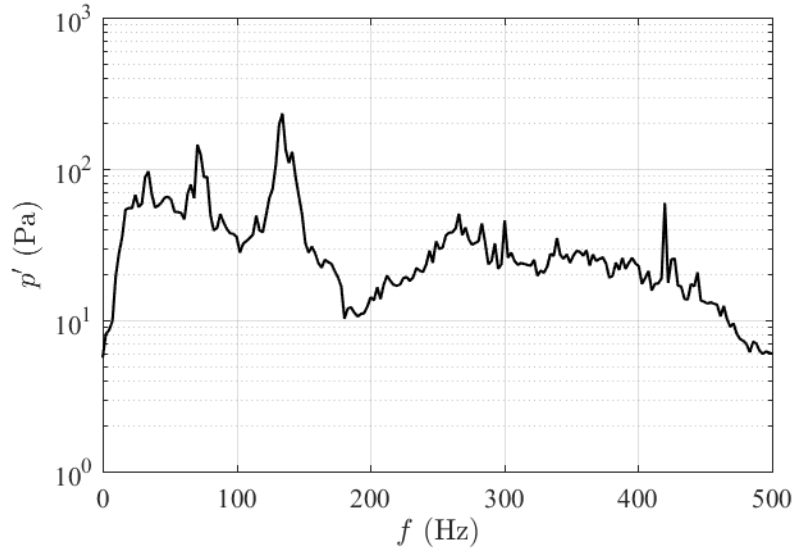

Figure B.12: The frequency spectrum for the pressure oscillations measured in the augmentor while performing secondary fuel injection at $\theta = 3\pi/2$.

Swirl Atomized Fuel Injection at $\phi_{aug} = 0.6$:

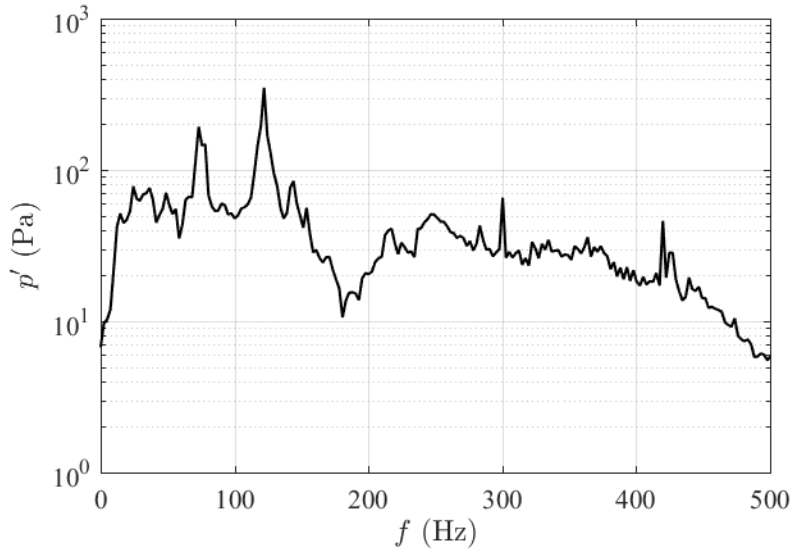

Figure B.13: The frequency spectrum for the pressure oscillations measured in the augmentor while performing secondary fuel injection at $\theta = 0$.

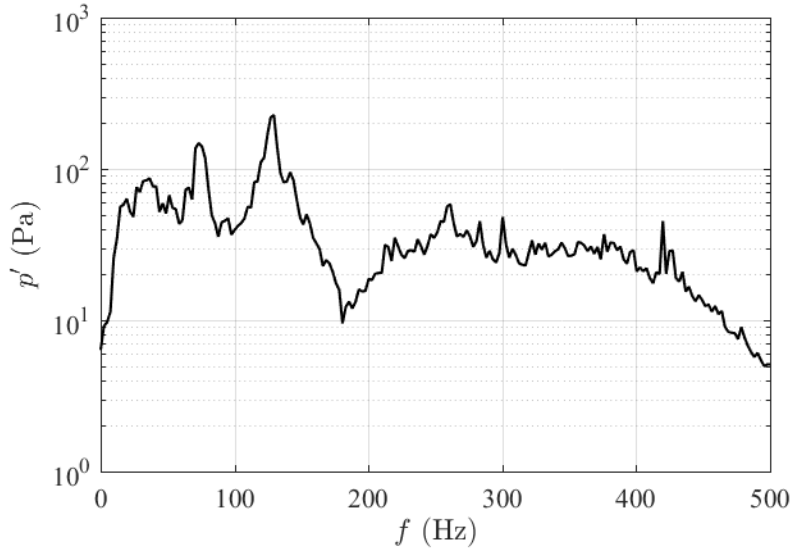

Figure B.14: The frequency spectrum for the pressure oscillations measured in the augmentor while performing secondary fuel injection at $\theta = \pi/4$.

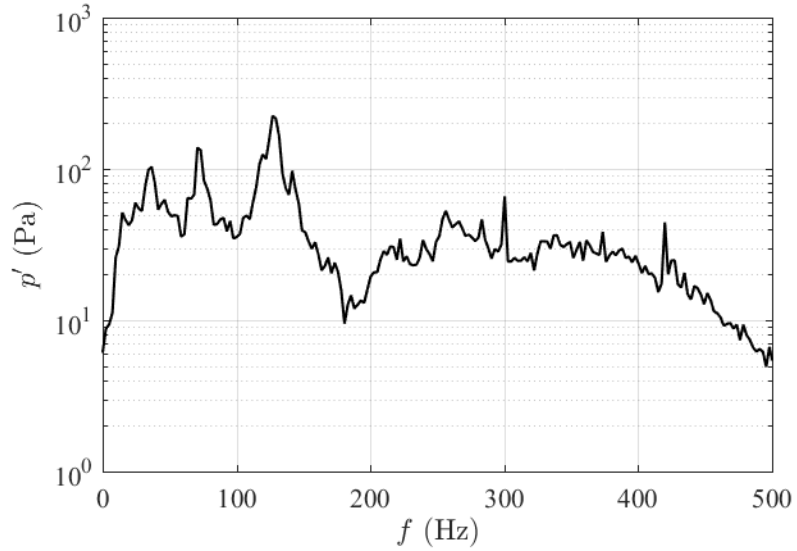

Figure B.15: The frequency spectrum for the pressure oscillations measured in the augmentor while performing secondary fuel injection at $\theta = \pi/2$.

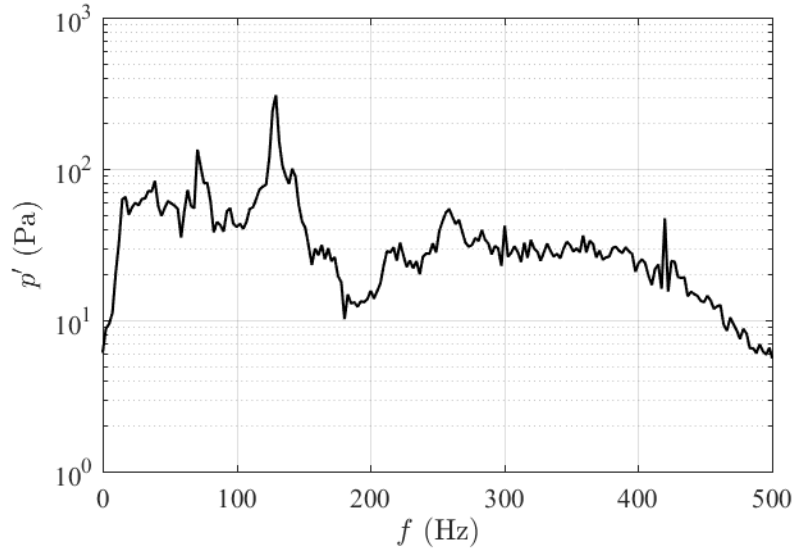

Figure B.16: The frequency spectrum for the pressure oscillations measured in the augmentor while performing secondary fuel injection at $\theta = 3\pi/4$.

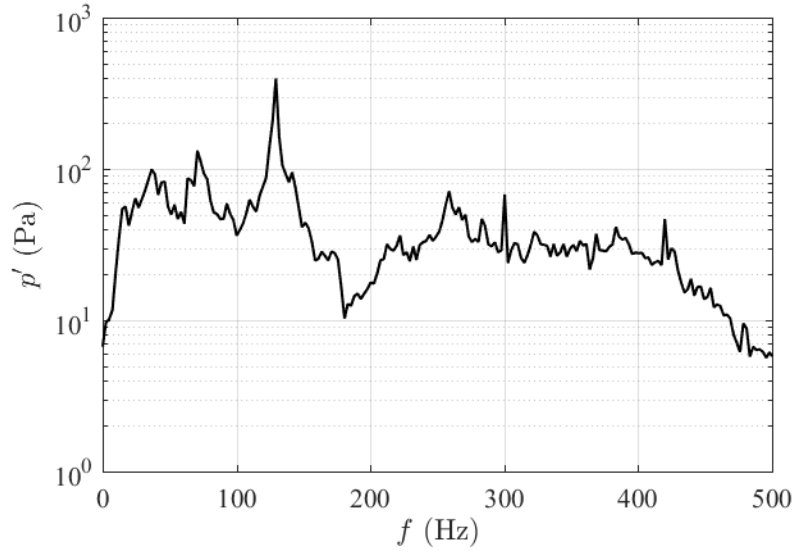

Figure B.17: The frequency spectrum for the pressure oscillations measured in the augmentor while performing secondary fuel injection at $\theta = \pi$.

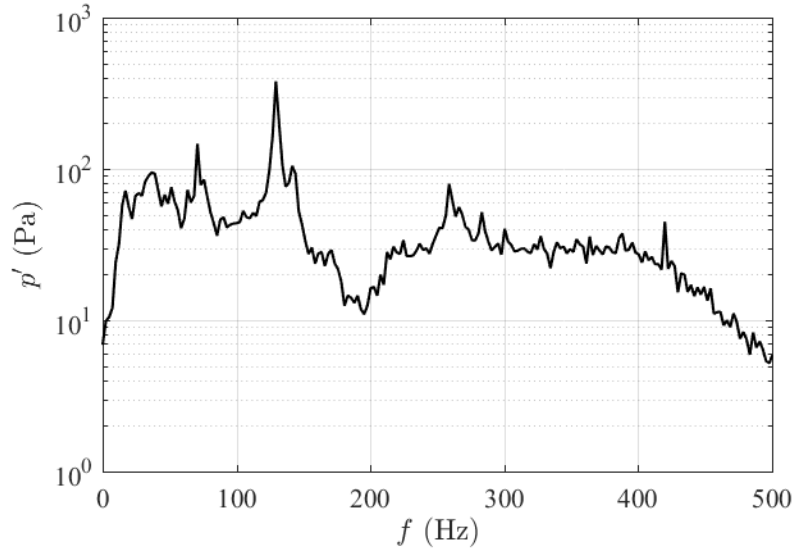

Figure B.18: The frequency spectrum for the pressure oscillations measured in the augmentor while performing secondary fuel injection at $\theta = 5\pi/4$.

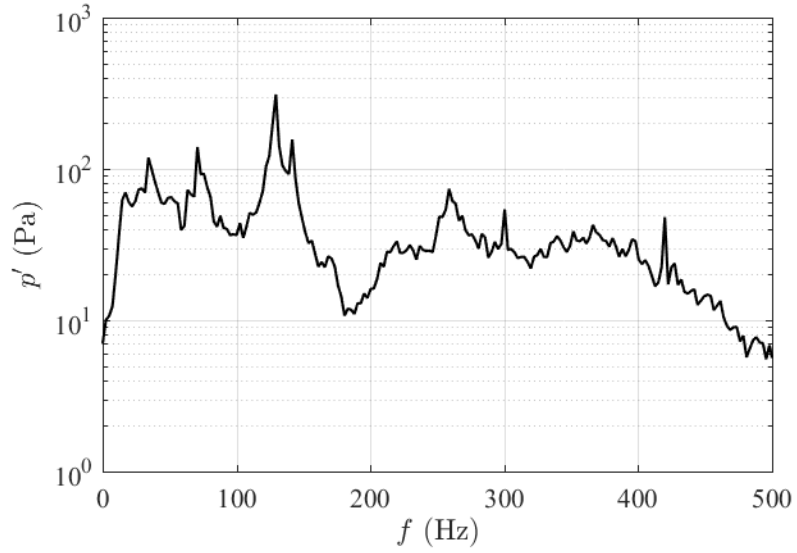

Figure B.19: The frequency spectrum for the pressure oscillations measured in the augmentor while performing secondary fuel injection at $\theta = 3\pi/2$.

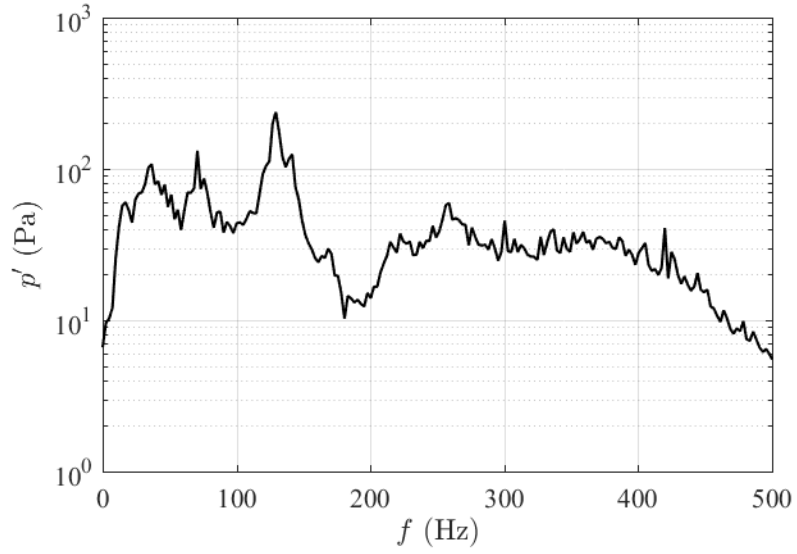

Figure B.20: The frequency spectrum for the pressure oscillations measured in the augmentor while performing secondary fuel injection at $\theta = 7\pi/4$.

Main Fuel Modulation Using Ethylene:

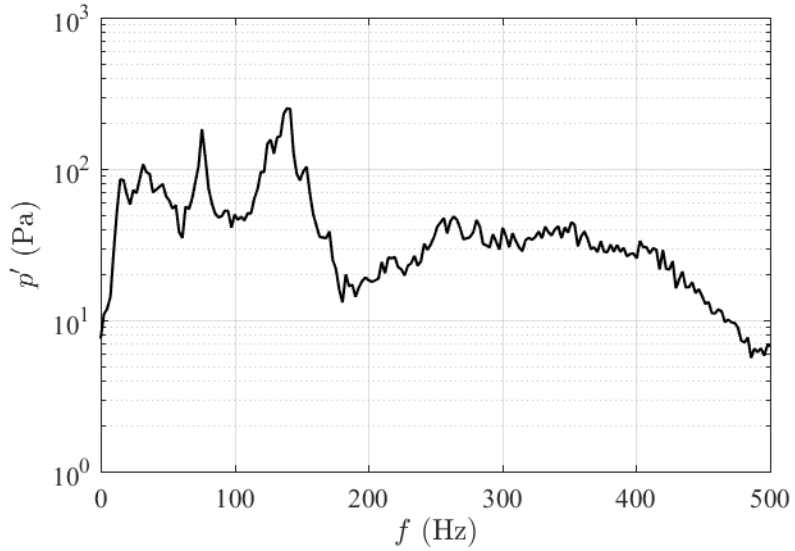

Figure B.21: The frequency spectrum for the pressure oscillations measured in the augmentor while performing main fuel modulation using C_2H_4 at $\theta = 0$.

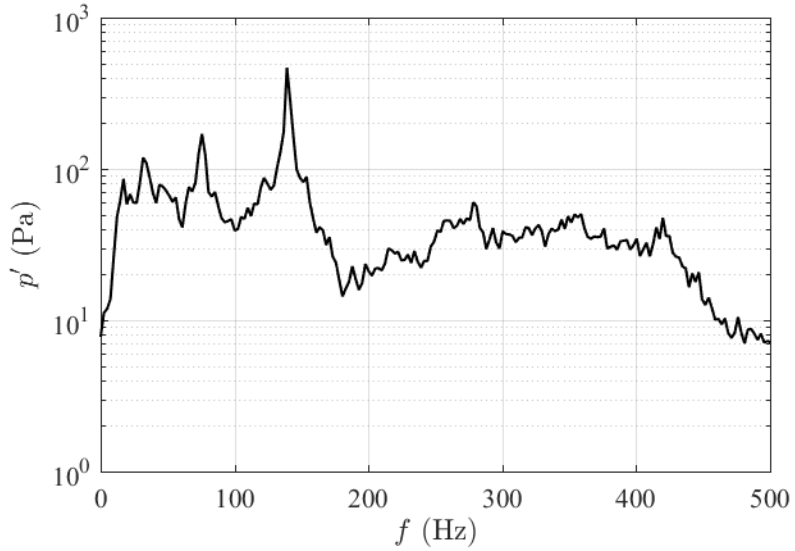

Figure B.22: The frequency spectrum for the pressure oscillations measured in the augmentor while performing main fuel modulation using C_2H_4 at $\theta = \pi/4$.

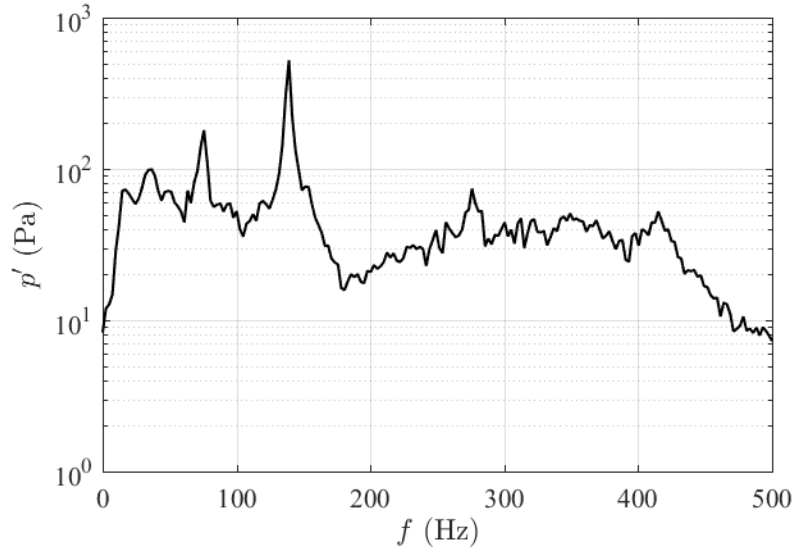

Figure B.23: The frequency spectrum for the pressure oscillations measured in the augmentor while performing main fuel modulation using C_2H_4 at $\theta = \pi/2$.

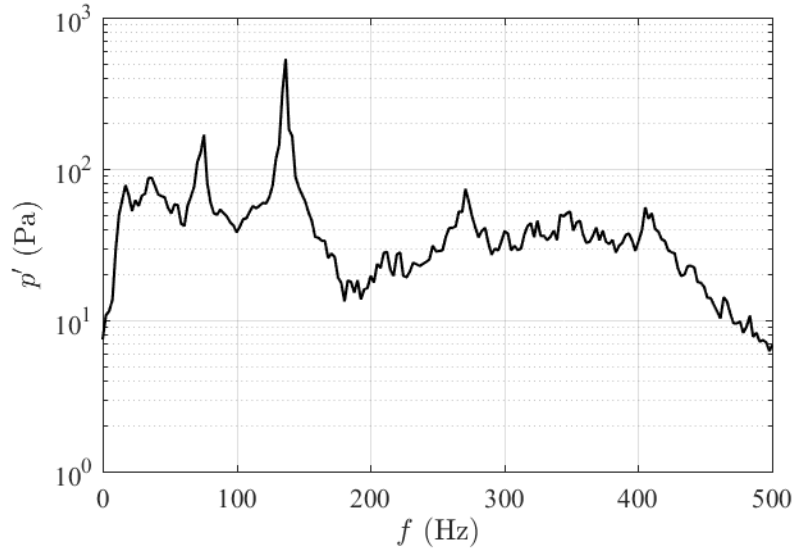

Figure B.24: The frequency spectrum for the pressure oscillations measured in the augmentor while performing main fuel modulation using C_2H_4 at $\theta = 3\pi/4$.

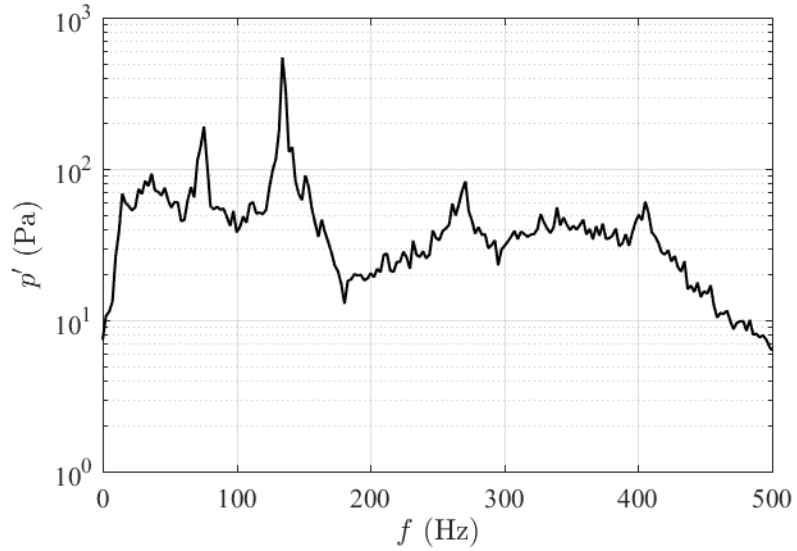

Figure B.25: The frequency spectrum for the pressure oscillations measured in the augmentor while performing main fuel modulation using C_2H_4 at $\theta = \pi$.

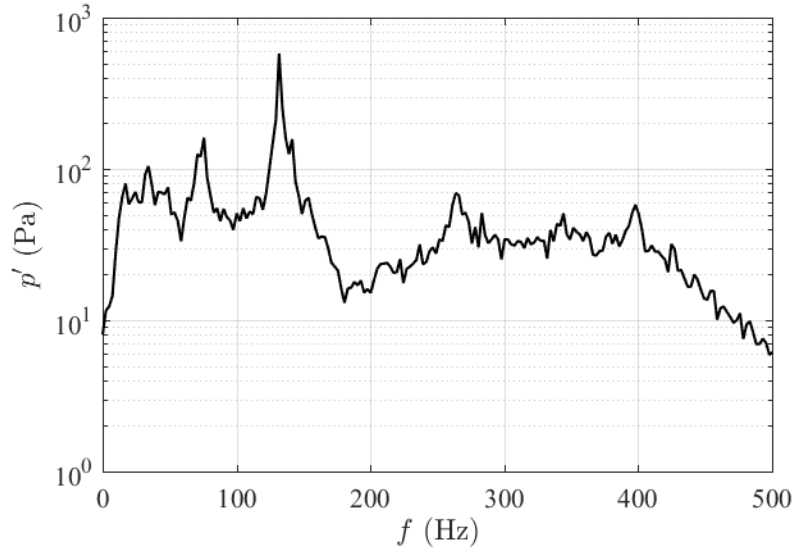

Figure B.26: The frequency spectrum for the pressure oscillations measured in the augmentor while performing main fuel modulation using C_2H_4 at $\theta = 5\pi/4$.

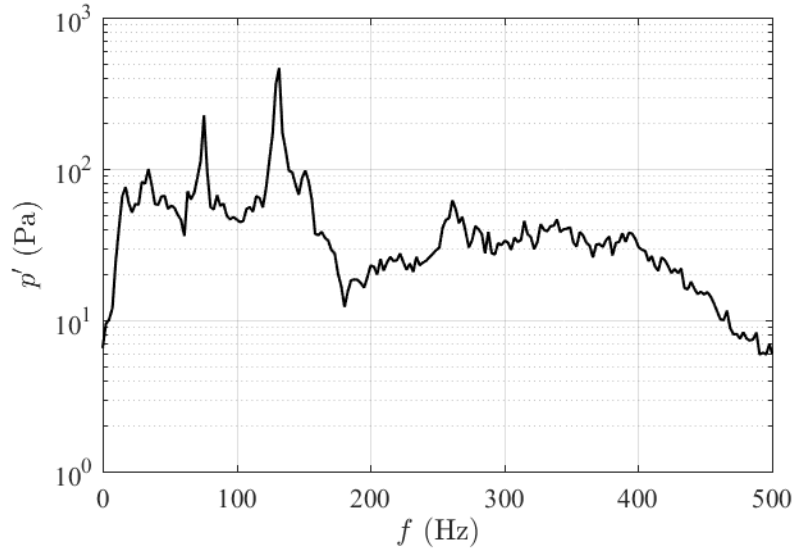

Figure B.27: The frequency spectrum for the pressure oscillations measured in the augmentor while performing main fuel modulation using C_2H_4 at $\theta = 3\pi/2$.

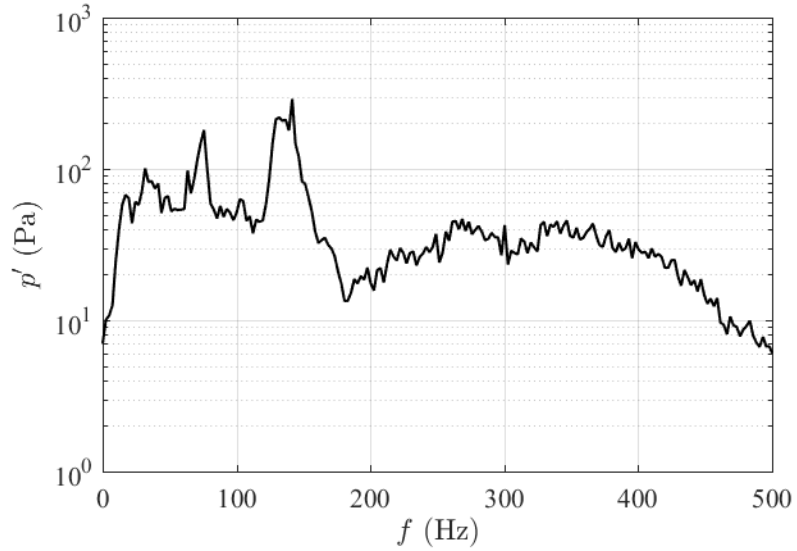

Figure B.28: The frequency spectrum for the pressure oscillations measured in the augmentor while performing main fuel modulation using C_2H_4 at $\theta = 7\pi/4$.

Secondary Air Injection with Prevaporized Fuel:

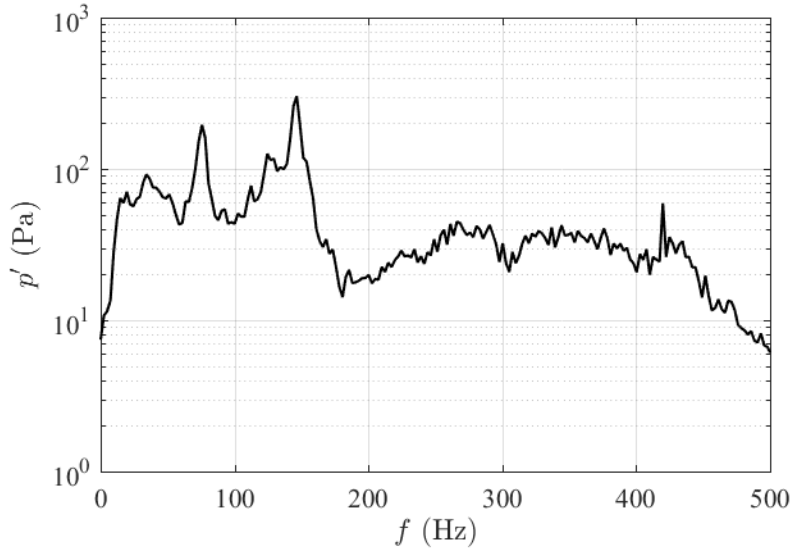

Figure B.29: The frequency spectrum for the pressure oscillations measured in the augmentor while performing secondary air injection with prevaporized fuel at $\theta = 0$.

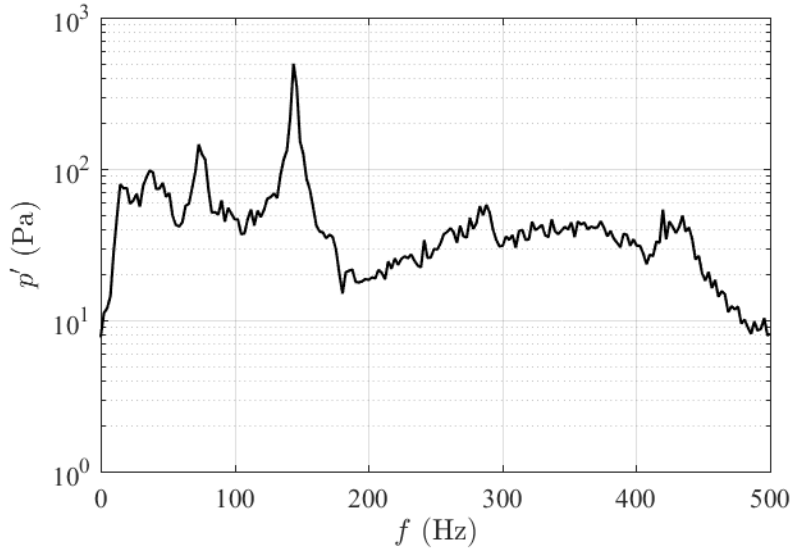

Figure B.30: The frequency spectrum for the pressure oscillations measured in the augmentor while performing secondary air injection with prevaporized fuel at $\theta = \pi/4$.

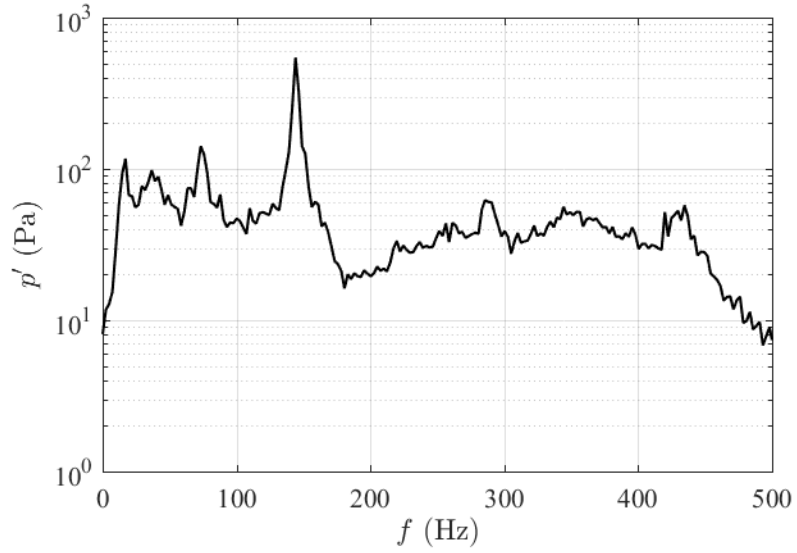

Figure B.31: The frequency spectrum for the pressure oscillations measured in the augmentor while performing secondary air injection with prevaporized fuel at $\theta = \pi/2$.

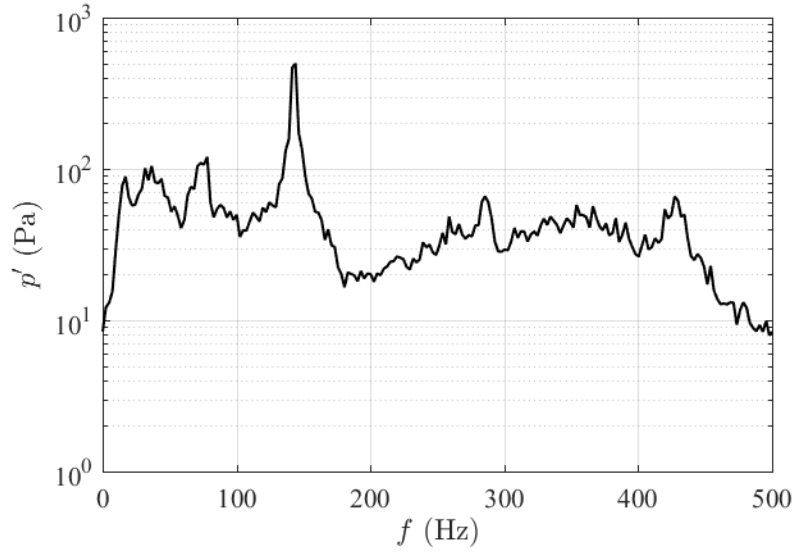

Figure B.32: The frequency spectrum for the pressure oscillations measured in the augmentor while performing secondary air injection with prevaporized fuel at $\theta = 3\pi/4$.

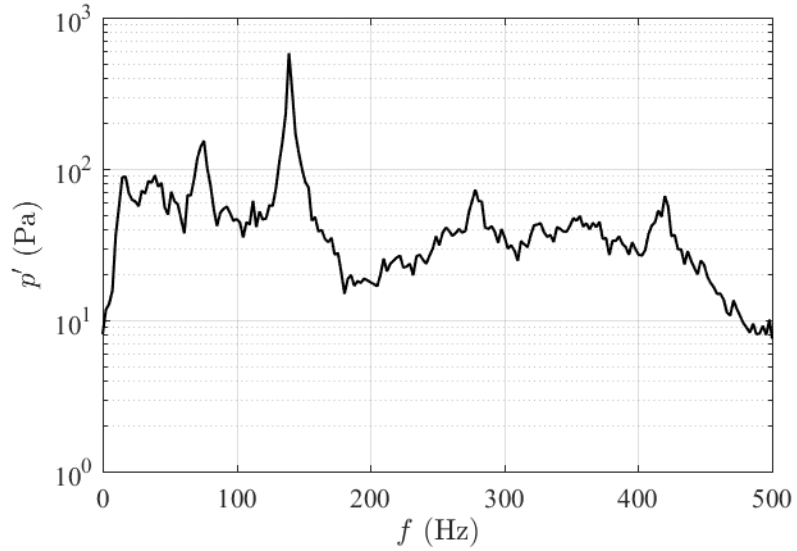

Figure B.33: The frequency spectrum for the pressure oscillations measured in the augmentor while performing secondary air injection with prevaporized fuel at $\theta = \pi$.

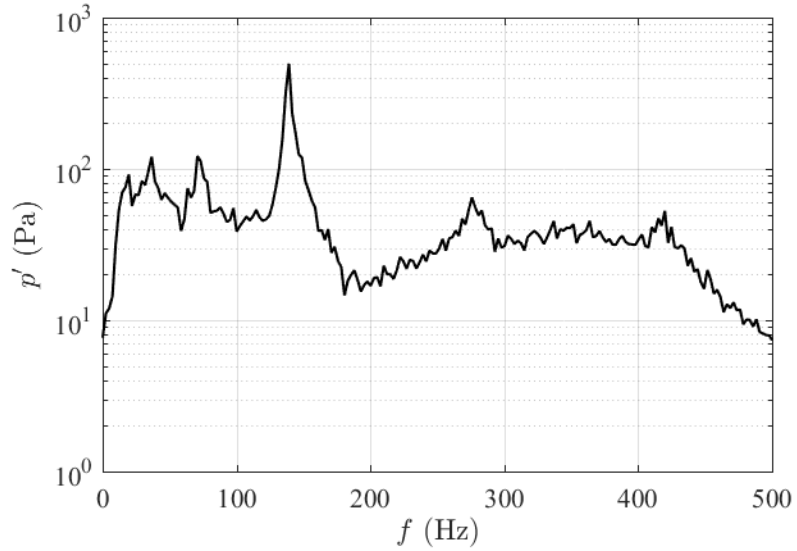

Figure B.34: The frequency spectrum for the pressure oscillations measured in the augmentor while performing secondary air injection with prevaporized fuel at $\theta = 5\pi/4$.

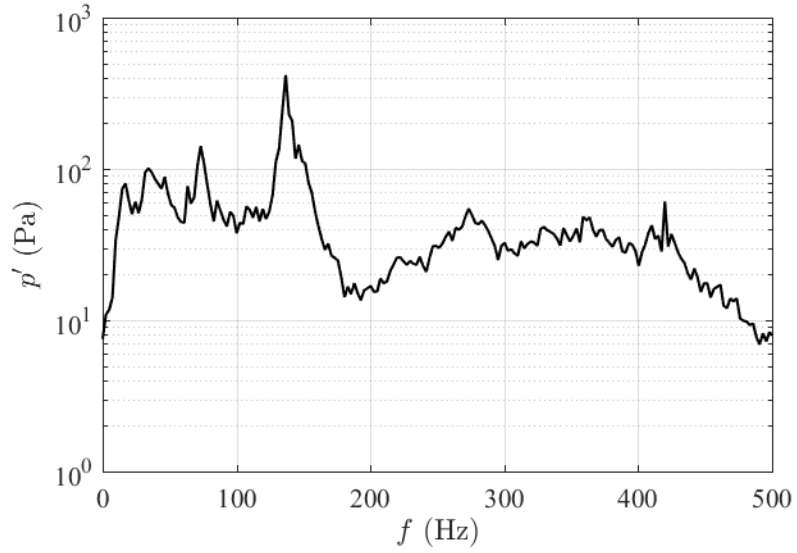

Figure B.35: The frequency spectrum for the pressure oscillations measured in the augmentor while performing secondary air injection with prevaporized fuel at $\theta = 3\pi/2$.

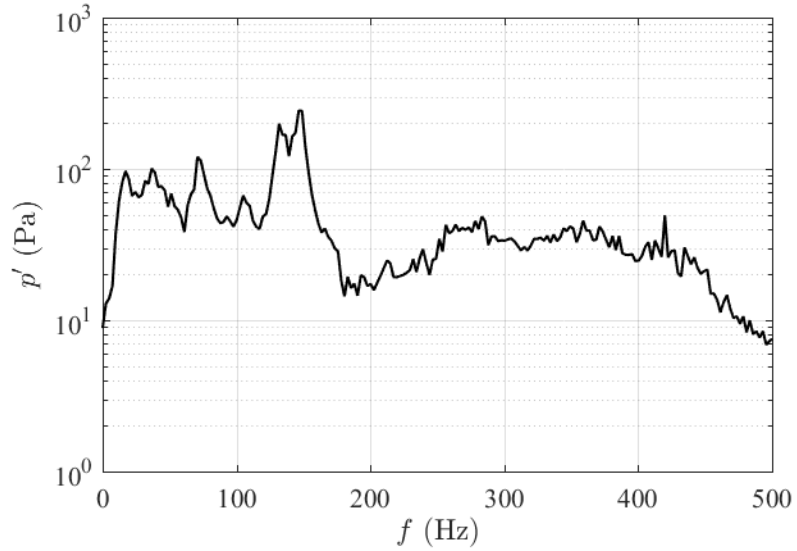

Figure B.36: The frequency spectrum for the pressure oscillations measured in the augmentor while performing secondary air injection with prevaporized fuel at $\theta = 7\pi/4$.

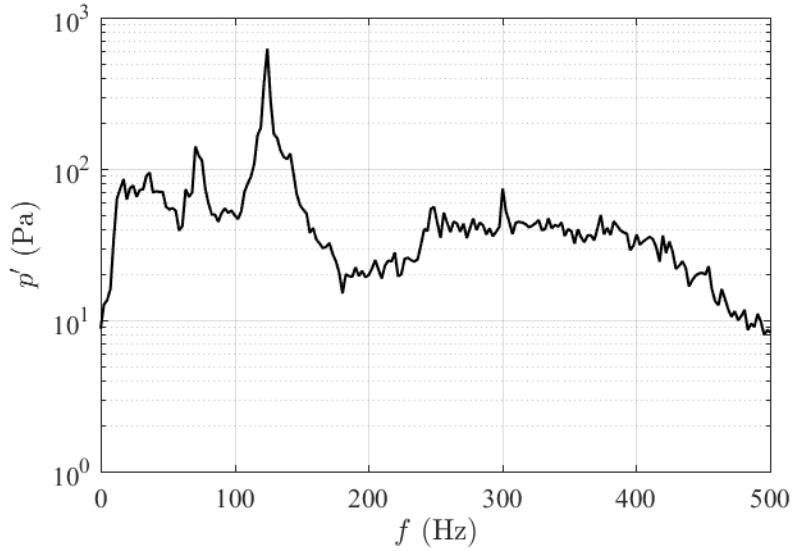

Figure B.37: The frequency spectrum for the pressure oscillations measured in the augmentor while performing secondary air injection with liquid fuel at $\theta = 0$.

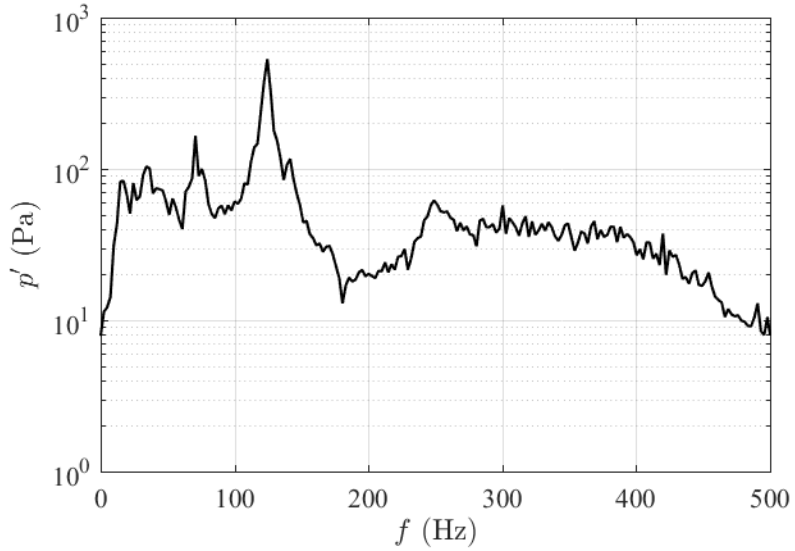

Figure B.38: The frequency spectrum for the pressure oscillations measured in the augmentor while performing secondary air injection with liquid fuel at $\theta = \pi/4$.

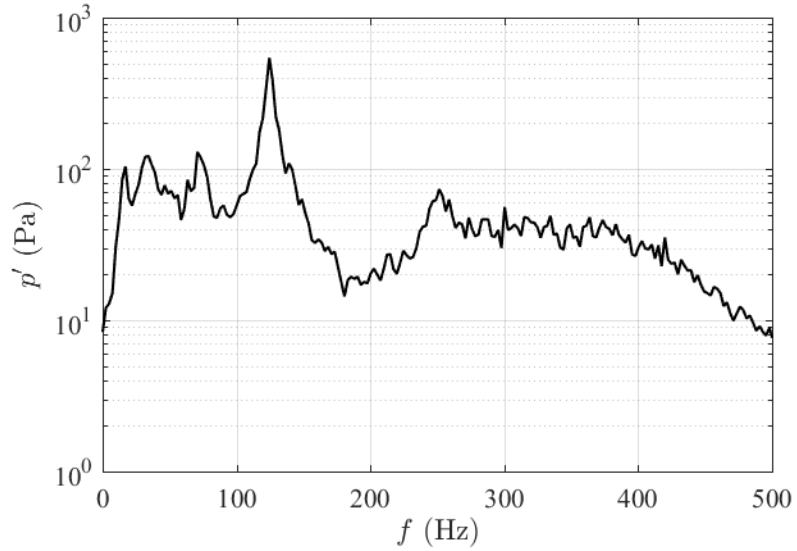

Figure B.39: The frequency spectrum for the pressure oscillations measured in the augmentor while performing secondary air injection with liquid fuel at $\theta = \pi/2$.

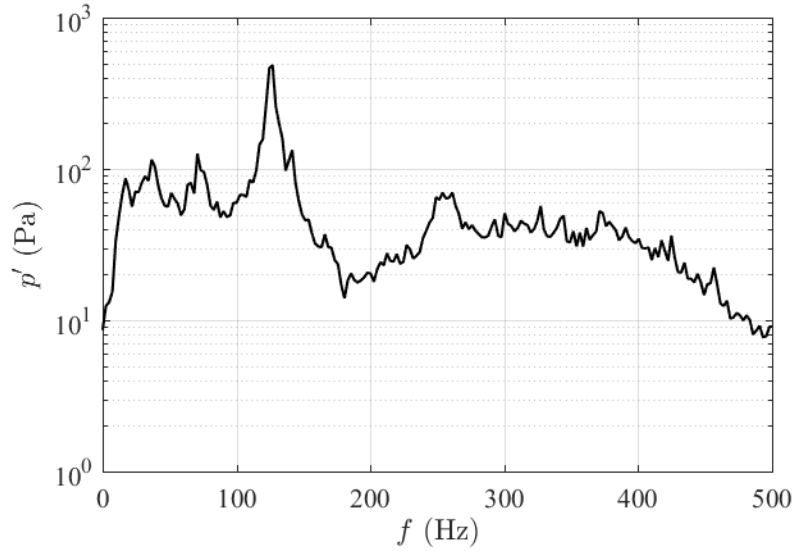

Figure B.40: The frequency spectrum for the pressure oscillations measured in the augmentor while performing secondary air injection with liquid fuel at $\theta = 3\pi/4$.

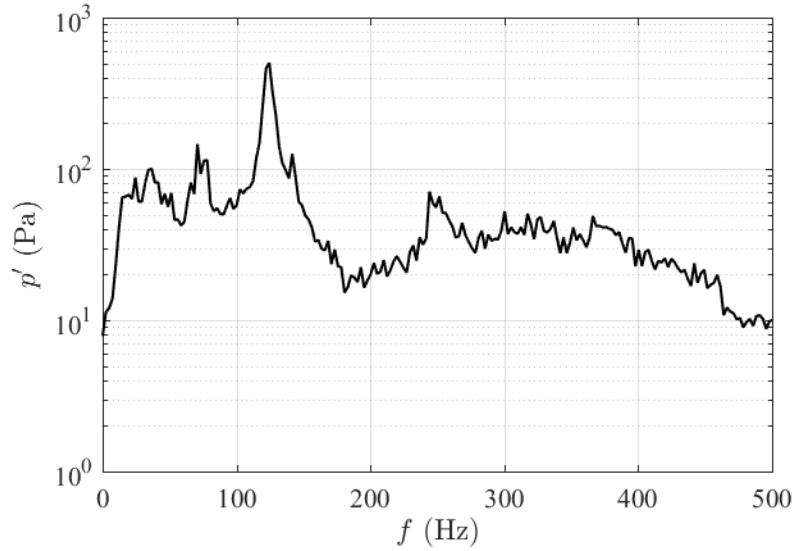

Figure B.41: The frequency spectrum for the pressure oscillations measured in the augmentor while performing secondary air injection with liquid fuel at $\theta = \pi$.

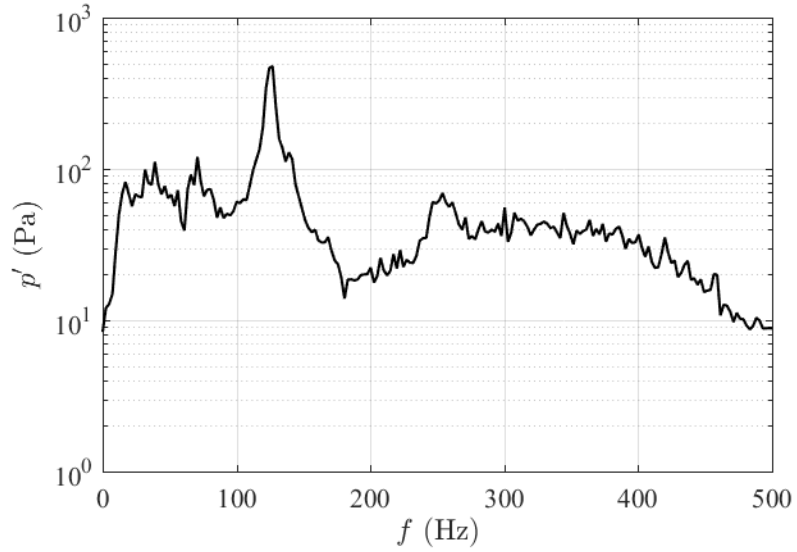

Figure B.42: The frequency spectrum for the pressure oscillations measured in the augmentor while performing secondary air injection with liquid fuel at $\theta = 5\pi/4$.

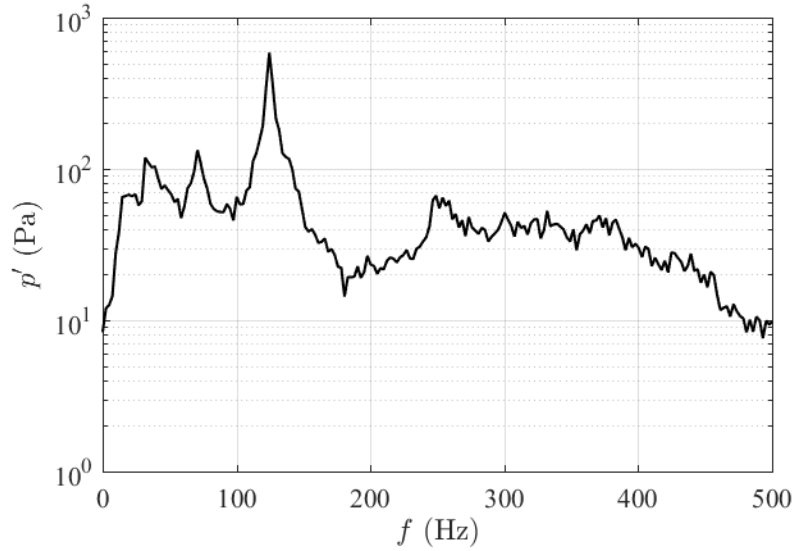

Figure B.43: The frequency spectrum for the pressure oscillations measured in the augmentor while performing secondary air injection with liquid fuel at $\theta = 3\pi/2$.

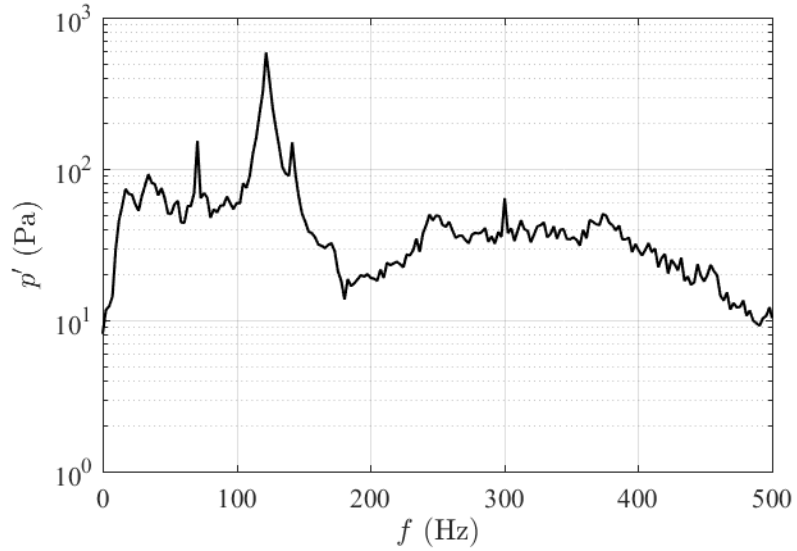

Figure B.44: The frequency spectrum for the pressure oscillations measured in the augmentor while performing secondary air injection with liquid fuel at $\theta = 7\pi/4$.

Bibliography

[1] J. W. S. Rayleigh. *The Theory of Sound*, volume 2. Macmillan Ltd., New York, 2 edition, 1896.

[2] F. E. C. Culick. Dynamics of combustion systems: Fundamentals, acoustics, and control. *RTO-EN-020, RTO AVT Course on Active Control of Engine Dynamics*, 2001.

[3] D. E. Rogers and F. E. Marble. A mechanism for high-frequency oscillations in ramjet combustors and afterburners. *Journal of Jet Propulsion*, pages 456–462, 1956.

[4] D. A. Smith and E. E. Zukowski. Combustion instability sustained by unsteady vortex combustion. In *AIAA/SAE/ASME/ASEE 21st Joint Propulsion Conference*, pages 1–9. American Institute of Aeronautics and Astronautics, 1985.

[5] T. J. Poinsot, A. C. Trouve, D. P. Veyante, S. M. Candel, and E. J. Esposito. Vortex-driven acoustically coupled combustion instabilities. *Journal of Fluid Mechanics*, 177:265–292, 1987.

[6] A. A. Putnam and W. R. Dennis. Burner oscillations of the gauze-tone type. *The Journal of the Acoustical Society of America*, 26(5):716–725, 1954.

[7] G. A. Flandro and H. R. Jacobs. Vortex generated sound in cavities. In *AIAA Aero-Acoustics Conference*. American Institute of Aeronautics and Astronautics, 1973.

[8] B. T. Chu and L. S. G. Kovásznay. Non-linear interactions in a viscous heat-conducting compressible gas. *Journal of Fluid Mechanics*, 3(5):494–514, 1957.

[9] B. T. Chu. On the energy transfer to small disturbances in fluid flow (part i). *Acta Mechanica*, 1(3):215–234, 1965.

[10] F. E. C Culick. Nonlinear behavior of acoustic waves in combustion chambers - i. *Acta Astronautica*, 3:715–734, 1976.

[11] F. E. C Culick. Nonlinear behavior of acoustic waves in combustion chambers - ii. *Acta Astronautica*, 3:735–757, 1976.

[12] S. Ducruix, T. Schuller, D. Durox, and S. Candel. Combustion dynamics and instabilities: Elementary coupling and driving mechanisms. *Journal of Propulsion and Power*, 19(5):722–734, 2003.

[13] H. J. Merk. An analysis of unstable combustion of premixed gases. *Symposium (International) on Combustion*, 6(1):500–512, 1957.

[14] T. Toong, R. F. Salant, J. M. Stopford, and G. Y. Anderson. Mechanisms of combustion instability. *Symposium (International) on Combustion*, 10(1):1301–1313, 1965.

[15] M. Barrere and F. A. Williams. Comparison of combustion instabilities found in various types of combustion chambers. *Symposium (International) on Combustion*, 12(1):169–181, 1969.

[16] W. C. Strahle. On combustion generated noise. *Journal of Fluid Mechanics*, 49(2):399–414, 1971.

[17] W. C. Strahle. Some results in combustion generated noise. *Journal of Sound and Vibration*, 23(1):113–125, 1972.

[18] H. H. Chiu and M. Summerfield. Theory of combustion noise. *Acta Astronautica*, 1(7):967–984, 1974.

[19] F. E. C. Culick. Combustion instabilities in liquid-fueled propulsion systems - an overview. *NATO AGARD Conference Procedding No. 450*, 1988.

[20] S. Candel. Combustion dynamics and control: Progress and challenges. In *Proceedings fo the Combustion Institute*, volume 29, pages 1–28. Combustion Institute, 2002.

[21] K. C. Schadow and E. Gutmark. Combustion instability related to vortex shedding in dump combustors and their passive control. *Progess in Energy and Combustion Science*, 18:117–132, 1992.

[22] D. T. Harrje and F. H. Reardon. Liquid propellant rocket combustion instability. *NASA Special Publication*, 194, 1972.

[23] J. D. Sterling and E. E. Zukowski. Longitudinal mode combustion instabilities in a dump combustor. In *AIAA 25th Aerospace Sciences Meeting*. American Institute of Aeronautics and Astronautics, 1987.

[24] J. D. Sterling. *Longitudinal Mode Combustion Instability in Air Breathing Engines*. PhD thesis, California Institute of Technology, 1987.

[25] K. H. Yu, A. Trouve, and J. W. Daily. Low-frequency pressure oscillations in a model ramjet combustor. *Journal of Fluid Mechanics*, 232:47–72, 1991.

[26] P. J. Langhorne. Reheat buzz: An acoustically coupled combustion instability. part 1. experiment. *Journal of Fluid Mechanics*, 193:417–443, 1988.

[27] G. J. Bloxsidge, A. P. Dowling, and P. J. Langhorne. Reheat buzz: An acoustically coupled combustion intsability. part 2. theory. *Journal of Fluid Mechanics*, 193:445–473, 1988.

[28] W. P. Shih, J. G. Lee, and D. A. Santavicca. Stability and emissions characteristics of a lean premixed gas turbine combustor. *Symposium (International) on Combustion*, 26(1):2771–2778, 1996.

[29] K. K. Venkataraman, L. H. Preston, D. W. Simons, B. J. Lee, J. G. Lee, and D. A. Santavicca. Mechanism of combustion instability in a lean premixed dump combustor. *Journal of Propulsion and Power*, 15(6):909–918, 1999.

[30] T. C. Lieuwen. *Investigation of Combustion Instability Mechanisms in Premixed Gas Turbines*. PhD thesis, 1999, Georgia Institute of Technology.

[31] S. Y. Lee, S. Seo, J. C. Broda, S. Pal, and R. J. Santoro. An experimental estimation of mean reaction rate and flame structure during combustion instability in a lean premixed gas turbine combustor. In *Proccedings of the Combustion Institute*, volume 28, pages 775–782. Combustion Institute, 2000.

[32] T. Lieuwen, H. Torres, C. Johnson, and B. T. Zinn. A mechanism of combustion instability in lean premixed gas turbine combustors. *Journal of Engineering for Gas Turbines and Power*, 123:182–189, 2001.

[33] A. F. Ghoniem, S. Park, A. Wachsman, A. Annaswamy, D. Wee, and H. M. Altay. Mechanisms of combustion dynamics in a backward-facing step stabilized premixed flame. In *Proceedings of the Combustion Institute*, pages 1783–1790. Combustion Institute, 2005.

[34] H. M. Altay, R. L. Speth, D. E. Hudgins, and A. F. Ghoniem. Flame-vortex interaction driven combustion dynamics in a backward-facing step combustor. *Combustion and Flame*, 156:1111–1125, 2009.

[35] H. M. Altay, R. L. Speth, D. E. Hudgins, and A. F. Ghoniem. The impact of equivalence ratio oscillations on combustion dynamics in a backward-facing step combustor. *Combustion and Flame*, 156:2106–2116, 2009.

[36] T. Poinsot, S. Candel, and A. Trouve. Applications of direct numerical simulation to premixed turbulent combustion. *Progress in Energy and Combustion Science*, 21:531–576, 1996.

[37] T. Poinsot. Using direct numerical simulations to understand premixed turbulent combustion. *Symposium (International) on Combustion*, 26(1):219–232, 1996.

[38] C. Fureby. A computational study of combustion instabilities due to vortex shedding. In *Proceedings of the Combustion Institute*, volume 28, pages 783–791. Combustion Institute, 2000.

[39] S. M. Candel. Combustion instabilities coupled by pressure waves and their active control. *Symposium (International) on Combustion*, 24(1):1277–1296, 1992.

[40] P. H. Renard, D. Thevenin, J. C. Rolon, and S. Candel. Dynamics of flame/vortex interactions. *Progressin Energy and Combustion Science*, 26:225–282, 2000.

[41] T. C. Lieuwen. *Unsteady Combustor Physics*. Cambridge University Press, New York, 2012.

[42] A. A. Putnam. *Combustion Driven Oscillations in Industry*. Elsevier, 1971.

[43] G. D. Garrison, P. L. Russell, and J. Stettler. Investigation of damping methods for augmentor combustion instability. *NTIS Technical Report*, 1972.

[44] J. E. F. Williams. Review lecture: Anti-sound. In *Proceedings of the Royal Society of London A: Mathematical, Physical and Engineering Sciences*, volume 395, pages 63–88. The Royal Society, 1984.

[45] T. Poinsot, F. Bourienne, S. Candel, E. Esposito, and W. Lang. Suppression of combustion instabilities by active control. *Journal of Propulsion and Power*, 5(1):14–20, 1989.

[46] A. Gulati and R. Mani. Active control of unsteady combustion-induced oscillations. *Journal of Propulsion and Power*, 8(5):1109–1115, 1992.

[47] P. J. Langhorne, A. P. Dowling, and N. Hooper. Practical active control system for combustion oscillations. *Journal of Propulsion and Power*, 6(3):324–333, 1990.

[48] C. Hantschk, J. Hermann, and D. Vortmeyer. Active instability control with direct-drive servo valves in liquid fueled combustion systems. *Symposium (International) on Combustion*, 26(1):2835–2841, 1996.

[49] K. H. Yu, T. P. Parr, K. J. Wilson, K. C. Schadow, and E. J. Gutmark. Active control of liquid-fueled combustion using periodic vortex-droplet interaction. *Symposium (International) on Combustion*, 26(1):2843–2850, 1996.

[50] K. H. Yu, K. J. Wilson, and K. C. Schadow. Liquid-fueled active instability suppression. *Symposium (International) on Combustion*, 27(1):2039–2046, 1998.

[51] Y. Neumeier and B. T. Zinn. Experimental demonstration of active control of combustion instabilities using real-time modes observation and secondary fuel injection. *Symposium (International) on Combustion*, 26(1):2811–2818, 1996.

[52] J. R. Seume, N. Vortmeyer, W. Krause, J. Hermann, C. C. Hantschk, P. Zangl, S. Gleis, D. Vortmeyer, and A. Orthmann. Application of active combustion instability control to a heavy duty gas turbine. In *ASME 1997 Turbo Asia Conference*, pages 1–8. American Society of Mechanical Engineers, 1997.

[53] K. R. McManus and C. T. Bowman. Effects of controlling vortex dynamics on the performance of a dump combustor. *Symposium (International) on Combustion*, 23(1):1093–1099, 1990.

[54] A. F. Ghoniem, A. Annaswamy, S. Park, and Z. C. Sobhani. Stability and emissions control using air injection and h2 addition in premixed combustion. In *Proceedings of the Combustion Institute*, pages 1765–1773. Combustion Institute, 2005.

[55] G. J. Bloxsidge, A. P. Dowling, N. Hooper, and P. J. Langhorne. Active control of reheat buzz. *AIAA Journal*, 26(7):783–790, 1988.

[56] J. Y. Lee, E. Lubarsky, and B. T. Zinn. "slow" active control of combustion instabilities by modification of liquid fuel spray properties. In *Proceedings of the Combustion Institute*, pages 1757–1764. Combustion Institute, 2011.

[57] L. Cammarata, A. Fichera, and A. Pagano. Neural prediction of combustion instability. *Applied Energy*, 72:513–528, 2002.

[58] B. S. Hong, V. Yang, and A. Ray. Robust feedback control of combustion instability with modeling uncertainty. *Combustion and Flame*, 120:91–106, 2000.

[59] B. S. Hong, A. Ray, and V. Yang. Wide-range robust control of combustion instability. *Combustion and Flame*, 128:242–258, 2002.

[60] A. Fichera and A. Pagano. Application of neural dynamic optimization to combustion instability control. *Applied Energy*, 83:253–264, 2006.

[61] C. M. Jones, J. G. Lee, and D. A. Santavicca. Closed-loop active control of combustion instabilities using subharmonic secondary fuel injection. *Journal of Propulsion and Power*, 15(4):584–590, 1999.

[62] K. Kim, J. G. Lee, and D. A. Santavicca. Spatial and temporal distribution of secondary fuel for suppression of combustion dynamics. *Journal and Propulsion and Power*, 22(2):433–439, 2006.

[63] N. Docquier and S. Candel. Combustion control and sensors: A review. *Progress in Energy and Combustion Science*, 28:107–150, 2002.

[64] I. R. Hurle, R. B. Price, T. M. Sugden, and A. Thomas. Sound emissions from open turbulent premixed flames. *Proceedings of the Royal Society of London*, 303(1475):409–427, 1968.

[65] A. G. Gaydon. *The Spectroscopy of Flames*. Chapman and Hall, London, 2 edition, 1974.

[66] J. G. Lee and D. A. Santavicca. Experimental diagnostics for the study of combustion instabilities in lean premixed combustors. *Journal of Propulsion and Power*, 19(5):735–750, 2003.

[67] G. S. Settles. *Schlieren and Shadowgraph Techniques: Visualizing Phenomena in Transparent Media*. Springer, 2012.

[68] R. C. Hendricks, D. M. Bushnell, and D. T. Shouse. Aviation fueling: a cleaner, greener approach. *International Journal of Rotating Machinery*, 2011.

[69] United States Department of Energy National Energy Technology Laboratory. Fischer-tropsch fuels. Factsheet, November 2011.

[70] J. T. Edwards, L. M. Shafer, and J. K. Klein. U.s. air force hydroprocessed renewable jet (hrj) fuel research. Technical report, Air Force Research Laboratory, United States Air Force, 2012.

[71] G. B. Bessee, S. A. Hutzler, and G. R. Wilson. Propulsion and power rapid response research and development (r&d) support: Analysis of synthetic aviation fuels. Technical report, Air Force Research Laboratory, United States Air Force, 2011.

[72] A. H. Lefebvre and D. R. Ballal. *Gas Turbine Combustion: Alternative Fuels and Emissions*. CRC Press, 2010.

[73] S. R. Turns. *An Introduction to Combustion: Concepts and Applications*. McGraw Hill, 2 edition, 2000.

[74] B. Pang. *Active Suppression of Vortex-Driven Combustion Instability Using Controlled Liquid-Fuel Injection*. PhD thesis, University of Maryland, College Park, 2005.

[75] J. G. Lee, K. Kim, and D. A. Santavicca. Effect of injection location on the effectiveness of an active control system using secondary fuel injection. In *Proceedings of the Combustion Institute*, volume 28, pages 739–746. Combustion Institute, 2000.

[76] M. M. Elkotb. Fuel atomization for spray modelling. *Progress in Energy and Combustion Science*, 8(1):61–91, 1982.